HEXA-X-II

A holistic flagship towards the 6G network platform and system, to inspire digital transformation, for the world to act together in meeting needs in society and ecosystems with novel 6G services

Deliverable D4.5

Final Results of 6G Radio Key Enablers

Co-funded by the European Union

6GSNS

Hexa-X-II project has received funding from the Smart Networks and Services Joint Undertaking (SNS JU) under the European Union's Horizon Europe research and innovation programme under Grant Agreement No 101095759.

Date of delivery:	28/02/2025	Version:	1.0
Project reference:	**101095759**	Call:	**HORIZON-JU-SNS-2022**
Start date of project:	01/01/2023	Duration:	30 months

Document properties:

Document Number:	D4.5
Document Title:	Final results of 6G Radio Key Enablers
Editor:	Ahmad Nimr (TUD), Italo Atzeni (OUL), Gustavo Tejerina (OUL), Nuwanthika Rajapaksha (OUL), Nurul Huda Mahmood (OUL).
Authors:	Mar Francis De Guzman (AAU), Hamed Farhadi (EAB), Italo Atzeni (OUL), Roberto Fantini (TIM), Sharief Saleh (CHA), Christian Drewes (APP), Nurul Huda Mahmood (OUL), Mohammad Hossein Moghaddam (QRT), Rafael Puerta (EAB), Gustavo Tejerina (OUL), Charitha Madapatha (CHA), Venkatesh Tentu (CHA), Tommy Svensson (CHA), Akshay Vayal Parambath (CHA), Efstathios Katranaras (SEQ), Alexander Chiskis (SEQ), Rami Verbin (SEQ), Olivier Marco (SEQ), Bikshapathi Gouda (OUL), Omer Haliloglu (EBY), Eduardo Noboro Tominaga (OUL), Henk Wymeersch (CHA), Yu Ge (CHA), Hui Chen (CHA), José Miguel Mateos (CHA), Marie Le Bot (ORA), Bruno Jahan (ORA), Thibaut Rolland (ORA), Emmanuelle Bodji (ORA), Rodolphe Legouable (ORA), Jean-Marc Conrat (ORA), Bruno Melis (TIM), Davide Sorbara (TIM), Elisa Zimaglia (TIM), Meik Dörpinghaus (TUD), Florian Gast (TUD), Simon Lindberg (QRT), Andreas Wolfgang (QRT), Hardy Halbauer (NGE), Ravi Sharan (NGE), Le Hang Nguyen (NGE), Raquel Esteban Puyuelo (EAB), Athanasios Stavridis (EAB), Bo Xu (EAB), Stanislav Zhekov (EAB), Heunchul Lee (EAB), Jaeseong Jeong (EAB), David Sandberg (EAB), Muris Sarajlić (EAB), Luis G. Uzeda Garcia (NFR), Andre Noll Barreto (NFR), Iman Hmedoush (NFR), Rafael Berkvens (IMEC), Dani Korpi (NFI), Jose Flordelis (SON), Rreze Halili (IMEC), Amitha Mayya (BI), Bertram Gunzelmann (APP), Benedikt Schweizer (APP), Philipp Schulz (TUD), Ivo Bizon Franco de Almeida (TUD), Bitan Banerjee (TUD), Sinuo Ma (TUD), Carl Collmann (TUD), Pekka Kyösti (OUL), Katsuyuki Haneda (AAU), Mikhail Wilhelm (APP), Nil Zaev (APP), Hannu Flinck (AAU), Tanesh Kumar (AAU), Petri Mähönen (AAU), Ilkka Harjula (NFI), Oskari Tervo (NFI), Arto Lehti (NFI), Nuwanthika Rajapaksha (OUL), Pasan Karunasena (OUL), Dileepa Marasinghe (OUL), Nandana Rajatheva (OUL), Mehdi Letafati (OUL), Ali Kourani (AAU), Jaime Luque Quispe (NGE), Yann Lebrun (QLC), Taesang Yoo (QLC), Mikko Honkala (NFI).
Contractual Date of Delivery:	28/02/2025
Dissemination level:	PU[1]
Status:	Finalized
Version:	1.0
File Name:	Hexa-X-II D4.5_v1.0

[1] SEN = Sensitive, only members of the consortium (including the Commission Services). Limited under the conditions of the Grant Agreement

PU = Public

Revision History

Revision	Date	Issued by	Description
0.1	18/12/2024	Hexa-X-II WP4	Document created
1.0	17/02/2025	Hexa-X-II WP4	v1.0 created
1.0	26/02/2025	Hexa-X-II WP4	v1.0 finalized

Abstract

This report provides final results on selected key enablers for 6G radio design, developed within Hexa-X-II work package 4: "Radio Evolution and Innovation". The report begins with an overview of holistic radio design and corresponding enablers. Subsequent technical studies cover a range of topics in channel modelling, radio architecture and deployment for communication and sensing, model and data-driven transmission schemes and signal processing algorithms, spectrum access, and radio trustworthiness. Evaluation results are obtained through simulation frameworks and proof-of-concept platforms. This analysis provides inputs for the second iteration towards the end-to-end 6G system design in the Hexa-X-II project.

Keywords

6G, radio access technology (RAT), physical layer (PHY), medium access control (MAC), channel modelling, multiple-input multiple-output (MIMO), distributed MIMO (D-MIMO), massive MIMO (mMIMO), multi-user MIMO (MU-MIMO), integrated access and backhaul (IAB), beamforming, 1-bit analogue-to-digital converter (1-bit ADC), reconfigurable intelligent surfaces (RIS), waveform, artificial intelligence/machine learning (AI/ML), AI-driven air interface design, joint communication and sensing (JCAS), terrestrial network/non-terrestrial network (TN/NTN), spectrum sharing, frequency range 1 (FR1), frequency range 2 (FR2), sub-terahertz (sub-THz), terahertz (THz), spectrum access, proof of concept (PoC), physical layer security (PHY security), trustworthiness.

Executive Summary

The Hexa-X-II project is a flagship initiative bringing together key stakeholders in Europe for 6G research, continuing the work of the Hexa-X project. Hexa-X-II includes the key industry players in telecom and major research institutes; a combination of innovative knowledge capable of introducing new value chains for future connectivity solutions. Furthermore, the Hexa-X-II project comprises several work packages that span over important parts of the 6G ecosystem.

The overarching objective of work package 4 (WP4) - "Radio Evolution and Innovation" is to develop a 6G system that will enable breakthrough technologies and interfaces for connectivity services, building on the progress of 5G-Advanced and meeting the demands of the 2030s. WP4 further aims to expand the scope of networks by enabling technologies and interfaces for novel digital services building on new network capabilities of sensing, compute, and AI.

This report is the final public deliverable (D4.5) of WP4 of Hexa-X-II. It provides an updated perspective on selected radio design enablers introduced in the public deliverable D4.3 [HEX224-D43] along with final results based on simulation and proof-of-concepts (PoC) evaluation. The report contributes towards the overall end-to-end sixth generation (6G) system design presented by the Hexa-X-II project.

The report begins with an overview of the holistic radio design process concept, aimed at fulfilling emerging communication and sensing requirements, considering regulatory aspects and value consideration in sustainability, trustworthiness, and inclusiveness. Moreover, some potential 6G applications and use cases impose extreme requirements, such as exploring new spectrum to enable high data rate communication and precise sensing. These deliberations pose constrains on material and energy usage and introduce new value-based radio design requirements.

In terms of radio channel characterization, this deliverable introduces measurements and results covering the sub-THz frequencies (100-300 GHz) as well as the mid-band or FR3 (7-24 GHz). Furthermore, the channel model components in the commonly used channel models that would require updates to reflect the operating condition of 6G systems are specified.

Various variants of MIMO systems, which will continue to play a dominant role in 6G, are thoroughly covered in this deliverable. The performance of D-MIMO systems considering factors such as resource allocation, deployment strategies, hardware constraints, and channel dynamics are examined; along with the potential integration of joint communication and sensing (JCAS) capabilities within D-MIMO deployments. Moreover, suitable architectures and hardware designs aimed at mitigating power consumption while maximizing system performance of massive MIMO systems are examined.

Reconfigurable intelligent surfaces (RIS) offer a novel way to enhance the performance of wireless networks. It has been identified as a potentially cost-effective and energy-efficient candidate to meet the increasing demand for high-speed and reliable wireless communication. Extended end-to-end validations of RIS is verified, and the challenges regarding the integration of RIS into existing and future wireless networks are examined in this report.

Given that future 6G systems will operate with a much larger bandwidth in the FR3 and sub-THz bands, designing innovative waveforms and modulation schemes is fundamental for harnessing the potential of such systems, regardless of the frequency band. Thus, waveform and modulation candidates for sub-THz communications and new enhancements to known techniques are investigated in this report. Examples include an adaptative multicarrier modulation resistant to Doppler shift and out-of-band emissions, and a new matrix design for low-density parity check (LDPC) codes.

Innovative solutions that leverage AI to refine the air interface design will inevitably play an integral role in future 6G systems are also explored in this deliverable. Examples include utilizing AI to enhance modulation and coding techniques, optimize MIMO waveforms, and advancing CSI acquisition & prediction. Furthermore, AI's role in revolutionizing MIMO transmissions through advanced antenna management, power control and user pairing strategies are discussed and its potential to address power amplifier non-linearities are highlighted.

Sensing capabilities as an integral part of the network, enabled through JCAS, will be a novel feature of future 6G systems. JCAS is considered in this deliverable from two perspectives, namely JCAS deployment scenarios and JCAS resource optimisation. Various modalities and enablers of JCAS are investigated in the former category, whereas methods to increase the sensing range bistatic scenarios and procedures and protocols involved in inter-UE bistatic sensing are studied in the latter.

The success of 6G will rely on its ability to leverage the scarce existing frequency ranges and the availability of new suitable spectrum enabling macro-cellular deployments to satisfy requirements of new use cases. When it comes to flexible spectrum usage, coexistence between terrestrial networks (TN) and non-terrestrial networks (NTN) will be a key aspect both from spectrum and global coverage point of view. In addition, flexible and unencumbered solutions allowing a smooth migration from 5G to 6G in a shared spectrum is crucial.

Trustworthiness, one of the three core values targeted by Hexa-X-II, is also covered in this report. Trustworthiness can be achieved through a trustworthy architecture design, covering security, privacy, and resilience enabled by an inclusive design that covers the entire network lifecycle. As a concrete example, different techniques to counter jamming attacks are required, e.g., through jammer localization. Moreover, the introduction of sensing capabilities in JCAS scenarios admits new security threats hitherto unheard of in existing 5G systems.

Finally, the last technical chapter in this deliverable gives proof for the emerging concepts in 6G. It includes the link modelling for 6G to evaluate the performance of 6G PHY, a flexible transceiver system to adapt to different requirements dynamically without changing the default static system configuration, AI-native air interface to address the emergence of AI in 6G, bi-static joint communication and sensing as a dual use of telecom infrastructure promised for 6G, power consumption analysis for sustainability and energy management mayhems, EMF assessments of D-MIMO deployments in an industrial indoor environment, and channel modelling as an inevitable part for 6G standardization.

Table of Contents

List of Tables

List of Figures

Acronyms and abbreviations

Term	Description
2D	Two-Dimensional
3D	Three-Dimensional
4G	Fourth Generation
3GPP	The 3rd Generation Partnership Project
5G	Fifth Generation
5GCM	5G Channel Model
6D	Six-Dimensional
6DoF	Six Degrees of Freedom
6G	Sixth Generation
A2C	Advantage Actor Critic
AAS	Active Antenna System
ACLR	Adjacent Channel Leakage Ratio
ADC	Analog-to-Digital Converter
AE	Antenna Element
AI	Artificial Intelligence
AMCM	Adaptive Multicarrier Modulation
ANN	Artificial Neural Network
AO	Alternating Optimisation
AoA	Angle-of-Arrival
AoD	Angle-of-Departure
AP	Access Point
API	Application Programming Interface
ARoF	Analogue Radio-over-Fibre
ASA	Azimuth Angle Spread of Arrival
ASD	Azimuth Angle Spread of Departure

ASV	Auxiliary Vector Synchronization
AU	Antenna Unit
AuE	Autoencoder
AWG	Arbitrary Waveform Generator
AWGN	Additive White Gaussian Noise
BCE	Binary Cross Entropy
BER	Bit Error Rate
BF	Beamforming
BG	Base Graph
BLER	Block Error Rate
BMMSE	Bussgang-based Minimum Mean Squared Error
BMRC	Bussgang-based Maximum Ratio Combiner
BO	Back-Off
BP	Belief Propagation
BPF	Bandpass Filter
BR	Best Response
BR-GS	Best Response – Group Specific
BS	Base Station
CA	Carrier Aggregation
CCO	Constrained Cardinality Optimization
CDF	Cumulative Distribution Function
CDL	Clustered Delay Line
CF	Consumption Factor
CFO	Carrier Frequency Offset
CHO	Conditional Handover
CI	Close-In
CJT	Coherent Joint Transmission
CM	Coded Modulation

CNN	Convolutional Neural Network
CoMP	Coordinated Multi-Point
CP	Cyclic Prefix
CPE	Common Phase Error
CP-OFDM	Cyclic Prefix Orthogonal Frequency Division Multiplexing
CPU	Central Processing Unit
CQI	Channel Quality Indicator
CRB	Cramér-Rao Bound
CRC	Cyclic Redundancy Check
CRLB	Cramér-Rao Lower Bound
CS	Common Signalling
CSF	Channel State Feedback
CSI	Channel State Information
CSI-RS	Channel State Information Reference Signal
CSMA/CA	Carrier-Sense Multiple Access with Collision Avoidance
CU	Central Unit
CZF	Centralized Zero Forcing
D/A	Digital/Analog
D2D	Device-to-Device
DAC	Digital-to-Analog Converter
DAPS	Dual-Active Protocol Stack
DAS	Distributed Antenna System
DBICM	Delayed Bit Interleaved Coded Modulation
DfD	Dataflow Diagram
DFE	Digital Frontend
DFT	Discrete Fourier Transform
DFT-s-OFDM	Discrete Fourier Transform-Spread-Orthogonal Frequency Division Multiplexing
DL	Downlink

D-MIMO	Distributed MIMO
DMRS	Demodulation Reference Signal
DNN	Deep Neural Network
DPD	Digital Pre-Distortion
DPoD	Digital Post-Distortion
DQN	Deep Q-Network
DRU	Distributed Radio Unit
DS	Delay Spread
DSO	Digital Storage Oscilloscope
DSP	Digital Signal Processor
DSS	Dynamic Spectrum Sharing
EA	Electrical Amplifier
EBG	Electromagnetic Band Gap
ECL	External Cavity Laser
EDLC	Early Detect Late Commit
EGT	Equal Gain Transmission
EIRP	Equivalent Isotropic Radiated Power
EM	Electromagnetic
eMBB	Enhanced Mobile Broadband
EMD	Empirical Mode Decomposition
EMF	Electromagnetic Field
ETSI	European Telecommunications Standards Institute
eType2	Enhanced Type2
EU	European Union
EVM	Error Vector Magnitude
FCNN	Fully Connected Neural Network
FDD	Frequency Division Duplexing
FFT	Fast Fourier Transform

FHPPP	Finite Homogeneous Poisson Point Process
FI	Floating-Intercept
FoV	Field of View
FPGA	Field Programmable Gate Array
FR	Frequency Range
FS	Fixed Services
FSS	Fixed Satellite Service
GEO	Geostationary Orbits
GFLOPS/W	Giga-Floating-Point Operations per Second per Watt
GG	Greedy Genie
gNB	Next Generation Node B
GNN	Graph Neural Network
GNSS	Global Navigation Satellite System
GPI	Gain-Phase Impairment
GPU	Graphics Processing Unit
GS	Geometric Shaping
HAPS	High Altitude Platform Station
HARQ	Hybrid Automatic Repeat Request
HO	Handover
HPBW	Half Power Beam Width
HW	Hardware
I/Q	In-Phase/Quadrature
IAB	Integrated Access and Backhaul
ICI	Intercarrier Interference
ICRB	Intrinsic Cramér-Rao Bound
IFFT	inverse fast Fourier transform
IIoT	Industrial Internet of Things
IMI	Incremental Multi-Inference

IMT	International Mobile Telecommunications
IoT	Internet of Things
ISAC	Integrated Sensing and Communications
ISD	Inter-Site Distance
ITU	International Telecommunication Union
JCAS	Joint Communication and Sensing
JD	Joint Data Detection
JS	Joint Scheduler
JSR	Jamming-to-Signal Ratio
KPI	Key Performance Indicator
K-S	Kolmogorov-Smirnov
KVI	Key Value Indicator
LBT	Listen-before-Talk
LCM	Life Cycle Management
LCS	Local Coordinate System
LDPC	Low Density Parity Check
LEO	Low-Earth Orbit
LINDDUN	Linking, Identifying, Non-repudiation, Detecting, Data Disclosure, Unawareness, and Non-compliance
LMMD	Linear Minimum Mean Dispersion
LNA	Low-Noise Amplifier
LO	Local Oscillator
LoS	Line-of-Sight
LPWAN	Low-Power, Wide-Area Networks
LR-FHSS	Long-Range Frequency Hopping Spread Spectrum
LSTM	Long Short-Term Memory
LTE	Long Term Evolution
MAA	Movable Antenna Array
MAC	Medium Access Control

MAPRT	Maximum A-Posteriori Ratio Test
MB-ML	Model-Based Machine Learning
MCS	Modulation and Coding Scheme
MIMO	Multiple-Input Multiple-Output
MISO	Multiple-Input Single-Output
ML	Machine Learning
mMIMO	Massive Multiple-Input Multiple-Output
MMSE	Minimum Mean Squared Error
mMTC	Massive Machine-Type Communications
mmWave	Millimetre Wave
MRAA	Movable and Rotary Antenna Array
MRC	Maximum Ratio Combining
MRSS	Multi-RAT Spectrum Sharing
MRT	Maximum Ratio Transmission
MS	Mobile Station
MSE	Mean Squared Error
MTD	Machine-Type Device
MU-MIMO	Multi-User MIMO
MUT	Material Under Test
MZM	Mach-Zehnder Modulator
NAM	Neural Antenna Muting
NCJT	Non-Coherent Joint Transmission
NCR	Network-Controlled Repeater
NEF	Network Exposure Function
NGSO	Non-Geostationary Orbit
NLoS	Non-Line-of-Sight
NN	Neural Network
NR	New Radio

NR-U	NR Unlicensed
NTN	Non-Terrestrial Network
NW	Network
OFDM	Orthogonal Frequency-Division Multiplexing
OLoS	Obstructed-Line-of-Sight
OQAM	Offset Quadrature Amplitude Modulation
O-RAN	Open Radio Access Network
OSTC	Orthogonal Space-Time Coding
OTA	Over-the-Air
PA	Power Amplifier
PAPR	Peak-to-Average Power Ratio
PB	Plasterboard
PB-DP	Plasterboard Coated with a Painted Relief Decorative Plaster
PB-OP	Plasterboard Coated by a Paint with an Increased Orange Peel Effect
PBR	Phase-Based Ranging
PB-Raw	Raw Plasterboard
PB-SP	Plasterboard Coated by a Smooth Paint
PB-WP	Plasterboard Coated by a Painted Relief Non-Woven Wallpaper
PCI	Physical Cell ID
PD	Photodetector
PDCP	Packet Data Convergence Protocol
PDF	probability density function
PDSCH	Physical Downlink Shared Channel
PEB	position error bound
PHY	Physical Layer
PLL	Phase-Locked Loop
PMI	Precoding Matrix Indicator
PN	Phase Noise

PoC	Proof-of-Concept
PPS	Pulse-Per-Second
PRB	Physical Resource Blocks
pRSG	Pseudorandom Sequence Generator
PSD	Power Spectral Density
PSK	Phase Shift-Keying
PSO	Particle Swarm Optimisation
PTRS	Phase Tracking Reference Signal
QAM	Quadrature Amplitude Modulation
QC-LDPC	Quasi Cyclic – Low Density Parity Check
QoS	Quality of Service
QRM	Quadrature Reflection Modulation
QUIC	General-purpose transport layer network protocol (“Quick UDP Internet Connections”)
RAA	Rotary Antenna Array
RAN	Radio Access Network
RAT	Radio Access Technology
RCS	Radar Cross Section
RE	Resource Element
RED	Radio Equipment Directive
ReLU	Rectified Linear Unit
RF	Radio Frequency
RFFI	Radio Frequency Fingerprinting Identification
RFIC	Radio-Frequency Integrated Circuit
RF-SU	RF Sensing Units
RIS	Reconfigurable Intelligent Surface
RL	Reinforcement Learning
RLC	Radio Link Control
RM	Reflection Modulation

RMS	Root Mean Square
RMSE	Root-Mean-Square Error
RNN	Recurrent Neural Network
RPC	Remote Procedure Calls
RPM	Reflection Pattern Modulation
RR	Round Robin
RRC	Root Raised Cosine
RRH	Remote Radio Head
RS	Reference Signal
RTT	Round-Trip Time
RU	Radio Unit
RULA	Rotary Uniform Linear Array
Rx	Receiver
SB	Sub-Band
SCF	Sensing Control Function
SCM	Spectrum Consumption Model
SCS	Subcarrier Spacing
SDR	Software-Defined Radio
SE	Spectral Efficiency
SER	Symbol Error Rate
SF	Spreading Factors
SFN	Single Frequency Network
SGCS	Squared Generalized Cosine Similarity
SINDR	Signal-to-Interference-Noise and Distortion Ratio
SINR	Signal-to-Interference-plus-Noise-Ratio
SISO	Single-Input Single-Output
SLA	Service Level Agreements
SMF	single-mode fibre

SMI	Shifting Multi-Inference
SMTC	Satellite Measurement Timing Configuration
SNR	Signal-to-Noise Ratio
SNS JU	Smart Network and Services Joint Undertaking
SPCTM	Sensing Policy, Consent, and Transparency Management
SPF	Sensing Processing Function
SRG	Specular Reflection Gain
SSB	Synchronisation Signal Block
STRIDE	Spoofing, Tampering, Repudiation, Information Disclosure (Breach or Leak), Denial of Service, and Elevation of Privilege
SU	Sensing Unit
SUD	Single-UE Data Detection
SVD	Singular Value Decomposition
TAM	Transmit Antenna Muting
TDD	Time-Division Duplex
TDL	Tapped Delay Line
TLS	Transport Layer Security
TN	Terrestrial Network
ToF	Time-of-Flight
Tx	Transmitter
TXRU	Transceivers Unit
UAV	Unmanned Aerial Vehicle
UDP	User Datagram Protocol
UE	User Equipment
UL	Uplink
ULA	Uniform Linear Array
UMa	Urban Macro-Cellular
UMi	Urban Micro-Cellular

URLLC	Ultra-Reliable Low-Latency Communication
USRP	Universal Software Radio Peripheral
VCO	Voltage-Controlled Oscillator
VNA	Vector Network Analyser
WAN	Wireless Area Network
WP4	Work Package 4
ZF	Zero Forcing
ZXM	Zero-Crossing Modulation

1 Introduction

Hexa-X-II is the sixth generation (6G) flagship project under the European Union Horizon Europe research and innovation program, Smart Network and Services Joint Undertaking (SNS JU), for building a system blueprint of sustainable, inclusive, and trustworthy 6G platform. This document is the fifth deliverable (D4.5) of work package 4 (WP4) - "Radio Evolution and Innovation". The work in WP4 focuses on the development of radio access solutions that meet the requirements of 6G services for communication and sensing. The research and innovation within WP4 focus on the following key aspects:

- Sustainable, trustworthy and inclusive holistic radio design
- Towards THz communications
- Joint communications and sensing
- Intelligent radio air interface design
- Flexible spectrum access solutions

The second deliverable of WP4 (D4.2) [HEX223-D42] analyses 6G use cases and defines 6G radios scenarios and, along with corresponding key performance indicators (KPIs) and key value indicators (KVIs) requirements for communications and sensing. It also presents and describes key 6G radio design enablers which guide the work in WP4. Initial analysis results of selected radio enablers are presented in the third deliverable (D4.3) [HEX224-D43].

1.1 Objective of the document

This report presents final results of selected radio enablers, which are described in (D4.2) [HEX223-D42] and initially evaluated (D4.3) [HEX224-D43]. These enablers cover various aspects of holistic radio design at both the physical layer (PHY) and medium access layer (MAC), including new spectrum and access solutions, efficient transmission schemes, architecture and deployment approaches for both communication and sensing. It also discusses radio link modelling and simulation tools, advanced signal processing and algorithms based on artificial intelligence (AI) and machine learning (ML), as well as proof-of-concept (PoC) and prototyping platforms. In addition, solutions are considered for enhancing KVI-related to social and environmental sustainability. These include optimization methods for improving energy efficiency, integration of terrestrial network (TN) and non-terrestrial network (NTN), physical layer security, and techniques to overcome jamming. The report contributes to the Hexa-X-II WP4 objectives as outlined in the following:

WPO 4.1: Develop an inclusive, trustworthy, and flexible radio design tailored to meet given 6G KPIs and KVI requirements through analysis and integration of HW architectures, transmission schemes and security solutions.

Holistic radio design is discussed in D4.2, which defines radio scenarios and determines KPIs and KVIs requirements for communications and sensing services based on an initial analysis of use cases. Moreover, D4.2 presents the impact of these use cases and scenarios on various components of the radio design. Additionally, D4.2 describes various enablers for 6G radio design. These enablers are organized into multiple categories within the holistic radio design framework presented in D4.3, along with initial results of various radio enablers, which are further investigated in D4.5.

Chapter 2 introduces a review and refinement of the holistic radio design framework and its corresponding categorizes, as well as the radio scenarios and use cases. Chapter 10 provides final design and evaluation results on radio enablers focusing on trustworthiness. These include a proposal of resilient-by-design concept in Section 10.1, Jamming analysis in Section 10.2, which provides insights into the impact of various interference conditions on the communication performance and the evaluation of techniques for identifying and localizing jammers, and a security and privacy analysis in Section 10.3, presenting evaluation results on the use 6G joint communications and sensing (JCAS) for a cross-road monitoring system. With respect to the inclusive radio interface, Section 9.4 focuses on TN/NTN enhancement, particularly presenting solutions for improving handover efficiency, approaches to mitigate TN and NTN mutual interference, and a comparison of the performance of high altitude platform stations (HAPS) versus satellites in improving coverage. In addition, Section 11.6 presents a simulation tool and evaluation results on electromagnetic field (EMF) assessment for

distributed multiple-input multiple-output (D-MIMO), whereas Section 3.8 discusses the implications of sub-THz link budget on EMF compliance.

WPO 4.2: Provide a suitable channel model and develop novel broadband air-interface techniques to enable energy-efficient operations in the (sub-)THz bands, including new energy-efficient waveforms/modulations and advanced massive MIMO techniques.

While D4.2 provides descriptions of the corresponding enablers for transmissions in the sub-THz range, including channel modeling, massive multiple-input multiple-output (mMIMO), and waveforms, D4.3 introduces initial numerical results, which are further evaluated in D4.5.

Chapter 3 presents a refined channel modeling framework applicable to sub-THz frequencies, along with results on various modeling aspects. Section 3.1 provides measurements and assessments for material reflection; Section 3.2 derives a simplified model to characterize molecular absorption loss above 100 GHz; Section 3.3 presents results on path loss parameters for two industrial environments at 234 GHz and 318 GHz; Section 3.4 assesses near-field models; Section 3.5 presents improvements to the 3GPP channel model; and Section 3.6 introduces a ray-tracing calibration process to generate realistic data through simulation. Additionally, channel measurements at FR3 (15 GHz) are conducted and presented in Section 3.7.

Massive MIMO architectures for sub-THz are further evaluated in Section 4.3, with performance analysis of power consumption considering various architectures and deployment options in Section 4.3.1, and a revision of the hybrid beamforming architecture in Section 4.3.2. Additionally, an analysis of low-complexity architectures with one-bit DAC/ADC is presented in Section 4.5, evaluating reliability under various configurations.

Further results on sub-THz waveforms are presented in Section 6.1, including simulation and measurement results for evaluating the feasibility of fifth generation (5G) New Radio (NR)-compatible waveforms, a proposal for polar constellation, and additional insights into zero-crossing modulation (ZXM) for energy efficiency compared to conventional modulation. Additionally, Section 9.3.1 presents a solution for low-latency access based on a sub-THz booster RAT.

WPO 4.3: Provide solutions that enable flexible, cross-functional joint communication and sensing over a unified radio infrastructure, including new architectures, signals, methods, and protocols.

JCAS enablers are discussed in D4.2, covering aspects such as deployment, waveforms, resource allocation, as well as security and privacy considerations. D4.3 presents evaluation results on various topics, including integrated monostatic and bistatic sensing, along with resource allocation for six degrees of freedom (6DoF) tracking in reconfigurable intelligent surface (RIS)-aided scenarios. Additionally, D4.5 provides an overview of JCAS channel modelling and initial PoC results on bistatic JCAS, with further complementary findings also included in D4.5.

Chapter 8 focuses on JCAS in relation to infrastructure, resource allocation, and signal processing. Section 8.1 explores various JCAS deployment scenarios, including the integration of NTNs with low-Earth-orbit (LEO) satellites and RISs for localizing terrestrial user equipment (UE) in Section 8.1.1. Section 8.1.2 examines the performance of multistatic sensing for detecting and localizing unmanned aerial vehicles (UAVs) using terrestrial base stations (BSs). In addition, Section 4.2 discusses the potential of D-MIMO for JCAS. Section 8.2 investigates protocols and techniques to enhance sensing performance. Specifically, Section 8.2.1 explores improvements in sensing range by adjusting the cyclic prefix (CP) of orthogonal frequency-division multiplexing (OFDM) systems. Section 8.2.2 delves into the procedures and protocols involved in inter-UE bistatic sensing, addressing aspects such as discovery, encryption, synchronization, and sensing.

AI-based JCAS waveform design and processing are presented in Section 7.2.2. Further development and evaluation of bistatic JCAS PoC are detailed in Section 11.4, while Section 11.5 assesses JCAS power consumption in relation to performance requirements.

WPO 4.4: Design intelligent radio air interface to improve one or a combination of KPIs including spectral efficiency, energy efficiency, coverage, or lower cost at FR1 and FR2 spectrum.

D4.2 explores various air interface techniques aimed at enhancing communication in frequency range 1 (FR1) and FR2. These techniques include AI-driven air interface design, mMIMO and D-MIMO transmissions, as

well as RIS-assisted transmission schemes. Initial evaluation results regarding throughput, spectral efficiency, and coverage are presented in D4.3, with further extensions and refinements provided in D4.5.

Chapter 4 focuses on multiple-input multiple-output (MIMO) enhancements, particularly the application of data-driven methods to optimize precoding performance for multi-user MIMO (MU-MIMO), as discussed in Section 4.4. The deployment of D-MIMO systems and their associated technical challenges are analysed in detail to optimize spectral efficiency, mitigate blockage, and improve the link budget, and thus enhancing coverage and reliability. Performance evaluations consider key factors such as resource allocation, deployment strategies, hardware constraints, and channel dynamics. Section 4.1 examines various transmission schemes, including coherent precoding for blockage mitigation, space-time coding in scenarios lacking channel state information, and distributed beamforming to address fronthaul capacity limitations. D-MIMO deployment strategies and architectures are detailed in Section 4.2, which covers the integration of rotary arrays using movable and rotatable antennas to dynamically enhance coverage and efficiency, as well as the adoption of analogue fronthaul to achieve precise synchronization across distributed antennas.

Chapter 5 is dedicated to RIS, an emerging technology designed to effectively control the propagation environment, enhance signal coverage, and minimize energy consumption. Evaluation results are presented across multiple sections; Section 5.1 analyses received signal quality, Section 5.2 investigates the impact of RIS on coverage improvement in conjunction with D-MIMO deployment, and Section 5.3 explores RIS applications in integrated access and backhaul networks. Additionally, Section 5.4 examines reflection modulation, where RIS reflection patterns are leveraged to convey information, and introduces a generalized framework applicable to both single-user and multi-user scenarios.

Chapter 6 focuses on AI/ML-based solutions for improving spectral efficiency, reliability, and network flexibility. Section 7.2 discusses AI/ML techniques for enhancing MIMO precoding, waveform design, modulation, and coding. Section 7.3 presents evaluation results on AI/ML-driven channel acquisition and prediction, antenna management, power control, and user pairing strategies. Lastly, Section 7.4 explores AI/ML-based solutions for mitigating hardware impairments, such as compensating for power amplifier nonlinearities.

WPO 4.5: Develop spectrum sharing and medium access mechanisms for enabling an efficient transition to 6G (coexistence) and low-latency service access.

D4.2 outlines solutions for flexible spectrum access, including enablers for spectrum sharing and low-latency spectrum access. D4.3 presents initial studies on the assumptions and models for spectrum sharing, including co-channel coexistence between International Mobile Telecommunications (IMT) and Fixed Satellite Service (FSS) ground stations, terrestrial network (TN) and non-terrestrial network (NTN) spectrum sharing in the S-band (2 GHz), multi-radio access technology (RAT) spectrum sharing (MRSS) with 5G, spectrum access methods for sub-THz frequencies, and risk-informed random access. These studies are further refined in D4.5, with additional results provided in Chapter 9.

Section 9.1 explores spectrum sharing and coexistence, analysis boundaries for sharing with FSS earth stations to prevent excessive protection of services in the upper mid-bands (3.8–4.2 GHz). Additionally, spectrum sharing in the centimetric range (7–15 GHz) is evaluated through interference analysis in various deployment scenarios. Section 9.2 examines the 5G–6G multi-RAT MRSS mechanism, focusing on the dynamic sharing of FDD and TDD carriers between 5G and 6G RATs. Section 9.3 introduces low-latency spectrum access mechanisms for sub-THz frequencies, including the use of a booster RAT operating at lower frequencies to coordinate access, as well as a risk-aware spectrum access mechanism.

1.2 Structure of the document

Chapter 2 presents an overview of the holistic radio design concept and introduces group of enablers, around which the remaining chapters are structured. Each main section in these chapters consists of subsections focusing on interrelated topics. Subsections present studies and initial results following an extended abstract structure; They begin by presenting the main problem, then introduce the methodology and system model, and finally summarize the numerical results and their discussions. Further details are presented in the appendices under similar tiles.

Chapter 0 is dedicated to channel modelling in various scenarios, including sub-THz, coverage analysis for THz, link modelling for RIS, and channel modelling concepts for JCAS. Chapter 4 introduces MIMO transmission solutions, with a particular focus on architectures and deployment scenarios for D-MIMO, mMIMO, and RIS-assisted transmission. Chapter 5 presents waveforms and modulations for 6G radio transmissions in sub-THz and other frequency ranges. Chapter 7 discusses radio air interface design leveraging AI/ML methods, covering techniques for waveform and constellation learning, channel state information (CSI) prediction and feedback, solutions for tackling MIMO challenges, and AI for hardware (HW) impairment compensation. Chapter 8 covers radio enablers for joint communications and sensing, focusing on deployment and recourse optimization. Chapter 9 focuses on MAC layer aspects for flexible spectrum sharing and coexistence, random access methods, and enhancement of TNs/NTNs integration. Chapter 10 summarizes topics and studies related to trustworthiness in communication and sensing. Chapter 11 is dedicated to validation, including PoC and simulation tools. The report is concluded in Chapter 12.

2 Sustainable, trustworthy and inclusive holistic radio design

This chapter presents a brief overview of holistic radio design aspects, which are detailed in D4.2 [Chapter 2, HEX223-D42]. First, Section 2.1 provides an overview of the generic design process, highlighting various considerations. Section 2.2 describes the use cases analysis procedure and provides an update on the radio scenarios in relation to HEXA-X-II use cases. A radio design framework is presented in Section 2.3, with an overview of various modules and groups of enablers. Section 2.4 focuses on architecture and deployment options in the context of functional split placement.

2.1 Holistic radio design process overview and technical enablers

Holistic radio design integrates comprehensive considerations, from technical specifications to societal impacts, ensuring that the systems developed are not only technologically advanced but also sustainable, trustworthy, and inclusive.

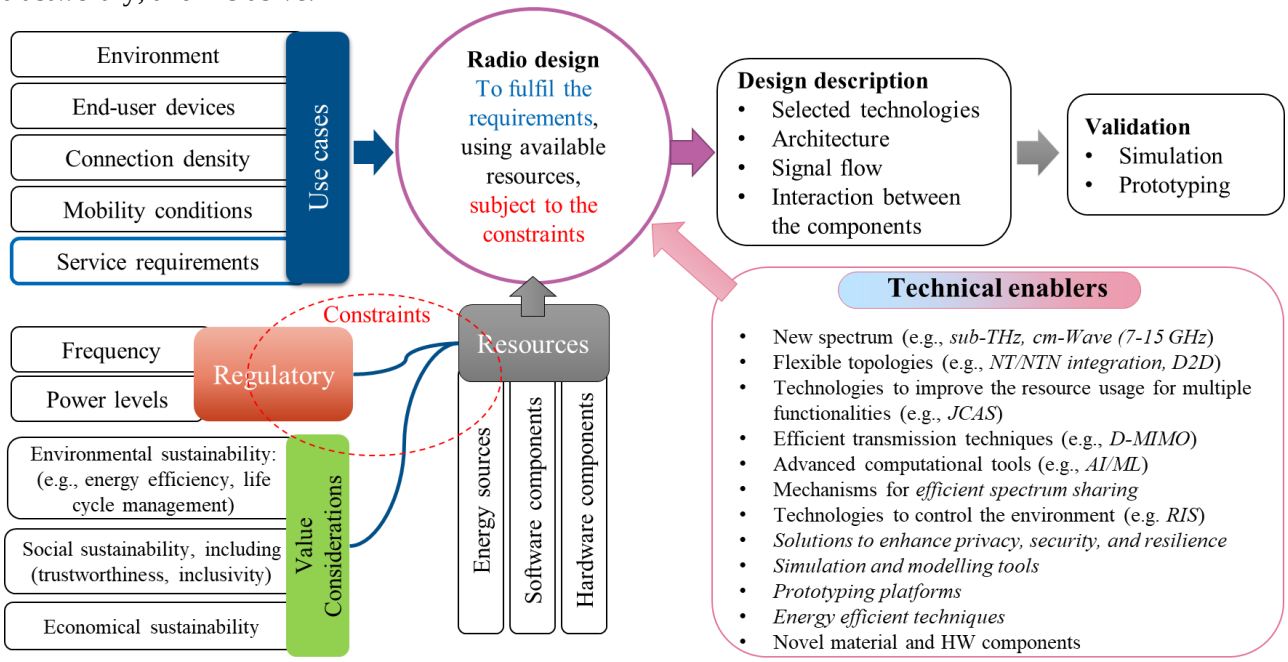

Figure 2-1: Radio design process, emphasising value consideration and technical enablers of HEXA-X-II.

As shown in Figure 2-1, the radio design process is a dynamic framework that evolves with each generation of technology. At its core, it takes specific use cases and their associated requirements as inputs, with the goal of satisfying these requirements through innovative solutions under given constrains, such as regulatory aspects for frequency and spectrum usage, as well as power level. Moreover, 6G radio design in HEXA-X-II emphasizes key values considerations for environmental, social, and economic sustainability [HEX223-D31]. These constraints impose restrictions on the usage of resources for energy, material, software/hardware components. Therefore, innovative technologies and solutions are needed to balance performance with value-based requirements. These include

- New spectrum for meeting the increased demand on data rate. This requires exploring the corresponding channel model, radio frequency (RF) transceiver, HW components, and advanced waveform and transmission techniques. In HEXA-X-II, WP4 studies (sub)-THz communication (above 100 GHz) and cm-Wave (7-15 GHz).
- Flexible topologies enable adaptable network configurations to efficiently meet varying use cases demands and environment, as discussed in [HEX223-D32]. WP4 investigates the impact of various topologies on the radio design, particularly the integration of TNs and NTNs, as well as device-to-device (D2D) communication.
- Technologies to improve the resource usage for multiple functionalities, such as JCAS, which aims to leverage network infrastructure and devices for providing sensing and localization information. Such

information in turns can be used to improve overall communication. WP4 explores various approaches for JCAS deployment and resource sharing across different frequency ranges in Chapter 8.

- Efficient transmission techniques to improve spectral efficiency (SE), energy efficiency, and coverage. WP4 considers various MIMO techniques in Chapter 4, at different frequency ranges, including D-MIMO, mMIMO, and MU-MIMO. WP4 also investigates advanced and enhanced waveforms and modulations schemes in Chapter 4.
- Advanced computational tools, such as AI/ML models. WP4 considers AI/ML for signal processing, resource allocation, and HW impairment compensation in Chapter 7.
- Mechanisms for efficient spectrum sharing to improve spectrum utilization and reduce interference among different radio access technologies (RATs). For instance, WP4 explores sharing solutions for NTN spectrum, such as fixed satellite, with TN, as well as multi-RAT spectrum sharing (MRSS) in Chapter 9.
- Technologies to control the propagation environment, such as deploying RIS, which is considered in WP4 for mitigating blockage and improving coverage, as introduced in Chapter 5.
- Solutions to enhance, privacy, security, and resilience, such as exploiting channel characteristics in physical layer (PHY) security, and sensing and localization to identify and localize jamming. Theses aspects are investigated in Chapter 10.
- Energy efficient techniques, including optimization of deployment, HW, and transmission schemes, in addition to solution for reducing signalling overhead. WP4 emphasises energy efficiency in the design and operation of radio systems.
- Novel material and HW components with minimal environmental impact in terms of reduced energy consumption, and improved durability and recyclability. HW related enablers are presented in [HEX224-D53].

The outputs of the design process are the technologies chosen, system architecture, and detailed mapping of signal flows and component interactions. Validation is executed through simulations and prototyping, ensuring that the system design meets its intended goals. The validation process is enabled by

- Simulation and modelling tools to provide mathematical models for channels and HW components for design and evaluation. WP4 focuses on channel and link modelling for link-level simulations, which are presented in Chapter 3.
- Prototyping platforms for experimental validation prior to commercialization. WP4 utilizes such platforms in various PoCs, as introduced in Chapter 11.

2.2 Use cases analysis and radio scenarios

A successful radio design begins with a precise definition of its use cases. These use cases represent diverse needs and scenarios in which the radio system operates, from urban high-density connectivity to remote access in rural areas. Over generations, use cases have evolved, with increased demands for bandwidth, low latency, high reliability, and massive connectivity. Defining specific radio scenarios and their requirements sets the foundation for a radio system design.

In a typical process, as illustrated in Figure 2-2, a wide range of application use cases are analysed and categorized into families with similar service requirements. The service requirements are mapped to corresponding radio requirements, and a set of scenarios are derived based on extreme radio requirements. The grouping based on extreme requirements provides the most challenging and demanding conditions for radio design. This approach ensures that a radio system designed and optimized for an extreme scenario can meet diverse economic and social needs. A comprehensive analysis based on HEXA-X-II 6G use cases is presented in [HEX223-D42, Sec. 2.3], leading to four scenarios, each focusing on extreme requirements in one parameter while allowing flexibility in other parameters as flexible.

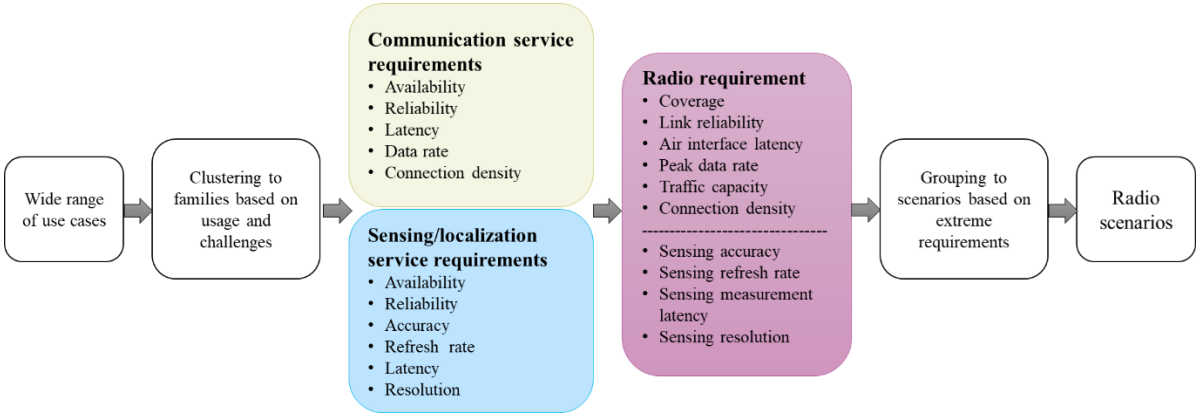

Figure 2-2: Framework for use cases analysis and radio scenario definition.

These scenarios are denoted as (1) Extreme coverage, (2) Extreme data rate, (3) Extreme connection density, (4) Extreme low latency and high reliability. Table 2-1 provides a summary of these scenarios, including radio requirements and various sub-scenario parameters, with a mapping to the HEXA-X-II use case families presented in [HEX223-D12], and the International Telecommunication Union (ITU) usage scenarios [ITU-M.2160].

Table 2-1: Summary of basic radio scenarios with corresponding radio requirements.

	Extreme coverage	**Extreme data rate**	**Extreme connection density**	**Extreme low latency and high reliability**
ITU usage scenario	Ubiquitous connectivity	AI and communication, Immersive communication	Immersive communication, Massive communication	Hyper reliable and low-latency communication, Integrated sensing and communication
HEXA-X-II use case family	Fully connected world, Physical awareness	Immersive experience	Digital twins Trusted environment	Collaborative robots
Representative HEXA-X-II use case	Ubiquitous network, Network-assisted mobility	Seamless immersive reality	Realtime digital twins Human-centric services	Cooperative mobile robots
Radio devices	Enhanced 5G (mMTC, eMBB) devices, Energy neutral devices	Access points for backhaul, Gateway for sensors	Reliable high data rate with bounded latency devices	High reliability & low latency devices
Environment	Mobile indoor, Public indoor, Outdoor (urban, suburban, rural),	Controlled and semi-controlled indoor and outdoor	Urban indoor/outdoor with high density of users High-rise	Indoor, Embedded network
Mobility	Static, up to 300 km/h	Static, up to 10 km/h, controlled mobility (velocity information available)	Static, up to 100 km/h	Static, up to 20 km/h, controlled mobility (velocity information available)
Deployment options	Long/short range, Fixed/temporary, Mobile infrastructure, TN/NTN integration	Small cell, Fixed access, D2D, Sensor network with a gateway	High density of cells, Macro cell, Micro cell, Cell-free	Small cell, On premises, Infrastructure, Sensor network
Frequency	Sub-GHz, sub-6 GHz, 7-15 GHz, satellite frequency ranges	mmWave, sub-THz, mixed and unlicensed for local connections	Sub-6 GHz, 7-15 GHz, mmWave	Private frequency, sub-GHz, sub-6, GHz, 7-15 GHz, mmWave, sub-THz for sensing

Peak data rate (PHY)	< 1 Gbit/s	(10-100 Gbit/s)	< 10 Gbit/s	< 10 Mbit/s
Link reliability	Variable	Variable	Variable	(99.999%-99.999 99%)
Air interface latency	Variable	Variable	Variable	(0.1-10) ms
Connection density	Variable	$<10^6$ device/km^2	(10^6-10^8) device/km^2	Variable
Coverage	Availability (99.99%-99.999 999%)	Local	Variable	Local coverage
Sensing capabilities	Variable	Variable	Variable	Positioning accuracy (0.1-1) cm

2.3 Overview of holistic radio design framework

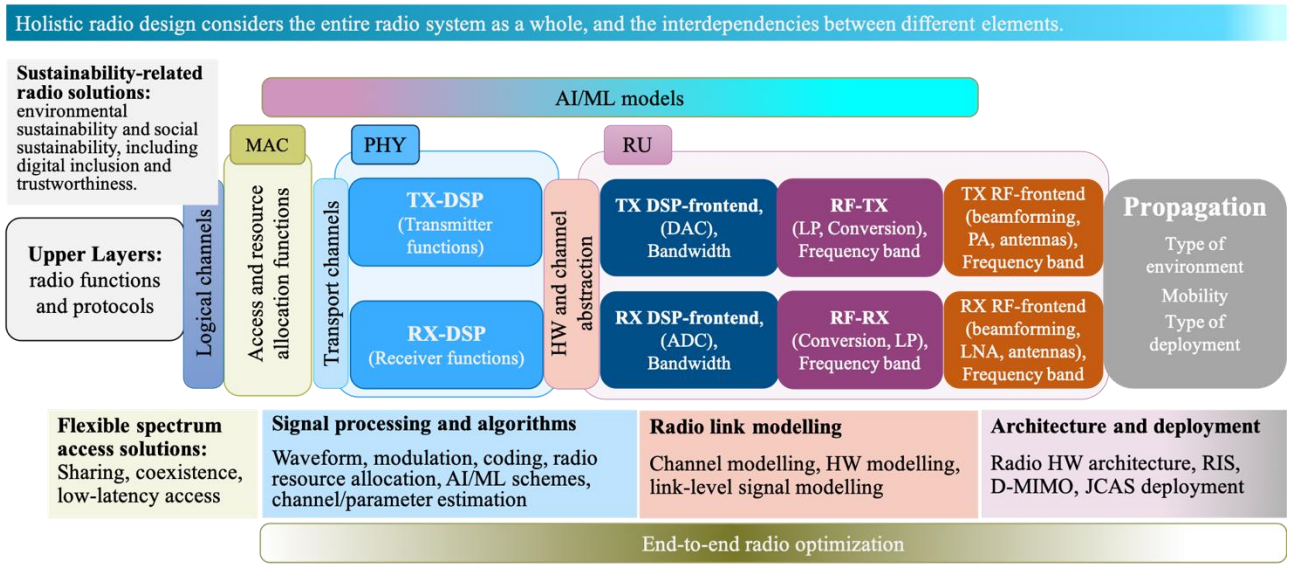

Figure 2-3: Holistic radio design framework.

The holistic radio design approach treats the entire radio system as a whole and considers the interdependencies between different elements. The radio hardware and software are jointly designed to optimize the performance and efficiency of the system. The radio design framework shown in Figure 2-3 illustrates the different modules within the radio system and their interfaces, as well as the group of enablers related to each module.

Propagation environment: It considers physical environment effects on the signal, including obstacles, reflectors, atmospheric effects, etc. It is influenced by the environment, deployment type, and mobility.

RU: The radio unit (RU) consists of RF frontend, frequency conversion, digital/analogue (D/A) conversion. It interacts with the propagation environment through the antennas and with the PHY via digital samples. From the PHY perspective, RU functionality can be abstracted by means of hardware and channel modelling. Various RF transceiver architectures can be implemented in RUs, determined by the number of RF chains and antennas, as well as the resolution of the digital-to-analogue converters (DACs) and analogue-to-digital converters (ADCs), as illustrated in Figure 2-4. For example, fully digital MIMO architecture, Figure 2-4(a), employs one chain per antenna, whereas hybrid beamforming, Figure 2-4(b), uses analogue beamforming, with more antennas than RF chains. Low-resolution DAC/ADC can be used in fully digital architecture, such as 1-bit ADC/DAC massive MIMO, as discussed in Section 4.5.3. Additionally, there are various types of analogue beamforming architectures using fully or partially connected phased arrays or switched beam antenna lenses [HEX224-D53].

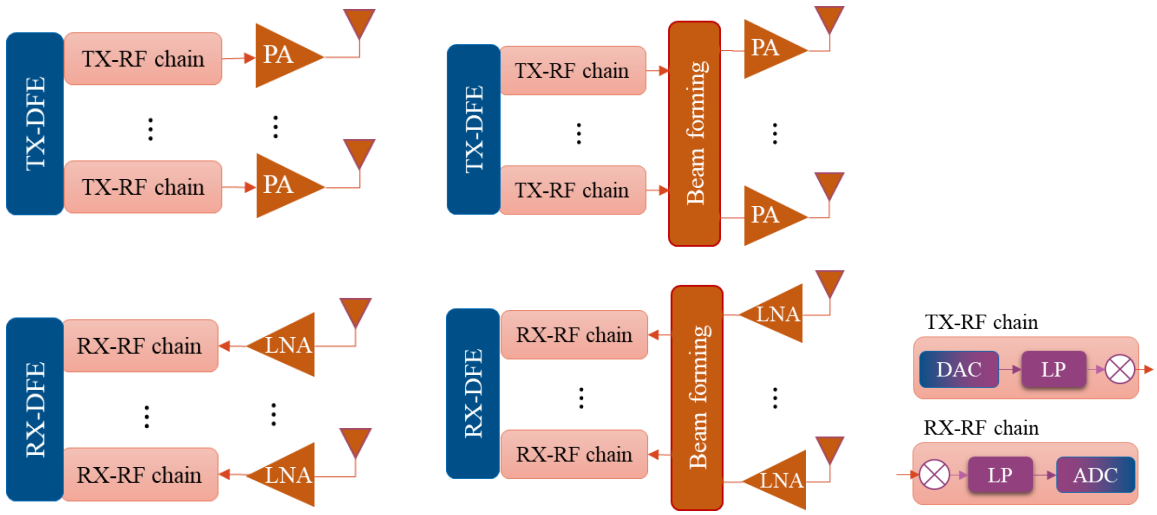

(a) Digital MIMO architecture **(b) Hybrid beamforming architecture** **(c) RF chains**

Figure 2-4: Radio unit architecture options.

Radio link modelling: This is an essential aspect in radio design, providing simulation models for the channel and HW components. Various abstracted channels can be obtained at different levels, as follows:

- Wireless channel: this abstracts the effects of the propagation channel and account for the impact of RF frontend. The characteristic of this channel depends on the frequency range, bandwidth, beamforming, RUs distribution, and deployment scenario. Channel modelling aims to capture the key characteristics and behaviours of wireless channels with respect to the radio signal [TR 38.901]. Details on channel modelling are presented in Chapter 0. Modelling at this level also includes aspects like obtaining models for antenna coupling, power amplifier (PA), and low-noise amplifier (LNA). HW modelling focused on sub-THz is presented in [HEX224-D53, Ch. 2].
- Baseband channel: This extends the wireless channel by considering the effects of frequency converters, including phase noise (PN) and low-pass (LP) filtering.
- Digital baseband channel: This incorporates, in addition to the baseband channel, the effects of DAC and ADC resolution, and digital frontend (DFE) processing, such as filtering and pre-distortion.

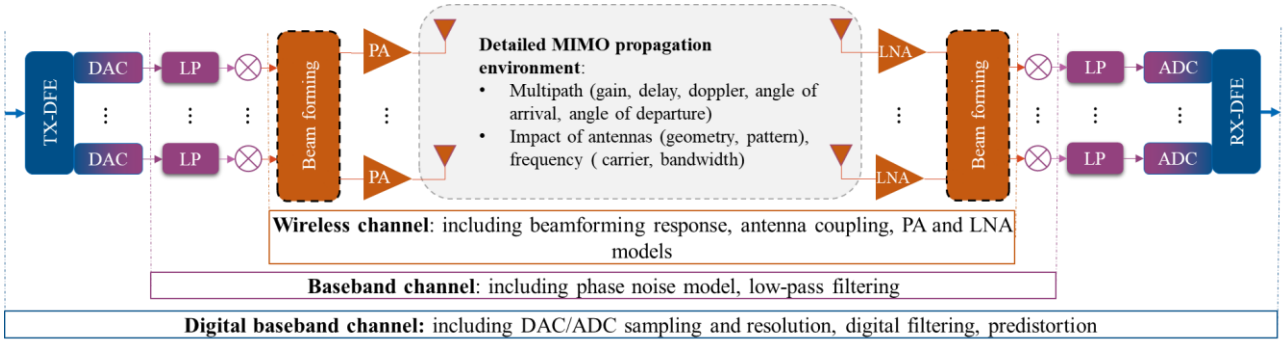

Figure 2-5: Link modelling and equivalent channels.

PHY: It encompasses a broad range of functions related to transmission, detections, CSI feedback, and sensing, as illustrated in Figure 2-6. It provides transport channels to the MAC layer and interacts with the discrete baseband channel. The PHY functions can be implemented using conventional model-based solutions, or employing AI/ML data-driven models, which can address individual functions or a combination of them. Various AI/ML solutions are presented in Chapter 7, whereas Chapter 6 focuses on conventional PHY methods.

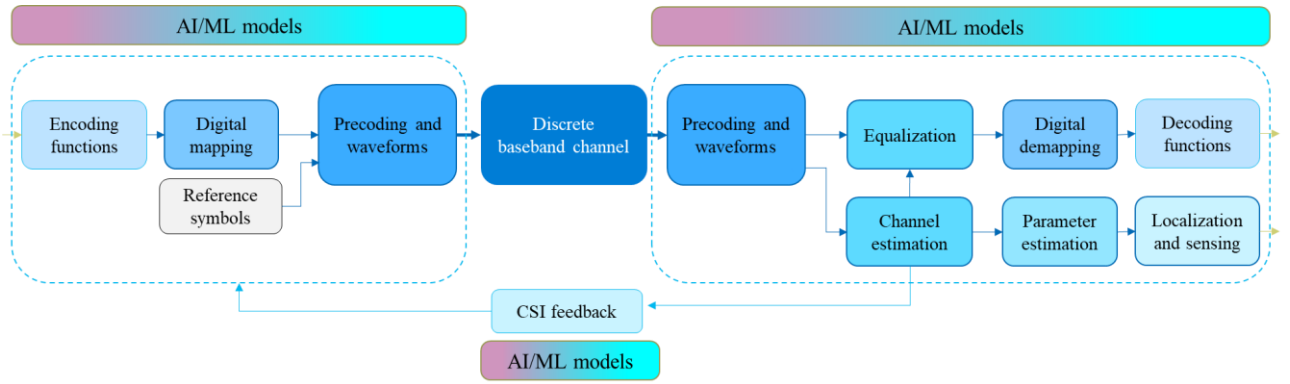

Figure 2-6: PHY functions.

MAC: It is responsible for spectrum access and physical resource allocation. It includes functions for flexible spectrum sharing, coexistence, and low-latency random access. It provides logical channels to the upper layers. Various MAC aspects are presented in Chapter 9.

Upper layers: These layers consist of various radio function and protocols, such as radio link control (RLC), packet data convergence protocol (PDCP), and radio resource control, which operate on top of MAC/PHY [HEX223-D22].

Values focused solutions: These include operational techniques that work alongside the radio infrastructure and PHY/MAC, such as PHY security and anti-jamming mechanisms to improve trustworthiness, as discussed in Chapter 10. Other solutions are discussed in [HEX224-D43].

2.4 Flexible radio architecture and deployment

In radio design, multiple degrees of flexibility in terms of implementation and deployment of various functions can be achieved. Flexibility at PHY/MAC is typically implemented through variable waveform numerologies, adaptive modulation and coding, and dynamic radio resource allocation. This allows the system to adjust to changing conditions and requirements. In the RU, flexibility can be achieved following a software-defined radio (SDR) approach that enables the configuring of carrier frequencies, bandwidth, power level, the number of active chains, as well as controlling the radiation patterns in the case of analogue beamforming frontend.

Different layers within the system may generate configuration commands for various modules, providing the ability to tailor the radio system to specific requirements and operating conditions.

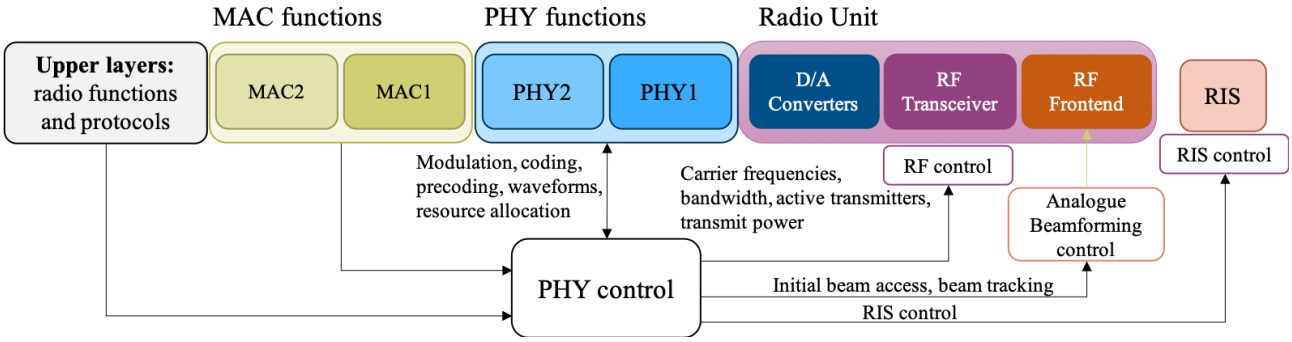

Figure 2-7: Radio logical functional split and configuration parameters.

Figure 2-7 illustrates a logical functional split of MAC, PHY, and RU functions, along with their corresponding configuration parameters. In typical devices, these functions are often collocated to achieve higher integration and reduce material costs. However, in the radio access network (RAN) infrastructure, implementing various functional splits can offer additional flexibility, enabling a more modular approach. These splits can be beneficial in a range of scenarios, allowing for optimized resource usage and scalability. However, they also affect infrastructure requirements, such as fronthaul capacity and signal processing design. Figure 2-8 provides examples of the functional splits discussed in this deliverable:

- Centralized RAN: In this configuration, the MAC, PHY, and RU functions are collected and controlled at higher layer. This setup can support, e.g., multi-connectivity at PDCP or carrier aggregation with individual cell- or site-specific MAC schedulers.
- Distributed MAC: Here, the MAC functions are split into centralized and distributed entities. Partially centralized MAC functions enable carrier aggregation across different frequency ranges, offering flexibility in managing resources. While the focus of this document is more on physical layer and data plane, a similar split in centralized and distributed units can be done for the control plane according to, for instance, configuration latency requirements where low-latency tasks are distributed and closer to the antennas.
- Centralized MAC: In this setup, multiple PHY instances are centrally controlled by MAC. This allows, for example, carrier aggregation in the same frequency range with a system-wide scheduler. Latency requirements might require a more distributed topology, though.
- Distributed PHY: This deployment corresponds to D-MIMO with distributed processing. It reduces fronthaul capacity requirements by offloading part of the PHY processing close to RUs, such as partial channel estimation and precoding, as discussed in Section 4.1.3.
- Centralized PHY: This is a conventional D-MIMO setup with centralized processing, where all samples from RUs are collected and centrally processed, as in Section 4.1.1. Other related D-MIMO split options is using analogue fronthaul, as in Section 4.2.2, where the D/A converters are placed closer to PHY.

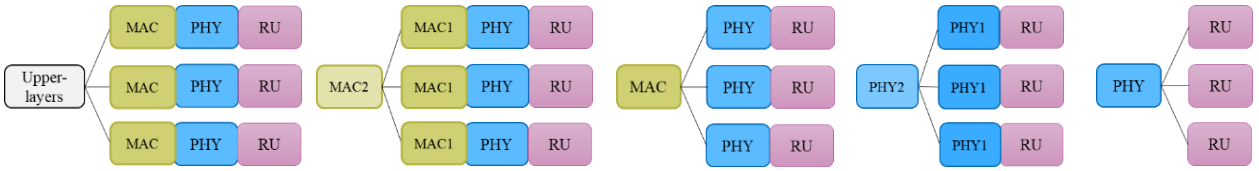

(a) Centralized RAN **(b) Distributed MAC** **(c) Centralized MAC** **(d) Distributed PHY** **(e) centralized PHY**

Figure 2-8: Potential RAN deployment options.

Further deployment scenarios correspond to the placement of transmitters and receiver as in JCAS deployment, such as bistatic, monostatic, and multistatic sensing, as discussed in Section 8.1.

3 Channel modelling

Radio channel characterization, i.e., propagation measurements, analysis and channel modelling, is needed when new radio frequencies, deployments or use cases are researched. Sub-THz frequencies (100-300 GHz) have been actively investigated and, e.g., new channel sounding equipment have been developed in recent years. Now industry views and agreements on spectrum regulations are turning the focus onto so called mid-band or FR3 (7-24 GHz). This Chapter introduces measurements and results covering both frequency ranges. Another objective is to specify channel model components to update and complement the widely used 3rd Generation Partnership Project (3GPP) [38.901] and similar channel models. Versatile contributions of the Chapter are sketched in Figure 3-1.

Wave-material interactions on various building materials are measured on a wide range of frequencies from Frequency Range 1 (FR1) up to sub-THz and some key findings are described in Section 3.1. Measured reflection coefficients are important, e.g., for deterministic channel modelling. Measurement based ray-launching calibration at 140 GHz is described in Section 3.6. Dual band sub-THz measurements in industrial environments are introduced in Section 3.3 and FR3 outdoor measurements in Section 3.7.

Several parameter and method updates for the 3GPP model concerning sub-THz are introduced in Section 3.5 and a simple extension to incorporate molecular absorption loss at above 100 GHz is provided in Section 3.2. A model component for supporting near-field and large bandwidth at sub-THz and lower frequencies is briefly defined in Section 3.4. Among new deployments is the RIS concept, which has been already discussed from a propagation point of view in [HEX224-D43, Sec. 3.5] as well as the applicability of existing channel model for JCAS use cases which was discussed in [HEX224-D43, Sec. 3.6].

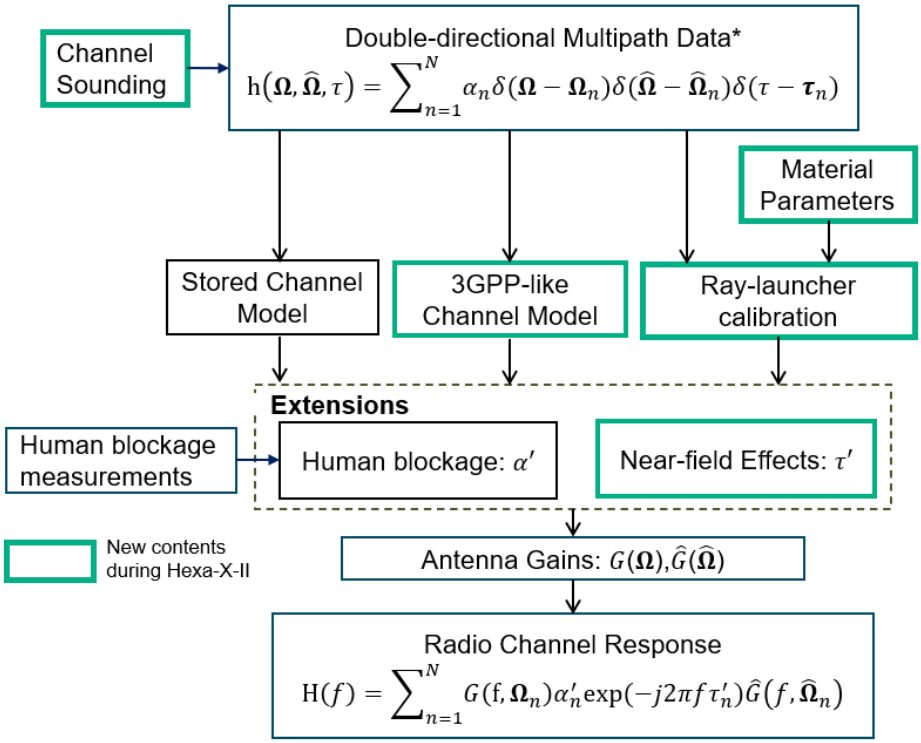

Figure 3-1: Summary of channel modelling at new radio frequencies and for new deployments.

3.1 Impact of coated surfaces on reflection coefficients

Problem statement: Sub-THz wireless communications are thought to work mainly in line-of-sight (LoS), but the receiver (Rx)- transmitter (Tx) visibility line might be temporarily blocked by an object. The transmission can be maintained by exploiting indirect paths such as reflected paths. But exploiting reflected paths degrades the link budget as the path loss is increased by the additional loss due to the reflection. Therefore, it is essential to characterize the reflection loss frequency-dependency in order to assess radio performances at sub-THz frequencies and compare them with performances of wireless systems operating at

lower frequencies. The reflection coefficient indicates the reflection gain (inverse of the loss) and is theoretically given by the Fresnel equations for a planar smooth surface. The reflection coefficient depends on the material relative permittivity. [CAC+24], [CAC+24a] show that the permittivity for homogeneous and smooth surface materials such as glass or plexiglass is constant implying that the reflection coefficient does not depend on the frequency but points out that the reflection coefficient may differ from the theoretical Fresnel equations with coated or rough surfaces. [HEX224-D43] provides a first analysis dealing with rough masonry surfaces and shows that the reflection coefficient decreases due to the scattering effect when the frequency increases or when the material becomes rougher. A detailed analysis and scattering model are given in [CCB25]. This section provides reflection measurement on coated/relief plasterboard surfaces at a normal incidence and complements the previous work.

Methodology: The measurement equipment described in Figure 3-2 is based on a vector network analyser (VNA) and frequency extenders. The measurement is divided into three sub-bands (SBs) defined by the frequency limits of the VNA, extenders, or antennas (5-40 GHz, 110-170 GHz, 170-260 GHz). Figure 3-2 illustrates the mechanical part that allows a free space measurement for reflection coefficients. The material under test (MUT) was placed at normal incidence in front of the Tx/Rx antenna. $H^{\mathrm{MUT}}(f,m,n)$ represents the intrinsic reflection frequency response of the MUT. Details on the measurement procedure and data processing can be found in [CON25]. $ppH_{mean}^{MUT}(f)$ is defined as the average power profiles of $H^{\mathrm{MUT}}(f,m,n)$ and is equal to $10log_{10}\left(\frac{1}{mn}\sum_{m,n}|H^{Mut}(f,m,n)|^2\right)$ when expressed in dB. $\sigma^{Mut}(f)$ is defined as the standard deviation of $ppH_{\square}^{Mut}(f,m,n)$ at frequency f calculated on the $m \times n$ measurement point matrix. Plasterboard (PB) samples with various finishing multi-layers were measured: raw plasterboard (PB-Raw), plasterboard coated by a smooth paint (PB-SP), plasterboard coated by a paint with an increased orange peel effect (PB-OP), plasterboard coated by a painted relief non-woven wallpaper (PB-WP), plasterboards coated with a painted relief decorative plaster (PB-DP1 and PB-DP2).

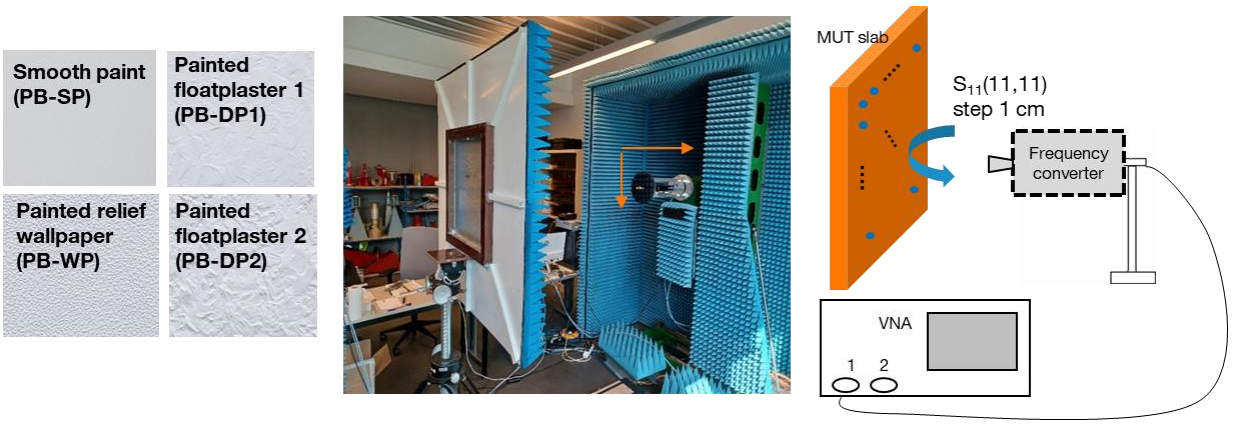

Figure 3-2: Measurement system for material reflection loss estimation.

Results: Figure 3-3 shows $ppH_{mean}^{MUT}(f)$ and $\sigma^{Mut}(f)$ and illustrate the coating effect or the joint effect of coating/scattering. For frequency below 40 GHz, the coating layer does not change the reflection coefficient that is close to the specular reflection gain (SRG) given by the Fresnel equations. But at frequency above 100 GHz, the reflection gain differs from SRG by several dBs. For instance, the reflection coefficient is higher than SRG for painted surfaces. This apparent amplifying effect and the apparent invisibility of coating layers at frequency below 40 GHz is due to the interference between the reflected path at the interface air/coating and the reflected path at the interface coating/material. The interference is mainly destructive at frequency below 40 GHz and mainly constructive between 100 GHz and 300 GHz. Additional results can be found in [Con24]. Measurements on PB-DP1, PB-DP2 and PB-WP illustrate the joint coating/scattering effect. The scattering effect is clearly highlighted by the increase of $\sigma^{Mut}(f)$, but $ppH_{mean}^{MUT}(f)$ does not systematically decreases

with the frequency as was the case for rough raw mortar. The coating effect may be predominant compared to the scattering effect.

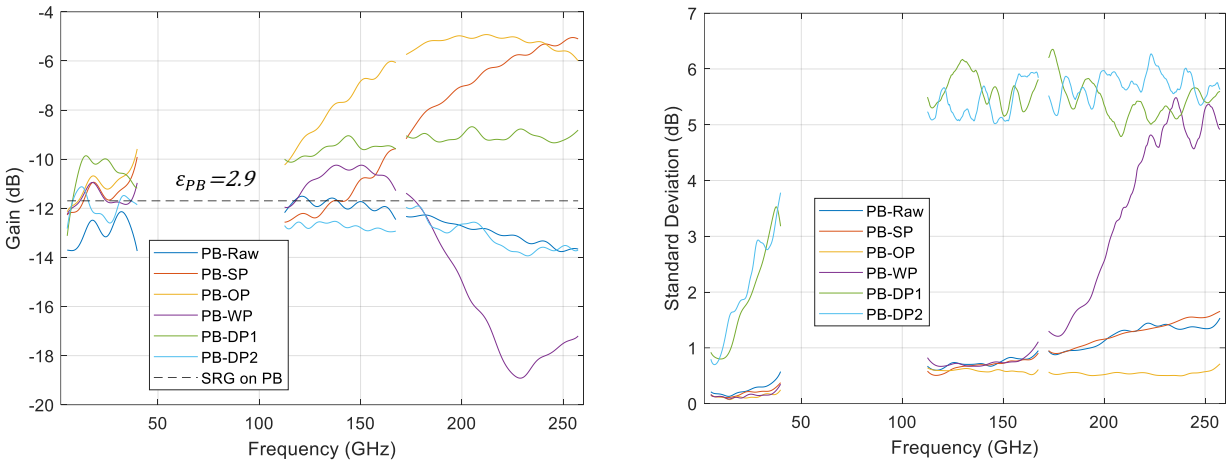

(a) Averaged profiles $ppH_{mean}^{MUT}(f)$ **(b) Standard deviation $\sigma^{Mut}(f)$**

Figure 3-3: Reflection coefficient statistical characterization as function of the frequency.

3.2 Simplified model for molecular absorption loss above 100 GHz

Problem statement: Radio systems operating above 100 GHz will suffer from severe path loss, penetration loss, and molecular absorption, which significantly reduces the link distance. However, the existing 3GPP TR38.901 model only characterizes oxygen absorption loss below 100 GHz. Accurate modelling of the absorption of various molecules above 100 GHz relies on large databases and is not well suited to standards due to its complex description.

Results: Here, a simplified model is developed to characterize the molecular absorption loss above 100 GHz:

$$\alpha(f) = a_o \exp[b_o(f - f_0)] + c_o \left[\frac{\text{dB}}{\text{m}}\right] \quad \textbf{(3-1)}$$

where a_o, b_o, and c_o are the fitting parameters, f_0 in GHz is the break-point frequency. The break-point frequencies are the resonant frequencies, where the molecular absorption effect is locally maximised and many molecular absorption peaks are generated. Within the specific frequency range, the absorption coefficient is fitted with an exponential function. Using HITRAN database [GRH+22], the best fitting results are listed in Table 3-1. Note that the parameters listed in Table 3-1 are suitable only for the condition: a reference pressure of 1013.25 hPa, temperature of 20 ℃, and relative humidity of 50%. Six most abundant molecular species are considered, including water, carbon dioxide, nitrous oxide, carbon monoxide, methane, and oxygen.

Table 3-1: Frequency dependent parameters for the characterization of molecular absorption attenuation

Frequency range [GHz]	f_0 [GHz]	a_o	b_o	c_o
[100, 119]	119	0.0472	0.5778	0.0040
(119, 129]	129	0.0001	-0.5820	0.0066
(129, 183]	183	0.7136	0.2640	0.0114
(183, 224]	224	0.00005	-0.2345	0.0239
(224, 325]	325	0.9355	0.2186	0.0239
(325, 342]	342	0.0034	-0.3374	0.1320
(342, 380]	380	7.8736	0.2642	0.1696
(380, 411]	411	0.0034	-0.2499	0.2615

(411, 448]	448	9.1267	0.2232	0.3105

Figure 3-4(a) shows the specific attenuation using the line-by-line model with HITRAN [GRH+22] spectroscopic data (red dashed line). The specific attenuation coefficients generated via line-by-line model are treated as raw data for the development of simplified model. Figure 3-4(a) also compares the fitting results using the proposed piecewise functions with the original results extracted from line-by-line model. Figure 3-4(b) shows the fitting difference over 100-448 GHz, where significant differences occur around molecular absorption peaks, e.g., 183 GHz, 325 GHz, 380 GHz, and 448 GHz. The highest fitting error occurs around absorption peaks and consequently the relative fitting error remains very small throughout the covered frequency range.

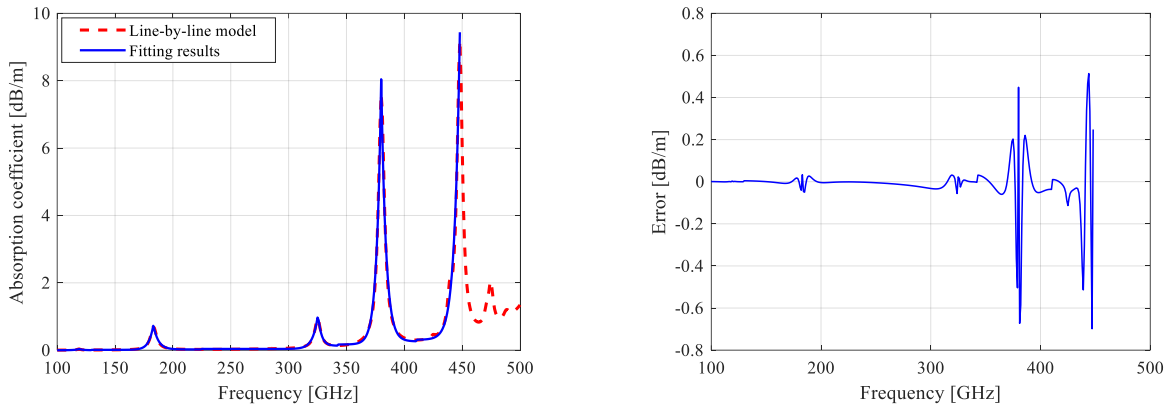

(a) Original and fitted **(b) Fitting error**

Figure 3-4: Fitting results with piecewise functions and fitting error.

To include the molecular absorption loss in a wideband channel model, we need to first transform the time-domain channel impulse response of each path into frequency-domain channel transfer function, and apply the proposed simplified model of molecular absorption loss to the channel's frequency-domain channel transfer function at each frequency point of $f_c + \Delta f$ within the considered frequency range $[f_c - B/2, f_c + B/2]$, where B is the bandwidth. In turn, the molecular absorption loss for the n-path at the frequency of $f_c + \Delta f$ is modelled as

$$L_n^{\text{molecular}}(f_c + \Delta f) = \alpha(f_c + \Delta f) c \tau_n \quad \textbf{(3-2)}$$

where c the speed of light, τ_n is the absolute propagation delay of the n-path, and $\alpha(\cdot)$ is the absorption coefficient from (3-1**)**. Then, the frequency-domain channel transfer function of the multipath channel is obtained by the summation of frequency-domain channel transfer functions of all paths. Finally, the time-domain channel impulse response can be obtained by the inverse Fourier transform from the obtained frequency-domain channel transfer function.

3.3 Sub-THz dual-band channel characterization for IIoT

Problem statement: Industrial Internet of Things (IIoT) could be a priority scenario for the successful roll-out of sub-THz communications in the future. Understanding how industrial environments support radio propagation is fundamental to the design, development, and implementation of sub-THz communication systems for such environments.

Methodology: Bidirectional channel measurement campaigns in two industrial environments at 234 GHz and 318 GHz have been carried out using a VNA based channel sounder. For the factory hall as shown in Figure 3-5(a), Tx was fixed at the middle of the workspace, and 11 LoS and two non-line-of-sight (NLoS) Rx locations were selected, which were distributed in the environments. For the warehouse environments as shown in Figure 3-5(b), Tx was located near the glass wall and a total of 11 LoS and nine obstructed-line-of-sight (OLoS) Rx locations were measured, where these Rx locations were along the walkways/paths between these pallet racks. During the measurements, Tx horn antenna was rotating within a specific angular range for sector coverage

(approximately 120°), and Rx horn antenna was rotating in 2π azimuth plane with fixed steps, which were determined by the half power beam width (HPBW) of the antenna at the specific frequency. Note that dual-band measurements were conducted at identical Tx and Rx locations, enabling a fair comparison of frequency-dependent channel characteristics.

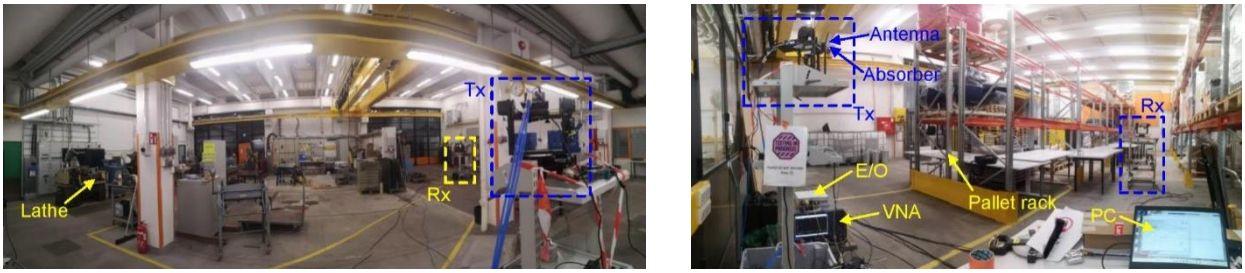

(a) Factory hall **(b) Warehouse**

Figure 3-5: Setup showing the measurement scenario in an industrial IoT network environment.

Results: Here, two widely used path loss models are fitted to data. The close-in (CI) free-space reference distance model at the free-space reference distance d_0 m is given by

$$PL_{\mathrm{CI}}(d)\ [\mathrm{dB}] = PL_0(d_0) + 10n_{\mathrm{CI}}\log_{10}(d/d_0) + X_{\mathrm{CI}} \quad \textbf{(3-3)}$$

where $PL_0(d_0)[\mathrm{dB}] = 20\log_{10}(4\pi d_0/\lambda)$ is the free-space path loss with a wavelength λ in meters, d_0 is the reference distance, n_{CI} is the path loss exponent (PLE), and X_{CI} is a zero-mean Gaussian random variable with standard deviation σ_{CI} in dB. The d_0 is generally set as 1 m, which would make comparisons of measurements and models simpler and provide a standard definition for the PLE. The floating-intercept (FI) path loss model is expressed as

$$PL_{\mathrm{FI}}(d)\ [\mathrm{dB}] = \alpha + 10\beta\log_{10}(d) + X_{\mathrm{FI}} \quad \textbf{(3-4)}$$

where α is the FI in dB, β is the slope of the fitting line, and X_{FI} is a zero-mean Gaussian random variable with standard deviation σ_{FI} in dB. Here model parameters α and β are obtained via linear least-squares fitting method. The model fitting parameters are summarized in Table 3-2. The '*omni*' and '*best dir.*' denote the cases of omnidirectional channel and directional channel with highest received power, respectively.

Table 3-2: Path loss model parameters for two industrial environments at 234 GHz and 318 GHz

Configurations				CI model with $d_0 = 1$ m			FI model		
Envi.	Freq.	Scen.	Case	PL_0 [dB]	n_{CI}	σ_{CI} [dB]	α [dB]	β	σ_{FI} [dB]
Factory hall	234 GHz	LoS	Omni.	79.82	1.87	2.44	85.08	1.34	2.35
			Best dir.		2.19	1.68	84.11	1.76	1.59
	318 GHz	LoS	Omni.	82.49	2.08	2.27	90.38	1.29	2.02
			Best dir.		2.50	1.82	79.99	2.39	1.81
Warehouse	234 GHz	LoS	Omni.	79.82	1.44	1.37	83.73	0.99	0.84
			Best dir.		2.25	2.24	85.12	1.65	1.69
		OLoS	Omni.		1.54	1.55	90.33	0.47	0.87
			Best dir.		2.64	4.23	/	/	/
	318 GHz	LoS	Omni.	82.49	1.54	2.39	86.97	1.02	2.02
			Best dir.		2.32	4.41	91.52	1.28	3.62
		OLoS	Omni.		1.74	2.16	97.19	0.26	1.21
			Best dir.		2.71	5.72	/	/	/

Figure 3-6 compares the cumulative distribution functions (CDFs) of the measured root mean square (RMS) delay spread (DS) for LoS links in two environments and two frequency bands along with the log-normal fitting results. The goodness of the fit is evaluated by Kolmogorov-Smirnov (K-S) test at 5% significance level. Since the dual-band measurements were performed at identical Rx locations, frequency-dependent behaviour can be observed. For example, the mean values of RMS DS generally reduce with frequency. Comparing the results in two environments, the RMS DSs of the warehouse are slightly larger than the ones of the factory hall.

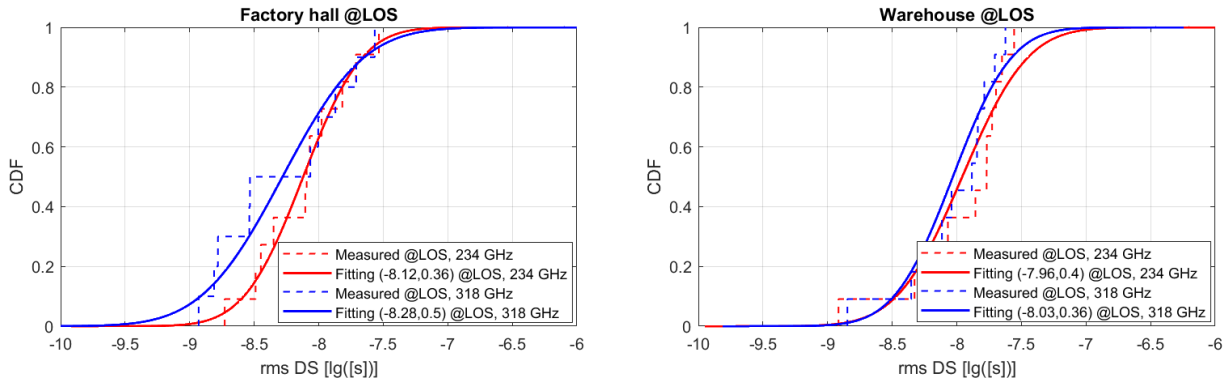

(a) Factory hall **(b) Warehouse**

Figure 3-6: Comparison of the empirical and fitting CDFs of the omnidirectional DS in LoS scenario.

3.4 Channel model components for near-field condition

Problem statement: This section proposes updates for making the legacy channel modelling approach in 3GPP TR 38.901 [38.901] more physical and to solve issues related to prior prerequisites of confined array sizes, relatively small bandwidths, and link distances satisfying the far field condition. Detailed problem statement describing deficiencies of the 3GPP model, such as 1) lack of spherical wavefronts, 2) missing support for beam squint effect, and 3) missing wideband Doppler components is given in [HEX224-D43, Sec. 3.2].

Methodology: The idea of the proposed solution is to provide a simple means to determine the propagation distance between each Tx and Rx antenna element applying the path parameters specified by the original model. Once having Tx-Rx antenna element distances along path trajectories, it is straightforward to determine MIMO channel coefficients incorporating spherical wavefronts and consistently frequency dependent Doppler shifts.

Results: Determining Tx-Rx distances can be divided into three cases: 1) LoS which is trivial, 2) scattering/diffraction which takes place mainly on lower frequencies like FR3, 3) specular reflection which is presumed the dominant interaction at sub-THz. For LoS path the distances from each Tx element to each Rx element can be calculated, since antenna coordinates and array geometries are defined in the model. The current 3GPP definition for rays in Figure 3-7(a) contains angles of arrival/departure and propagation delay, but no coordinates of scatterers. The first/last bounce *scattering* coordinates can be drawn randomly to angle-of-departure (AoD)/angle-of-arrival (AoA) directions by specifying a minimum antenna-scatterer distance $d^{\min}$ and drawing from uniform distribution $d_{\mathrm{Tx},i} \sim U\left(d^{\min}, \tau_i c_0 - d^{\min}\right)$ and $d_{\mathrm{Rx},i} \sim U\left(d^{\min}, \tau_i c_0 - d_{\mathrm{Tx},i}\right)$ as in Figure 3-7(b). Now distance differences between antenna elements can be calculated based on Euclidian distances to/from newly defined scatterer points. Here it is assumed each scattering point is a source of new spherical wavefront.

Specular reflection requires different treatment since the spreading (the curvature) of waves does not change in those interactions. For that case the Tx array is translated and rotated to new virtual location for each ray as shown in Figure 3-7(c). Then Euclidian distances from virtual Tx antenna locations to Rx antenna locations can be calculated similarly as in LoS case. Detailed mathematical description of the proposed method is given for specular reflection and scattering in [DZK25].

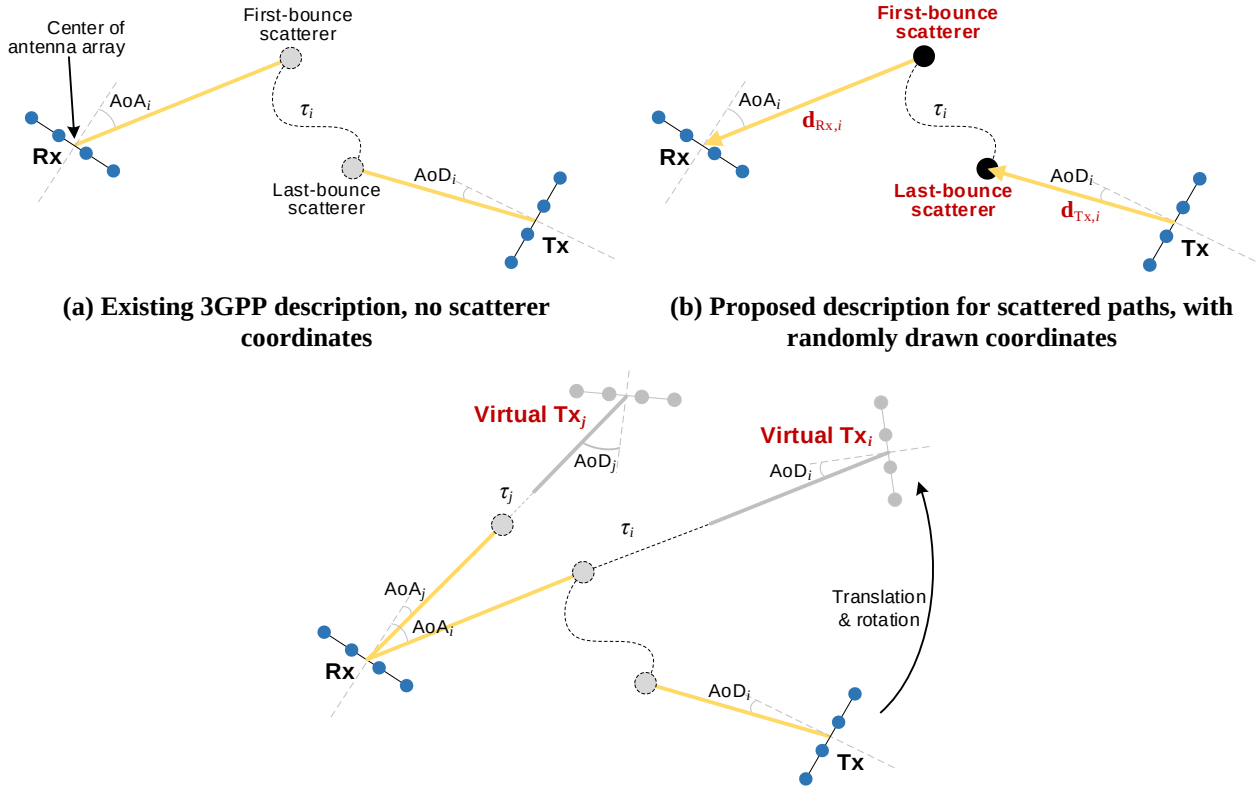

(a) Existing 3GPP description, no scatterer coordinates

(b) Proposed description for scattered paths, with randomly drawn coordinates

(c) Proposed description for specular reflected paths

Figure 3-7: Geometric description of antenna arrays, scatterers and rays.

3.5 3GPP-like channel model at 140 GHz

Problem statement: The 3GPP channel model for new radios, described in 3GPP TR 38.901 [38.901], is one of the most widely used channel models in the cellular wireless community. Originally established at below-6GHz radio frequencies and gradually expanded to cover new frequencies, its applicability to the new frequencies has always been an interest of the community. The mathematical model framework of 3GPP TR 38.901 is complemented by new channel parameter values extracted from the measurements in entrance hall and residential environments at 142 GHz [HEX224-D43]. They are based on the double-directional multipath data reported in [DHK23] using a measurement-based ray-launcher [DH23]. Furthermore, our comparison of the radio channel responses from the measurements and the original 3GPP channel model, along with their variants adapted to sub-Terahertz frequency, sheds light on the possible improvement of the model.

Results: The original model defines cluster azimuth angles such that stronger clusters are always concentrated around a reference direction. Meanwhile, the measured azimuth power spectrum indicates that strong clusters randomly come from any direction. An alternative approach to iteratively generate cluster angles is therefore proposed [DH25], which provides improved agreement of the angular spread and eigenvalue statistics between measured and generated channels, at the expense of increased computational complexity in generating clusters. Figure 3-8 shows the improved agreement of the angular spread and normalized eigenvalues between the measured and generated channels using the proposed approach compared to the original approach.

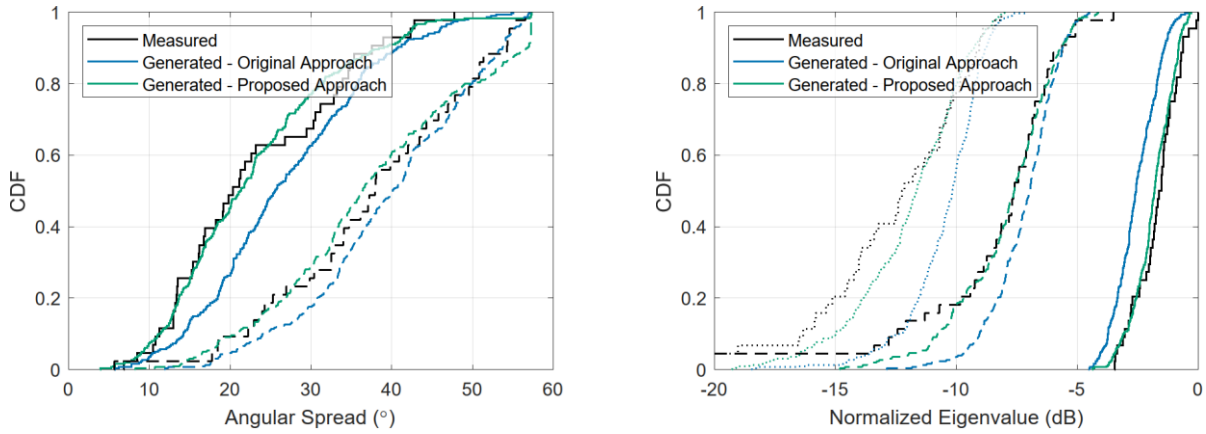

(a) Azimuth angular spread of departure (solid line) and arrival (dashed line).

(b) First (solid line), second (dashed line), and third (dotted line) highest normalized eigenvalues.

Figure 3-8: Comparison of angular spread and normalized eigenvalues of measured and generated channels in the entrance hall environment at 142 GHz.

3.6 Calibration of Ray-Launcher for coverage study at 140 GHz

This section presents a ray-launcher tool calibrated using the sub-THz channel measurement data in an entrance hall environment reported in [DHK23]. Such a ray-launcher can generate realistic propagation channel responses for link simulations and coverage analysis with preferred antenna configurations and locations within the site.

The calibration consists of a two-step process of finding the set of material parameters that minimize the total absolute difference between the measured and simulated (using ray-launcher) gain of each path. The first step involves successively solving the path loss equation from single to higher-order interactions as described in [DH25a]. The material parameters, especially those of objects with parameters that cannot be estimated using the previous step, are further refined using a genetic algorithm. Figure 3-9(a) shows a good agreement between the measured path loss and simulated path loss obtained using the calibrated ray-launcher. All measured links were used for the calibration. The root mean square error (RMSE) between the measured and simulated path losses is 3 dB. The estimated real part of the relative permittivity of the objects in the entrance hall environment is shown in Figure 3-9(b). A sample coverage map using the calibrated ray-launcher is shown in Figure 3-10. The Tx and Rx antenna gains are set to 0 dBi, transmit power to 0 dBm, and noise floor to -148 dBm with 2 GHz of bandwidth. The received power of the measured links is also shown for comparison. It can be seen that the majority of the environment has a received power of above -130 dBm, while some areas (coloured grey) in the environment are considered outage, where the received power is less than –148 dBm. These outage areas are behind the corners, desks, and foliage.

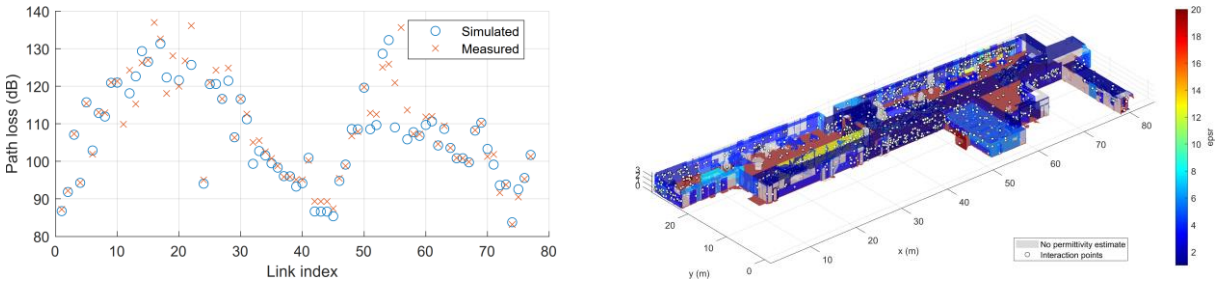

(a) Measured and simulated path losses.

(b) Estimated real part of the relative permittivity.

Figure 3-9: Comparison of measured and simulated path loss, and estimated material parameters.

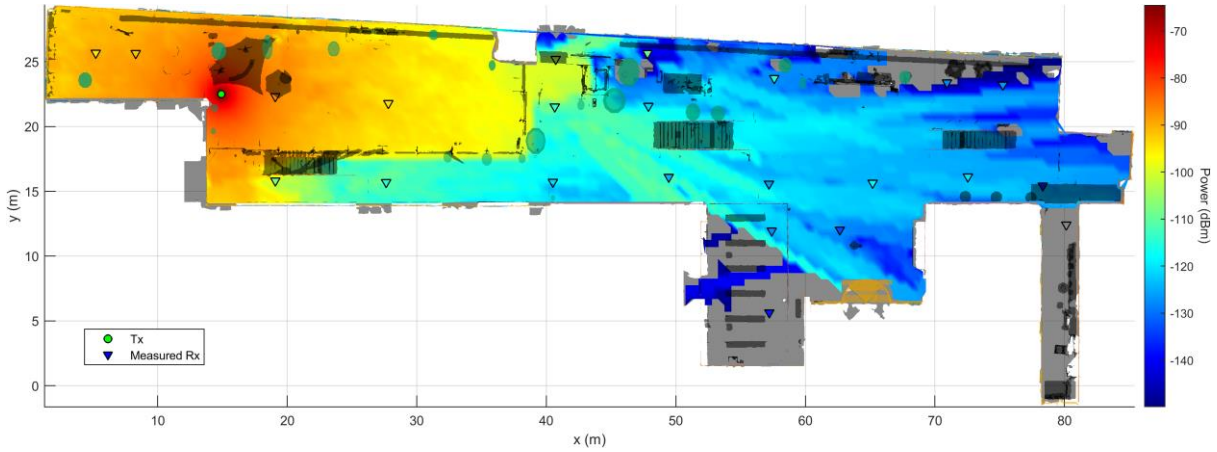

Figure 3-10: Exemplary coverage map showing the received power in dBm with assumed antenna gains of 0 dBi, transmit power of 0 dBm, and noise floor of -148 dBm.

3.7 FR3 Channel Sounding at 15 GHz: Dynamic Wideband Measurements in UMa and UMi Scenarios

Problem statement: The use of intermediate radio frequency spectrum between below-6 GHz and millimetre-wave 26 GHz, known as frequency range three (FR3) and centred around 15 GHz, has recently gained significant interest. Despite its potential, this band remains largely unexplored for wide-area mobile communications, especially under NLoS conditions, where coverage can be severely affected by urban obstacles and significant path loss.

Methodology: To address the experimental gap at 15 GHz, a wideband channel sounder based on universal software radio peripheral (USRP), described in Figure 3-11, has been implemented and employed in measurement campaigns. The channel sounder supports non-stationary measurements, where the mobile station (MS), equipped with an omnidirectional antenna, is installed on a moving cart. The measurement scenarios include urban macro-cellular (UMa) [ATK+25] and urban micro-cellular (UMi) environments, with multiple base station (BS) locations per site.

Results: Signal coverage maps produced by the developed channel sounder are provided in Figure 3-12 for some sites to demonstrate the feasibility of NLoS link connectivity. The work provides initial insights into propagation losses in NLoS conditions in this frequency band, influenced by foliage and urban structures. The measurements revealed a 20 dB loss due to building corner shadowing and a 10–15 dB loss from foliage blockage.

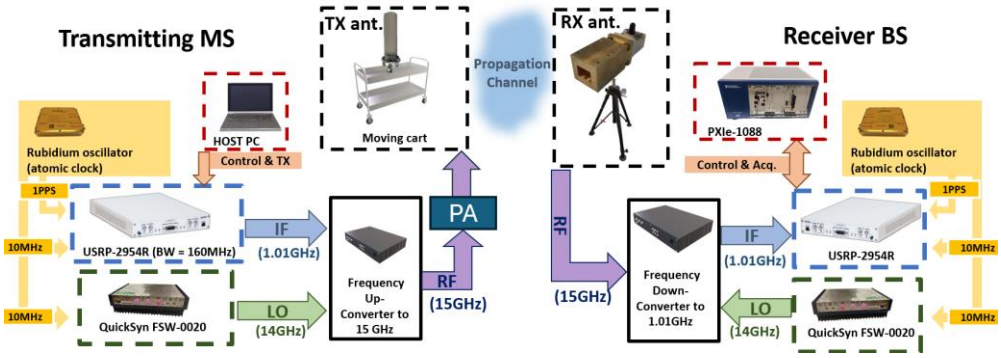

Figure 3-11: USRP-based channel sounder setup at 15 GHz.

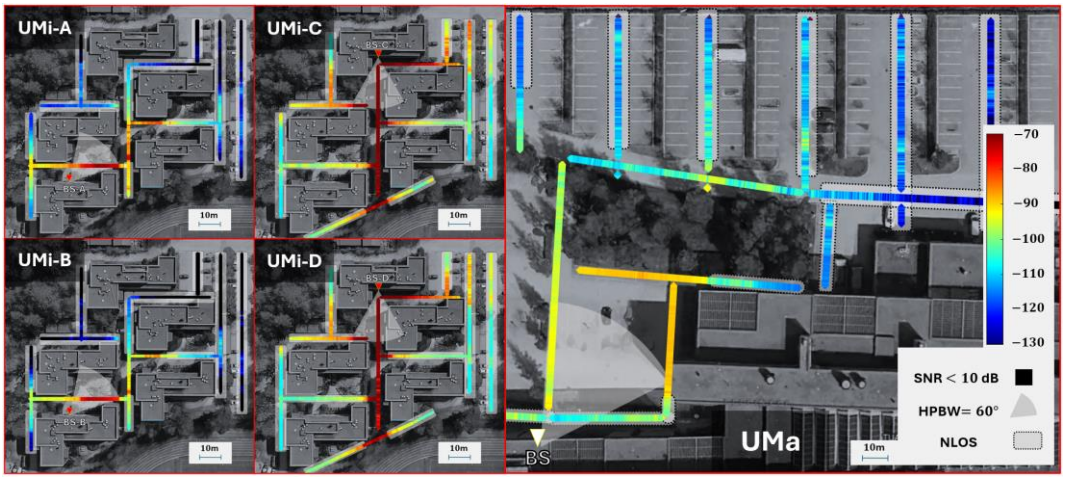

Figure 3-12: Coverage map showing path gain (dB) along the measurement routes in a UMi (left) scenario (residential area) and a UMa (right) scenario (university campus/ parking lot).

3.8 Implication of sub-THz link budget on EMF compliance

To protect people from substantiated health effects due to very high level of exposure to RF EMFs, science-based RF EMF exposure limits up to 300 GHz are developed by the International Commission on Non-Ionizing Radiation Protection (ICNIRP), formally recognized by the World Health Organization. The limits are based on reviews of all relevant scientific literature and have been set with large margins to protect from substantiated short-term and long-term health effects. The ICNIRP guidelines from 1998 [ICNIRP98] have been adopted in most countries and form the basis of both the Council Recommendation 1999/519/EC with recommended EMF limits for the general public [1999/519/EC] and of the EU Directive 2013/35/EU with EMF limits for workers [2013/35/EU]. In 2020, the ICNIRP published updated guidelines [ICNIRP20] considering the latest available scientific information and data. The limits in the new guidelines are largely the same as those from 1998. The 2020 ICNIRP limits have already been adopted in several national regulations and the Council Recommendation as well as the EMF Directive are expected to be updated based on the new guidelines in the coming years. Radio equipment for 6G will need to comply with the same EMF requirements as previous generations of mobile technologies. To assess the conformity with the EMF related safety requirements of the radio equipment directive (RED), products shall comply with the relevant EMF standards, for example, the European Standard EN 50385 [EN50385]. This standard prescribes that BS products shall be evaluated in accordance with the international standard IEC 62232 [IEC62232] to determine EMF compliance boundaries (exclusion zones) for general public and workers.

In [RKL+20], to achieve 10–100 Gbps data rates in DL at a distance around 80 m, sub-THz radio with 512 Tx antennas should provide EIRP levels of 55.6–65.6 dBm. Assuming a TDD DL duty cycle of 75%, the EIRP levels of such sub-THz radios (55.6–65.6 dBm) are similar to existing micro cell and street coverage deployments, giving maximum compliance distances in the range of 1.5–4.7 m for theoretical maximum exposure conditions. When establishing EMF compliance boundaries according to the actual maximum condition [IEC62232], a power reduction factor should be introduced to account for the effects of beam scanning on the time-averaged EIRP. For a typical FR2 radio, this value is ≤ 0.14 [XAC+22][XCJ+22]. By introducing this factor, the compliance distance becomes 0.6–1.7 m. The compliance distances for such sub-THz radios are similar to those for FR2 radios available today.

3.9 Summary

This chapter introduces new channel model components and parameters to address some of identified needs and to enable simulation studies of other work packages. Furthermore, new propagation measurements at radio frequencies of interest are described. The study items listed below relate to this chapter and have been investigated in this project. However, they were completed before the publication of deliverable D4.3 and hence they are not repeated in this chapter. An interested reader is referred to [HEX224-D43, Chapter 3] for a detailed presentation of their final results.

- JCAS channel models at any frequencies
- Coverage analysis at THz frequencies
- Signal level analysis for RIS in a simplified scenario

4 MIMO transmissions

MIMO systems have become foundational in modern communication technologies, particularly in advanced wireless standards like fourth generation (4G), 5G, and beyond 5G. By utilizing multiple antennas at both the transmitter and receiver, MIMO achieves superior communication quality through multiplexing and diversity gains, which enhance SE and data throughput. This improvement is achieved without necessitating additional bandwidth or power, making MIMO a highly efficient solution for addressing the growing demands of wireless communication.

To further optimize SE, D-MIMO systems have emerged as an evolution of traditional MIMO technology. In D-MIMO systems, multiple BS/access points (APs) cooperate to simultaneously serve a single user. This coordinated transmission strategy effectively eliminates inter-cell interference, which is a significant limitation in conventional cellular networks, while enhancing overall network performance. By strategically distributing APs throughout the network, D-MIMO reduces path loss, strengthens signal reception, and lowers the likelihood of signal blockage. These benefits translate to improved coverage and more reliable communication, even in challenging environments. Despite the substantial performance gains offered by D-MIMO systems, realizing their full potential requires overcoming several technical challenges. Advanced beamforming techniques and precise CSI are essential for effective coordination among distributed APs. Furthermore, the deployment of D-MIMO systems often entails higher costs due to the increased hardware requirements and the complexity of signal processing. These challenges must be addressed to ensure the feasibility of widespread D-MIMO adoption. In this section, we examine the performance of D-MIMO systems in detail, considering factors such as resource allocation, deployment strategies, hardware constraints, and channel dynamics. Additionally, we explore the potential integration of joint sensing and communication capabilities within D-MIMO deployments, which could unlock new applications and further enhance system performance.

As communication systems advance toward higher carrier frequencies, such as millimetre wave (mmWave) bands, maintaining robust cell coverage becomes increasingly challenging. These frequencies suffer from higher path loss and limited penetration capabilities, necessitating the use of a greater number of antennas to ensure sufficient signal coverage. This requirement has driven the development of massive MIMO technology, which employs a large array of antennas to facilitate highly directional beamforming. Such beamforming is crucial for extending coverage and achieving the high data rates associated with mmWave frequencies. However, the adoption of massive MIMO introduces new challenges. The increased flexibility in beamforming requires multiple RF chains, which can significantly elevate power consumption. This trade-off between performance and energy efficiency is a critical consideration in the design of massive MIMO systems. In this chapter, we investigate suitable architectures and hardware designs aimed at mitigating power consumption while maximizing system performance. This analysis encompasses innovative approaches to hardware design, energy-efficient algorithms, and architectural optimizations to support the deployment of massive MIMO in next-generation wireless networks.

The problem statements and relevant KPIs for the assessment of the developed methods for MIMO technology within Hexa-X-II initiative are outlined in [HEX223-D42]. The preliminary results for the assessment of the proposed methods are presented in [HEX224-D43]. The extended and final evaluation results with some reflections on the systemization aspects of the proposed methods are presented in the following sections. Section 4.1 present joint transmission schemes for D-MIMO transmissions; Section 4.2 presents proposed D-MIMO architectures for communication and JCAS; Massive MIMO architectures is discussed in Section 4.3; and Multi-user massive MIMO transmission schemes are presented in Section 4.4; and finally, methods for low-complexity optimization for MIMO has been discussed in Section 4.5.

4.1 D-MIMO transmission schemes

This section addresses the design of beamformers to tackle specific challenges that arise due to channel and resource limitations. The aim is to ensure robust system performance in practical deployment scenarios by adapting the design to these constraints:

- **Partial Blockage Environments**: In scenarios where signal blockage is partial and varies over time, coherent precoding schemes are crucial. These schemes adapt to changes in the channel, mitigating

the impact of blockage by dynamically adjusting the transmission parameters. This ensures consistent performance even in challenging propagation conditions, such as urban or indoor environments.

- **No CSI at APs/BSs**: When CSI is unavailable at APs or BSs, non-coherent precoding methods become essential. Techniques like **orthogonal space-time coding (OSTC)** can be employed to exploit spatial diversity and improve system performance without relying on CSI. These methods are particularly effective in dynamic environments where channel conditions change frequently.
- **Fronthaul Signalling Limitations**: Limited capacity of fronthaul links, which connect distributed APs or BSs, can restrict the exchange of full CSI across the network. To address this, coherent beamforming strategies are designed to optimize the network-wide precoder and combiner at each AP using only local information and minimal feedback. This reduces the reliance on extensive signalling while enabling effective coordination and maintaining high performance.

By addressing these constraints, these beamforming approaches ensure reliable and efficient communication in diverse deployment scenarios, making them essential for the success of advanced MIMO systems.

4.1.1 Coherent joint transmission – D-MIMO link-level performance evaluation and theoretical analysis

Problem statement: D-MIMO is studied as a solution to address the issue of propagation channel blockage in mmWave and sub-THz frequency bands. These frequency bands are essential for achieving higher throughput required by modern applications, but they introduce new challenges in terms of communication reliability due to increased signal attenuation and worsened blockage effects. One key challenge is the severe impact of blockage on the bit error rate (BER), often degrading performance to unacceptable levels. D-MIMO systems address this by leveraging spatial diversity and distributed antennas to mitigate blockage effects, ensuring more reliable communication and improved BER in high-frequency bands.

Methodology: The methodology involves implementing a complete 6G physical layer communication chain, using Python, to assess the BER as a function of signal-to-noise ratio (SNR). This chain incorporates coding, modulation, and the combined D-MIMO and orthogonal frequency division multiplexing (OFDM) techniques, with energy focusing through precoding towards the UE. The challenge lies in accurately modelling the channel in the sub-THz frequency range, especially in terms of modelling blockage characteristics such as time, size of blockers, and their statistical distribution, which will significantly impact performance. The D-MIMO system is evaluated under 3GPP scenarios.

Additionally, a theoretical model was derived to characterize BER performance under blockage conditions, further validating the simulation results. This model focuses on the statistical analysis of the equalized channel gains affected by blockage. Specifically, probability density functions (PDFs) were derived for the received symbols under different blockage scenarios, modelling the equalized signal as a ratio of correlated complex Gaussian random variables. This approach quantifies the impact of blockage on communication reliability and allows for a comparison between the theoretical and simulated outcomes, ensuring that the system performance under blockage aligns with the expected analytical results across varying scenarios.

System and channel model: The system uses a distributed antenna system (DAS) with multiple base stations (BS) transmitting to a single user equipment (UE). Each BS's downlink channel impulse response is characterized using a tapped delay line (TDL) model. To address the challenge of blockage, a cluster-based propagation model is introduced, where certain clusters of BSs are blocked, reflecting real-world scenarios where high-frequency signals are highly susceptible to obstacles (see Figure 4-1(a)).

The methodology also integrates Monte Carlo simulations, using 3GPP-specified clustered delay line (CDL) channel models, to validate the theoretical BER expressions. These simulations allow for performance comparisons between scenarios with and without blockage, under different configurations of BSs and UE positions. The simulations aim to quantify how much performance degrades due to blockage, while analysing the impact of distributed transmission in mitigating such degradations.

Results and conclusions: The results from the simulation confirm the theoretical expectation that D-MIMO can significantly improve BER performance, even in challenging blockage conditions. Increasing the number of BSs in the distributed system leads to an improvement in BER, as more APs can simultaneously provide the UE with multiple signal paths, compensating for blocked signals. The impact of blockage, however,

remains substantial, especially when high-power clusters are blocked. This results in a significant degradation of the communication quality, where the BER reaches an asymptotic floor—meaning the system's performance becomes capped beyond a certain blockage intensity (see Figure 4-1(b))**.**

The statistical analysis of blocked channels indicates that the equalized channel gains are affected, leading to erroneous symbol detection. The derived PDFs for received symbols in blocked scenarios show a clear distinction from those in unobstructed conditions. The BER analysis, based on the distribution of estimated symbols, provides general expressions that are applicable to various modulation constellations.

The performance of the D-MIMO system will continue to be evaluated by incorporating more complex channel models closer to real-world sub-THz propagation environments, including advanced blockage models.

In conclusion, the D-MIMO technique proves effective in overcoming the challenges posed by signal blockage at higher frequencies, thanks to its distributed architecture and joint transmission capabilities. Although blockage leads to performance degradation, particularly when high-power signal clusters are obstructed, the D-MIMO configuration demonstrates resilience by distributing transmission sources. Future work will focus on enhancing the system's accuracy with advanced channel modelling and further validation against statistical models.

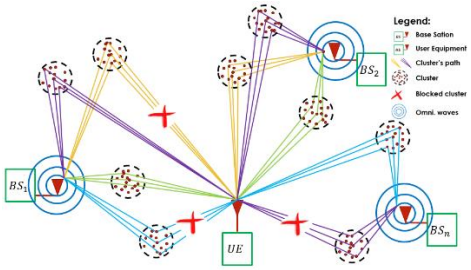

(a) Distributed antenna network

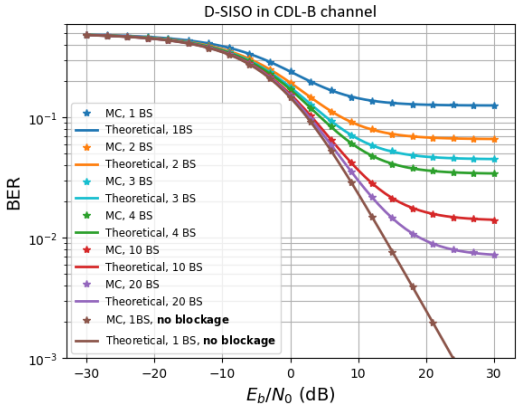

(b) Theoretical and simulated BER with variable number of BS. Blocked clusters = {1,2,3} for BS 1

Figure 4-1: Coherent joint transmission illustration and performances.

4.1.2 Non-coherent Space-time Coded Transmission

A robust transmission mode for D-MIMO precoding without precise CSI has been motivated to enhance diversity at the UE side in challenging conditions. A RU and UE clustering algorithm has been proposed for Alamouti-like OSTC in D-MIMO. The details regarding achievable ergodic and outage data rates and corresponding initial numerical simulations can be found in [HEX224-D43, Ch. 4.1].

***Complexity Analysis*:** Under the assumption $ML \gg K$, it can be shown that the asymptotic complexity of the proposed Alamouti-like transmission algorithm is $O(MLK^2)$ where M, K, L denote the number of RUs, UEs and antennas at each RU. The proof is given in [KHR23].

***Numerical Evaluations*:** Alamouti-like OSTC in D-MIMO has been evaluated for different number of RUs and UEs deployed in an indoor factory scenario operating at 28 GHz, and compared with small cells, single frequency network (SFN) transmission, maximum ratio transmission (MRT) with perfect and statistical receiver CSI and zero forcing (ZF).

Figure 4-2 shows the median SEs for different number of RUs and UEs. The performance of Alamouti-like scheme in terms of both outage and ergodic SEs increases as the number of RUs (M) increases. Orthogonal coding outperforms small-cell and SFN for all M values in terms of outage rates. Median ergodic SEs of these three methods are similar. In small-cell and MRT (1 RU) methods, the UEs are served by a single RU and hence increasing M does not enhance the performance much. On the contrary, MRT using multiple RUs (95%) outperforms orthogonal coding for large M values as more RUs can cooperate to serve UEs. Regarding the effect of the number of UEs, both ergodic and outage SE decreases with increasing number of UEs. Orthogonal

coding outperforms small-cell and SFN for all K values in terms of outage SEs. For $K > 4$, we observe a dramatic decrease in outage SEs.

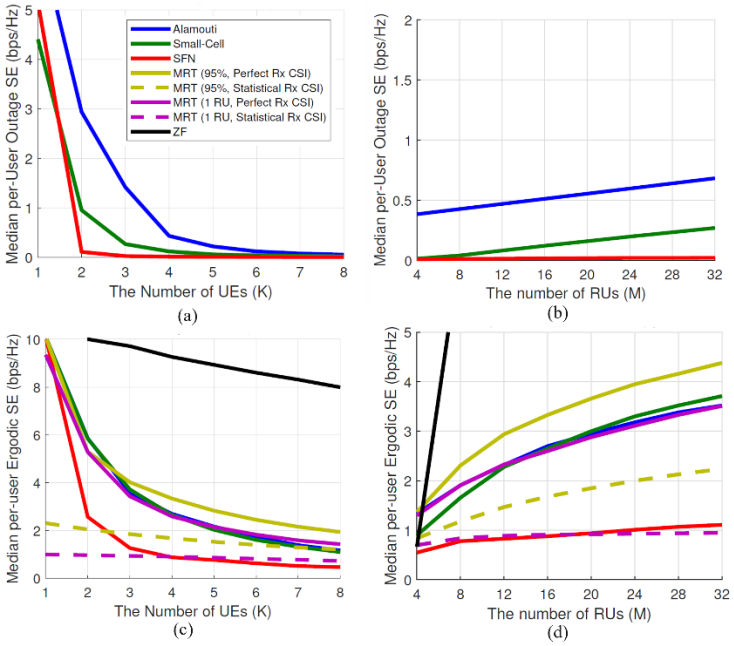

Figure 4-2: Median SE per UE values for Alamouti-like OTSC, small cell, SFN, MRT and ZF schemes: (a) Outage SE versus number of UEs, (b) Outage SE versus number of RUs, (c) Ergodic SE versus number of UEs, (d) Ergodic SE versus number of RUs.

4.1.3 Distributed over-the-air cooperative beamforming design

Problem statement: Distributed massive MIMO is a promising technology, where multiple APs work together to serve UEs coherently, enhancing SE by reducing inter-cell interference, making it ideal for small-cell applications. While traditional approaches often focus on non-cooperative beamforming, our previous works [AGT21, GAT24] demonstrated a distributed precoding framework using bi-directional training, allowing APs to design network-wide beamformers locally through over-the-air (OTA) signalling without fronthaul CSI exchange. In this work, we extend the framework to further optimize training resources, particularly by leveraging scenarios where one set of UEs requires downlink communication and another set requires uplink (UL) communication.

Methodology: We consider a distributed massive MIMO system where multi-antenna UEs are served in both DL and UL within a given resource block. In this system, one set of UEs is served exclusively in either the DL (DL-only) or UL (UL-only), while another set is served in both DL and UL (DL-UL), as depicted in Figure 4-3. Instead of separately designing the beamformers for DL and UL communication, we propose a unified approach. Specifically, the DL precoders at the APs and combiners at the UEs are jointly designed with the UL precoders at the UEs and combiners at the APs. This combined design reduces the resources required for beamforming training.

In this framework, we assume all UEs are served in the DL, and the DL precoders at the APs and combiners at the UEs are optimized using the sum mean squared error (MSE). These optimized DL beamformers are then reused for UL communication after scaling them to meet the UE power constraints. The downlink MSE for UE k is defined as

$$MSE_k = \sum_{\bar{k}} |\sum_{b} \boldsymbol{v}_k^H \boldsymbol{H}_{b,k}^H \boldsymbol{w}_{b,\bar{k}}|^2 - 2\mathrm{Re}\left[\sum_{b} \boldsymbol{v}_k^H \boldsymbol{H}_{b,k}^H \boldsymbol{w}_{b,k}\right] + \sigma^2 |\boldsymbol{v}_k|^2 + 1 \qquad \textbf{(4-1)}$$

where $\boldsymbol{v}_k$ is the combiner at UE k, $\boldsymbol{w}_{b,k}$ is the UE k precoder at BS b. σ^2 is the additive white Gaussian Noise (AWGN) power at UE k.

Since the MSE is not jointly convex with respect to both the combiner and precoder, we use alternating optimization to minimize the MSE. In this approach, the combiners are optimized for a fixed set of precoders and vice versa, iteratively refining the solution through bi-directional training. The DL beamformers are then scaled and reused for the active UL UEs. This iterative bi-directional training approach facilitates the distributed design of these beamformers, ensuring efficient utilization of training resources.

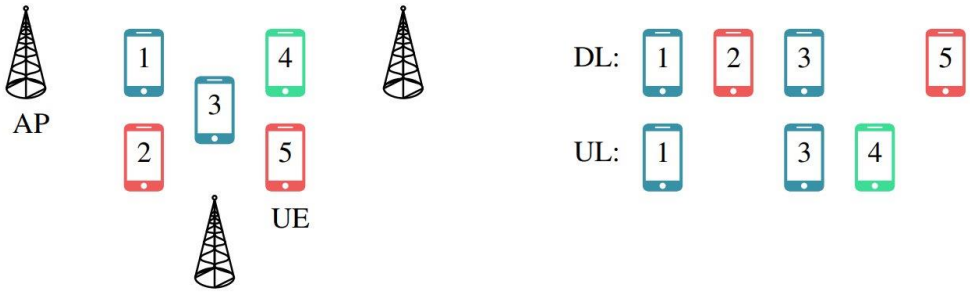

Figure 4-3: An example D-MIMO system with UEs to be served only in DL (red) and only in UL (green) and in both DL and UL (blue).

Results: We consider a system with 25 BSs and 32 UEs, all requiring both DL and UL data, operating in a time-varying channel at a 2.5 GHz carrier frequency. The results, illustrated in Figure 4-4, show that the effective rate of the combined beamforming design (Comb.) outperforms the separate beamforming designs (Sep.), where separate resources are allocated for DL and UL UE beamformer training. Moreover, 'OTA' designs that utilize additional UL signalling to obtain the implicit channel information of other APs perform better than 'local' designs that rely solely on local channel information at each AP, for more details please check papers [AGT21, GAT24]. In Figure 4-5, we vary the ratio of UEs requiring both DL and UL data to those requiring only DL or UL data. Across all fractions, the combined beamforming design consistently demonstrates superior performance compared to the separate beamforming design.

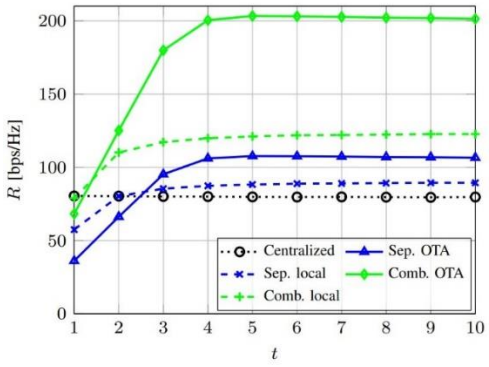

Figure 4-4: Rate versus block count for time-correlated block fading channels

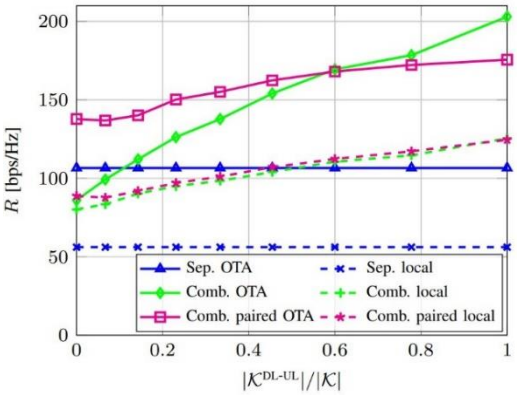

Figure 4-5: Rate versus the fraction of DL-UL UEs and UL-only or DL-only UEs.

4.2 D-MIMO architectures

This section focuses on optimizing the performance of D-MIMO systems by considering different architectural approaches:

- **Rotary Uniform Linear Array**: Improve system performance by incorporating movable and rotatable antennas, such as a rotary uniform linear array (RULA), to adaptively enhance coverage and efficiency.
- **Analog Fronthaul**: Utilize analogue fronthaul for achieving tight synchronization across distributed antennas in the D-MIMO system. Evaluate the system's error vector magnitude (EVM) to assess synchronization and overall performance.
- **JCAS**: Enhance D-MIMO performance by designing beamformers optimized for both sensing and communication. Evaluate the system performance to balance these dual functions effectively.

These architectural considerations aim to maximize the capabilities of D-MIMO systems in various deployment scenarios.

4.2.1 D-MIMO with rotary ULAs

Problem Statement: The idea of APs equipped with antennas (or antenna arrays) that have movement capabilities has gained a lot of attention in the research community. Many recent works have proposed and evaluated the performance of movable antennas, which are antennas that can move within a confined two-dimensional (2D) area [ZMZ24]. In the previous contribution [HEX224-D43], [TLS+24], we studied D-MIMO networks where each AP can be equipped with a fixed uniform linear array (ULA) of antennas or RULA. The numerical results showed that the optimal angular positions of the RULAs bring substantial gains to the SE. In our new contribution, we compare the performance of the proposed RULAs and the movable antennas studied in the literature. We also propose a new architecture where the ULAs can both move within a confined 2D area and rotate.

Methodology: We consider a square indoor industrial scenario with dimensions $L_A \times L_A$. We also consider the UL of a MU-MIMO system. A single AP located at the centre of the coverage area serves K active machine-type devices (MTDs) that are active simultaneously. All the MTDs are equipped with a single antenna and transmit data in the UL with the same fixed power p.

The AP can be equipped with a fixed antenna array (FAA), a movable antenna array (MAA), a rotary antenna array (RAA) or a movable and rotary antenna array (MRAA). In all those cases, the antenna array is an ULA of M half-wavelength spaced antenna elements. The FAA has no movement capabilities. Equipped with two servo motors, cables and slide tracks, the MAA can move within a square movement area with dimensions $L_B \times L_B$. The RAA is equipped with only a single servo motor and can rotate around its own axis. Finally, the MRAA is the combination of MAA and RAA: the antenna array can move within a square area and rotate. The RAA and MRAA systems are illustrated in Figure 4-6.

Similarly to the contributions in [HEX224-D43], [TLS+24], the optimization of the rotation and/or movement of the antenna array is computed based on estimates of the locations of active devices and using particle swarm optimisation (PSO).

Results and Conclusions: We adopt a spatially correlated Rician channel model with adjustable Rician factor κ. As the performance metric, we adopt the mean per-user achievable SE in the UL, denoted by $\bar{R}$. Resorting to Monte Carlo simulations, we compare the performance of FAA, RAA, MAA and MRAA. We set $M = 16$, $K = 10$ and $L_A = 100$ m. Figure 4-7 shows $\bar{R}$ versus κ considering different sizes of the square movement area. As expected, the MRAA achieves the best performance, since it has three degrees of freedom (DoF) for the movement, while FAA achieves the worse performance. Interestingly, RAA (which has only one DoF for movement) outperforms MAA (which has two DoFs for movement) when the size of the movement area is constrained, that is, $L_B < L_A$. Considering that the MAA and MRAA systems are very complex, bulky and expensive, the RAA emerges as the option that achieves the best balance between the performance gains and complexity, size and cost.

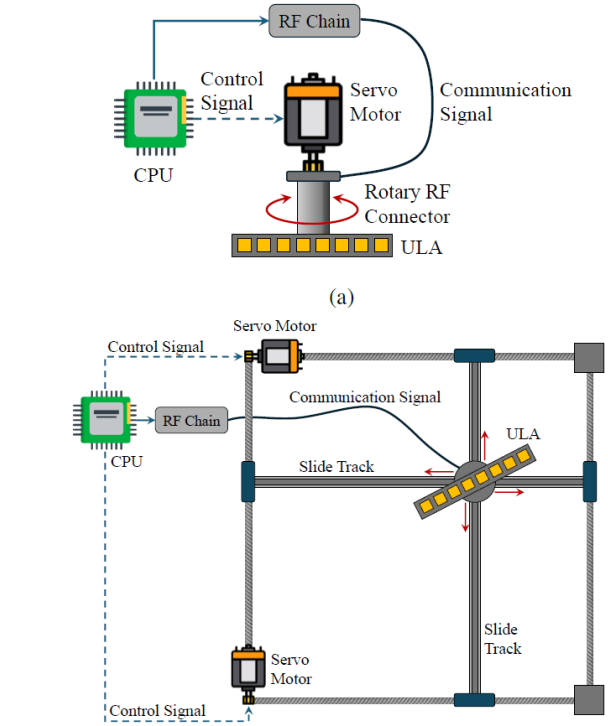

Figure 4-6: illustration of the RAA and MRAA systems.

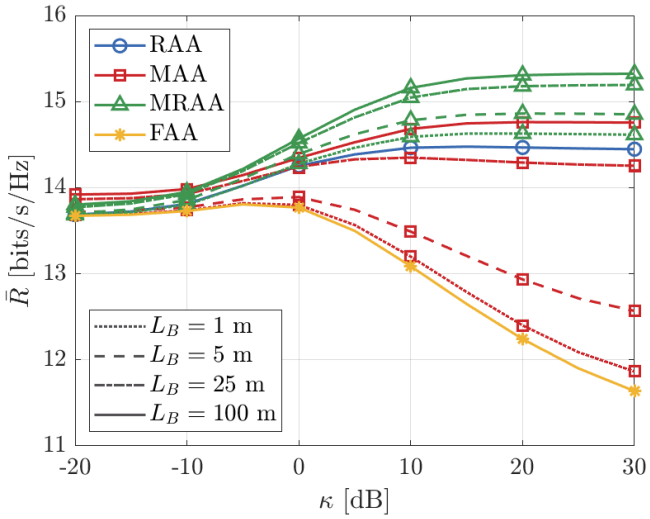

Figure 4-7: Mean per-user achievable SE versus the Rician factor, considering different sizes of the movement area.

4.2.2 D-MIMO coherent joint transmission with analogue fronthaul

Methodology: A critical aspect of D-MIMO performance is the synchronization of transmission/reception points (TRxPs) with sub-nanosecond precision. In response to this, we explore the potential of analogue radio-over-fibre (ARoF) as a viable alternative for 6G D-MIMO networks. Thanks to analogue fronthaul, RF carriers can be generated from the same centralized source, meeting the stringent synchronization and phase stability requirements of coherent joint transmission (CJT). For instance, if the maximum allowed phase error is 25°, the maximum delay permitted is ~20 ps for a carrier frequency of 3.5 GHz. This level of precision is very challenging to achieve with conventional digital fronthaul and independent local oscillators (LOs) in each antenna unit (AU). Furthermore, these links in combination with centralized signal processing, enable synchronization of TRxPs, where channel estimation includes the phase and amplitude changes due to both wired and wireless paths.

Results: Additional tests were conducted to validate the consistency of CJT with analogue fronthaul in a four-TRxP D-MIMO network. The experimental setup is illustrated in Figure **4-8**. An arbitrary waveform generator (AWG) with four channels operating at 120 GSa/s was used to generate OFDM signals at a carrier frequency of 3.2 GHz, with a bandwidth of 100 MHz and a subcarrier spacing (SCS) of 480 kHz. Although this SCS is not standard for a 100 MHz bandwidth, we used it due to the limited memory capacity of the AWG. The subcarriers were modulated using 64-quadrature amplitude modulation (64-QAM) symbols. TRxP 1 was connected through an ARoF fronthaul link, where the RF signal modulated an external cavity laser (ECL) optical carrier via a Mach-Zehnder modulator (MZM) driven by the first AWG channel. This signal travelled through 800 m of single-mode fibre (SMF) and was detected by a 10 GHz photodetector (PD). The other three TRxPs were directly connected to the remaining AWG channels using coaxial cables. All TRxPs and the receiver used omnidirectional antennas with a peak gain of about 8 dBi. The TRxPs were spaced with over ten wavelengths at 3.2 GHz between them. At the receiver, the signal was filtered using a bandpass filter (BPF, 3.1-3.3 GHz), amplified by an electrical amplifier (EA), and then recorded by an 80 GSa/s digital storage oscilloscope (DSO) for offline processing.

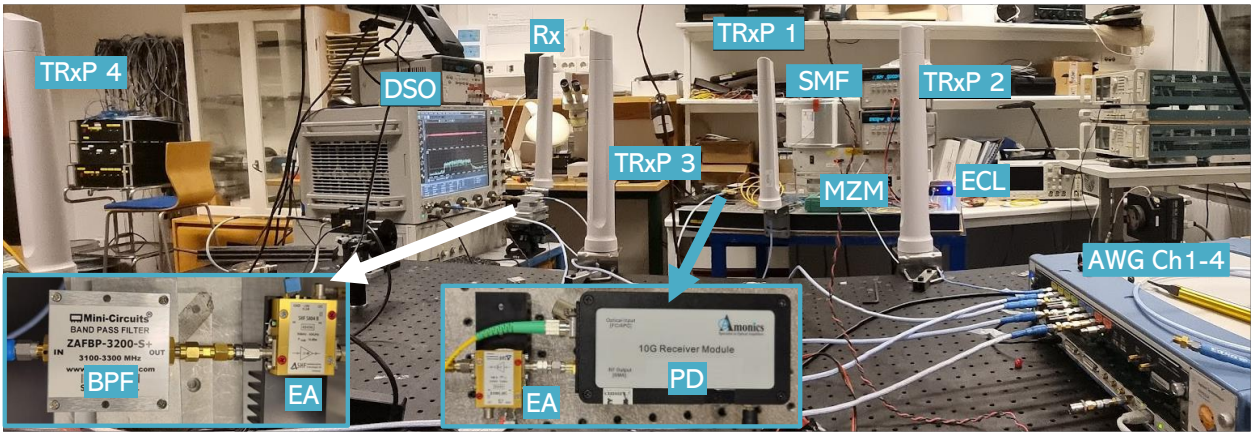

Figure 4-8: Experimental setup: transmitter/receiver configurations for the 4-TRxP D-MIMO network.

First, the performance of transmissions from TRxP 1 alone is analysed. Figure **4-9(**a) shows the received symbol constellation with an RMS EVM of 2.64%. For channel estimation, the signal is transmitted separately from each TRxP, using the LS estimation method as described in

$$\widehat{\mathbf{H}} = \overleftarrow{\mathbf{Y}}\mathbf{X}^{\mathrm{H}}\left(\mathbf{X}\mathbf{X}^{\mathrm{H}}\right)^{-1} \quad \textbf{(4-2)}$$

where $\mathbf{X}$ is a diagonal matrix containing known symbol sequences, $\overleftarrow{\mathbf{Y}}$ denotes the time-aligned sequences after transmission, and $\widehat{\mathbf{H}}$ is the estimated channel, capturing amplitude and phase variations from the wireless channel, analogue front-ends, and fronthaul links. A digital low-pass filter is used to refine these estimates. For CJT, only the signals from TRxPs 2, 3 and 4 undergoes time alignment and precoding. Time alignment is done by adding an appropriate time shift to the waveform, while precoding uses the complex ratio $\hat{\mathbf{h}}_1/\hat{\mathbf{h}}_N$, where $\hat{\mathbf{h}}_N$ is the vector channel estimates of subcarriers for TRxP N. This ensures TRxP 2, 3 and 4 signals are synchronized in time and phase with TRxP 1, with each subcarrier symbol from TRxP N expressed as follows:

$$x_N = \frac{\hat{h}_1}{\hat{h}_N}\tilde{s} \quad \textbf{(4-3)}$$

where $\tilde{s}$ is the time-aligned subcarrier symbol, adjusted to match the measured delay between the fronthaul links. To make a fair comparison for CJT, the geometry of the experimental setup was adjusted to create nearly flat-fading channel conditions, ensuring similar EVM performance across signals from all TRxPs. Figure **4-9**(c) through (f) show the symbol constellations for TRxPs 1, 2, 3, and 4, each transmitting independently, with RMS EVM values of 11.68%, 11.51%, 11.65%, and 10.69%, respectively. Figure **4-9**(g) and (h) show the results of non-coherent joint transmission (NCJT) and CJT, where all four TRxPs transmitted simultaneously. Without precoding and time alignment, the transmission RMS EVM is 63.96%, which improved significantly

to 3.96% with CJT processing. This corresponds to a CJT gain of roughly 9.4 dB compared to TRxP 1 transmission alone, as illustrated in Figure **4-9**(c). Although the theoretical gain for a four-TRxP distributed MIMO system is 12 dB, our experimental results fall short since achieving flat-fading conditions over a 100 MHz bandwidth for all four TRxPs is challenging, given the complex scattering environment in the lab where the test were done, leading to performance deviations from the theoretical values.

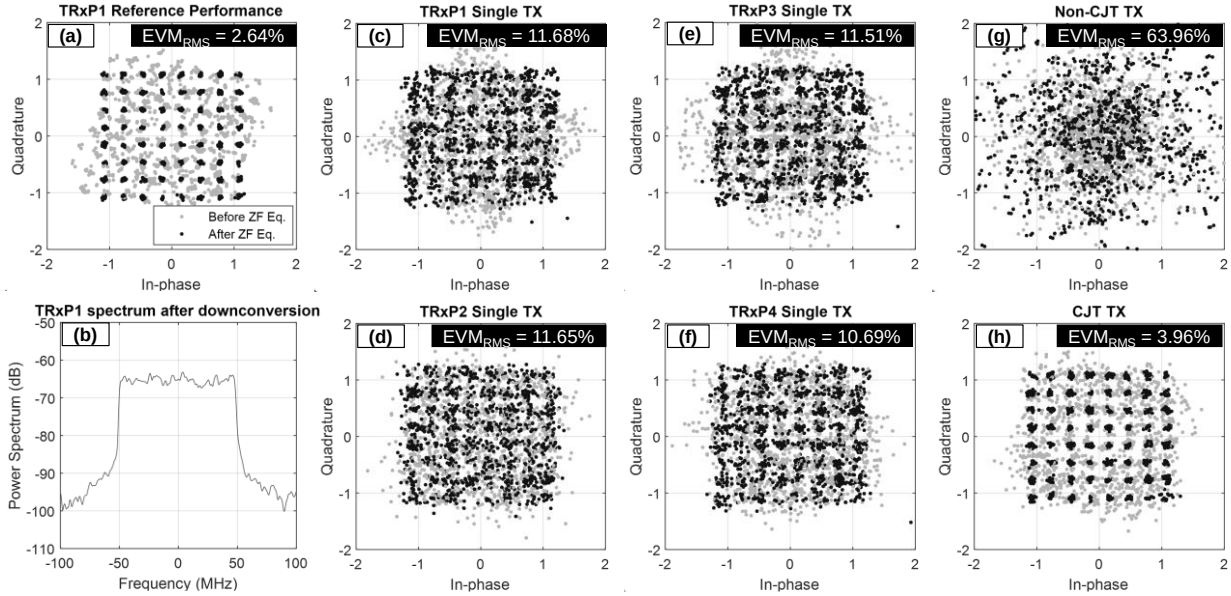

Figure 4-9: Received constellation diagrams for a 4-TRxP D-MIMO network with EVM measurements before and after ZF equalization are presented: (a) optimal individual transmission from TRxP 1, (c-f) attenuated individual transmissions from TRxPs 1 to 4, and (g) simultaneous NCJT and (h) CJT. Additionally, (b) shows the receiver baseband spectrum for TRxP 1 individual transmission.

4.2.3 D-MIMO for JCAS

Problem Statement: We address the challenge of simultaneously providing communication and sensing functionalities within the same time-frequency resources in a D-MIMO system. In this work, we consider that all APs are phase-synchronized and have single antenna each. Each AP allocates fraction of its total power for sensing, and remaining power is allocated to communication UEs. We quantify the sensing and communication performance through position error bound (PEB) and UEs sum rate metrics, for different power allocation for sensing and communication.

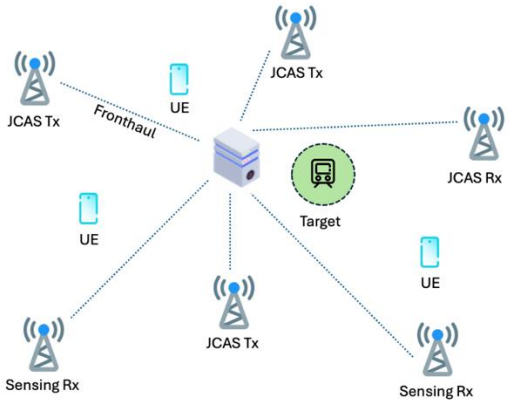

Figure 4-10: D-MIMO JCAS system with K UEs and single target.

Methodology: In Figure 4-10, we consider a downlink D-MIMO JCAS system, where M APs serve K communication UEs while simultaneously sensing the environment to detect targets. Each AP either serves as a JCAS transmitter or a sensing receiver. At a given time instant, a subset of the JCAS APs jointly serve UEs by transmitting precoded signals containing both communication and sensing signals. Simultaneously, the rest

of the APs receive the reflections from the sensing target. We consider a non-isotropic target and model the sensing channel by taking into account i) different path delays from the distributed APs. The theoretical PEB and UE's sum rate are derived and used as sensing and communication metric, respectively. Both the sensing and communication channels are modelled using the free-space path loss model. We perform numerical analysis based on these communication and sensing metrics.

Results: We consider a total area of 100m x 100m, where the APs, UEs and a target are randomly deployed within the coverage area. We set the number of APs to 20 and consider the transmit and receiver AP pairs (M_{tx}, M_{rx}) as (15,5) and (19,1). The number of UEs is assumes to be $K=5$ and considered a single target. The pathloss for both the communication channel and the sensing channel is modelled using the free-space path loss model. Each AP has a total transmit power of P_m, where a fraction of ρP_m power is allocated to sensing and (1-ρ)P_m fraction is allocated to communication UEs. Here ρ is the sensing weight factor. In Figure 4-11(a), we investigate the sensing target PEB and the UEs sum rate for different (M_{tx}, M_{rx}) pairs and total transmit power at each AP. The $(M_{tx}, M_{rx}) = (15,5)$ configuration achieves the better PEB compared to the (19,1) case. This improvement is because the phase synchronized distributed receiving APs help decrease the PEB by providing spatial diversity, as they receive the target reflected signal from different locations. For communication, however, the (19,1) case achieves higher sum rate than (15,5) configuration. This is because the increase in transmit APs increases the macro diversity. Also, as the transmit power P_m increases, the target PEB for sensing reduces, while the communication UE's sum rate remains constant. In Figure 4-11(b), we further investigate the effect of sensing weight ρ on target PEB. For $\rho < 10^{-5}$, as we increase ρ, more power is allocated to the sensing beam, improving the target estimate and thus reducing the target PE. For $\rho \geq 10^{-5}$, the target PEB remains constant as ρ increases. This indicates that the optimal sensing weight ρ to achieve the lowest PEB for the considered D-MIMO system is 10^{-5}.

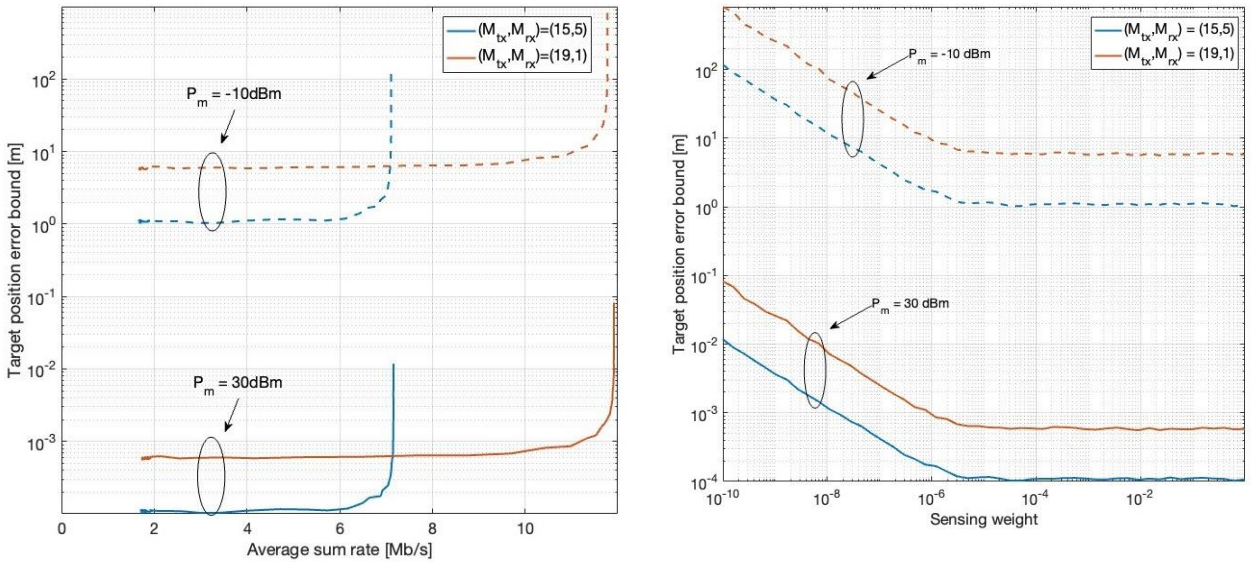

(a) Target PEB versus UE sum rate **(b) Target PEB versus sensing weight**

Figure 4-11: Comparison of communication SE and sensing PEB performance in a D-MIMO system.

Conclusion: We analysed the sensing and communication performance in the phase-synchronized case for different transmit and receiver AP pairs, and for different sensing power allocation weight factors. We next extend this work to the case where the APs are not phase-synchronized and have deterministic but unknown phase offsets.

4.3 Massive MIMO architectures

This section focuses on evaluating various hybrid beamforming architectures and deployment strategies to enhance energy efficiency in massive MIMO systems, along with analysing link-level signal models to optimize hybrid beamforming performance.

4.3.1 Energy efficient beamforming architecture and deployment for sub-THz

Problem statement: Scope of this study is the spectral and energy efficiency trade-off of different beamforming architectures and BS placements. With system level simulations the coverage and throughput of different deployments within an indoor scenario is assessed and presented in [HEX224-D43]. For evaluating the related energy efficiency, in addition a dedicated power consumption model has been derived.

Methodology: The coverage and throughput of an indoor scenario of 30 x 60 m, served with different number of BS using different hybrid BF architectures and transmit power, is evaluated. Exemplary results see in [HEX224-D43]. For each of the deployments the total power consumption within the deployment scenario is assessed with a specifically derived power consumption model. For the analogue parts it is based on published data of existing sub-THz devices [SSH+20], [EHH+20], [WDV23] and scaled to the assumed transmit power and architecture according to the procedure introduced in [HW21]. The power consumption of the baseband parts is derived from the computational complexity of the assumed algorithms and an "educated guess" for the intrinsic efficiency in Giga-floating-point operations per second per watt (GFLOPS/W), using the basic procedure introduced in [DWZ+20], [DD16] and including scaling to present technology.

Results: Performance results in [HEX224-D43], only considering PA power consumption, show that in an exemplary deployment 8 BS can achieve similar performance as 4 BS, but with less total PA transmit power and related power consumption. But there is a trade-off because a higher number of RF chains including baseband processing is needed, consuming additional power. With the newly derived power consumption model for the baseband parts this trade-off can be assessed for various deployments and BF architectures.

An exemplary analysis is given in Figure 4-13 derived for the throughput CDFs in Figure 4-12. For one subpanel and 4 BS the model derives a total power consumption of about 400 W, whereas with 8 BS only 250 W are needed. In the latter case the power consumption of the Rx part and the analogue BB and upconverter part of the Tx are doubled, but the Tx parts including the PA consume significantly less power for achieving similar throughput CDF.

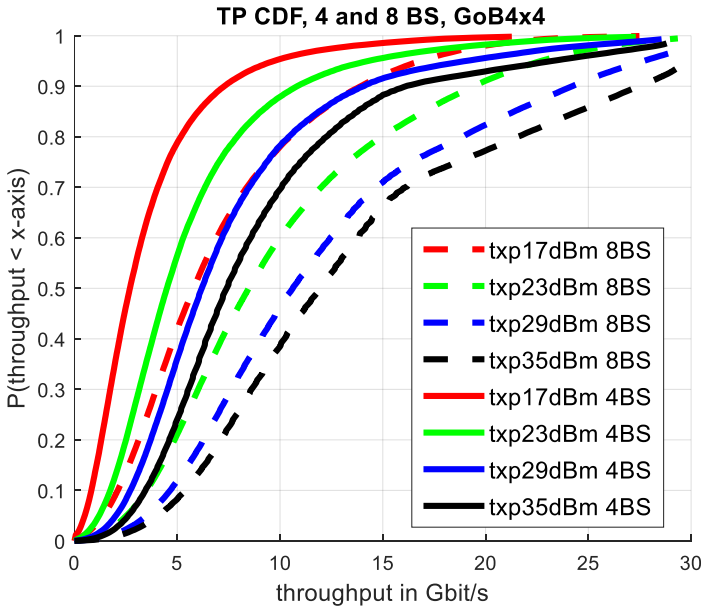

Figure 4-12: 8 BS with 17 dBm Tx power each (dashed red line) lead to similar throughput CDF as 4 BS with 29 dBm Tx power each (solid blue line) at 1/8 of PA power consumption [HEX224-D43].

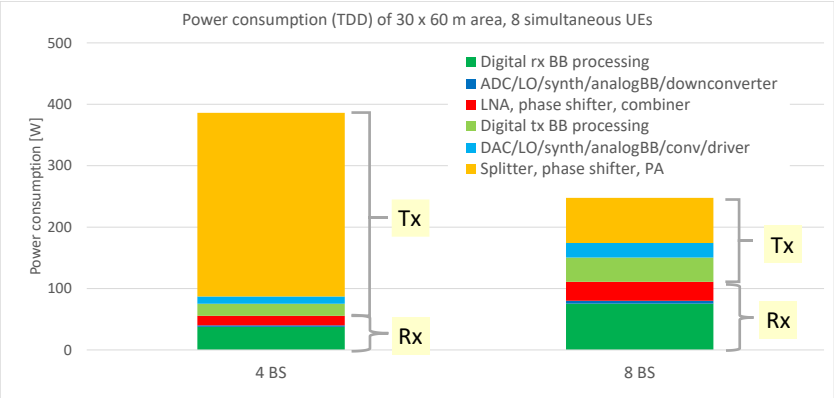

Figure 4-13: Power consumption for 4 BS and 8 BS deployment achieving similar throughput CDF as shown in Figure 4-12 (solid blue and dashed red line).

Conclusions: The exemplary result above shows that the targeted number of BS and related range has significant impact on the overall power consumption. Of course, there are further trade-offs to be considered, e.g. which overall throughput is needed, how many UEs need to be served (optimum hybrid architecture), and which device capabilities will be available. A flexible and scalable power consumption model in combination with system level throughput simulations will help to find the design parameters for energy efficient deployments.

4.3.2 Hybrid analogue-digital architectures – Link-level signal modelling

Problem statement: In radio communication systems, the general MIMO precoding architecture is a hybrid scheme including a baseband digital part and an analogue part, as illustrated by Figure 4-14. Digital precoding offers flexibility but requires a dedicated transceiver chain per antenna element. Nevertheless, at high frequencies such as in mmWave and sub-THz contexts, the closely spaced antenna elements, resulting from the shorter wavelengths, pose challenges in allocating physical space for individual RF chains. The implementation of RF chains per antenna element, which includes components like power amplifiers, becomes impractical and costly. As a result, hybrid precoding has emerged as a preferred solution in mmWave contexts. Hybrid precoding combines baseband digital processing with analogue components, enabling a more efficient utilization of hardware resources while still achieving the desired performance. This approach not only addresses the physical space limitations but also helps mitigate the high costs associated with RF chains.

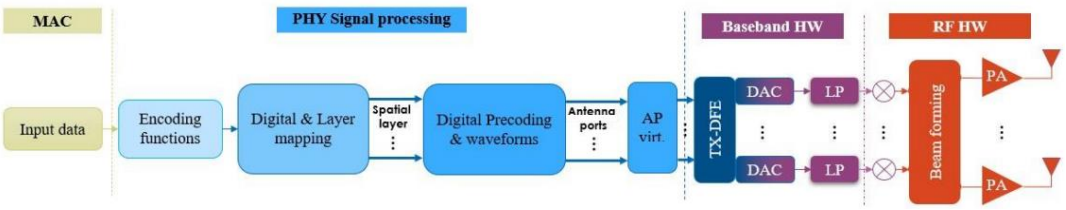

Figure 4-14: General hybrid MIMO precoding.

Methodology: This section presents possible hybrid beamforming solutions for mmWave/sub-THz communications in 2 steps. First, the streams of complex symbols at the spatial layers are first multiplied with a baseband frequency selective digital precoder, so before OFDM modulation. Then, analogue beamforming is applied per spatial layer. The antenna ports are logical antenna from the receiver point of view, linked with reference signals (RSs), e.g. CSI- reference signal. A two-stage virtualization then applies. The first stage maps the antenna ports to the transceivers units (TXRU), each one including a digital to analogue converter. The second virtualization maps the TXRUs to the antenna elements (AE) via an analogue precoder applied to the time-domain signal, the waves are then transmitted in a preferred direction (beam) thanks to phase shifters. The analogue precoder can be configured with fully or partially connected antenna array structures. The hybrid MIMO precoding architecture proposed in this study is shown by Figure 4-15. The antenna panel is either single polarized or cross-polarized, and one spatial layer is assumed per polarization. In case of cross-polarization, half of the AE corresponds to a first polarization slant angle, the other half corresponds to a

second polarization slant angle, orthogonal to the first one. As for the antenna port-to-TXRU virtualization, a one-to-one mapping is assumed in this study.

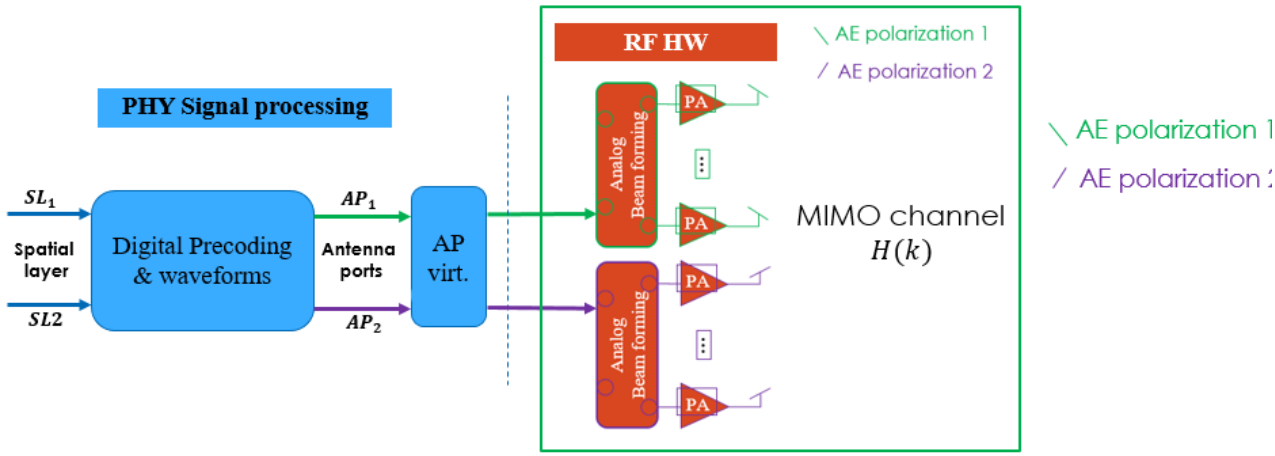

Figure 4-15: Proposed hybrid MIMO precoding.

The analogue beamforming $\boldsymbol{W}_A$ is first optimized for the MIMO channel frequency responses $\boldsymbol{H}(k)$, across the whole bandwidth. Then, the digital precoding is optimized at each subcarrier frequency k, based on the effective channel matrix defined by $\boldsymbol{H}_{\text{eff}}(k) = \boldsymbol{H}(k)W_A$.

4.4 Multiuser massive MIMO

This section explores channel estimation for multi-user MIMO using data-driven methods, targeting scenarios where pilot-based CSI is unavailable, or the channel conditions change rapidly. Building on the estimated channel information, precoders are then designed using the most up-to-date data to optimize performance in multi-user MIMO scenarios.

4.4.1 MU-MIMO optimisation in diverse device scenarios

Problem statement and Methodology: In [HEX224-D43, Sec. 4.2.4 and A.2.3], we introduced the effective antennas which is envisioned to allow to solve fundamental MU-MIMO problems, allowing for practical implementations, including: (i) incorporate very large and diverse arrays into MU-MIMO (ii) speed up the UE-BS communication for channel knowledge and update (iii) incorporate the outer cell interference rejection inside dimensionality reductions and (iv) address the TDD channel ageing problem. Here, we present the progress related to the last important problem where the accuracy of the channel from data reconstruction ability is investigated (we present the reconstruction Mean Square Error, the reconstruction error histogram and further insights in the following section). The main concept relates to the fact that the large BS array operates in low-moderate SNR regime and due to its size rises is able to increase the SNR of the users with MIMO decoding. However, for the channel reconstruction, the large MU-MIMO matrix individual components have to be estimated and the low-moderate SNR of the UL signals poses the channel reconstruction challenge for the “channel-from data” approach presented in D4.3. This part of our research thus investigates ability to reconstruct channel with improved accuracy. This is a necessarily step before the EAs optimization which will determine EAs under constraint that the same set of effective antennas is used by UE for downlink and UL (UE Tx effective antennas = UE Rx effective antennas), thus allowing DL transmission based on the UL channel recovered from the data. More information on the methodology and theoretical analysis can be found in Section A.1.

Results: Simulations over TDLA30-5/Low (assuming 4 closely spaced users) show ability of channel reconstruction even at low and moderate SNR, as observed in Figure 4-16(a). The channel matrix over the whole 100 MHz spectrum (and having dimensions of 4x32 at every RE) is possible to reconstruct with approximately -25 dB error. The averaging is performed here along the frequency dimension over $N_E = 45$ elements. The averaging gain together with SNR $= 10$ dB should ideally be (for the simplistic scalar case of non-correlated averaging) about $10 + 10\ \log_{10} 45 = 26.5$ dB, while for the proposed algorithm (which performs reconstruction of large matrix) it is only slightly smaller. Hence, we observe ability of the channel

reconstruction. We consider this to be a very positive result, upon which further optimizations of effective antennas can be built for this channel-from-data decoding. Note that the error corresponds to the "raw" decoding, before further post-processing, as we observe in Figure 4-16(b). It is expected that further improvement can come from post-processing approach with classical smoothing or a smoothing based on future AI/ML approaches (which in the simplest form represents kind of regression curve construction). Regarding the iterative matrix inversion, the convergence is reached in about 8 steps.

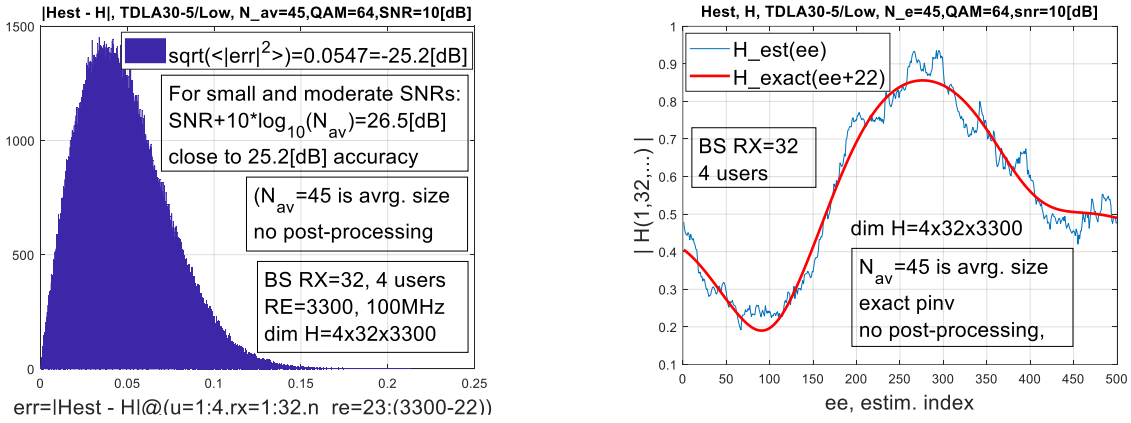

(a) MU-MIMO channel reconstruction error

(b) Example of channel matrix reconstruction (ee is RE index)

Figure 4-16: MU-MIMO channel reconstruction accuracy with the channel from data proposed approach (and $N_{av} = 45$) achieves 25.2 dB despite the BS SNR is low-moderate 10dB.

4.5 Low-complexity optimization for MIMO

This section investigates a low-complexity 1-bit ADC and DAC architecture as an energy-efficient approach for massive MIMO systems with fully flexible digital beamforming. The focus areas include:

- **D-MIMO with 1-Bit ADCs**: Enhance UL D-MIMO performance with 1-bit ADCs by optimizing UE transmit powers and managing noise levels at APs or remote radio heads (RRHs). This ensures robust communication despite the limitations of 1-bit quantization.
- **Enhanced Data Detection**: Improve detection accuracy for higher-order QAM in massive MIMO systems with 1-bit ADCs by compensating for quantization distortion. This is achieved by leveraging the expected received constellation to refine signal recovery.
- **1-Bit ADC/DAC in Massive MIMO**: Evaluate the performance of a doubly quantized system using 1-bit ADCs and DACs, focusing on its extremely low complexity while assessing its impact on overall system efficiency and reliability.

4.5.1 One-bit ADC for multicell setup

Problem statement: Some of the next-generation wireless systems beyond 5G are also expected to operate at frequencies up to 1 THz, requiring large antenna arrays and precise beamforming. However, current ADCs/DACs are power-intensive. Low-resolution ADCs/DACs, especially 1-bit variants, offer a solution by enabling massive MIMO arrays with minimal power consumption. Fully digital architectures also address limitations of hybrid beamforming at sub-THz frequencies. In the UL, the signal-to-interference-noise and distortion ratio (SINDR) with 1-bit ADCs is non-monotonic with UE transmit power, making the UE transmit power optimization critical in distributed massive MIMO systems.

Methodology: The distributed massive MIMO system under consideration comprises B RRHs and K single-antenna UEs. All RRHs are connected to a central unit (CU) via fronthaul links for data and CSI exchange. The RRHs are equipped with 1-bit ADCs, and this study focuses on the UL scenario. To optimize the system performance, we explore two designs: the minimum-power design and the max-min SINDR design, aimed at optimizing the UE power levels and RRH noise levels under Bussgang-based maximum ratio combiner

(BMRC) and Bussgang-based minimum mean squared error (BMMSE) receivers. The max-min SINDR design is given as

$$\max_{p_k,\sigma_b} \min SINDR_k$$
$$p_k \leq p_{UE} \quad \textbf{(4-4)}$$
$$\sigma_b \geq \sigma_{min}$$

where $SINDR_k$ is the signal-to-interference-noise and distortion ratio of UE k considering 1-bit ADC RRHs. p_k is the UE k power and p_{UE} is the maximum UE transmit power. σ_b is the noise and dithering level at the BS and σ_{min} is the minimum noise level at the BS corresponding to the AWGN.

Since the UE transmit power and RRH noise levels cannot be optimized simultaneously, an alternating approach is employed: UE transmit powers are optimized for a fixed RRH noise level, and the RRH noise levels are updated using line search. Once the optimal RRH noise levels are determined via line search, they are further fine-tuned using gradient-based methods for improved accuracy.

Results: We consider a system with 4 RRHs, each equipped with 256 antennas, and 4 single-antenna UEs clustered as shown in Figure 4-17. The carrier frequency is set at 28 GHz, and a Rayleigh fading channel is assumed. The channel of each UE is estimated at each RRH using orthogonal resources. As shown in Figure 4-18, the achievable and target SINDR levels are enhanced by introducing dithering (noise) at the RRHs. Additionally, the BMMSE receiver outperforms the BMRC receiver due to its superior ability to mitigate quantization distortion.

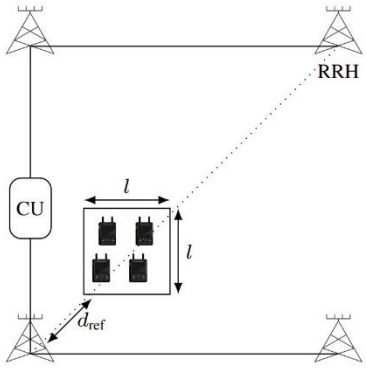

Figure 4-17: D-MIMO with RRH and UE placement.

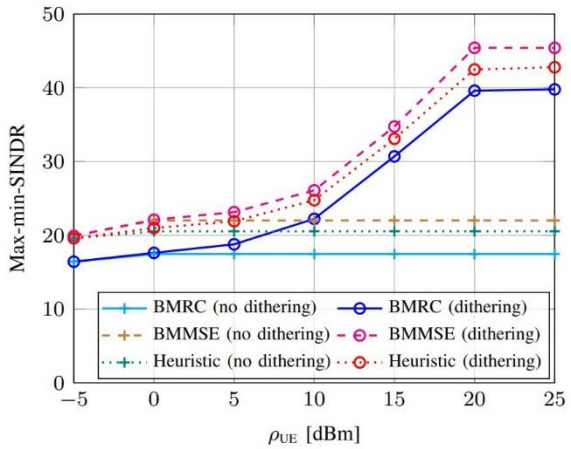

Figure 4-18: Max-min SINDR with UE transmit power and RRH dithering level optimisation.

4.5.2 Enhanced data detection for massive MIMO with 1-bit ADCs

Problem statement: We present a new analytical framework on the UL data detection for massive multiple-input multiple-output systems with 1-bit ADCs [RAT24]. We first characterize the expected values of the soft-estimated symbols (after the linear receiver and prior to the data detection), which are affected by the 1-bit quantization during both the channel estimation and the UL data transmission. In our analysis, we consider conventional receivers such as maximum ratio combining (MRC), ZF, and minimum mean squared error (MMSE), with multiple UEs and correlated Rayleigh fading. Additionally, we design a linear minimum mean dispersion (LMMD) receiver tailored for the data detection with 1-bit ADCs, which exploits the expected values of the soft-estimated symbols previously derived. Then, we propose a joint data detection (JD) strategy that exploits the interdependence among the soft-estimated symbols of the interfering UEs, along with its low-complexity variant. These strategies are compared with the robust maximum likelihood data detection with 1-bit ADCs.

Methodology: Consider a single-cell massive MIMO system where a BS, equipped with M antennas, serves K UEs in the UL. Each BS antenna is connected to two 1-bit ADCs, one for the in-phase and one for the quadrature component of the received signal. The system model is illustrated in Figure 4-19.

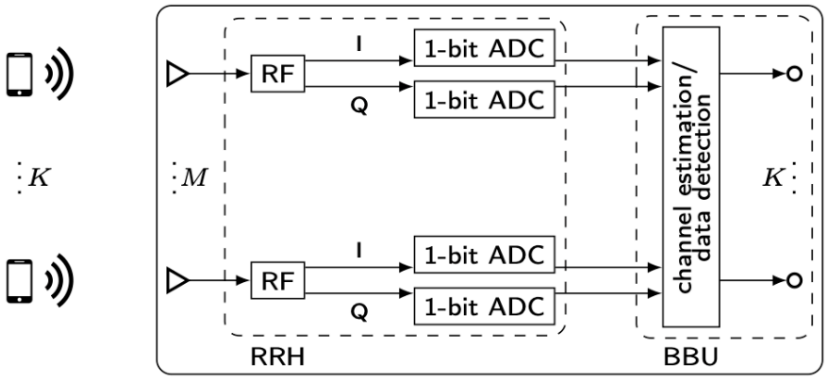

Figure 4-19: Fully digital massive MIMO system with 1-bit ADCs.

The received signal before the 1-bit ADCs is given by $\boldsymbol{y} = \sqrt{\rho}\boldsymbol{H}\boldsymbol{x} + \boldsymbol{z} \in C^{M\times 1}$, where ρ is the SNR, $\boldsymbol{H} \in C^{M\times K}$ is the channel matrix, $\boldsymbol{x} \in C^{K\times 1}$ is the data symbol vector, and $\boldsymbol{z} \in C^{M\times 1}$ is the AWGN vector. A general correlated Rayleigh fading model is assumed for the channel. Then, the received signal after the 1-bit ADCs is given by $\boldsymbol{r} = Q(\boldsymbol{y}) \in C^{M\times 1}$, where $Q(.)$ is the 1-bit quantisation function. Finally, the BS obtains a soft estimate of $\boldsymbol{x}$ via linear combining as $\hat{\boldsymbol{x}} = \boldsymbol{V}^{\mathbf{H}}\boldsymbol{r} \in C^{K\times 1}$, where $\boldsymbol{V} \in C^{M\times K}$ is the combining matrix. Imperfect CSI, obtained via the Bussgang linear MMSE estimator with pilot length τ, is assumed for the design of the combining matrix. The expected values of the soft-estimated symbols with can be derived in closed form as a function of the SNR, the pilot matrix used during the channel estimation, the Bussgang gain matrix resulting from the Bussgang decomposition, the covariance matrix of the quantised received signal during the channel estimation, and the cross-covariance matrix between the quantised signals received during the UL data transmission and channel estimation.

Results: 16-QAM data symbols are considered. The channel covariance matrices are generated based on the one-ring channel model with no pathloss. Numerical results examining the symbol error rate (SER) show that MMSE exhibits a considerable performance gain over MRC, whereas the proposed LMMD receiver significantly outperforms all the conventional receivers. Lastly, the proposed JD and its low-complexity variant provide a significant boost in comparison with the single-UE data detection (SUD) [RAT24]. In general, there is a significant gain for all the data detection strategies obtained with the ZF and MMSE compared with their MRC counterparts. The SER gain for the ZF/MMSE receivers is not due to their expected values but the reduced dispersion of the soft-estimated symbols around them. The proposed JD and its low-complexity variant (N-JD) provide a significant boost in comparison with the exhaustive SUD (Exh. SUD) with the ZF/MMSE receivers. This means that taking advantage of the interdependence among the soft-estimated symbols of the interfering UEs gives a notable gain over the data detection strategies that treat each UE individually. This is illustrated in Figure 4-20(b). Therein, it can be observed that the SER curves feature an optimal SNR operating point: at low SNR, the AWGN is dominant; at high SNR, the soft-estimated symbols

corresponding to the data symbols with the same phase are hardly distinguishable. In between these regimes, the right level of AWGN produces a proper scrambling of the 1-bit quantised signals at the M antennas [AT22, RAT24].

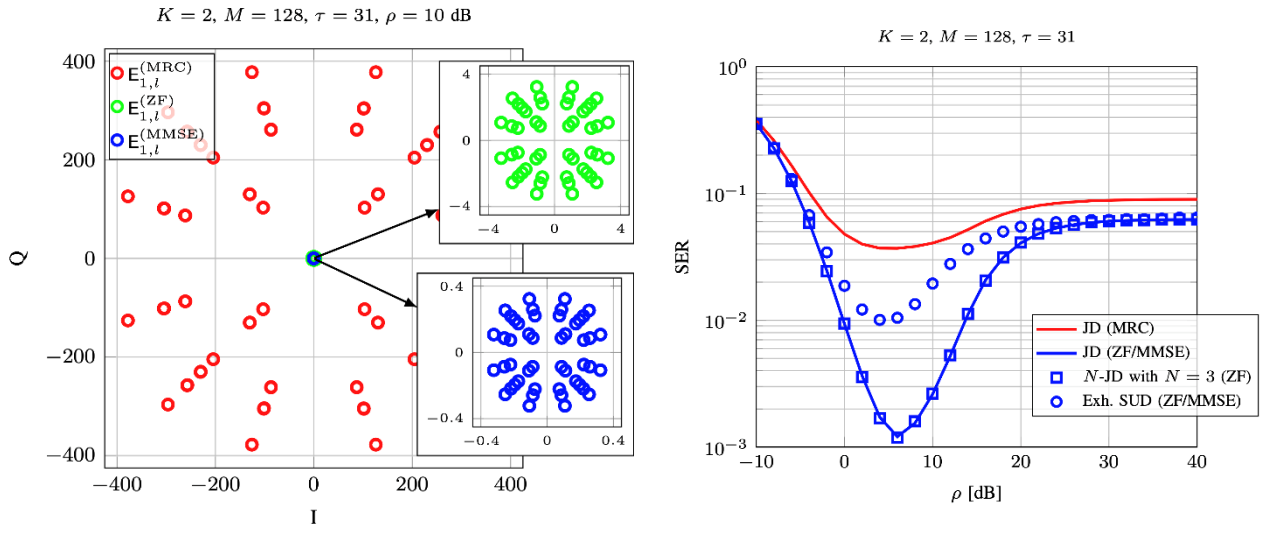

(a) Expected values of the soft-estimated symbols of UE 1 when UE 2 transmits all the possible data symbols and MRC, ZF, or MMSE is adopted at the BS

(b) SER versus SNR obtained with different data detection strategies and different receivers

Figure 4-20: Evaluation of enhanced data detection for massive MIMO with 1-bit ADCs.

4.5.3 Massive MIMO with 1-bit DACs and ADCs

Problem statement: Enabling communications in the (sub-)THz band will call for massive MIMO arrays at either the transmit- or receive-side, or at both. To scale down the complexity and power consumption when operating across massive frequency and antenna dimensions, a sacrifice in the resolution of the DACs/ADCs will be inevitable. Simple 1-bit DACs/ADCs can also alleviate the overall complexity and power consumption of the RF chains. For instance, 1-bit DACs at the transmitter allow the use of low-cost power amplifiers that are not constrained to operate with backoff [LMS+21], whereas 1-bit ADCs at the receiver relax the requirements on the automatic gain control [NSN21]. Massive MIMO systems with low-resolution data converters have been generally studied assuming coarse quantisation at the base station (either in the DACs [ATD21] or in the ADCs [ATD21], [AT22], [RAT24]) and full-resolution UE. The extreme scenario where both the transmit- and receive-side are equipped with fully digital massive MIMO arrays and 1-bit DACs/ADCs is analysed here, which is referred to in the following as *doubly 1-bit quantized massive MIMO* [ATN+23]. Indeed, combining 1-bit DACs and ADCs leads to a fully digital system with minimum RF complexity, cost, and power consumption. Note that the system model considered in this section can be considered as an extension of the model in Figure 4-19 by including 1-bit DACs.

Considering a point-to-point system, the Bussgang decomposition is utilised to unfold the relation between the transmitted data symbols (at the input of the transmitter's 1-bit DACs) and the soft-estimated symbols acquired via linear combining of the quantized received signal (at the output of the receiver's 1-bit ADCs). Assuming perfect CSI, a tractable approximation of the MSE between the transmitted data symbols and their soft estimates is derived along with the combining strategy that minimizes it. This approximation is accurate in the regime of a large number of transmit antennas. Numerical results show that, despite its simplicity, a doubly 1-bit quantized massive MIMO system with very large antenna arrays can deliver an impressive performance in terms of MSE and SER, which is not far from that of a massive MIMO system with full-resolution DACs and 1-bit ADCs.

Methodology: Consider a point-to-point doubly 1-bit quantised massive MIMO system where a transmitter, equipped with N antennas and 1-bit DACs, transmits K data streams to a receiver with M antennas and 1-bit ADCs. Such a point-to-point system may represent, e.g., a wireless backhaul scenario. The system model is illustrated in Figure 4-21.

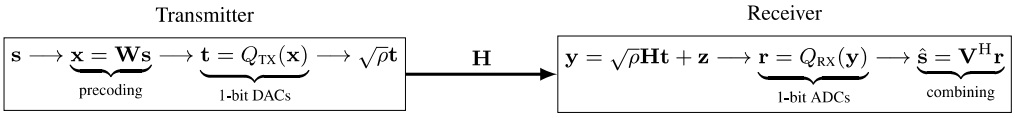

Figure 4-21: Doubly 1-bit quantised massive MIMO system.

The transmitter aims at conveying the data symbol vector $\boldsymbol{s} \in \mathbf{C}^{K\times 1}$ to the receiver. In this setting, $\boldsymbol{s}$ is first precoded as $\boldsymbol{x} = \boldsymbol{W}\boldsymbol{s} \in \boldsymbol{C}^{N\times 1}$, where $\boldsymbol{W}$ is the precoding matrix, and then quantised at the 1-bit DACs as $\boldsymbol{t} = \boldsymbol{Q_{tx}}(\boldsymbol{x}) \in C^{N\times 1}$, where $\boldsymbol{Q_{tx}}(.)$ is the 1-bit quantisation function at the DACs. Then, the signal arriving at the receiver is $\boldsymbol{y} = \sqrt{\rho}\boldsymbol{H}\boldsymbol{t} + \boldsymbol{z} \in C^{M\times 1}$, where ρ is the SNR, $\boldsymbol{H} \in C^{M\times K}$ is the channel matrix, and $\boldsymbol{z} \in C^{M\times 1}$ is the AWGN vector. At the 1-bit ADCs, $\boldsymbol{y}$ is quantized as $\boldsymbol{r} = \boldsymbol{Q_{rx}}(\boldsymbol{y}) \in C^{M\times 1}$, which is the signal observed at the receiver and is the result of a double quantisation step. Finally, the receiver obtains a soft estimate of $\boldsymbol{s}$ via linear combining as $\hat{\boldsymbol{s}} = \boldsymbol{V}^{\mathbf{H}}\,\boldsymbol{r} \in C^{K\times 1}$, where $\boldsymbol{V} \in C^{M\times K}$ is the combining matrix. Perfect CSI is assumed for the design of both the precoding and the combining matrix. The MSE between $\boldsymbol{s}$ and its soft estimate $\hat{\boldsymbol{s}}$ can be written as $\epsilon = \frac{1}{K}E_{\boldsymbol{s},\boldsymbol{z}}[||\hat{\boldsymbol{s}} - \boldsymbol{s}||^2]$. To obtain a tractable expression of the MSE, Gaussian data symbols are considered. This allows one to apply the Bussgang decomposition to express the doubly 1-bit quantized signal observed at the receiver as a linear function of the original transmitted signal. In general, the Bussgang decomposition allows one to write the output of a nonlinear system as a scaled version of the input plus an uncorrelated distortion.

Results: We consider far-field propagation. The transmitter and the receiver are equipped with square uniform planar arrays with half-wavelength spacing and are placed with their broadsides facing each other. Between them lies a cluster of scatterers confined within an angle spread of π/ around the broadside direction in both the azimuth and elevation. We observe that truly massive antenna arrays at both the transmitter and receiver (e.g., $N, M \geq 1000$) are necessary to achieve impressive values of the MSE. This is illustrated in Figure 4-22, where $\tilde{\epsilon}$ denotes the approximate MSE (which is derived analytically as described above). Assuming 16-phase shift-keying (16-PSK) data symbols, remarkably small SER values can be obtained with truly massive antenna arrays at both the transmitter and receiver, although an acceptable SER can be achieved also for moderate array sizes [ATN+23]. In general, the performance of the considered doubly 1-bit quantised massive MIMO system is not far from that of a massive MIMO system with full-resolution DACs and 1-bit ADCs. In particular, replacing the 1-bit DACs with full-resolution ones provides a modest MSE or SER gain at the cost of much higher RF complexity and power consumption at the transmitter. It can be observed that, for fixed numbers of antennas, there is an optimal number of data streams: on the one hand, judiciously increasing the number of data streams generates a useful scrambling of the 1-bit quantised signals at the M receive antennas; on the other hand, the inter-stream interference becomes dominant for large values of K [ATN+23].

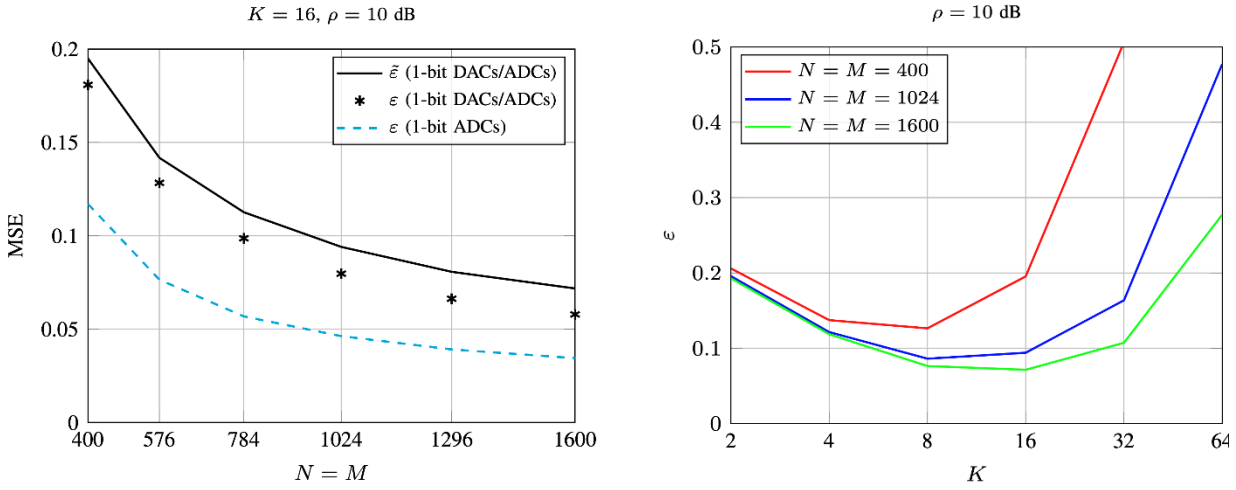

(a) MSE for 1-bit DACs/ADCs and full-resolution DACs/1-bit ADCs versus the number of transmit/receive antennas

(b) approximate MSE for 1-bit DACs/ADCs versus the number of data streams

Figure 4-22: Evaluation results of doubly 1-bit quantised massive MIMO.

4.6 Summary

Coherent and non-coherent beamforming strategies have been proposed for D-MIMO transmissions to address varying CSI availability and fronthaul signalling limitations, ensuring robust system performance. In terms of D-MIMO architecture, the use of rotary and movable antennas has demonstrated significant performance improvements in both MIMO and D-MIMO systems, while analogue fronthaul integration enhances EVM performance by improving synchronization and signal quality. Additionally, the optimization of JCAS beamforming within D-MIMO systems has been identified as a promising area for future research. For massive MIMO, energy-efficient hybrid beamforming architectures and deployment strategies have been proposed to minimize power consumption while maintaining high performance, supported by the development of a link-level signal model to optimize hybrid beamforming. In the context of MU-MIMO, low-complexity, data-driven channel estimation techniques have been introduced to handle scenarios where pilot-based CSI is unavailable, or channels vary rapidly. Lastly, for low-complexity MIMO, techniques to enhance the performance of 1-bit ADCs have been proposed for both single-cell and multi-cell scenarios, addressing quantization challenges, and the performance of 1-bit ADCs and DACs has been analysed and compared to full-resolution counterparts, showcasing their potential for energy-efficient massive MIMO implementations.

5 RIS-assisted transmission

Reconfigurable intelligent surface (RIS) is an emerging technology in the field of telecommunications, offering a novel way to enhance the performance of wireless networks. These surfaces consist of electronically controllable elements that can manipulate electromagnetic waves, allowing for improved signal propagation in wireless communication systems. At its core, a RIS is a thin layer of material with many small programmable elements. These elements can alter the phase, amplitude, and polarization of incoming radio frequency (RF) signals. By doing so, a RIS can effectively control the propagation environment, which is a major shift from traditional approaches where the environment is typically considered given and uncontrollable. The primary advantage of RIS is its ability to direct or reflect signals to areas that are otherwise hard to reach with direct transmissions, such as blocked indoor regions or non-line of sight regions. This can significantly enhance signal coverage and reduce dead zones in a network. Moreover, RIS can be used to focus energy more efficiently towards intended users, improving the overall energy efficiency of the network.

These capabilities have been acknowledged also by the European Telecommunications Standards Institute (ETSI), which released its first use cases for RIS in May 2023, [ETSI25]. ETSI defined RIS as follows [ETSI24]:

> *Reconfigurable Intelligent Surfaces (RIS) corresponds to a planar surface composed of unit-cells, whose properties can be controlled dynamically to 'tune' the incident wireless signals through reflection, refraction, focusing, collimation, modulation or absorption. RIS can be potentially deployed for both indoor and outdoor usage, including offices, airports, shopping centers, lamp posts and advertising billboards, and may take any shape or be integrated onto objects. Its characteristics may also result in low energy consumption, making RIS a sustainable technology solution. RIS can be configured to operate at any part of the radio spectrum, including frequencies from below 6 GHz to THz, and may harness tools from AI and ML to enable systems operation and optimization. As RIS is envisaged to be a new enabling candidate wireless technology for the control of the radio signals between a transmitter and a receiver in a dynamic and goal-oriented way, turning the wireless environment into a service. This has motivated a host of potential new use cases targeting at:*
>
> > *i) the enhancement of various system key-performance-indicators (KPIs), and*
> >
> > *ii) the support of new wireless technology applications and capabilities.*
>
> *These include enhancements to the capacity, coverage, positioning, security, and sustainability, as well as the support of further sensing, wireless power transfer, and ambient backscattering capabilities.*

Thus, RIS has been identified as a potentially cost-effective and energy-efficient candidate to meet the increasing demand for high-speed and reliable wireless communication. However, this require extended end-to-end validations to be verified, and there are challenges regarding the integration of these surfaces into existing and future wireless networks, which includes developing effective algorithms for dynamic RIS configuration, understanding the interaction of RIS with various signal propagation environments, and integrating RIS with other advanced technologies like MIMO and beamforming.

In [HEX224-D43, Sec. 4.3 and Sec. 3.5] we investigated some of these challenges, in particular, integration of RIS for D-MIMO and IAB transmissions, channel estimation methods for RIS transmissions, RIS control procedures, RIS reflecting modulation, and received signal level analysis for RIS in a simplified propagation scenario. In this chapter we report results on our further studies on RIS for D-MIMO and IAB, RIS reflecting modulation, and received signal level analysis for RIS in a simplified scenario.

5.1 Signal level analysis for RIS in a simplified scenario

Problem statement: The pathloss of the reflected link through the RIS is usually much larger than that of the direct link. For this reason, the expected coverage extensions from the introduction of RIS may reduce when the attenuation on the direct link is not increased by the blocking effect of any obstacles. To overcome this physical limit, the concept of active RIS that can also amplify the reflected signal has been recently proposed.

Methodology: A signal model for calculation of the SNR at the user receiver is derived, considering both passive and active RIS. The signal model highlights the “double fading” effect, for which the pathloss of the

reflected link through the RIS is normally much larger than that of the direct link between transmitter and receiver.

Results: The Figure 5-1(a) shows the gain in terms of SNR at the receiver in an RIS-assisted wireless system that exploits a 16×16 elements passive RIS operating at 7 GHz. The SNR gain is calculated with respect to a baseline system without RIS, for different RIS positions (reported in the abscissa) and for different levels of signal blockage (L_{blk}) in the direct link. The considered scenario, signal model and system parameters are described in [HEX224-D43, Sec. 3.5]. The approach for pathloss modelling used in this analysis is based on [Ell21], where the scattering by the RIS is computed as the discrete sum of fields scattered from each RIS element.

The results show that a passive RIS provides a significant coverage enhancement when the direct propagation path is strongly attenuated (i.e., blockage $L_{blk} \leq -40$ dB in the considered scenario). In case of an active RIS the coverage can be further improved and the SNR difference at the user receiver, with respect to the passive RIS, is approximately equal to the gain of the active RIS. The calculation of the noise power generated by the active RIS shows that it is not yet a limiting factor, for the selected configuration and system parameters [HEX224-D43].

The effect of the quantization of the RIS reflection coefficients has been also analysed by applying the signal model in a simplified setup, composed by a source that illuminates the RIS with a plane wave impinging from the broadside direction and a receiver that moves on a sphere around the RIS and measures the power of the reflected signal. The Figure 5-1(b) shows the calculated power of the reflected signal in the azimuth plane (x-y plane) around the RIS. The diagram of the received power in turn represents the RIS radiation diagram. The RIS coefficients are configured to reflect the impinging wave in the azimuth x-y plane in a direction corresponding to $\varphi_{MAX} = 40°$. The selected value of the RIS reflection angle is sufficiently spaced apart from the broadside direction, from which arrives the source signal that illuminates the RIS, and it is thus valuable to test the signal model.

The results show the emergence of a secondary lobe caused by the quantization in the direction specular to the main reflection lobe (i.e., $\varphi = -40°$) when the phase ϑ of the RIS reflection coefficients is quantized using only 1-bit (i.e., $\vartheta \in [0; \pi]$). Besides, the results show also that most part of the SNR gain introduced by the RIS can be captured using $n = \{2, 3\}$ bits for coefficient quantization (i.e., $\vartheta_n = k \cdot (2\pi)/2^n$, with $k = 0,1,..,2^{n-1}$).

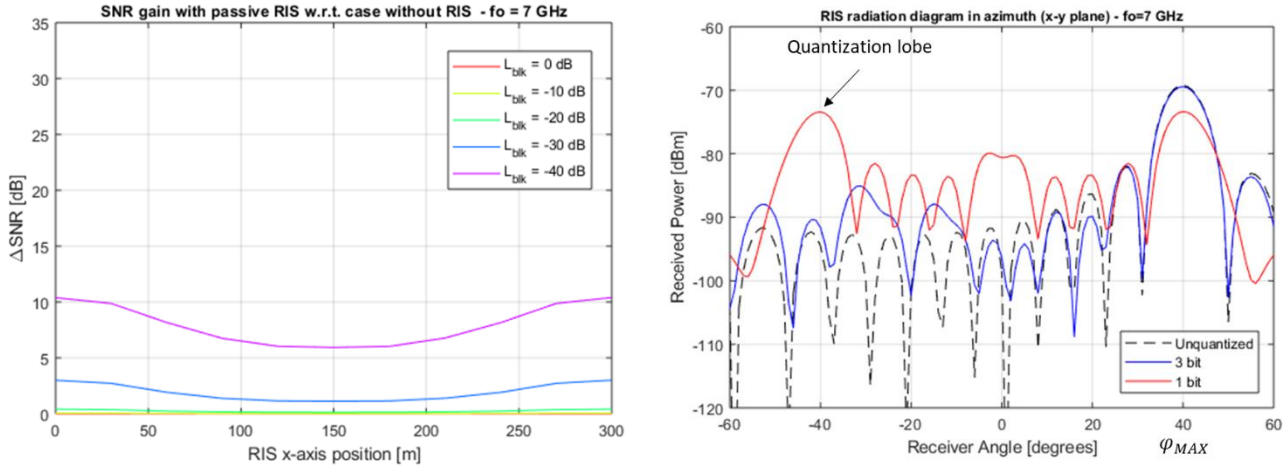

(a) SNR gain at the receiver **(b) Effect of RIS coefficient quantization**

Figure 5-1: Signal level analysis of a passive RIS.

5.2 D-MIMO assisted with RIS

Problem statement and methodology: This work explores the benefits of integrating RISs into D-MIMO systems focusing on signal-to-interference-plus-noise-ratio (SINR), energy efficiency, and service coverage probability; see [HEX224-D43]. We also explore assisting a UE with multiple RISs and using active RISs. A

description of the research methodology, including simulation parameters and algorithm descriptions, can be found in [PFM+24], which reports our initial results.

Final results and conclusions: We consider 18 cells over an area of 300 m x 150 m, with an AP deployed at the centre of each cell. 100 UEs are dropped following a finite homogeneous Poisson point process (FHPPP) and served by UE-centric clusters of APs. Furthermore, 18 RISs are placed at specific locations that maximize the service coverage probability afforded by the RISs in single-cell deployments; see [PFM+24] [Par24]. As the baseline for comparison, we consider conventional D-MIMO deployments, without RIS assistance, for various AP cluster sizes ζ_{AP}, where $\zeta_{\mathrm{AP}} = 1$ corresponds to cell MIMO, and $\zeta_{\mathrm{AP}} > 1$, to actual D-MIMO. Increasing the cluster size up to three or four improves the distribution of the UEs SINRs, i.e., it pushes the SINR CDFs to the right; see [PFM+24]. However, the SINR declines for larger cluster sizes.

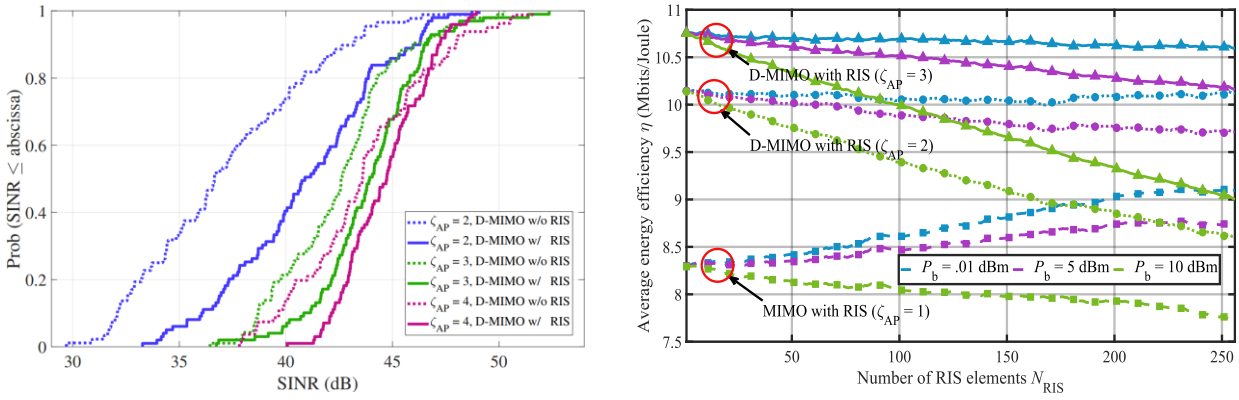

(a) SINR ($N_{RIS} = 128$). **(b) Energy efficiency.**

Figure 5-2: Key performance indicators (KPIs) of various RIS-assisted D-MIMO deployments ($f_c = 4$ GHz, $B = 100$ MHz, $P_T = 25$ dBm).

Figure 5-2(a) shows the CDFs of the SINR experienced by the UEs in D-MIMO deployments with and without RIS assistance for cluster sizes ζ_{AP} of two, three, and four. In general, RIS assistance improves the SINR of D-MIMO systems, especially for small cluster sizes. An interesting finding is that RIS-assisted D-MIMO with $\zeta_{\mathrm{AP}} = 3$ outperforms conventional D-MIMO with $\zeta_{\mathrm{AP}} = 4$. Thus, RISs not only improve the performance of D-MIMO systems but may also lower deployment costs, i.e., by trading off APs and RISs for a target KPI. Figure 5-2(b) shows the average energy efficiency when varying the number of RIS elements N_{RIS} from 1 to 256 for cluster sizes $\zeta_{\mathrm{AP}} = 1, 2,$ and 3. For the power dissipated by each RIS element, the values 0.01 dBm, 5 dBm, and 10 dBm were selected.[2] Improvements to the system's energy efficiency are observed for cluster size one. However, care must be taken for larger cluster sizes to ensure low power operation of the RISs, and not to decrease the overall energy efficiency of the system. The corresponding plots for the service coverage probability can be found in Figure A-2 of Section A.2. As expected, the service coverage probability increases with the number of RIS elements, with the largest improvement (13%) occurring for $\zeta_{\mathrm{AP}} = 1$. For AP cluster sizes 2 and 3, the service coverage probability grows at more modest rates. Overall, RIS assistance proves most valuable for smaller cluster sizes, such as ones with two or three APs, which are also expected to be the most common at 6G roll-out or in low-populated areas with less dense deployments. For larger cluster sizes, D-MIMO inherently provides macro diversity, making RIS assistance less impactful except in RF dead zones due to obstacles, where it can still enhance signal quality and coverage.

In our study, we also investigate more advanced assistance schemes. Particularly, in Figure A-3(a) of Section A.2, we compare D-MIMO assisted with one RIS, as before, versus two—the AP cluster size is two in both cases. As we see, a notable improvement of about 5 dB is observed. Moreover, we also consider increasing the density of deployed RISs where we observe hefty gains when the RIS density is doubled. This hints at the importance of deploying enough RISs and/or deploying them at strategic locations, such as close to the users they serve. Thus far, we have only considered passive RISs. Figure A-3(b) of Section A.2 illustrates the benefit

[2] RIS implementations based on PIN diodes dissipate in the order of 10 dBm [WTL+22], while CMOS-based consume power only during state transitions and are expected to be much more energy efficient.

of active RISs, i.e., capable of amplifying incident signals before re-radiating them. With a 20 dB gain for the RIS elements, an overall SINR gain of about 5 dB is achieved.

To summarize, we have shown the potential of integrating RISs with future 6G networks. RISs can improve the performance of D-MIMO or lower deployment costs by trading off APs and RISs. Attention should be paid to designing truly low-power RISs, which should be deployed in sufficient numbers and/or at strategic locations. Moreover, advanced techniques such as multi-RIS UE assistance and active RIS can further enhance the performance of D-MIMO systems. On the other side of the balance, RISs can give rise to unintended reflections [APK+23], which can be challenging in multi-operator deployments. To alleviate this problem, spatially selective RISs have been proposed in [RFZ+24]. Further research is needed to enable RIS integration in future 6G systems.

5.3 RIS assisted integrated access and backhaul

Problem statement and methodology: This work studies the advantages of integrating RISs into integrated access and backhaul (IAB) networks focusing on the service coverage probability and backhaul rates in order to ensure reliable backhaul link connectivity in the presence of tree foliage; see [HEX224-D43]. In our methodology, we optimize the IAB network for suburban environments with a focus on backhaul links. A mmWave channel model is adopted, using the 5G channel model (5GCM) UMa close-in pathloss model [RXM+17] to provide realistic simulations. To reduce complexity and enhance efficiency, we implement codebook-based beamforming.

Final results and conclusions: We consider 1 IAB donor and 1 IAB child node over an area of 1 km^2. The donor node is deployed at the centre of each cell and varying number of UEs are dropped following an FHPPP. Next, 3 RISs supporting the backhaul links are placed in pre-planned locations in order to maximize the service coverage probability when the direct link is blocked by tree foliage due to seasonal variations.

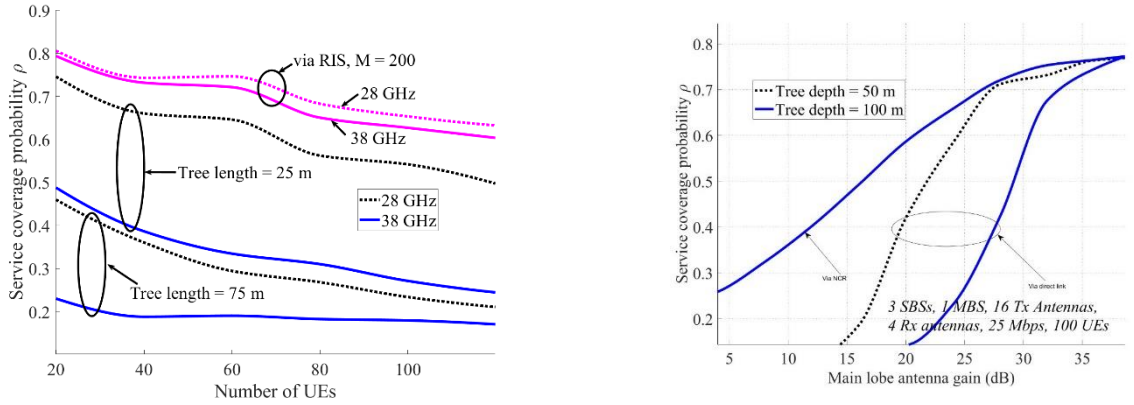

(a) Service coverage probability as a function of number of UEs for different carrier frequencies.

(b) Service coverage probability as a function of main lobe antenna gain.

Figure 5-3: KPIs of RIS-assisted IAB deployments ($f_c = 28$ GHz, $B = 1$ GHz)

Figure 5-3(a) shows the service coverage probability of the network with and without RIS assistance for different carrier frequencies. Figure 5-3(b), illustrates the service coverage probability as a function of main lobe antenna gain in the backhaul links where we also characterize network-controlled repeater (NCR) performance for the same use case. As we see in the figures, the service coverage probability remains resilient for tree foliage when backhaul link is connected via RIS, highlighting the importance of having such setup especially in the use case of wide-area IAB for sub-urban use cases. Further, we can notice that the service coverage probability of network with NCR improves by a considerable margin. However, having NCRs will be costly both in energy efficiency and financial viability. Simulations are on-going and further investigations are to be made.

In conclusion, we have shown the potential of integrating RISs with IAB networks, especially in wide-area deployments. RISs can improve the performance of the IAB networks during seasons with higher tree foliage obstructing the direct link from the donor to child. However, RISs can give rise to unintended reflections

[APK+23], which can be challenging in multi-operator deployments. Additionally, it is important to consider the elevation profiles, real-world distribution of tree lines and nature of the terrain. Further research is needed to enable RIS integration in IAB networks.

5.4 Reflection modulation via RIS with jointly active and passive beamforming

Problem statement: RIS-based communications with reflection modulation (RM) is a novel area of research that opens up a range of unconventional modulation techniques. In RM, the RIS passively conveys information via activation patterns. The existing RM techniques mainly consider single-user communications. In [HEX224-D43, Sec. 4.3.5], a scalable, less restricted solution that reduces BER for the more general application jointly mapped RM is proposed considering a single-user system, such that the RIS reflection patterns and transmit signals are jointly incorporated for the constellation design, and the research findings are also published in [KRR+24]. Extending the work in [HEX224-D43], here this work proposes a generalised framework for RIS-RM for single and multi-user multiple-input single-output (MISO) downlink communications, with activation pattern generation, constellation designs, and bit-mapping.

Methodology: Two activation pattern generating methods are considered, quadrature reflection modulation (QRM) [LCW+22] and reflection pattern modulation (RPM) [LZA+21]. In QRM, a subset of RIS elements add an orthogonal phase to the reflected signal, while in RPM, a subset of RIS elements is deactivated, to generate activation patterns. Instead of a common passive beamforming design for spatially separated multiple users, we propose to divide the RIS into subunits, such that each subunit is dedicated to an individual user for RM and passive beamforming. We formulate the jointly active and passive beamforming problem considering RIS subunits and propose approaches for solving the problem with alternating optimization (AO) and decoupled (two-stage) passive and active beamforming techniques based on semi-definite relaxation methods.

Results: Numerical results evaluated the BER performance of a single user and 2-user systems that convey 6 bits from the AP and 2 bits via the RIS. Single-user results are compared with the respective BER upper bound. Multi-user results are compared with beamforming approaches without considering RIS subunits. Figure 5-4 illustrates the BER performance of the near-end user and the far-end user of a 2-user RIS-RM system comparing the performance of the different approaches. Beamforming with dedicated RIS subunits shows faster convergence with lower transmit power. It can be observed that for both users, QRM-based methods deliver lower BER compared to their RPM counterparts, agreeing with the single-user results. In QRM-based schemes, the performance of beamforming solutions without subunits shows more drastic fluctuations depending on the user placement. An important observation from the results is that QRM-based separately mapped RM approach with dedicated subunits behave more robustly with considerably superior performance regardless of user placement, as opposed to RPM and beamforming strategies without dedicated subunits. Moreover, the two-stage algorithm with QRM shows consistent BER performance for both users.

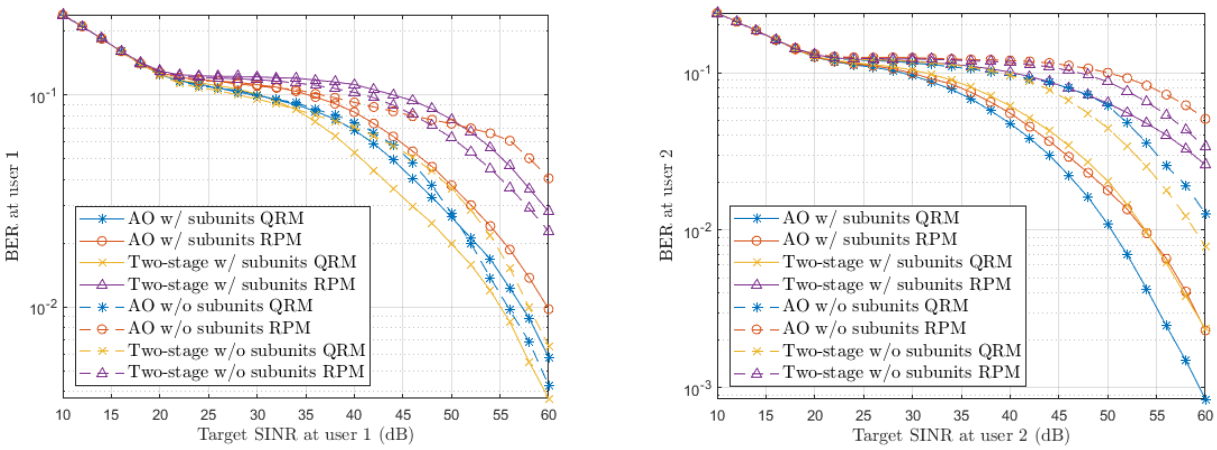

(a) BER of the near-user of the 2-user system **(b) BER of the far-user of the 2-user system**

Figure 5-4: Performance comparison of different RM methods for the two-user system.

5.5 Summary

In this chapter we reported on our further investigations on RIS for D-MIMO and IAB, RIS reflecting modulation, and received signal level analysis for RIS in a simplified scenario. Key findings and insights based on our accumulated studies within WP4 on RIS are as follows:

- RIS can provide a substantial coverage enhancement when the direct propagation path is strongly attenuated or fully blocked, also with low precision phase shifters.
- RISs can improve the performance of D-MIMO or lower deployment costs by trading off APs and RISs, providing we can design truly low-power RISs, and they can be deployed in sufficient numbers and/or at strategic locations. Moreover, advanced techniques such as multi-RIS UE assistance and active RIS can further enhance the performance of D-MIMO systems.
- Service coverage probability in IAB networks remains resilient for tree foliage when backhaul link is connected via RIS, which is important in e.g. wide-area IAB deployments in sub-urban areas. However, service coverage probability with NCR outperforms passive RIS. Thus, the advantage of RIS depends on its potentially better energy efficiency and lower cost.
- Reflection modulation methods via RIS shows promising performance gains for single and multi-user multiple-input single-output downlinks compared with beamforming approaches without considering RIS. Quadrature reflection modulation-based separately mapped RM approach with dedicated subunits behave more robustly with considerably superior performance regardless of user placement, as opposed to reflection pattern modulation and beamforming strategies without dividing the RIS into dedicated subunits.
- RIS control is a complex challenge that needs further investigations towards standardization.

Thus, RIS shows promising performance to motivate integration in 6G RAN, but there are still remaining challenges:

- Passive RIS needs many tunable elements, which is difficult to design and manufacture.
- Aggregated channel state information between transmitter, RIS, and receiver is difficult to acquire in dynamic environments.
- Power consumption of RIS surface and control unit need to be small for overall performance gains, which is a challenge. Energy harvesting RIS would be the target for low-cost deployment.
- Uncontrolled interference, especially between operators, is a challenge due to broadband nature of RIS, requiring complex interference management techniques.
- Dynamically configuring the RIS in real time based on CSI and user needs might require complex algorithms that are challenging to implement with low cost and high energy efficiency.
- Multi-RIS deployment requires efficient algorithms and network protocols.
- Non-transparent RIS needs to be integrated into existing protocols, which requires standardization.
- RIS might need to be regulated, depending on deployment and adaptive control mechanisms.

6 Waveforms and modulations

In modern wireless systems, waveform and modulation schemes are essential for efficient and reliable transmission. With these techniques, communication systems can increase SE while balancing energy constraints. As technology evolves, new applications arise demanding unprecedented data rates leveraged mostly by expanding the transmission's frequency to sub-THz levels. This novel approach will substantially increase the system's bandwidth whilst affecting power consumption, phase noise, and other performance factors. In this context, designing innovative waveforms and modulation schemes is fundamental for harnessing the potential of future communications systems, regardless of the frequency band.

Hence, this chapter investigates waveform and modulation candidates for sub-THz communications and new enhancements to known techniques. The first section introduces the candidates by analysing 5G NR numerology and standardized waveforms, i.e., cyclic prefix orthogonal frequency division multiplexing (CP-OFDM), and by exploring 1-bit quantized ZXM and polar and hardware-friendly constellations. In the second section, enhancements to waveforms and modulation schemes are proposed, including an adaptative multicarrier modulation resistant to Doppler shift and out-of-band emissions, and a new matrix design for low-density parity check (LDPC) codes. Furthermore, the studies concluded in a prior phase of HEXA-X-II project such as an optimized delayed bit interleaved coded modulation (DBICM) are not covered in this deliverable. For more details, the interested reader can refer to [HEX224-D43, Ch. 5].

6.1 Sub-THz waveform and constellation candidates

This section analyses waveform and constellations candidates for sub-THz communications. Here, the contributions address some of the main challenges inherent to these frequencies, namely energy efficiency, high mobility speed, and phase noise. The first work investigates the waveform candidates for sub-THz systems by analysing their numerology and robustness towards phase noise and reduced energy consumption. The second contribution explores new polar constellations to resist phase noise and high doppler shifts. The third contribution assesses the feasibility of geometric shaped waveforms on sub-THz transceivers. The last contribution employs ZXM schemes to 1-bit ADC and explores their energy efficiency through an optimization problem.

6.1.1 Evolution of New Radio numerology and waveforms towards sub-THz frequencies

Problem Statement: In [HEX224-D43, Sec. 5.1.1] we discussed the changes needed in the 5G New Radio (5G NR) numerology, such as the SCS and cyclic prefix (CP) length, to support communications in the sub-THz frequencies. We also addressed the performance differences between the waveforms already standardized for the 5G NR, namely CP-OFDM and discrete Fourier transform-spread-orthogonal frequency division multiplexing (DFT-s-OFDM), in the presence of known hardware limitations specific for the sub-THz frequencies.

Methodology: In order to complete the study in [HEX224-D43], the performance of the CP-OFDM and DFT-s-OFDM in sub-THz frequencies was studied in the presence of non-linearities via link-level simulations in 140 GHz and 300 GHz carrier frequencies with 64-QAM modulation, and with different SCSs. The PN model used in the simulations was HEXA-X model presented in [HEX23-D23]. The output power of the waveforms was modelled by compensating the DFT-s-OFDM SNR following the required output backoff model in [TLP+20]. A complete list of simulation parameters is presented in Table 6-1.

Results: From the link level simulation results in Figure 6-1, we can see that DFT-s-OFDM outperforms CP-OFDM in both carrier frequencies, the difference being more considerable in 300 GHz. The main reasons are that DFT-s-OFDM is capable of providing more output power and handle the PN better. In principle, as the bandwidth increases, we integrate more PN. However, as the SCS increases at the same time, we effectively shorten the symbol length in time domain. This, in turn lowers the effect of the PN with low offset frequencies. From Figure 6-1(a), we can also see that the SCS of 960 kHz performs better than 1920 kHz in 140 GHz carrier. The main reason is that the CP starts to fall short on the highest SCS setting. According to the simulations, with 1920 kHz SCS, approximately 3% of the received energy falls outside of the CP, while with

960 kHz SCS the corresponding figure is 0.03%. In 300 GHz, the inter-carrier interference introduced by PN affects the performance of 960 kHz SCS, while the larger 1920 kHz SCS suffers from the shortness of the CP, thus providing almost equal results.

The above discussion demonstrates that in addition to CP-OFDM, it would be very beneficial to support DFT-s-OFDM also for DL for sub-THz communications. DFT-s-OFDM provides consistently better link performance under PN with only minor changes in the Rel-15 phase tracking reference signal (PTRS) design. The DFT-s-OFDM waveform can also enable better coverage, because it provides larger PA output power than CP-OFDM, especially with low-order modulations. For the overall numerology, it was also shown that SCSs of 960 kHz and 1920 kHz can provide a good baseline for sub-THz communications, allowing Tbps communications by supporting large bandwidths, and providing necessary enhancement in the PN mitigation for both CP-OFDM and DFT-s-OFDM waveforms. Although 3840 kHz SCS provides widest contiguous bandwidth still available in the W- and D-bands [HEX224-D43], insufficiently short CP may become a problem, and thus a more conservative value of 960 kHz should be taken as the starting point for the first efforts to design a system numerology for sub-THz communications.

As the bandwidth increases, we integrate more PN. However, as the SCS increases at the same time, we effectively shorten the symbol length in time domain. This, in turn lowers the effect of the PN with low offset frequencies.

Table 6-1: Simulation parameters

Parameter	**Value**
Carrier frequency	140, 300 GHz
Waveform	OFDM, DFT-s-OFDM
CBW	varies according to SCS, 400 MHz, 3.2GHz, 6.4GHz
SCS	120kHz, 960kHz, 1920kHz
Allocated RBs	256 physical resource blocks (PRBs), Full allocation
Propagation	TDL-A 10ns
Modulation and coding scheme (MCS)	22 (64QAM)
Channel coding	LDPC
HARQ	HARQ disabled
Rank	One
BS antenna configuration	2Tx
UE antenna configuration	2Rx
Antenna correlation (Tx and Rx)	Low correlation
Channel estimation	Pilot-based
Physical downlink shared channel (PDSCH) configuration	Type A mapping, Start symbol 2, Duration 12
Demodulation reference signal (DMRS) configuration	Two symbol, pos 3,10
PN model	Hexa-X D2.3 [HEX23-D23]
PTRS	According to NR specification OFDM every fourth PRB DFT-s-OFDM 16x4 (current NR spec allows max 8x4)

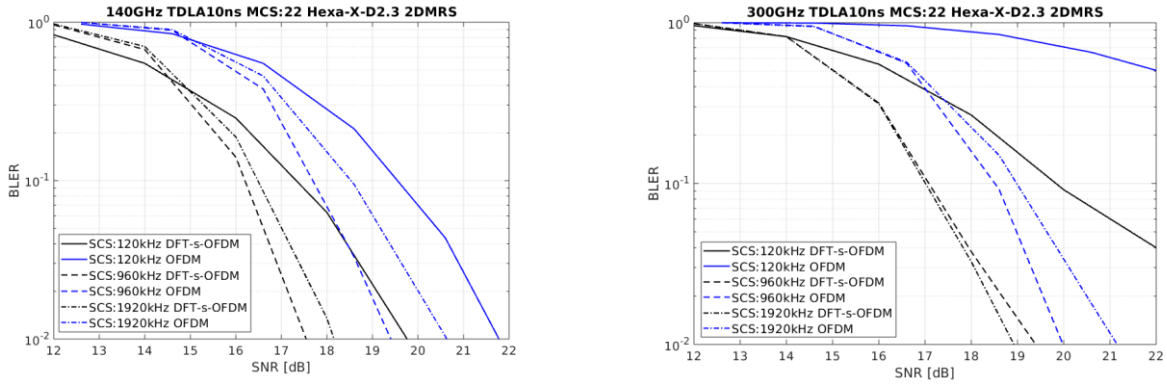

(a) 140 GHz carrier **(b) 300 GHz carrier**

Figure 6-1: Performance of CP-OFDM and DFT-s-OFDM with 64-QAM in (a) 140 GHz and (b) 300 GHz carriers with PN and different SCSs.

6.1.2 Polar constellations

Problem statement: The polar constellations are an alternative to the classical QAM mapping. It is especially well-adapted for FR2 bands and THz bands where the oscillators integrated on the devices are not very accurate, leading consequently to a greater lack of synchronization. This phenomenon will entail PN.

Furthermore, the proposal is agnostic to any frequency band and could be also used in frequency bands below 6 GHz and, in this case, mainly interesting for high mobility speed that entails Doppler shift. Both phenomena, high frequency and/or high mobility speed, will induce rotation of the constellation (bits to symbols mapping) in reception. The goal is to create new types of constellations robust to PN and Doppler shift.

Methodology: Polar constellations are combined, in the system design, to a multicarrier waveform like CP-OFDM (see description in [HEX224-D43]). In the case of THz, it is difficult to use high order constellations 64-QAM, 256-QAM and so on because of their low resistance to white noise and PN. There are an infinite number of possible solutions for Polar Constellations, in this document we propose two types of constellations: Spiral Constellation for high robustness against Doppler and the second type for a good compromise between resistance to PN while guaranteeing good performances to white noise.

Results: Two types of polar constellations are proposed, the first one is the spiral for order 4, 8 and 16 (Figure 6-2(a)) which is high robust against Doppler and the second one (x-PC) for the same order (Figure 6-2(b)). Note that polar constellation order 4 is the same than classical QPSK (4-QAM). Compared to the results provided in [HEX224-D43], the Figure 6-3 shows that 16-PC admits twice the Doppler shift, while the 16-Spirale offers very high robustness to the Doppler shift, more than 400% compared to 16-QAM.

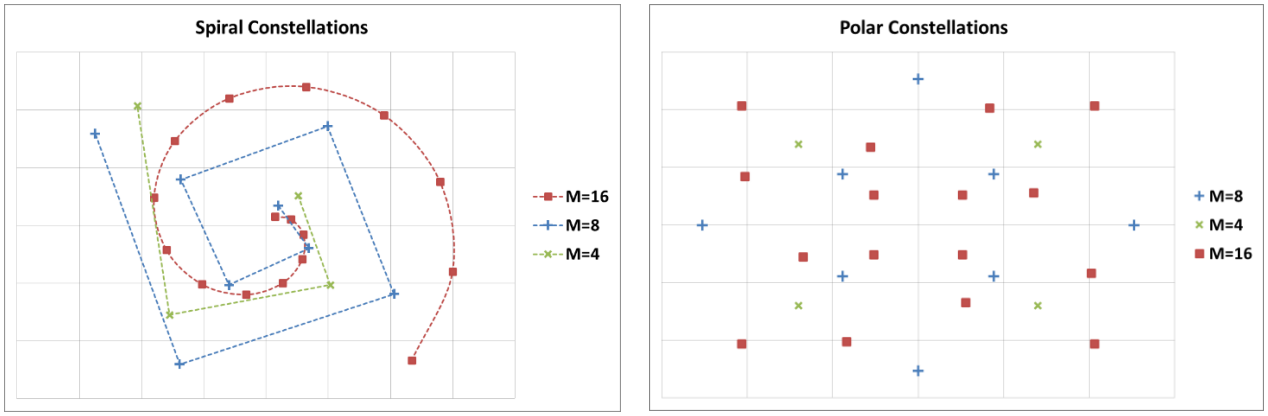

(a) Spiral Constellations for M = 4, 8 and 16 **(b) Polar Constellations for M = 4, 8 and 16**

Figure 6-2: Polar constellation types.

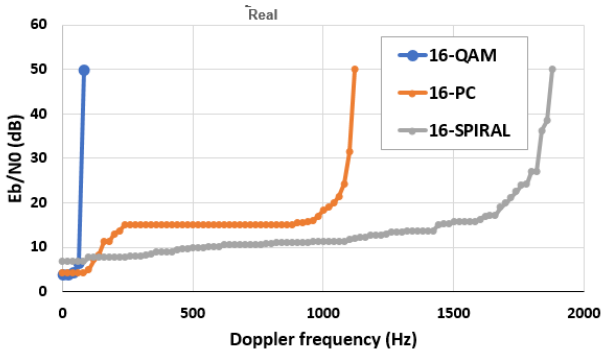

Figure 6-3: Polar constellation results.

6.1.3 Hardware-friendly waveforms

Problem Statement: In this task the feasibility and performance of the designed hardware-friendly waveforms for sub-THz communications, as reported in [NHM+24], is assessed by OTA transmissions using an inhouse proof-of-concept setup.

Methodology: The setup follows a 'hardware-in-the-loop' approach, combining non-real-time realization of baseband processing with real practical hardware for the sub-THz transmissions. For this purpose, the base band signals of the waveforms under test are generated offline, with the captured signals also offline processed. Sub-THz OTA transmissions are achieved using a Tx transceiver board equipped with radio-frequency integrated circuit (RFIC) components, specifically designed for the D-band. For a more detailed descriptions of the setup used, we refer to [HEX224-D43, Sec. 5.1.4] and [NHM+24].

Results: In [HEX224-D43], we validated the setup performance through measurements using 5G NR waveforms, applying a standard square constellation and traditional root raised cosine (RRC) filtering across different modulation orders. In this study, we specifically focus on 6-bit modulation signals. Reference measurement of NR waveform is referred to as '64-QAM'. We consider the newly designed low peak-to-average power ratio (PAPR) waveforms from [MNM+24a]. They are obtained by geometric shaping (GS) of the constellation under varying peak power constraints and are labelled according to their ϵ_p PAPR levels as 'GS 5.5 dB', 'GS 6.0 dB', 'GS 6.5 dB' and 'GS 7.0 dB'. These waveforms are optimized for conventional demapping techniques. Further, we extend our investigation to an optimized waveform that incorporates neural network (NN) functionality at the demapper, referred to as 'NN-demapper.' Details of the optimization procedure for the waveform 'NN-demapper' are provided in [MNM+24b].

Figure 6-4 shows the received constellations of the reference '64-QAM' and the studied hardware-friendly waveforms, along with their respective PAPR and EVM values. As can be seen, all waveforms exhibit an EVM below 8%, meeting the requirement for 64-QAM defined by 3GPP NR. For the 'GS'-waveforms specifically, lower target PAPR values reduce the number of low amplitude constellation points in the inner ring. The optimized constellation pattern gets closer to a disc shape, with closely packed points. This increased density leads to a higher decoding error probability, which reflects in the higher EVM value compared to other 'GS'-waveforms. A clear trend can be observed where the EVM value increases as the targeted PAPR decreases, except for the 'GS 7.0 dB' case. The observed exception may be attributed to the higher PAPR characteristics of the transmitted signal, which induce non-linear behaviour in the system, such as PA and thereby increasing the observed EVM value. Additional investigations are needed to underpin these findings. For the 'NN-demapper', it is important to note that the proposed waveform is derived from an end-to-end offline training, targeting a low $\epsilon_p = 5.5$ dB, under low residual phase noise channel conditions. Although trained on synthetic data, the EVM performance of this waveform meets the 3GPP requirements and exhibits a highly favourable PAPR characteristics, making the 'NN-demapper' a potential waveform candidate for sub-THz transmissions. Finally, considering the effect of channel coding protection, all the coded transmitted data bits can be error-free recovered during the considered measurement duration, regardless of the waveforms used. As a results, the coded BER is lower than 2×10^{-7} for all cases. Table 6-2 summarizes the investigated waveforms and the results.

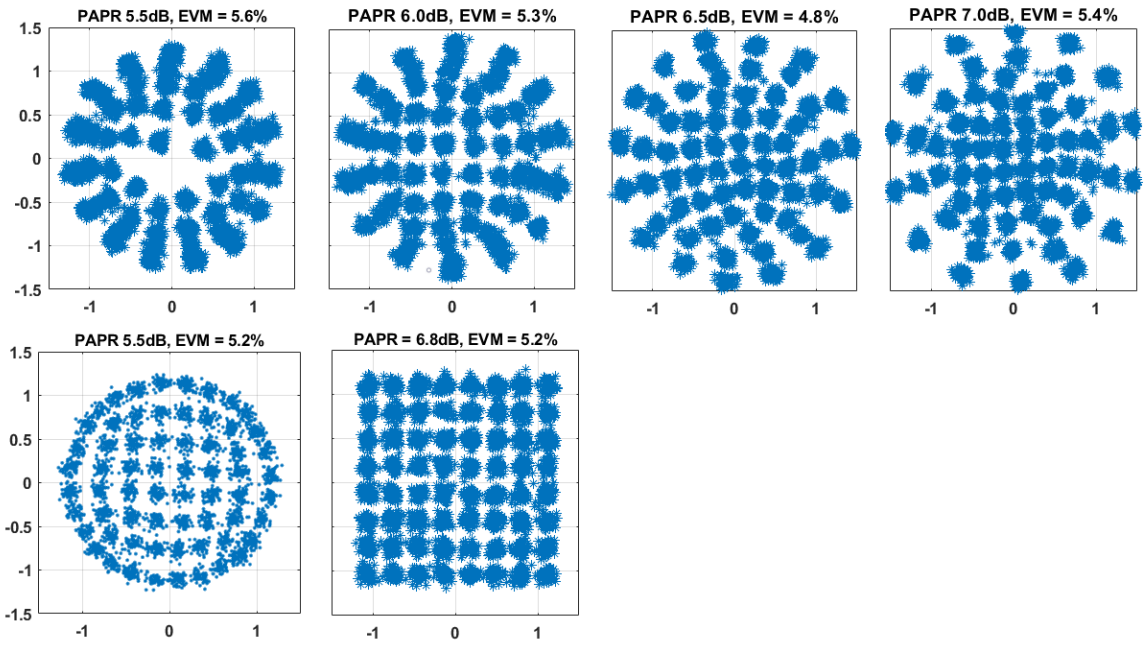

Figure 6-4: Received constellations of the investigated waveforms with corresponding PAPR and EVM values. Upper row: 'GS'-waveforms. Lower row: 'NN-demapper' and reference '64-QAM'.

Table 6-2: Investigated waveforms. ϵ_p and ϵ_A are peak power and adjacent channel leakage ratio (ACLR) constraints imposed in the optimization.

Waveform	Constellation	Filter	Demapper	PAPR [dB]	EVM [%]
64-QAM	NR standard square	RRC	conventional	6.8	5.2
GS 5.5dB	Learned ϵ_p= 5.5 dB	RRC	conventional	5.4	5.6
GS 6.0dB	Learned ϵ_p= 6.0 dB	RRC	conventional	5.9	5.3
GS 6.5dB	Learned ϵ_p= 6.5 dB	RRC	conventional	6.4	4.8
GS 7.0dB	Learned ϵ_p= 7.0 dB	RRC	conventional	6.8	5.4
NN-demapper	Learned ϵ_p= 5.5 dB	Learned $\epsilon_A = -35$ dB	NN	5.3	6.5

6.1.4 Energy-efficiency of 1-bit quantized zero crossing modulation

Problem Statement: Future wireless link applications, like high-resolution video streaming for virtual reality (VR) headsets, will likely require enormous data rates and, thus, very high bandwidths, which cannot be found in the currently utilized spectrums. The sub-THz and THz regime, however, offers a vast unused spectrum. Nevertheless, a problem with the high carrier frequencies and bandwidths is the problematic increase in hardware power consumption of components. Even components that exhibit a relatively unproblematic power consumption at low carrier frequencies can form a power bottleneck preventing the full utilization of the available bandwidth. The power consumption of the ADC, for instance, scales linearly with the bandwidth for low sampling frequencies but scales quadratically with the Nyquist sampling frequency for bandwidths greater than 300 MHz [Mur97].

Methodology: To mitigate the inevitable increase in ADC power consumption for high bandwidths, it was proposed to reduce the amplitude resolution down to a minimum of 1 bit. As the ADC is practically reduced to a comparator, a dedicated modulation scheme is needed for communications with 1-bit quantization at the receiver. One such scheme is ZXM [FDB+19], which encodes the information in the time distances between zero-crossings.

In previous project stages, we assessed the energy consumption in energy per bit and compared the energy consumption of ZXM with that of conventional QAM, showing significant efficiency gains, especially for high carrier frequencies. In these analyses, the up- and down-conversion stages, consisting of the local LO and mixer, turned out to be the power-dominating components at low data rates due to their modelling as components with fixed power consumption. As such, these components were examined in more detail, especially with a focus on the trade-off for LOs regarding their phase noise performance and power consumption.

This trade-off has multiple dimensions as low-power oscillators often exhibit high phase noise, degrading the communications performance. This degradation is most severe for high-order modulation schemes. However, as high-order modulation schemes need a high-resolution ADC, which can extract more detailed phase information, these schemes can partly mitigate the impact of phase noise with the help of phase noise tracking. This tracking, however, is mostly based on pilot symbols, reducing the effective data rate as it reduces payload data. Finding an energy-optimal setting is, thus, not trivial.

The influence of the oscillator on the required energy per bit was evaluated in more detail by combining an LO power model [Raz21] and a phase noise model [KKP+14], allowing us to model the influence of phase noise on both the LO power consumption and the communication performance [GRD+25]. To have a valid estimate of the resulting energy per bit, we also consider the other *main* components of the analogue front end, namely the DAC, mixer, PA, LNA, and ADC [GRD+25].

The power consumption of the DAC increases with bandwidth and amplitude resolution, while the mixer is modelled to only depend on the carrier frequency. The PA's power consumption depends on the required output power, the carrier frequency, and the PAPR of the modulation scheme. The LNA power only depends on the bandwidth, while the ADC power is modelled to depend on the bandwidth and the amplitude resolution [GRD+25].

As we want to evaluate the minimum achievable energy per bit, we perform an optimization over the system parameters bandwidth B and duty cycle of transmit time γ (given as transmit time divided by maximum transmit time), as well as over parameters regarding the LO, i.e., the pilot spacing for tracking F and the phase noise variance σ_J^2, i.e.,

$$\min_{\mathrm{B},\gamma,\mathrm{F},\sigma_\mathrm{J}^2} \mathcal{E}_{\mathrm{bit}} = \frac{\big(\gamma + \epsilon_{Tx}(1-\gamma)\big)P_{Tx} + \big(\gamma + \epsilon_{Rx}(1-\gamma)\big)P_{Rx}}{R}, \qquad \textbf{(6-1)}$$

as well as considering the constraints given in [GRD+25] (maximum transmit power and limited bandwidth), where P_{Tx} and P_{Rx} describe the transmitter and receiver power consumption, respectively, and R denotes the required data rate.

Results: The results of the optimization can be seen in Figure 6-5. Due to ZXM's robustness to phase noise, a lower energy per bit can be achieved. Please note that here, we allow an optimal σ_J for every rate R, corresponding to the choice of the optimal oscillator at design time. In [GRD+25] we consider only one oscillator per modulation scheme resulting in energy efficiency gains up to three orders of magnitude.

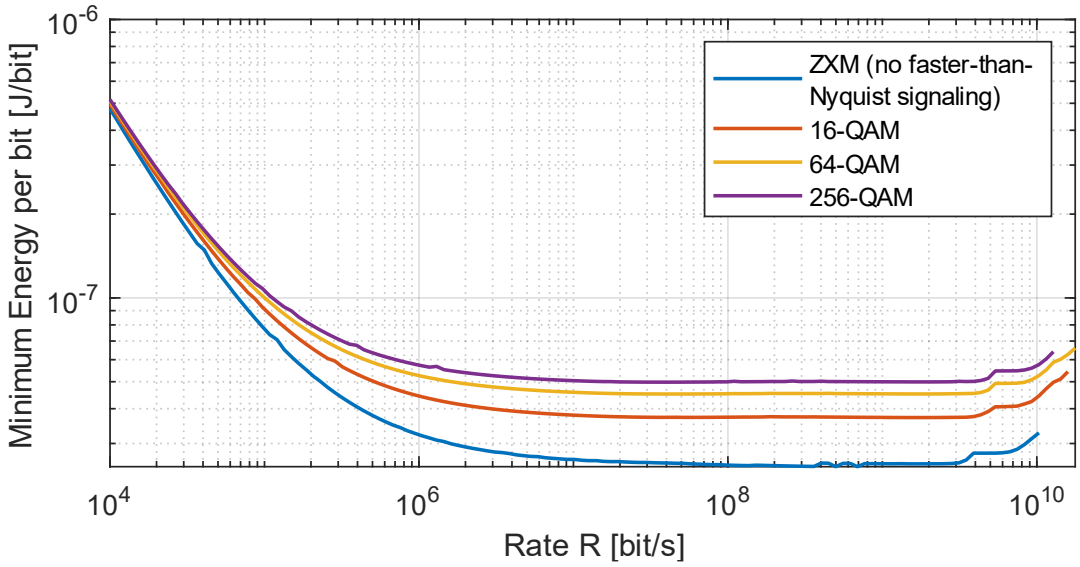

Figure 6-5: Minimum energy per bit for various modulation schemes for $f_c = 120$ GHz (see [GRD+25] for more detailed results).

6.2 Waveform and modulation enhancements

This section introduces enhancements to waveform and modulation schemes for wireless systems operating in all frequency bands. As known, waveforms and modulations schemes are an important asset to achieving higher rates and SE. However, as new applications arise, other—now essential—aspects such as mobility, energy consumption, and latency must be considered. These new challenges demand low-complexity techniques capable of tackling known issues, including high Doppler shifts, PAPR, and out-of-band emissions. The following subsections address some of these issues by enhancing and optimizing known standardized solutions.

6.2.1 Adaptive multicarrier modulation

Problem statement: Multicarrier modulations (e.g., CP-OFDM) have established themselves in various standards thanks to their advantages compared to the single-carrier system: robustness against multiple paths, simple equalization, and natural association with MIMO systems, etc. But there are still areas for improvement such as resistance to Doppler, out-of-band radiation, PAPR, etc. In that sense, a new type of multicarrier modulation is proposed, flexible and robust in the face of the areas of improvement listed above. The new multicarrier scheme called adaptive multicarrier modulation (AMCM) was described in the [HEX224-D43].

Methodology: The flexibility of the modulation is related to the parameter R, this parameter can take the value 0 which corresponds to the OFDM modulation, if $R = 1$ it corresponds to the OFDM offset QAM (OQAM) modulation for all the other integer values it typically corresponds to the AMCM modulations. R is also the number of periods of a sinusoid during the duration T0 of a symbol (number of points of the fast Fourier transform (FFT)/ inverse fast Fourier transform (IFFT)) as shown in Figure 6-6(a).

To maintain a very good power spectral density (PSD) see Figure 6-7, it is necessary to insert a guard interval whose number of points corresponds to the number of points of the FFT divided by R. It should be noted that the larger R is the smaller the offset between channels I and Q and the smaller the potential duration of the guard interval that is represented in Figure 6-6(b).

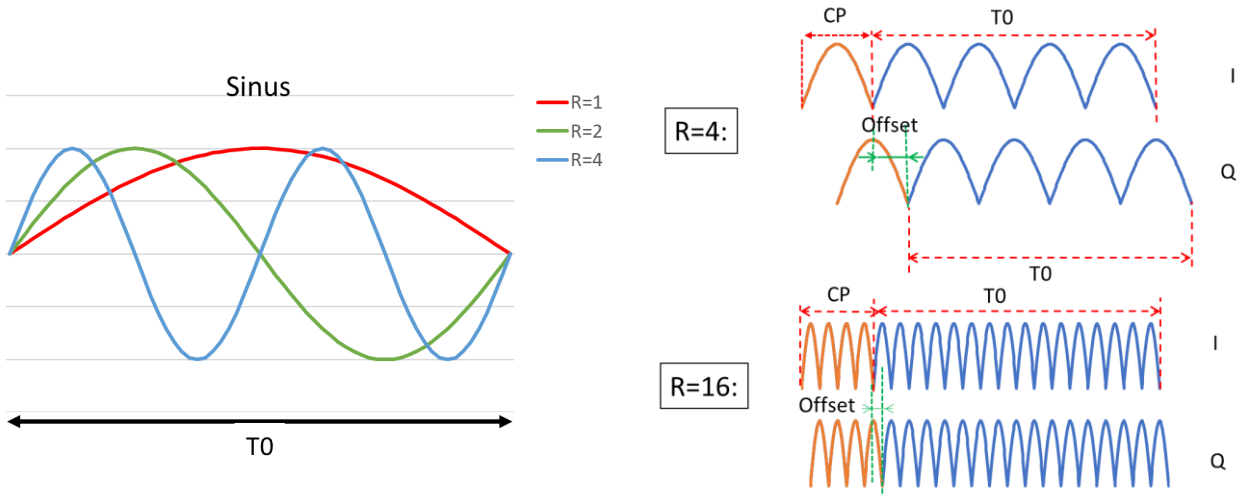

(a) **(b)**

Figure 6-6: (a) The number of sinus period during T0 is proportional of the value R; and (b) the duration of the CP is also linked to R.

Results: Figure 6-7 illustrates the difference between OFDM and AMCM modulations in PSD point of view. We can observe the different PSD obtained depending on the R parameter. More "R" high is, more the PSD level close to the OFDM (without CP) one is but more the CP granularity length is fine. If we need to adapt the PSD level very low to respect some spectrum mask regulation, then the choice of one small "R" is expected. There is a compromise to be found between the quality of the PSD, the duration of the CP and the offset between the I and Q channels, all of which are linked to the R parameter.

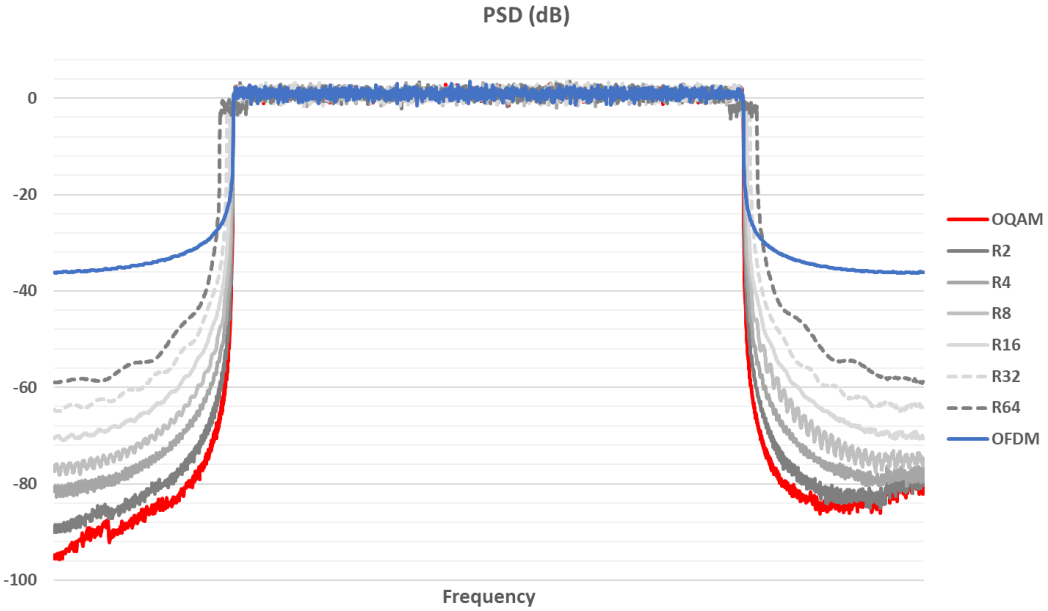

Figure 6-7: The PSD of OFDM (R=0) and OQAM (R=1) and typical AMCM modulation R=2, …, 64.

6.2.2 New LDPC code parity matrix design

Problem statement: Correction codes are one of the essential functions of the digital communication chain. LDPC codes have been selected by 3GPP for 5G, they offer a wide variety of size and code rate, called MCS. In [HEX224-D43], we presented a new parity matrix structure based on the structure of 3GPP, which improves the performance according to the number of iterations of the decoder allowing to decrease the energy consumption of the system.

In this part we regarding the performances for the short length with the specific base matrix BG2, LDPC is known for the weakness with short messages. The characteristic and performances of new matrices BG1 were presented in [HEX224-D43]. In this part we propose to focus on BG2 structure and performance.

Methodology: To evaluate the gains of the new LDPC matrixes, link simulations are performed over AWGN channel and compute curves in terms of block error rate (BLER) versus SNR. Figure 6-8(a) shows the connections of the new BG2 matrix. The number of connections of this new matrix is less compared to the BG2 matrix defined by 3GPP, 190 vs 197.

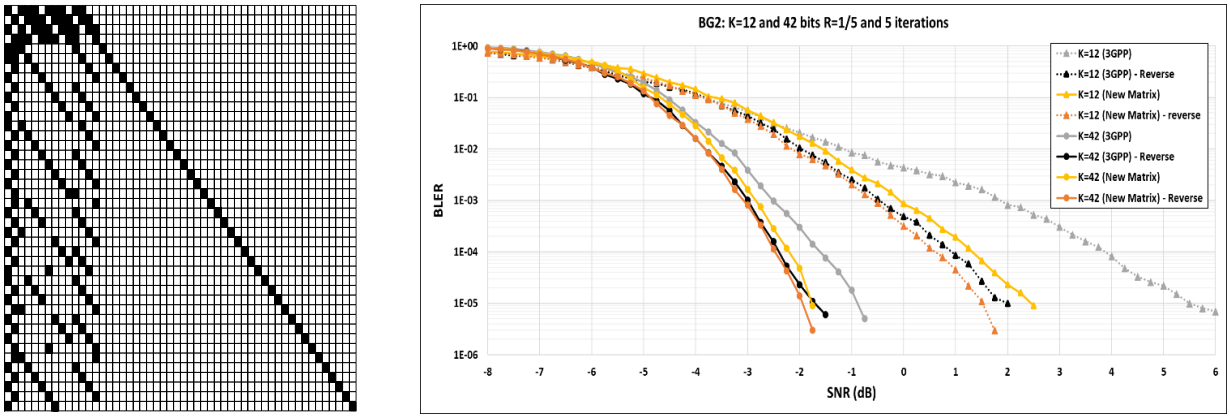

(a) **(b)**

Figure 6-8: (a) Connections of new matrix BG2 and (b) Performance for short length (BG2).

Results: The performance results (BLER vs SNR) are given in AWGN channel. In the simulation campaign, we use as the decoder side the Normalize MinSum (alpha=0.7) and the Reverse Normalize MinSum. Figure 6-8(b) shows the performance with two types of decoders, the reverse mode always gives the better performances. The 3GPP Matrix is very sensible to the type of decoder and we observe an error floor around a BLER of 10^{-5}. The performances with new matrices are always better with no error floor this is the consequence on a better repartition of the connections for rows and columns in the matrix that outperforms the decoding process especially for low iterations (< 10). With these new results where $K = 12$ and $K = 42$, show that it's possible to use LDPC for encoding short messages.

6.3 Summary

In this chapter, waveform and modulation schemes were proposed to address power consumption, PN, and out-of-band radiation for FR2, FR3, and sub-THz bands. First, a link-level simulation was implemented to analyse the performance of 5G NR numerology and waveforms (CP-OFDM and DFT-s-OFDM) at 140 GHz and 300 GHz under the effect of PN. The results indicated that sub-THz communications would benefit from supporting CP-OFDM and DFT-s-OFDM with numerology SCS 960 MHz and 1920 MHz, allowing larger bandwidth and enhancement to PN mitigation. Then, polar constellations were proposed to integrate FR2 and sub-THz systems due to their high resistance to white noise and Doppler shifts, achieving better performance than M-QAM. A new optimised constellation pattern was developed to support sub-THz transmissions under varying peak power constraints. This solution is based on NN-demapper and provided PAPR and EVM values smaller than 64-QAM. Another contribution investigated the energy efficiency of 1-bit quantised ZXM at 120 GHz, proving its efficiency in the face of other M-QAM modulations. Regarding out-of-band radiation, the proposed AMCM modulation outperformed OFDM by at least 20 dB, being an important asset for stricter spectrum mask regulations. Lastly, the new LDPC code parity matrix showed a remarkable decoding performance with reduced complexity.

7 Intelligent radio air interface design

The past few years have seen significant evolution in wireless technologies, paralleled by machine learning breakthroughs to meet the increasing demands for SE, reliability, and network flexibility. This synergy is fostering the development of intelligent radio air interfaces aimed at boosting network performance and adaptability through AI optimization. This chapter explores innovative solutions that leverage AI to refine air interface design, marking a shift towards smarter, more efficient networks.

This chapter presents four key areas where AI can be effectively integrated:

- Learning for Waveform, Modulation, and Coding. Utilizing AI to enhance modulation and coding techniques, including the optimization of MIMO waveforms and error correction strategies.
- AI-Based CSI Acquisition. Advancing CSI acquisition and prediction through AI, optimizing network SE while reducing overhead.
- AI-Enhanced MIMO Transmissions. Discussing AI's role in revolutionizing MIMO transmissions through advanced antenna management, power control and user pairing strategies.
- AI solutions for hardware (HW) impairments. Highlighting AI's potential to address hardware challenges, specifically by compensating for power amplifier non-linearities.

In addition to the contributions detailed in the following sections, previous studies related to this chapter have been conducted within the HEXA-X-II project, in particular:

- Beamforming with imperfect CSI.
- Access point selection and UL power control for D-MIMO.

These studies, completed before the publication of Deliverable D4.5, are not covered in this chapter. For more comprehensive insights into their outcomes, the interested reader can refer to [HEX224-D43, Sec. 6.3].

7.1 The framework to enable AI-driven air interface

The integration of AI-driven air interfaces into communication systems requires new radio procedures, protocols, and signalling mechanisms to enable effective and efficient operation. Several potential areas for standard support are needed to accommodate the AI/ML-based functionalities across different layers, especially in the physical (PHY) layer. The following points highlight the need for such mechanisms:

- AI/ML Model Life Cycle Management (LCM):

One of the essential aspects for enabling AI-driven air interfaces is the LCM of AI/ML models, particularly for PHY use cases. This includes processes like data collection, model training, and real-time monitoring. Standards need to support procedures for triggering these processes to ensure that the AI/ML models can be updated when and where needed and retrained to adapt to evolving communication environments.

- Revision of Signals and Waveforms:

AI/ML-based capabilities within the network can drive the need to revise traditional signals and waveforms. For instance, new learned LDPC codes or non-QAM learned constellations may emerge as more optimal alternatives. Protocols and signalling would be required to accommodate these new waveforms and ensure their seamless integration into existing radio environments. For practical example of such learned waveforms, please refer to Section 7.2.

- Signalling and Protocols for PHY Layer Integration:

The physical layer would need specific signalling and protocol revisions to support the integration of AI/ML-based functionalities. This may involve new signalling methods to initiate data collection processes that AI/ML-based receivers rely on. Additionally, signalling may need to be adjusted to support use cases like power headroom reduction in UE based on AI/ML-driven digital post-distortion (DPoD) capabilities at the next generation node B (gNB) BS.

- Reduction of Reference Signals:

Another area requiring revision is the reference signalling for AI-driven air interfaces. With AI/ML technologies like DeepRx, the need for traditional RSs like DMRS may be reduced, resulting in more efficient utilization of spectral resources. Standards will need to outline how such reductions can be implemented while maintaining system integrity and performance. Essentially, this might require more flexible DMRS configurations to be standardized.

- Revision of Requirements Based on AI/ML Capabilities:

With AI/ML integrated into the network, certain physical layer requirements might need adjustments. For example, in-band distortion requirements could be relaxed based on the AI/ML DPoD capabilities. This could lead to more flexible and efficient operation, but it would necessitate new protocols and signalling to ensure compatibility and performance consistency.

- Testing of AI/ML-Based Methods:

To comply with regulatory requirements, it is essential to establish protocols for testing AI/ML-based methods. The dynamic nature of an AI-driven air interface means that testing procedures must be designed to ensure that these systems adhere to regulatory standards. This would involve creating test frameworks for real-time adaptability and the proper functioning of AI/ML algorithms within the air interface.

In conclusion, the transition to an AI-driven air interface requires updates to radio procedures, protocols, and signalling. These updates ensure the seamless operation, adaptability, and compliance of AI/ML-based functionalities within modern communication systems.

7.2 Learning for waveform, modulation, and coding

The design of modulation and coding schemes is central to achieving high levels of SE, reliability, and flexibility in modern wireless systems. As demands for these metrics continue to grow, traditional techniques are reaching their limitations. By incorporating AI and machine learning into the PHY layer, it becomes possible to address these challenges with novel approaches and unlock new potential in wireless communication performance.

This section examines several AI-driven approaches for enhancing waveform, modulation, and coding processes in wireless systems. Specifically, it explores methods for optimizing MIMO waveforms, improving JCAS capabilities, and advancing LDPC coding structures for more robust error correction. Through these AI-based advancements, future wireless networks can achieve greater adaptability, reduced overhead, and increased reliability, paving the way for next-generation PHY layer designs that are more intelligent and capable of responding dynamically to network demands.

7.2.1 MIMO waveform for communication

Problem statement: Here, the focus is on end-to-end optimized MIMO system, where the transmitter and receiver utilize ML to jointly optimize their behaviour and consequently maximize the SE. A detailed description of the approach can be found in [HEX224-D43]. In a nutshell, the improvement in SE is achieved due to the fact that the AI-based approach can learn to communicate without any DMRS pilot overhead, relying on learned constellations.

However, one issue with this approach is the need to agree on the learned constellations between transmitter and receiver, which can incur some overhead. Moreover, the more transmission layers there are, the more complicated the system becomes as each transmission layer requires its own constellation shape [HEX224-D43]. To address this issue and to come up with a more favourable framework for low-overhead AI-based MIMO link, we consider the use of superimposed pilots. These are pilot symbols that are overlapping with the data, which means that all resource elements (REs) are still used for data, but in some REs the power is divided between pilots and data.

Methodology: We assume the same system model as in [HEX224-D43] but instead utilize a single learned constellation for all MIMO layers and add superimposed pilots that overlap with the data symbols. The

considered scheme is illustrated in Figure 7-1. The approach is compared against the pilotless scheme as well as against DMRS-based system using link-level simulations.

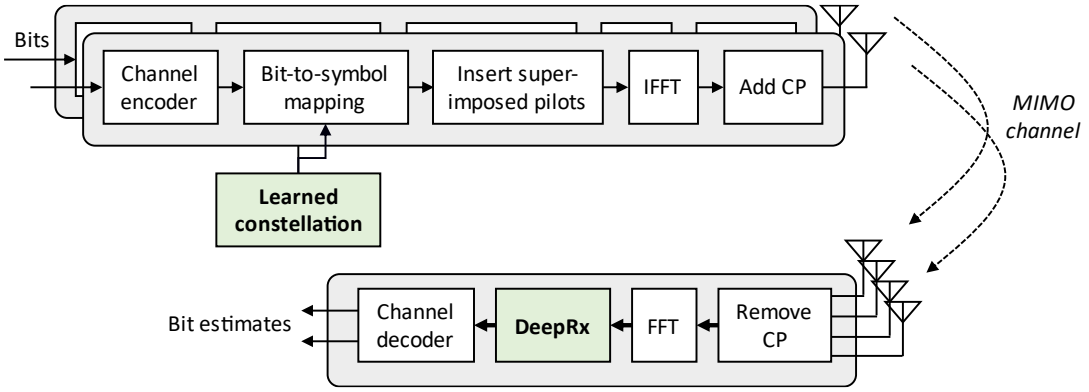

Figure 7-1: The proposed learned MIMO scheme with superimposed pilots.

Results: The BLER results, which are shown in Figure 7-2, demonstrate that superimposed pilots are a practical alternative to a fully pilotless system. In fact, in the considered simulation scenario, such a scheme achieves even a higher throughput gain over conventional systems, while lending itself more readily for standardization and practical systems. Indeed, it suffices to agree on a common constellation shape for all MIMO layers and define superimposed pilot patterns and symbols in largely the same way as is done for DMRS in current 5G systems. This can therefore be considered a more practical approach for utilizing AI-based MIMO Tx and Rx schemes.

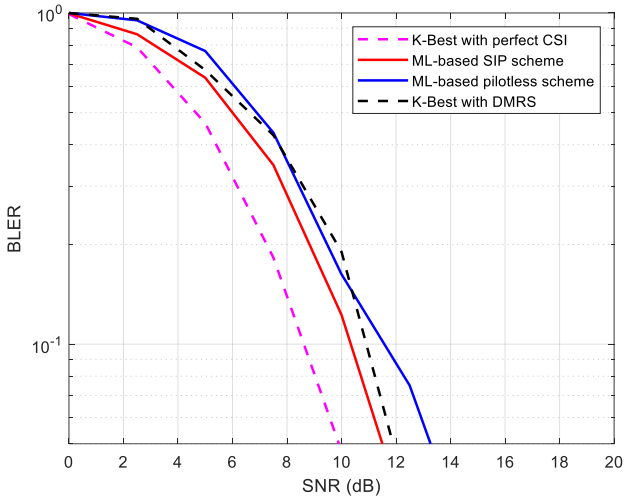

Figure 7-2: Block error rates (BLERs) of different communication schemes with CDL-B channel model, 5 m/s velocity, code rate of 0.46 and 6 bits per symbol.

7.2.2 Waveform and precoding for JCAS

Problem statement: The problem of gain-phase impairments (GPIs) affecting both communication and sensing in 6G JCAS systems is addressed. The impairments arise from hardware imperfections and can significantly degrade the performance of model-based algorithms used for signal processing in integrated sensing and communications (ISAC). While deep learning offers a potential solution, it lacks interpretability, unlike model-based machine learning (MB-ML). Existing MB-ML methods for GPI mitigation often rely on supervised learning, which requires challenging and time-consuming ground-truth data collection.

Methodology: The article proposes an unsupervised learning approach within the MB-ML framework to jointly compensate for GPIs and estimate target locations. The method is applied to a monostatic SIMO radar system using OFDM signals for single-target detection and position estimation. The approach builds upon the

maximum a-posteriori ratio test (MAPRT) detector, which incorporates prior information about the channel gain, target angle, and range. Two specific unsupervised loss functions are proposed to learn the GPIs.

1. Maximising the maximum value of the angle-delay map (L1): This loss function exploits the fact that unknown GPIs reduce the magnitude of the angle-delay map used for target localization.
2. Minimising the error of the received observation signal (L2): This loss function compares the received signal affected by the true GPIs with a reconstructed signal based on the estimated impairments.

The proposed unsupervised learning MB-ML algorithm iteratively updates the GPI estimates using gradient descent and normalisation to achieve optimal compensation.

Results: In Figure 7-3, the misdetection probability and the position error are represented as a function of the false alarm rate. Results show that the considered GPIs result in a performance degradation when their model is unknown. Harnessing the proposed UL framework yields a performance close to the case of perfect knowledge of the impairments. Both loss functions exhibit similar performance, potentially stemming from their shared derivation from the MAPRT objective. This demonstrates the effectiveness of the proposed approach to compensate for GPIs.

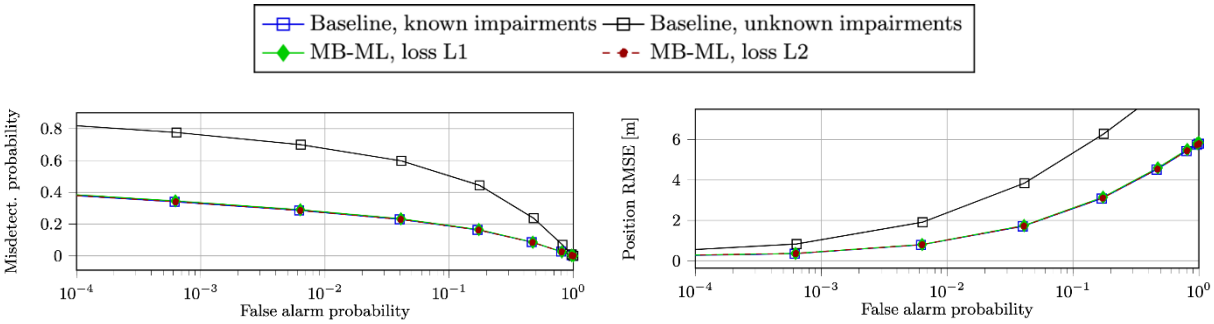

Figure 7-3: Sensing results as a function of the false alarm probability.

The proposed model-based unsupervised learning approach effectively accounts for GPIs in the receiver ULA of an JCAS system. The proposed unsupervised learning function avoid the need of labelled data to perform training and compensate for the impairments. Simulation results confirm the capability of the proposed approach to compensate for gain-phase errors effectively, resulting in target detection and position estimation performance comparable to scenarios with full impairment knowledge. This demonstrates the potential of the proposed unsupervised learning framework for online impairment compensation in ISAC scenarios.

7.2.3 AI for LDPC matrix structure optimisation

Problem statement: LDPC is a type of error-correcting code used in digital communication systems to detect and correct errors that occur during transmission. It consists of adding redundancy bits to the original message of K bits transmitted resulting of the codeword of N bits leading to the code rate R=K/N. The original message is encoded by the generator matrix G and then solving equations at the receiver to recover the original message. These equations are called check equations and are given by the parity check matrix H. LDPC codes are currently used in the communication chain of 5G with a specific structure quasi cyclic low density parity check (QC-LDPC) and may be continued for 6G. In this structure photograph matrix (called Base Graph in 5G context) are extended by using an expansion factor (Zc). To ensure evolution and improvement of the communication chain, it is essential to improve the performance of error-correcting codes in this chain. This improvement could potentially be achieved through artificial intelligence where theoretical methods are limited. Artificial intelligence has proven its worth in many domains and could also be used for LDPC codes. This is why the topic of optimizing LDPC codes using artificial intelligence for 6G is being addressed.

Methodology: The 5G communication chain consists of several blocks, including the LDPC encoder and LDPC decoder (see Section 6.2.2). Recent research focuses on modelling the decoder using a RNN to optimize the parity check matrix for a given codeword length [LDL+21]. The weights of this neural network are the coefficients of the parity check matrix as shown in the Figure 7-4. Since belief propagation (BP) decoding involves a recursive exchange of information, a recurrent neural network (RNN) is used to calculate the decoding iterations. The output of each iteration is then used as input for the next iteration. The weights are

updated automatically, and each new weight value undergoes a binary selection to ensure correspondence with the parity matrix structure.

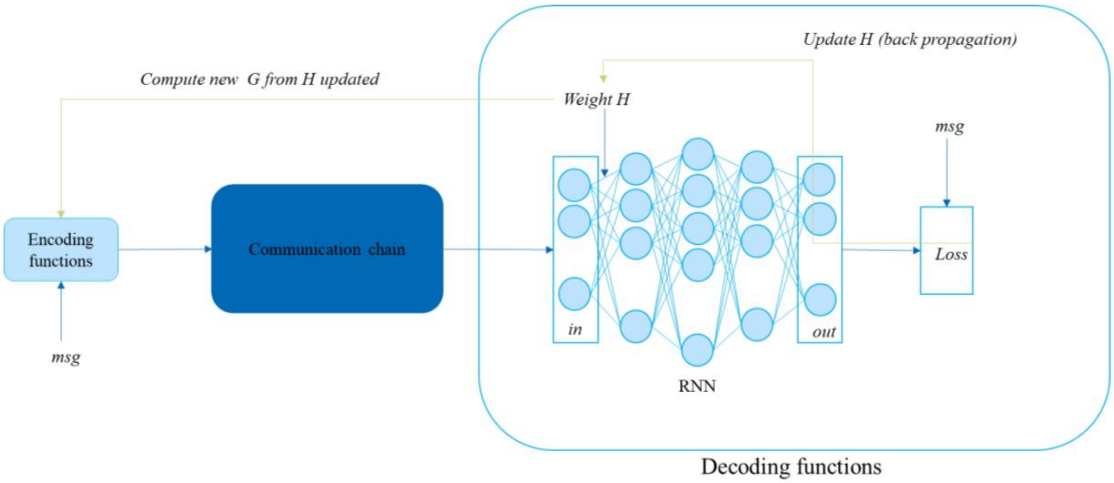

Figure 7-4: System architecture with RNN decoder.

After multiple decoding iterations, the proposed RNN tends to converge the weights, and thus the parity matrix, towards an optimal solution. These works address a classical LDPC structure, but the 5G LDPC structure (see Section 6.2.2) presents several challenges:

• The structure - Maintaining the structure after weight updates is important because the neural network updates are relative to Parity check matrix without considering a base matrix.

• Size diversity - finding an algorithm capable of improving all the BG1 and BG2 matrices, regardless of Zc (expansion parameter).

• Cycles - it is difficult to reduce cycles for small Zc.

Starting from the work in Section 6.2.2, we apply the RNN technique to find one matrix scheme for the smallest BG2 matrix structure, i.e. $K = 12$, $Zc = 2$ and $R = 1/5$. Applying the min-sum decoding with 5 iterations to messages transmitted in AWGN channel, this matrix obtained via IA (red curve in Figure 7-5) was compared to the classical 3GPP matrix and new one proposed in Section 6.2.2, green and blue curves respectively in Figure 7-5.

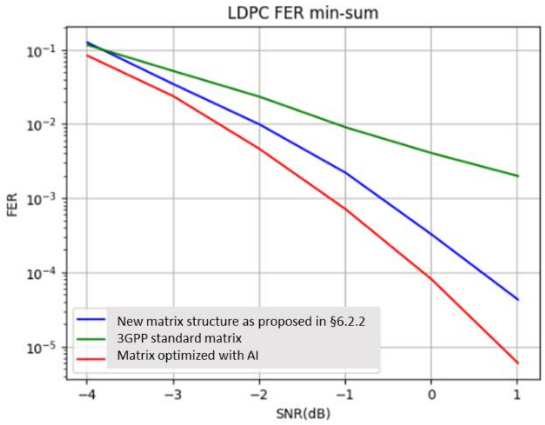

Figure 7-5: Performance results for BG2 matrix K=12, R=1/5 and Zc=2

This result is very interesting as it shows more than 2 dBs gain compared to conventional 3GPP results but needs to be generalized to all matrixes sizes defined in 3GPP.

7.3 AI-based CSI acquisition

CSI is crucial for optimizing MIMO and beamforming operations, directly impacting system performance. However, as the complexity of wireless networks increases with larger antenna arrays and more devices, the challenge of efficiently obtaining and managing CSI grows. Traditional methods often face trade-offs between feedback accuracy and overhead. In this section, we explore innovative AI-based techniques for enhancing CSI acquisition and compression, also in multi-vendor environments where interoperability can further complicate the process. By leveraging machine learning, these approaches aim to maintain high accuracy in CSI feedback while minimizing the associated data burden. Key areas of focus include OTA implementation of AI algorithms for improved CSI encoding and decoding, advanced compression and precoding schemes to optimize SE, and predictive models that anticipate channel variations. Together, these solutions offer pathways to more scalable, flexible, and efficient CSI handling in future wireless networks.

7.3.1 ML-based channel state feedback compression in a multi-vendor scenario

Problem statement: CSI feedback is a key element to enable MIMO and beamforming techniques and improve system performance. However, as the number of antenna elements increases the CSI overhead becomes significant.

CSI acquisition relies on uplink signalling (SRS) for acquiring the channel state, which requires resources (pilots), or through feedback from the UE. Codebook based approach can reduce overhead at the expense of reduced accuracy which may limit the gain that could be provided through MIMO operations either through higher interference or lower system gain.

The target of this contribution is a demonstration that cooperative AI-based techniques can improve the SE and accuracy of channel state feedback (CSF) compared to legacy CSI schemes. In this proof-of-concept, an AI/ML algorithm runs at the device to encode/compress the CSI to be sent. At the gNB a reciprocal AI-based technique decompresses the CSI. Together, those two AI algorithms can improve CSI resolution for a given number of bits or equivalently reduce overhead for a fixed CSI resolution.

Methodology: This contribution is a proof of concept that aims to demonstrate the feasibility of cross-vendor cooperation to enable joint ML solutions for CSI feedback compression. This section presents the performance evaluation of the proposed solution based on OTA measurements. Section 11.3.1 details the system configuration and data collection process.

In the considered PoC, the gNB and UE cooperate to enable compressed CSF. End-to-end joint training of the ML models (CSI decoder and CSI encoder, respectively) by sharing data set, with a single entity that does the training is not a preferred solution as it requires sharing the proprietary models. Instead, the ML models are obtained through sequential and separate training of the UE and gNB models: the models at UE and gNB sides are trained independently. The UE starts with training the UE encoder and UE reference decoder (both using UE-proprietary models) and then share the dataset so that the gNB would be able to learn a decoder (using gNB-proprietary model) capable of regenerating the UE encoder input.

This mechanism enables ML-based CSF without sharing the proprietary ML models at the UE and gNB. The process is detailed below.

1. The UE-side starts by collecting channel state measurement, these are the features and labels for training the models.
2. When enough channel measurements have been collected, the UE-side starts training the ML model encoder and the reference decoder for CSF compression.
3. UE-side shares a dataset to the gNB-side containing compressed CSF-samples and the channel state inputs, i.e., the ground truth.
4. With this dataset, the gNB-side trains a ML model capable of decoding the compressed CSF.
5. After training at the gNB-side, the UE-side and gNB-side ML models are deployed to the UE and the gNB, respectively.

Results: The results are based on 8 ports per SB, with each UE having 4 Rx antennas, providing a channel matrix of rank 4. The layer i in Table 7-1 denotes the eigenvector i, where layer 0 is for the strongest layer.

The first set of results compares the accuracy of the end-to-end joint training and the sequential multi-vendor approaches on the reconstructed CSI samples compared to ground truth CSI using the squared generalized cosine similarity (SGCS) metric. The results shows that the reconstructed CSI accuracy with sequential training is similar to that of the joint training. This indicates that the sequential-based training is a promising solution for ML-based CSF.

Table 7-1: CSI reconstruction accuracy under different training methods.

Eigenvector	End-to-End	Common decoder
1	0.973	0.969
2	0.872	0.871
3	0.759	0.748
4	0.655	0.638
Average	0.815	0.806

The second set of results compares the downlink throughput of the proposed sequential multi-vendor ML-based solution to Type I codebook CSF for varying mobility scenarios. A channel emulator generates five different Doppler offsets to evaluate performance with varying mobility. Table 7-2 summarizes the results across five different Doppler frequencies. Results show that ML-based CSF produces a more accurate beamforming as it can achieve, on average, a ~14% DL throughput gain over the baseline CSI feedback method. Note that the Type I baseline utilizes wideband precoding, unlike the ML-based CSF which is SB precoded.

Table 7-2: DL throughputs gain over Type I CSF using a channel emulator with varying Doppler configurations.

0.1Hz	10Hz	30Hz	50Hz	75Hz	Average
25.0%	34.7%	2.0%	8.7%	4.4%	13.8%

7.3.2 Intelligent CSI compression

Problem statement: CSI-feedback via precoder construction allows to better the communication channel. This research work (a continuation of initial analysis shown in [HEX224-D43, Sec. 6.2.2]) concentrates now on two topics: a) study of intelligent pre-processing approach for CSI compression with classical and AI schemes; b) treatment of the interference which is known at UE and not at the BS side. Construction of a precoder based only on the channel-related CSI can be non-optimal, and additional feedback of the noise correlation matrices could be expensive (for moderate and especially for large UE array size, which can be typical for 6G applications). Our approach to this problem is to merge the interference treatment into the CSI report delivering "sufficient information" only. This represents also an additional compression.

Methodology: Traditionally, the CSI compresses the channel information related to the DL BS precoder construction, e.g., channel eigenvectors or of the precoding matrix $\boldsymbol{x}_n$, which are thus the "input" matrices having υ columns each and usually defined per SB where υ is the number of the information layers. We propose to pre-process these inputs to compression at UE side via linear transforms to make the new modified inputs more similar and for better compression.

$$\boldsymbol{x}_n^{(\text{modified})} = \boldsymbol{x}_n \mathbb{U}_n \ \text{ for } n = 1{:}N_{SB},\ \dim \mathbb{U}_n = \upsilon \times \upsilon \qquad \textbf{(7-1)}$$

The transform matrices, $\mathbb{U}_n$, are *hidden* CSI compression degrees of freedom preserving the communication properties, e.g., capacity or the total power over UE array antennas). Unitary matrices (full or diagonal) can be such transforms *optimized* per SB.

The optimization block scheme with unitary matrices is shown in Figure 7-6. The reconstruction error is calculated due to the modified input. Pre-processing can precede future AI-based or existing 5G CSI compression engines (with minimal modification presented in the Results Section below).

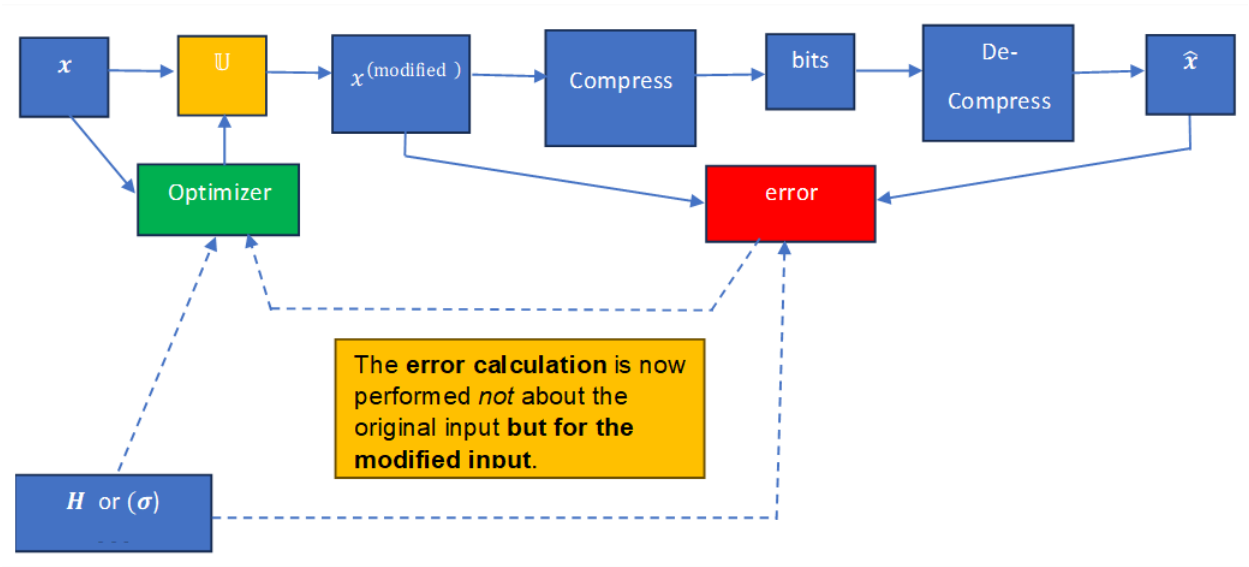

Figure 7-6: Optimization block scheme of pre-processing or CSI compression.

Further details on methodology, theoretical analysis, and prior art can be found in Section A.3.

Results: The optimized input columns phasor modification is examined (diagonal unitary matrices) for 3 information layers, where strong compression is essential. We consider TDLA-30-5/LOW channel, L=4 beams, N_{SB}=19. Note that 5G enhanced type 2 (eType2) precoding performs a simple but not optimal phase modification, based on a single "most significant beam" row which is de-phased [ATM19], [STM+22] and warped to equal amplitude, thus not reported. The compression engine of eType2 may remain the same with the only difference that all non-zero coefficients are now reported back (the feedback size is preserved).

Figure 7-7 shows importance of the phasors optimization leading to a better than eType2 performance and closeness to the singular value decomposition (SVD) bound with L=4 beams for 1 OFDM symbol for challenging 3 information layer lossy compression. Note that the only difference from 5G eType2 is that we do not utilize amplitude warping but just perform eType2 coefficient quantization. The total number of non-zero coefficients is identical.

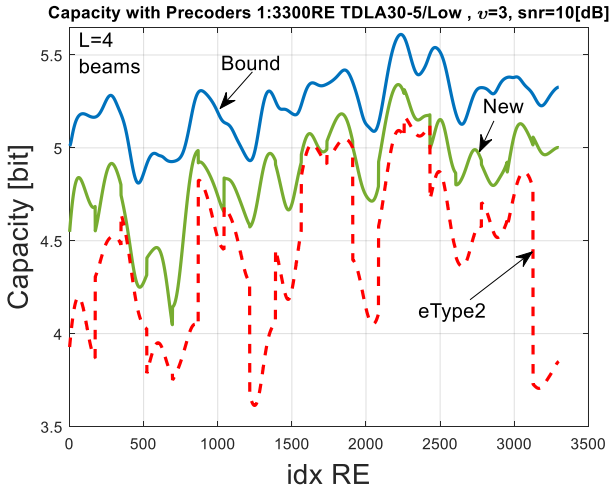

Figure 7-7: Capacity via RE for 1 OFDM symbols, 100 MHz (strategy "0" is used for New).

Figure 7-8 presents gaps about 5G eType2 during 100 ms with yet heuristic optimizations based on 1 and 20 ASV strategies (explained in Section A.3). Further improvements are plausible with further better optimizations. These optimizations can be based on the ASV approach presented in Section A.3 or an optimization based on Barrier Functions approach.

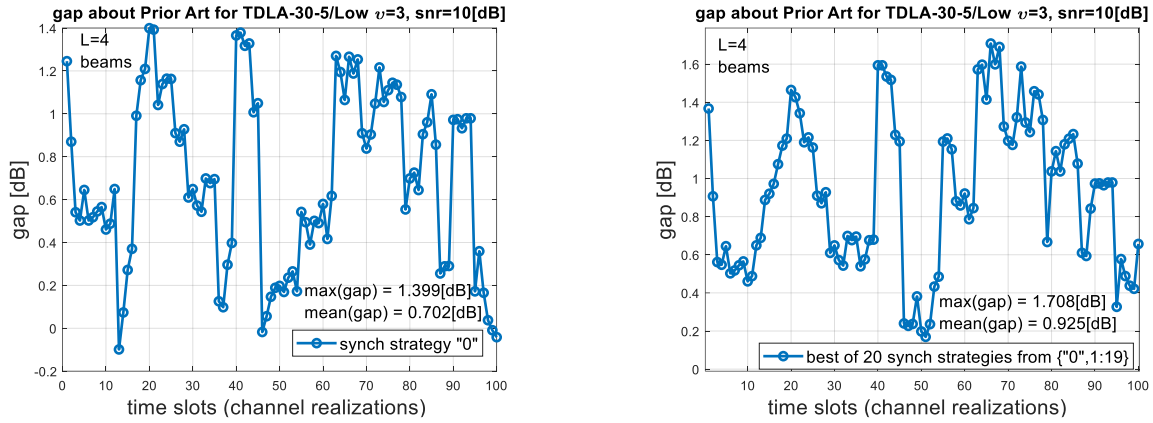

(a) 1 ASV strategies is used **(b) 20 ASV strategies are used**

Figure 7-8: Gap in [dB] per 100 ms relative to eType2 using 1 and 20 ASV strategies. eType2 parameters are $\boldsymbol{v = 3, L = 4, N_{SB} = 19, p = 1/4, \beta = 3/4}$.

7.3.3 CSI prediction

Problem statement: In frequency division duplexing (FDD) systems, where channel reciprocity is not available, the downlink CSI is estimated at the UE and the estimated CSI is sent to the BS through a feedback report in UL. In FDD systems, the CSI feedback incurs high overhead, motivating the study of ML-based CSI feedback enhancements in 3GPP. An autoencoder (AuE) can be used for dimensionality reduction and minimize feedback overhead, improving feedback accuracy at a maintained overhead compared to the conventional CSI feedback techniques. The AuE-based CSI compression has been studied for the ML-based CSI feedback enhancement in the Release-18 [38.843]. The AuE-based CSI compression may suffer performance degradation due to channel aging in a dynamic network since the AuE model cannot capture the time-varying nature of the wireless channel.

Methodology: To avoid the channel aging issues, this study aims at developing a deep learning-based solution that allows the BS to accurately predict radio channel variations under the 3GPP CSI feedback mechanism. Aiming at multi-step-ahead prediction based on a single feedback information under the CSI feedback process, this study proposes a new CSI framework, called an evolutional CSI neural network (evoCSINet) [HEX224-D43]. The proposed evoCSINet applies the combination of autoencoder and dynamicNet to identify state-level and latent-level representation of channel dynamics from radio channel images given by channel states H_k. Through learning the dual-level dynamics representation, we can optimize our evoCSINet towards multi-step predictions. More specifically, the proposed evoCSINet provides a factorized representation of radio channel dynamics that allows evoCSINet to fit into the CSI feedback procedure. As a result, the evoCSINet can achieve an accurate multi-step-ahead prediction only based on the single feedback information of an encoded vector, called latent code.

A diagram of the proposed evoCSINet is shown in Figure 7-9. The evoCSINet applies the combination of autoencoder and dynamicNet, parameterized with configurable strides Δ_φ and Δ_f, respectively. The autoencoder, composed of encoder φ and decoder φ^{-1}, achieves a single-step-ahead prediction with a state-level stride Δ_φ by learning the end-to-end state dynamics in the original channel state space while the dynamicNet $\mathcal{F}$ learns a representation of channel dynamics in a low-dimensional latent space derived by the autoencoder. In order to achieve a single-step-ahead prediction model with a state-level stride Δ_φ, an autoencoder model should meet the following condition:

$$H_{k+\Delta_\varphi} = \varphi^{-1}\big(\varphi(H_k)\big) \quad \textbf{(7-2)}$$

and the latent dynamic model $\mathcal{F}$ identifies a lowdimensional representation of channel dynamics from channel data to predict a latent code one step forward in time as follows:

$$z_{k+\Delta_f} = \mathcal{F}(z_k) \quad \textbf{(7-3)}$$

where Δ_f denotes a latent-level stride.

In the proposed evoCSINet model, these two ingredients of autoencoder in (7-2**)** and dynamicNet in (7-3**)** enable a dual-level dynamics representation of radio channel with state-level stride Δ_φ and latent-level stride Δ_f as

$$H_{k+\Delta_\varphi+m\Delta_f} = \varphi^{-1}\left(\mathcal{F}^{(m)}\varphi(H_k)\right) \quad \textbf{(7-4)}$$

where $\mathcal{F}^{(m)}(\cdot)$ indicates a m-time recursive process of $\mathcal{F}$ to the latent code $\varphi(H_k)$.

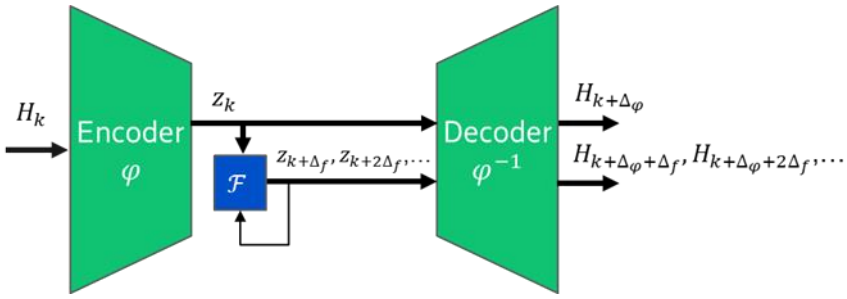

Figure 7-9: Proposed evoCSINet that applies the combination of autoencoder with dynamicNet

As can be seen in Figure 7-9, the proposed evoCSINet is able to predict an infinite number of time points $k + \Delta_\varphi + m\Delta_f$ for $m = 1,2., \ldots$ with a stride Δ_f over an infinite time horizon, all measured in slot time. A loss function can be defined over a finite time window for $m = 1,2, \ldots, M$. Hyperparameters, including Δ_φ, Δ_f, and M can be chosen to achieve a balance between state-level and latent-level prediction errors. We consider four different hyperparameter sets illustrated by prediction time grids in Figure 7-10, where the initial time point at $k + \Delta_\varphi$, depicted by a red box, is the first time step to predict, relative to a current step time k, and the additional M time steps, depicted by a blue box, are to be predicted recursively via dynamicNet $\mathcal{F}$ with a stride Δ_f.

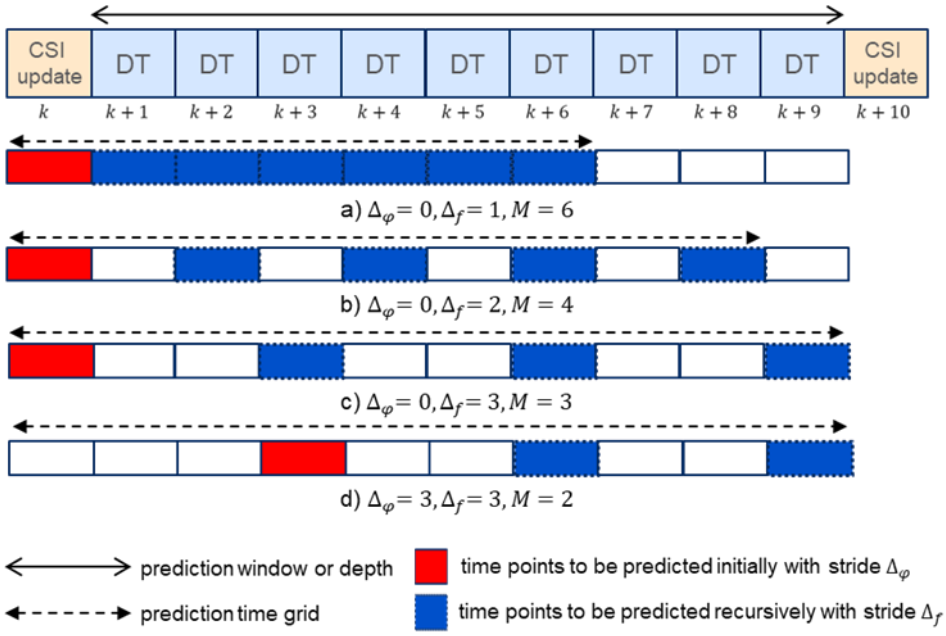

Figure 7-10: Four prediction time grids with different hyperparameters Δ_ϕ , Δ_f, and M.

Results: The performance metric considered is ϵ-outage capacity, which is defined as maximum rate below which reliable transmission is possible at outage probability ϵ. In this work, the 10% outage capacity ($\epsilon = 10\%$) performance has been evaluated under three different CSI assumptions, perfect CSI, compressed CSI, and predicted CSI by evoCSINet, and it has been normalized by the upper capacity bound with perfect CSI in order to quantify prediction performance loss relative to the upper bound. The prediction time grids generate a specific set of time points with the same initial point k. MRT precoding method is used in this evaluation. MRT is known as optimal for this MISO setup by maximizing the signal gain, and CSI at the transmitter is required to enable the precoding.

In Figure 7-11, we compare the percentage capacity obtained with the first three prediction time grids illustrated in Figure 7-10. The first thing we notice from Figure 7-11 is that the MRT precoding with the compressed CSI suffers from a severe performance loss due to channel aging. For instance, the performance loss reaches 23% at the CSI aging of 9 slots, compared to the ideal CSI. The second observation from Figure 7-11 is that performance degradations due to channel aging are marginal over the first few slots, which encourages us to consider stride values Δ_f greater than one. In order to evaluate the change in accuracy with increasing values of latent-level stride Δ_f, we have simulated for the predicted CSI cases using the three values of $\Delta_f = 1,2,3$. The values of M have been chosen for each time grid to achieve the best balance between immediate and long-term performance within the given prediction window. The plot in Figure 7-11 shows that the best average performance can be achieved by applying the evoCSINet using Δ_f=3 and $M = 3$, meaning that the stride value Δ_f=3 does not hurt the performance at the time points off the prediction time grid even though channel states at these points are estimated from the predicted states at its neighbour time points via the simple procedure of rounding and linear interpolation. Note that increasing values of $\Delta_f = 1,2,3$ resulted in the reduced values of M, which may have contributed to the better performance with Δ_f=3 since an evoCSINet model that is trained to predict the smaller numbers of time points will outperform the same evoCSINet trained to predict the larger numbers of time points. The results in Figure 7-11 demonstrate that the evoCSINet-based CSI prediction can reduce the performance loss due to channel aging by 79%, which corresponds to 95% of the maximum capacity.

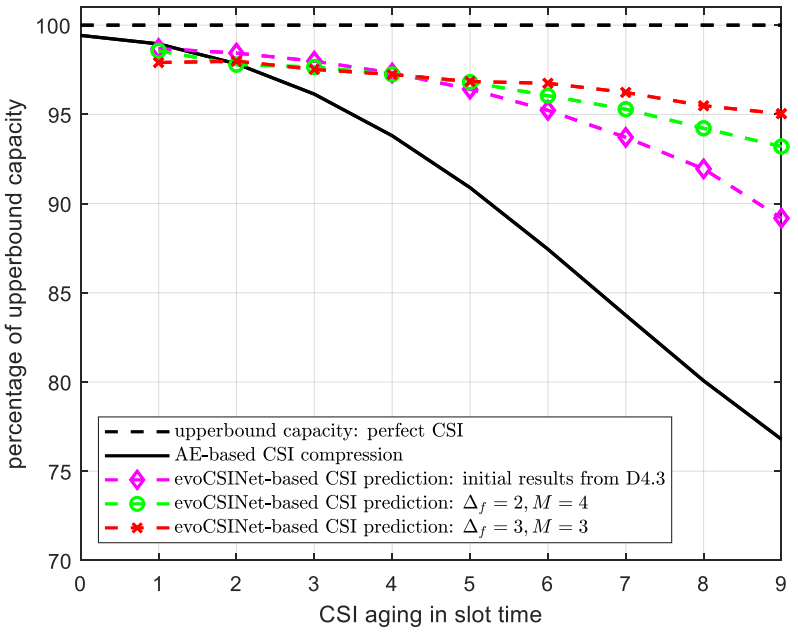

Figure 7-11: Impact of hyperparameters in prediction accuracy.

As wireless networks evolve, the demands on MIMO technology grow increasingly complex. Traditional MIMO techniques often encounter challenges such as limited or imperfect CSI, suboptimal power management, and heightened power consumption. These issues are particularly critical in scenarios with multiple users or D-MIMO configurations, where efficient resource allocation and interference management become essential for maintaining high network performance.

This section explores AI-based solutions designed to address the inefficiencies of conventional MIMO systems. Through machine learning, new approaches for antenna muting, user pairing, pilot assignment, and power control are introduced, each aimed at optimizing specific aspects of MIMO transmission. These AI-driven strategies not only enhance SE and quality of service (QoS) but also contribute to energy savings and operational scalability in complex network environments. By integrating AI, future MIMO systems can become more adaptive, achieving superior performance and robustness across a range of transmission conditions.

7.3.4 Antenna muting

Problem statement: The transmit antenna muting (TAM) problem for the DL transmission of a MU-MIMO setting is considered in this contribution. TAM allows to reduce a base station's power consumption by efficiently utilizing only a subset of antennas available at the BS. Formally, TAM is posed as an optimization problem to minimize the number of active antennas at the BS with per-UE throughput requirements as constraints.

TAM optimization problem: The TAM problem of minimizing the number of active antenna elements subject to per-UE rate constraints capturing the QoS guarantees can be formally written as:

$$\begin{aligned} &minimize_{a_i \in \{0,1\}} \left|\left|\boldsymbol{a}_{\mathcal{A}}\right|\right|_0 \\ s.t. &r_k\left(\boldsymbol{H}_{k,\mathcal{A}}, \boldsymbol{W}_{k,\mathcal{A}}\right) \geq r_{min}, \forall k, \\ &\left|\left|\boldsymbol{a}_{\mathcal{A}}\right|\right|_0 \leq M - M_{min}, \end{aligned} \quad \textbf{(7-5)}$$

where, $r_k\left(\boldsymbol{H}_{k,\mathcal{A}}, \boldsymbol{W}_{k,\mathcal{A}}\right)$ is the per-UE rate with $\boldsymbol{H}_{k,\mathcal{A}}$ and $\boldsymbol{W}_{k,\mathcal{A}}$ being the UE's channel matrix and transmitter matrix respectively; r_{min} is a predetermined value indicating the minimum allowed per-UE rate to guarantee the QoS requirements and M_{min} is the minimum number of active antennas (per-polarization) in the BS which is also a predetermined value. By selecting a subset of antennas at the BS, the goal is to implicitly reduce the power consumption while satisfying UEs' QoS requirements.

Methodology: The above optimization problem (henceforth referred to as **P1**) is a constrained cardinality optimization (CCO) problem and non-convex in nature. On top of being non-convex, CCO problems in general also happen to be combinatorial in nature (NP-hard in this case) w.r.t the optimization variables. For instance, the processing runtime scales exponentially as the number of antennas increase at the BS in **P1**. To overcome the computational complexity issues posed by hand-tuned heuristic algorithms, which are typically used for solving CCO problems resembling **P1,** this work follows a data-driven approach.

A neural antenna muting (NAM) approach is proposed, where a feed-forward neural network architecture comprising of a single convolutional layer followed by 2 dense layers is trained offline to solve the optimization problem in **P1**. Training is performed as a supervised learning approach, where the training inputs are given by $\boldsymbol{X}_k = [Re(\boldsymbol{W}_{k,pol}), Im(\boldsymbol{W}_{k,pol}), Re(\boldsymbol{H}_{k,pol}), Im(\boldsymbol{H}_{k,pol})]$ and the corresponding labels are given by one-hot vectors $\boldsymbol{y} = \boldsymbol{1}_y \in \mathbb{R}^N$. Here, $\boldsymbol{1}_y$ denotes an N-dimensional vector where the y^{th} element is one and zero otherwise, with N being the number of array configuration classes (as considered in [RMW+24]).

Results: The proposed NAM approach is compared with greedy heuristics as described in Section V of [RMW+24]. The proposed approach is evaluated w.r.t the SE and power consumption, where SE is defined in terms of UEs' throughput and the expression for power consumption is modelled after the RF frontend power model provided in [HWW+18]. From Figure 7-12, it is evident that the proposed NAM closely follows the greedy heuristics for both SE and power consumption. More specifically, NAM ensures that the target QoS requirements (w.r.t SE) are reached for 95% of the times. Moreover, NAM achieves comparable power consumption w.r.t the greedy heuristics with a reduced computational complexity.

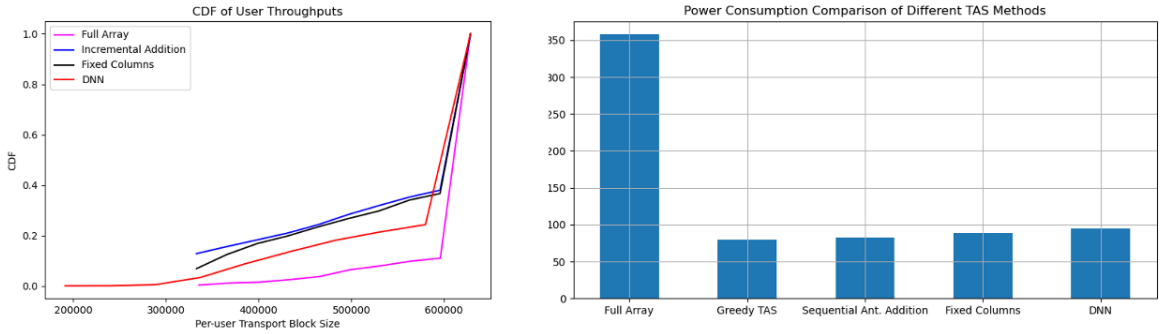

Figure 7-12: SE and power consumption comparisons for the proposed approach with different greedy heuristics.

7.3.5 User pairing for MU-MIMO

Problem statement: As it has been already explored in [HEX224-D43], one of the primary challenges in MU-MIMO systems, is the pairing of users and the application of precoding, especially when constrained by limited CSI. This issue is particularly prominent in scenarios such as the open radio access network (O-RAN) Use Case 22 [ORAN23], where only partial CSI, including channel quality indicator (CQI), precoding matrix indicator (PMI), and user buffer status, is available.

Considering then scenarios where more than one preferred direction for the signal is available, the channel information carried by the CSI Type I may be not enough to allow smart user pairing and precoding approaches that fully exploit channel characteristics.

Methodology: Reinforcement learning (RL), specifically deep Q-learning via a deep Q-network (DQN), is used to determine the best user pairing in a multi-user MIMO transmission, based on limited information such as CQI and PMI. Differently from the solution proposed in [HEX224-D43], this study exploits the channel state information of type 2 defined in 3GPP [38.214], where four different PMIs are reported by each user, together with their relative weight coefficient and phase shift. The precoding vector adopted for the transmission is then determined by a linear combination of the reported PMI vectors properly phase shifted. Consequently, the "state" for the RL algorithm is defined by the CQI, buffer status of users and by 4 PMI indices, with 4 PMI amplitude coefficients and 4 phase shifts.

To handle this more complex state information, the DQN structure needs to be updated, particularly by increasing the number of neurons in the intermediate dense layers to accommodate the input and output sizes.

In the end, the action selected by the AI agent determines which users to schedule together in the next transmission, and the reward for the agent is computed based on the total data served and adjusted with penalties for non-optimal actions.

Results: The results presented hereafter have been obtained in the same simulation setup described in [HEX224-D43]. With respect to that setup, two enhancements have been implemented: 3GPP CSI type 2 reporting has been included in the evaluation, and this requires a more complex neural network architecture. Moreover, the channel matrices used for simulations are Rayleigh distributed and spatially correlated but, instead of simulating a Laplacian distributed power angular spread around a single angle of arrival, the distribution is the linear combination of four Laplacian PAS around 4 randomly generated angles of arrival. This setup implies the existence of four different preferred direction, which means that, in principle, the new system should benefit more of the additional channel information given by CSI type 2. This is confirmed by data in Figure 7-13, where it can be observed how the new model with CSI Type 2 implementation is able to achieve better performance than with CSI type 1.

In general, as it has been already shown in [HEX224-D43], the DQN-based algorithm achieves comparable results with respect to the "greedy genie" (GG) algorithm and it significantly reduces the number of scheduling steps to empty user buffers compared to single user round robin (RR), thus providing higher user and cell rate, and overall SE (Table 7-3).

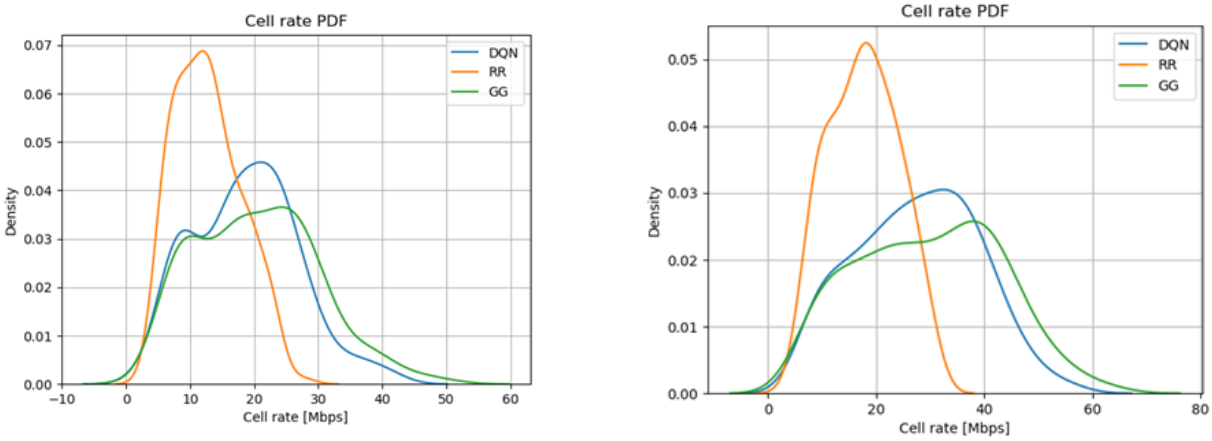

(a) CSI-Type 1 results **(b) CSI-Type 2 results**

Figure 7-13: Cell rate probability density function achieved with the proposed DQN algorithm, compared to RR and GG approaches, with different CSI reporting type.

Table 7-3: Steps to empty all users buffers with the different proposed approaches.

		Round Robin	DQN	Greedy Genie
Average # of scheduling steps to empty all buffer	CSI Type 1	46,8	**35,2**	32,2
	CSI Type 2	33,4	**23,0**	22,3
Average user data rate [Mbps]	CSI Type 1	4,39	**7,56**	10,06
	CSI Type 2	5,73	**10,32**	12,98
Average cell data rate [Mbps]	CSI Type 1	12,82	**18,69**	20,44
	CSI Type 2	17,74	**27,59**	29,76
Corresponding SE [bps/Hz]	CSI Type 1	1,28	**1,87**	2,04
	CSI Type 2	1,77	**2,76**	2,98

7.3.6 Power control for D-MIMO

Problem statement: In D-MIMO, since all the users are served simultaneously using the same time-frequency resource, proper resource allocation such as pilot assignment, power control, user association, etc. is essential to limit multi-user interference and optimize the overall network performance. ML techniques can be exploited to solve these resource allocation problems in a data-driven way with a reduced complexity, instead of using optimisation-based solutions. Specifically, in this study, ML-based joint pilot and data power control for sum rate maximization in a D-MIMO network is investigated [RRL+24].

Methodology: A D-MIMO network setup similar to the system model in [HEX224-D43, Sec. 6.3.5] with M access points and K users is considered, and the users undergo pilot transmission, channel estimation, and UL data transmission stages as usual. The difference here is that both pilot transmit power coefficients ρ_k^p and UL data transmit power coefficients ρ_k^u can be changed to maximize the overall sum rate maximisation objective, subject to total per-user maximum transmit energy constraint E_{max}. The optimisation problem can be formulated as,

$$\max_{\{\rho_k^p\},\{\rho_k^u\}} \sum_{k=1}^{K} R_k^{uplink}$$

$$\text{Subject to: } \tau\,\rho_k^p + (\tau_c - \tau)\rho_k^u \le E_{max},\ k = 1,2,\dots K, \qquad \textbf{(7-6)}$$

$$\rho_k^p \ge 0, \qquad \rho_k^u \ge 0, \qquad k = 1,2,\dots K.$$

To find solutions to the non-convex sum rate optimisation problem, a deep learning-based low-complexity approach is proposed, to learn the power allocation outputs to maximise the system sum rate subject to per-user maximum transmit energy constraints. An unsupervised learning approach similar to [HEX224-D43, Sec. 6.3.5] is used to learn the power allocation outputs using large-scale channel coefficients. The unsupervised learning-based method makes the data collection and model training more straightforward and simpler. Specifically, a fully connected deep neural network (DNN) is implemented, which takes in large-scale channel coefficients between the users and the access points as the inputs and is trained to learn the joint power control outputs by taking the negative Lagrangian of the sum rate optimisation problem as the loss function as

$$\text{loss} = -\mathbb{E}\{R(\boldsymbol{\beta},\boldsymbol{\theta})_{sum} + \sum_{k=1}^{K} \lambda\, ReLU\,(E_{k,total} - E_{max})\}, \quad \textbf{(7-7)}$$

where $R(\boldsymbol{\beta},\boldsymbol{\theta})_{sum}$ is the sum rate of all the users for large scale channel coefficient set $\boldsymbol{\beta}$ for a given channel realisation and the DNN model parameters set $\boldsymbol{\theta}$. The total transmit energy of user k for pilot and data transmission for a given DNN output $[\rho_k^p, \rho_k^u]$ corresponding to user k is denoted by $E_{k,total} = \tau\,\rho_k^p + (\tau_c - \tau)\rho_k^u$. Thus, the first part of the loss function focuses on maximising the system sum rate, and the second part tries to guarantee the total energy constraints by having a penalty when the constraints are violated. The parameter λ balances the trade-off between the two. The DNN is trained with a dataset to optimise over this loss function to learn the power allocation outputs.

Results: For performance comparison, a D-MIMO network with $M = 100,\ K = 20$ APs and users randomly distributed over the 1×1 km^2 simulation area is considered using orthogonal pilot assignment with $\tau = K = 20$ and random pilot assignment with $\tau = 10$. Two low-complexity heuristics based on equal power and energy allocation are used to compare sum rate performance of the proposed ML-based approach. Figure 7-14(a) illustrates the sum rate cumulative distribution curves for orthogonal pilot allocation and random pilot allocation. In non-orthogonal pilots-scenario, reduced signalling overhead and pilot power control help overcoming the sum rate degradation due to pilot contamination. Figure 7-14(b) presents the average transmit energy consumption where the equal power and equal energy schemes consume all the energy E_{max}. In contrast, the DNN-based power control results in significant energy savings by properly utilising the pilot and data transmit powers, while giving a better sum rate performance as seen in Figure 7-14(a). For $\tau = 20$ case, 63.35% of the energy is saved while 59.06% is saved when $\tau = 10$. As observed from these results, in conclusion, the proposed ML-based joint pilot and data power control algorithm improves the system sum rate compared to equal power and equal energy allocation heuristics, while resulting in significant energy savings at the transmitter side.

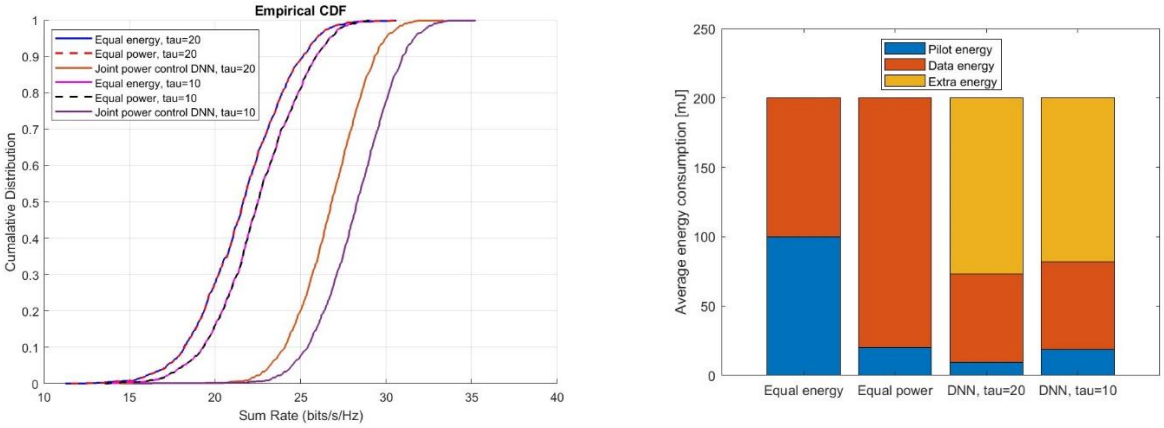

(a) Sum rate performance **(b) Average transmit energy consumption**

Figure 7-14: Joint power control for $M = 100$, $K = 20$ with orthogonal and non-orthogonal pilots.

7.4 AI solutions for hardware impairments

In wireless communication systems, hardware imperfections, particularly those related to PAs and other RF components, can significantly degrade signal quality, impacting both in-band and out-of-band performance. Traditional methods for compensating these impairments, such as power back-off and digital pre-distortion

(DPD), often involve trade-offs that reduce energy efficiency or add complexity to the transmitter design. As the demand for high-performance, energy-efficient wireless systems grows, innovative approaches are needed to manage and mitigate these hardware-induced distortions.

This section introduces AI-based techniques that offer more adaptable and effective solutions to hardware impairments. Leveraging neural networks and generative AI models, these approaches are designed to dynamically compensate for non-linearities and residual distortions, enhancing system throughput and energy efficiency. By enabling more precise and responsive distortion management, AI solutions pave the way for robust, high-quality communication in next-generation networks, reducing the limitations imposed by traditional hardware correction methods.

7.4.1 AI-driven PA-nonlinearity compensation

Methodology: A novel AI-based DPoD technique is introduced in [HEX224-D43] for compensating PA nonlinearity on the receiver side. This approach leverages an artificial neural network (ANN) de-mapper to mitigate the effects of PA memory in the receiver when DFT-s-OFDM signal transmission is employed. The receiver carries out channel estimation using RSs and applies equalization based on the estimated channel state information. The proposed ANN de-mapper facilitates RE soft bit de-mapping of the received signal prior to channel decoding.

Potential needs for standard support: The proposed method would require changes in the following areas to enable data collection for training of the AI/ML model and for the integration of this capability in the network:

- Network signalling for UE configuration for data collection for training AI/ML model.
- Network signalling for UE power headroom reduction based on AI/ML DPoD capability of the receiver at the base station.
- Possibility to revise the requirements on inband distortion (e.g. EVM requirements) based on the AI/ML DPoD capability of the receiver at the base station.

Data collection phase: The network can trigger data collection sessions by sending a command to the UE to transmit signal according to specific transmit hardware operation conditions to ensure that a sufficiently diverse dataset can be constructed for training the AI/ML model. This procedure is outlined in Figure 7-15. To generate training samples, pseudorandom sequence generator (pRSG) can be configured for generating a pseudorandom binary sequence. The same pRSG, with identical initial conditions, is configured at the transmitter and receiver. The pseudorandom binary sequence can be used as transmitted data bits and the labels to be used at the receiver for training the AI/ML model. Hence, the labels may not need to be transmitted over the air.

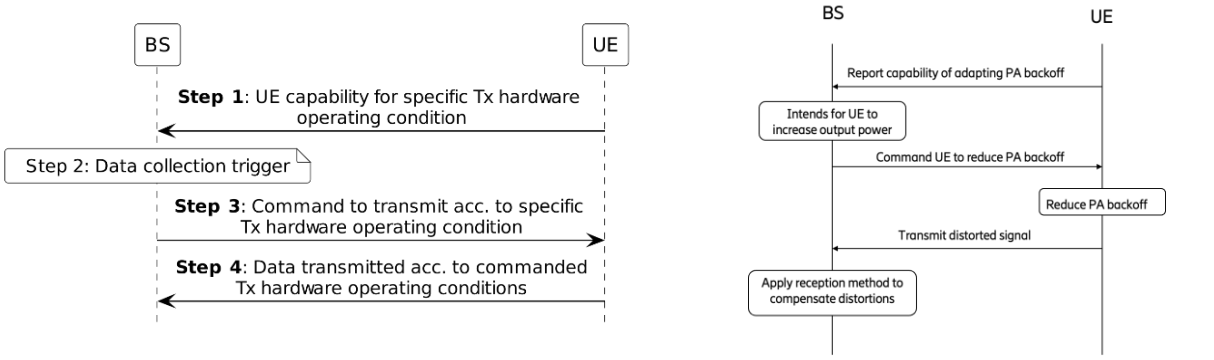

(a) Signalling for data collection

(b) Signalling for the operation of AI-driven DPoD.

Figure 7-15: Signalling procedures for the proposed technique.

Network operation: to integrate the AI-driven DPoD capability in the network for UL transmission, the network and the UE need to coordinate their operations as outlined in Figure 7-15(b). This capability can be utilized towards enhancing different performance metrics and each may lead to needs for different changes in the standard.

- Throughput enhancement: the DPoD capability at the receiver can lower the error probability for signal detection in the presence of distortions, hence, for a given transmitter configurations the throughput can be improved. In addition, this capability enables signal detection for higher order constellations with a given level of distortions. Hence, high order constatations may be supported with lower requirements in inband distortion leading to higher throughput.
- Coverage extension: the DPoD capability enables the receiver to tolerate higher distortions, hence, the PA back-off can be reduced as outlined in Figure 7-15(b) leading to higher PA output power and as a result extended UL coverage.
- Energy efficiency enhancement: the DPoD capability enables the receiver to tolerate higher distortions, hence, the PA back-off can be reduced as outlined in Figure 7-15(b) leading to higher energy efficiency of the PA. This would improve the UE energy efficiency in UL transmissions.

Results: The performance of the proposed AI-driven method in comparison with the legacy method for different PA back-off values is shown in Figure 7-16. The conducted evaluations confirm that the proposed method achieves 45% energy efficiency gain at 2 Gbps, reach 15% throughput gain in UL transmissions, and provide 3dB coverage gain with constellations up to 256-QAM.

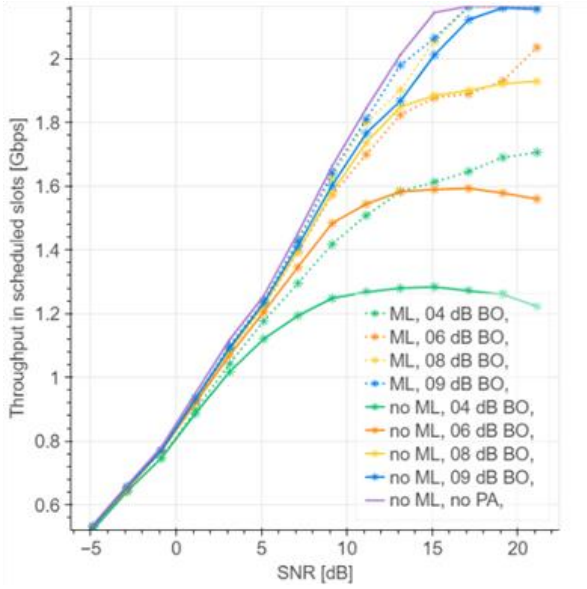

Figure 7-16: Throughout versus SNR performance of the proposed AI-driven receiver method compared to the non-AI legacy receiver for different PA back-off (BO) values.

7.4.2 Generative AI for hardware-impaired communication

Problem statement: Practical communication systems are affected by hardware-impairments due to the non-ideal transmitter and receiver hardware. The effects of hardware impairments are usually mitigated by compensation algorithms, implemented via analogue and digital signal processing algorithms. However, these techniques cannot fully remove the impairments. Because there remains *residual distortion noise* due to the time-varying characteristics of RF hardware that cannot necessarily be parameterized and estimated via compensation algorithms. This can cause additional distortions in the received signals, making it challenging to reconstruct data symbols.

Methodology: Denoising diffusion models are studied for removing the residual noise and impairments at the receiver of a communication system. The key idea behind diffusion models is that if we could develop an ML model that can learn the systematic *decay of information* due to noise and distortions, then it should be possible to "reverse" the process and recover the information back from the noisy/erroneous data. The unique characteristic of diffusion models, which makes them a technically viable choice in the applications of wireless communications [LAL23], [LAL24], [LAL24a], is that they learn how to denoise a degraded version of an information signal and reconstruct data samples accordingly. Inspired by this, the idea in this paper is to leverage the denoising objective of diffusion models to remove the hardware imperfections and residual errors to reconstruct downlink information.

A practical scenario of hardware-impaired communication based on a generic communication model from [BHK+14] is considered. The additive distortion model is considered, which has been experimentally verified in the literature for systems that apply compensation algorithms to mitigate the main hardware impairments. That is, we assume that appropriate compensation algorithms have been applied and focus on the residual hardware impairments and the denoising diffusion probabilistic model is applied at the receiver side to remove the residual hardware distortions and regenerate the ground-truth information signals.

Results: Diffusion model is parameterized by a neural network with 3 conditional hidden layers (with softplus activation functions), each with 128 neurons. The output layer is a linear layer with the same size as the input. The model takes the tensor of distorted signals as input and approximates distortions-plus-noise at the output. For training, we use Adam optimizer with learning rate $\lambda = 10^{-3}$ over 2000 epochs. We use Swiss roll dataset (widely used in the diffusion model literature) for evaluations and assume that the ground-truth information signals are sampled from this dataset. Transmit SNR is defined as $\Gamma = 10\log\frac{p}{\delta^2}$ dB. Without loss of generality, we normalize the average signal power to $p = 1$ and vary the SNR by setting the standard deviation (std) of noise δ. We set the transmitter and receiver impairment level to $(\kappa^t, \kappa^r) = (0.05, 0.15)$, respectively. Original data samples are first quantised into bitstreams and then mapped to QAM symbols for transmission. The MSE metric (averaged over 20 independent runs) between the original and the reconstructed data samples is evaluated. For benchmarking, we exploit the receiver DNN with three linear layers with 64 neurons and rectified linear unit (ReLU) activation function. Figure 7-17(a) highlights significant improvement in reconstruction performance across a wide range of SNR values, especially in low-SNR regimes. We also consider additive Laplacian noise with the same variance as that of AWGN scenario. This can reflect the non-Gaussian interference in multiuser scenarios. Although we do not re-train our diffusion model under Laplacian noise, the performance of our approach does not change. However, we can see from the figure that the DNN benchmark can experience significant performance degradation. This highlights the robust out-of-distribution performance of our proposed scheme. Figure 7-17(b) further showcases a near-invariant reconstruction performance over a wide range of hardware impairment level. This is achieved due to the variance scheduling characteristic of diffusion models, which allows the system to become robust against a wide range of distortions.

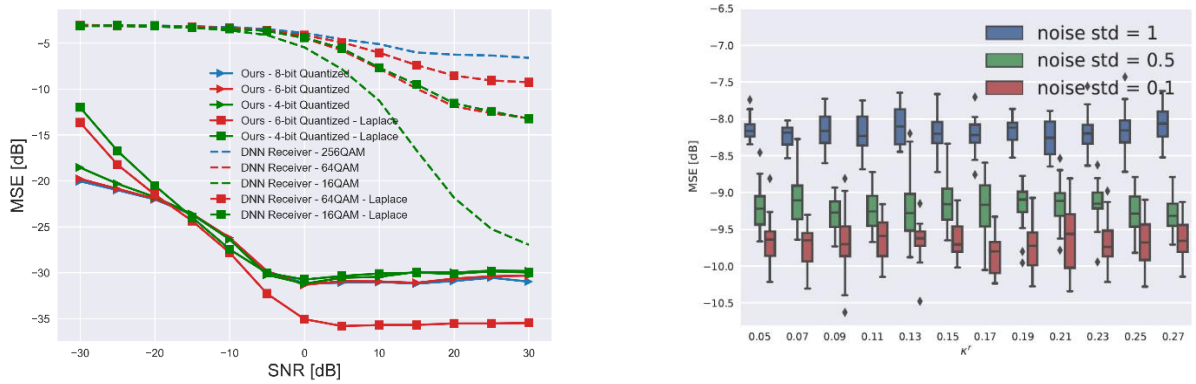

(a) MSE between the original signal and the reconstructed one under AWGN channel

(b) Invariancy of the model's performance over different levels of hardware impairment

Figure 7-17: Performance of diffusion model-aided receiver.

7.5 Summary

This chapter has explored the transformative role of AI in optimizing various aspects of the radio air interface for next-generation wireless networks. The contributions are organized into four key areas:

- **AI-Driven Waveform and Coding.** Leveraging AI in waveform, modulation, and coding design offers substantial improvements in SE and reduces transmission overhead. Through machine learning techniques, systems can evolve these elements to meet the demanding requirements of future wireless environments.

- **AI-Based CSI Acquisition.** Advanced techniques for AI-based CSI acquisition and compression are introduced, which can significantly enhance network SE while minimizing the feedback overhead. These solutions are especially advantageous in dynamic network scenarios, and it has been shown that it is possible to design solutions that can operate also in multi-vendor scenario.
- **AI-Based MIMO Transmission.** AI is applied to optimize MIMO transmissions, from power control and user pairing to antenna management. These enhancements unlock potential for more efficient communication schemes, including pilot-free transmissions, and introduce flexible strategies for maximizing throughput and user QoS.
- **AI Solutions for Hardware Impairments.** Finally, AI provides innovative solutions to manage power amplifier non-linearities and other hardware impairments, ensuring stable performance in the presence of distortion or non-ideal components. These AI-based compensations allow for higher efficiency and robustness in practical system implementations.

In summary, this chapter highlights the significant potential of AI to address critical challenges in waveform design, CSI acquisition, MIMO transmission, and hardware compensation. By adopting AI-driven strategies, future wireless networks can achieve enhanced SE, reduced overhead, and improved system robustness, paving the way for a more capable wireless infrastructure.

8 Joint communications and sensing

This chapter is a continuation of works presented earlier in [HEX224-D43, Ch. 7], which included six works, four of which are continued in this deliverable. Hence, this chapter focuses on 6G's JCAS from two perspectives, namely JCAS deployment scenarios and JCAS resource optimisation. In the former category, the chapter investigates various modalities and enablers of JCAS. For instance, Section 8.1.1 examines the integration of NTNs low-Earth-orbit (LEO) satellites and RISs to localize a terrestrial UE, which is a continuation of the work presented in [HEX224-D43, Sec. 7.1.1]. On the other hand, Section 8.1.2 investigates the performance of multistatic sensing to detect and localize unmanned aerial vehicles (UAVs) using terrestrial BSs, which is a continuation of the work presented in [HEX224-D43, Sec. 7.1.3]. Moreover, Section 8.1.3 examines the sensing capability of three frequency bands in an indoor bistatic scenario, exploring both sensing accuracy and resolvability. This is a new study that was not presented in previous deliverables. In the JCAS resource optimisation category, Section 8.2.1 continues the study started in [HEX224-D43, Sec. 7.2.1], which investigates how sensing range can be increased in bistatic scenarios by adjusting the CP of OFDM systems. Section 8.2.2, on the other hand, continues the work presented in [HEX224-D43, Sec. 7.2.3], which investigates the procedures and protocols involved in inter-UE bistatic sensing, covering various aspects that include discovery, encryption, synchronization, and sensing. Before delving into the content of the chapter, it is worth noting that two JCAS works, namely "integrated monostatic and bistatic sensing" and "resource allocation for six degrees of freedom (6DoF) tracking in RIS-aided scenarios", were presented and finalized in [HEX224-D43, Sec. 7.1.2 and 7.2.2], respectively, and will not be covered in this chapter. In summary, authors of the former work emphasised that by sharing information between monostatic and bistatic sensing, an enhanced sensing performance can be achieved. Hence, they explored utilisation of extended Kalman-Poisson multi-Bernoulli sequential filters to tackle the associated sensing challenges and to periodically fuse user states and maps derived from both sensing modalities. In the latter work, authors derived the intrinsic Cramér-Rao bound (ICRB) to benchmark six-dimensional (6D)—three-dimensional (3D) position and orientation localization in 5G/6G systems. Building on this, they designed two filters (pose fusion and error-state Kalman filters), which have shown significant improvements in tracking accuracy.

8.1 JCAS deployments

8.1.1 NTN and RIS-aided localization

Problem statement: In this work, localization of a static UE in an urban scenario is explored, utilising a single LEO satellite and a single RIS in a single-input single-output (SISO) system. The UE and the LEO satellite are assumed to have both a clock bias and a carrier frequency offset (CFO).

Methodology: A low-complexity multi-stage estimator is proposed to estimate the channel parameters and the position of the UE under random and beamforming (BF) RIS scenarios.

Results: Figure 8-1 shows the Cramér-Rao lower bound (CRLB) and the proposed estimator's performance for BF and random RIS configurations across SNR levels. Overall, the estimator reaches the CRLB at high SNR. Notably, for most parameters, BF enables the estimator to reach bounds at lower power than with random configurations, with BF configurations providing ~20 dB higher SNR on the RIS path. However, the effect varies across parameters. For instance, satellite-path delay estimation shows slight improvement at high SNR with random configurations due to RIS-path interference, while BF enhances RIS-path delay and AoD estimation, which also benefits position estimates. This suggests a bottleneck in RIS-path estimation, calling for further research on improvements, such as using so-called STAR-RIS or active RIS. Additionally, there is a small CRLB gap for BF and random configurations in position and time bias estimation but not in CFO estimation, which suggests that CFO estimation is more dependent on the quality of the satellite-path Doppler. Lastly, the RIS-path Doppler estimator surpasses the bound due to usage of a RIS-path Doppler estimator.

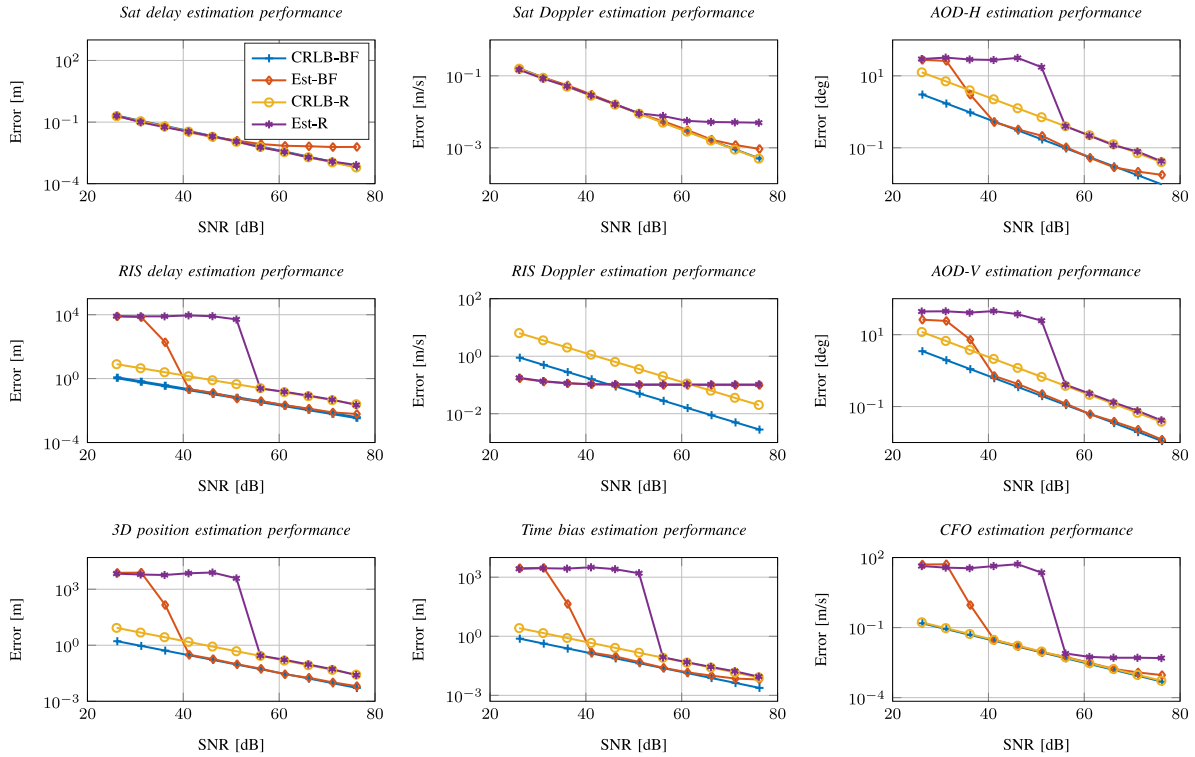

Figure 8-1: Simulation results of the estimator's performance with beamforming (BF) and random RIS configurations versus the CRLB of each scenario.

8.1.2 Multistatic sensing

Problem statement: For radar sensing, unlike to conventional radar deployments, where a limited number of dedicated and usually powerful sensors are strategically placed in space, the emerging field of JCAS establishes performance promises by means of reusing the network infrastructure and the occasionally present UEs. This is due to the increased probability of LoS between a target and the candidate sensing nodes, and the intrinsic diversity of a sensing involving a larger number of nodes. Motivated by this, we aim to provide an assessment of the performance of 3D positioning of UAVs from an urban cellular JCAS deployments.

Methodology: We focus on a scenario where a UAV is flying over London and its position is being estimated by a JCAS deployment. The considered JCAS deployment is composed by one transmitter and multiple spatially distributed receivers. Both the transmitter and the receivers are BS. The considered evaluation is theoretical and is undertaken using the RMSE metric of the estimated 3D positioning. In more detail, in the first step, for each local observation (receiver), the standard deviation of the positioning error is bounded using the Crammer-Rao bound (CRB). Note, that, a 10 dB margin is applied in order to account for the idealities of the CRB. This is done only for the case where there is a LoS links between the transmitter and target and the target and a receiver. While, in the absence of LoS, no sensing is undertaken using NLoS links. In the second step, using the standard deviations of the local observations, the overall performance of the considered multi-static sensing is assessed.

Results: In Figure 8-2(a) and (b), the performance map and the CDF of the predicted RMSE of the 3D positioning are given, respectively. This is done for a flying UAV over London. For the considered scenario, the inter-site distance (ISD) is 400 m. The utilized waveform is OFDM with a sub-carrier spacing of 30 Hz and utilized bandwidth of 30 MHz. The carrier frequency is 3.5 GHz. The BSs acting as sensing receivers are supplied with antenna arrays of size of 8×8 following a model given in [38.901]. In addition, a beamforming gain of 18dB is considered for the receiving BS, whereas there is no beamforming gain for the transmitting BS. Finally, the assumed target is a small UAV with a radar cross-section (RCS) equal to -17 dBsqm flying at an altitude of 300m. The joint inspection of Figure 8-2(a) and (b) shows that the predicted RMSE ranges between few cm, in places with good coverage, up to slightly higher than 4 m, in places with low coverage. As shown in Figure 8-2(a), for most of the considered region, the predicted RMSE is below 3 m. Exception to

this is some regions where the predicted RMSE reaches above 3 m. Furthermore, note that, as shown in Figure 8-2(b), the 50% percentile occurs at approximately 2 m.

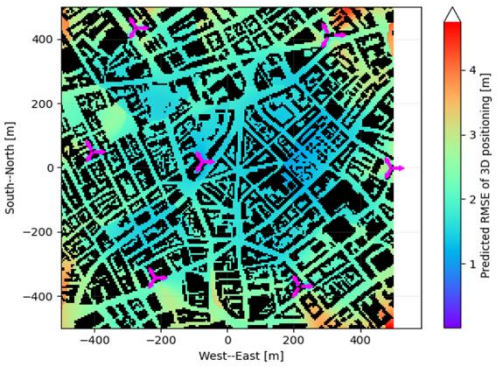

(a) Performance map for UAV flying over London. (Sensing is not performed in the black regions)

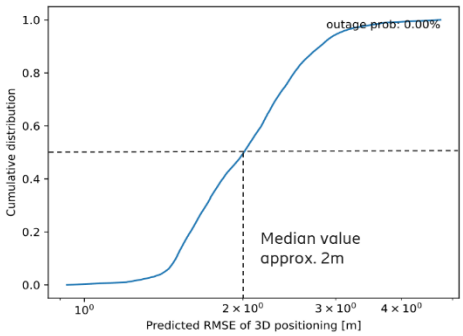

(b) CDF of UAV flying over London

Figure 8-2: Performance results for the estimation of the 3D position of a UAV flying over London.

8.1.3 Evaluation of bistatic sensing performance in indoor scenarios

Problem statement: This work investigates the performance of 6G bistatic sensing in detecting targets in indoor scenarios under three frequency bands, namely 10 GHz, 60 GHz, and 100 GHz.

Methodology: To examine the sensing performance in indoor scenarios, a MATLAB simulation environment (3D) was built, which consists of a transmitter and a receiver in a room (50m by 50m by 5m). A single target was placed in the room according to a predefined xy-grid (i.e., fixed z-axis at 2.5m for the Tx, Rx, and the targets in the grid). The transmitter and the receiver perform beam sweeping to scan the room over a number of OFDM transmissions (i.e., one Tx-Rx beamforming pair per transmission). The simulation was repeated for the three frequency bands highlighted above. The bandwidth and number of antenna elements were changed with every frequency band according to Table 8-1. The CRLB was then computed for each target placement and presented in a heat map (across the grid) and a CDF plot for each frequency band.

Table 8-1: Simulation configurations.

Frequency	Bandwidth	Tx antennas	Rx antennas
10 GHz	95 MHz	2x2	2x2
60 GHz	760 MHz	4x4	4x4
100 GHz	1520 MHz	8x4	4x4

Results: Figure 8-3 shows the generated heatmaps and CDFs of the target PEB of the three scenarios. Colours of each heatmap is divided into three categories, (i) white, (ii) black, and (iii) colours between blue and yellow. White blocks are areas that cannot be sensed because of geometry, and thus, are not affected by the radio configuration, and are not included in the CDF computations. For instance, white areas include areas that are behind the Tx and the Rx (i.e., targets that are outside the field of view (FoV) of the arrays) as well as targets that are exactly in the middle line between the Tx and Rx. Black coloured tiles, on the other hand, correspond to areas that can be sensed, but cannot be resolved from other paths. For instance, the black area surrounding the midline between the Tx and Rx cannot be resolved from the LoS path. Likewise, black areas surrounding walls cannot be resolved from paths that reflect off these walls. Resolvability in this case refers to resolvability in time domain (i.e., delay estimation) and angular domain (i.e., horizontal angles of arrival and departure). For an area to be deemed non-resolvable, it needs to be not resolvable in all domains. Unlike the white regions, unresolvable regions are related to the radio configuration of the Tx and the Rx, and hence, should be included in the CDF. For instance, delay resolvability is dependent on the bandwidth while horizontal angular resolution depends on the number of antennas present in the horizontal axis of the Tx and the Rx. For any unresolvable area, the position error bound is set to the maximum positioning error that can be incurred in a 3D room, which is equivalent to the distance between the centre of the room and one of its corners. The rest of the colours of

the heatmaps (i.e., blue to yellow) represent the target PEB according to the colour-bar attached to each heatmap. It can be seen from the figures that path resolvability is at its worst under the 10 GHz configuration, due to the limited bandwidth and number of antennas. Hence, at 10 GHz, only 60% of the room could be sensed, and an error of 0.1m can be achieved for 58% of the time. Increasing the frequency to 60 GHz yields a great sensing gains, as it can resolve paths within 86% of the room, and can achieve 0.1 m of error for 80% of the time. Increasing to 100 GHz yields a slight increment, as it increases the resolvable area of the room to 92% and can achieve 0.1m of error for 85% of the time. It is worth noting that hardware impairments, which are more pronounced at such high frequencies, were not included in the CRLB derivations, and thus, these results are optimistic. Additionally, the Tx power used for these simulations was set to 60 dBm (for all cases), which is considerably high compared to the current 5G standards.

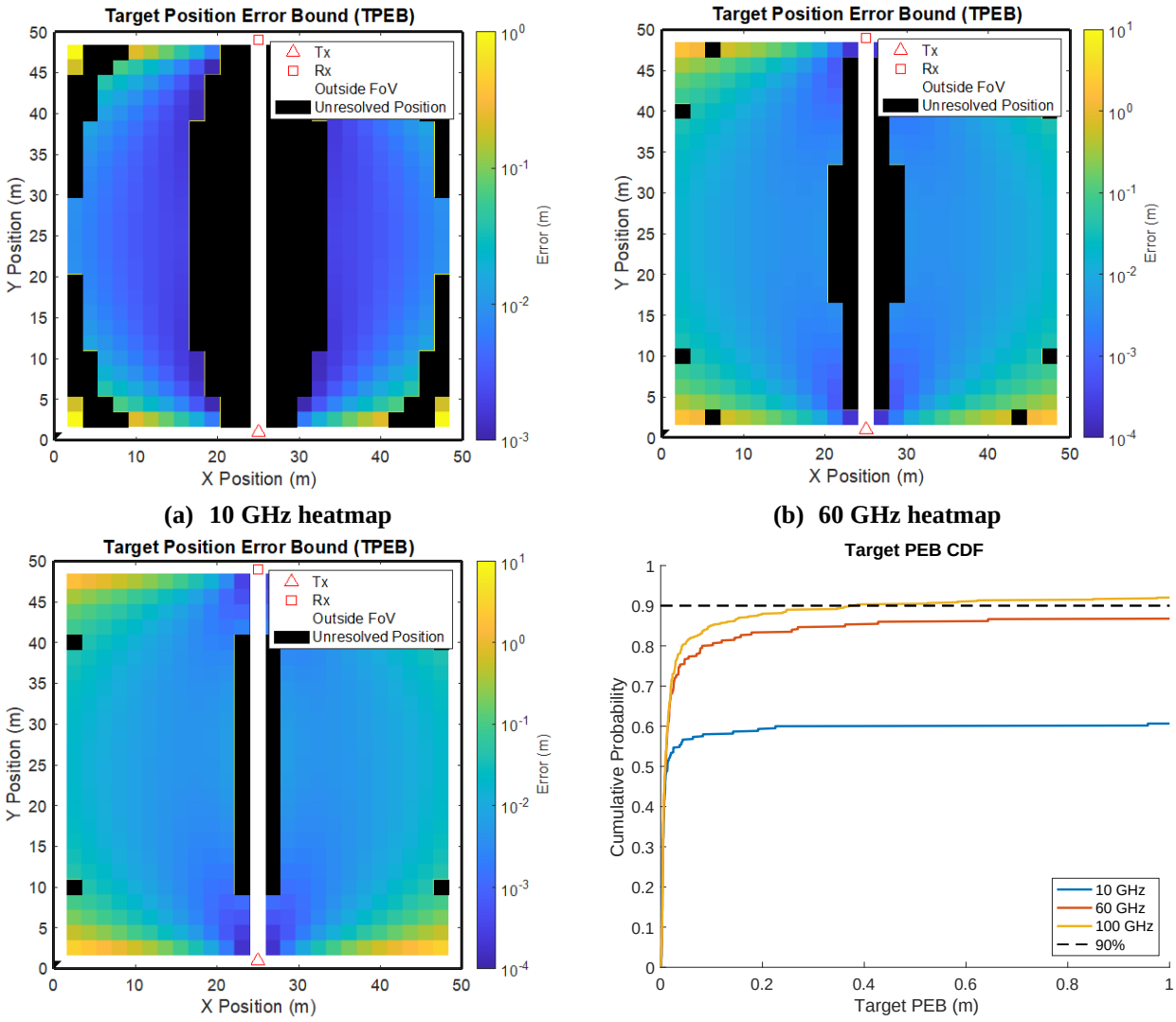

(a) 10 GHz heatmap **(b) 60 GHz heatmap**

(c) 100 GHz heatmap **(d) Target PEB CDF**

Figure 8-3: Heatmap and CDF performance plots of an indoor bistatic sensing scenario.

8.2 JCAS resource optimization

8.2.1 Optimization of OFDM-based bistatic sensing

Problem statement: For legacy and implementation purposes, the OFDM waveform appears as a strong candidate for the forthcoming sensing functionality of the future 6G networks. Furthermore, in terms of sensing deployments, bistatic sensing avoids the need for full duplex operation. In terms of sensing performance in a JCAS network, a dynamic bistatic deployment, where the sensing nodes are adaptively selected from the plethora of the permanently (BSs) and occasionally (UEs) present nodes, attains a better probability for

establishing LoS propagation between the sensing nodes and the targets of interest. Based on this background, in this contribution, aim to increase the maximum permittable sensed bistatic range distance and consequently the maximum permittable sensed Rx-target distance, when the legacy NR OFDM waveform is used for bistatic sensing.

Methodology: In OFDM-based bistatic radar sensing, which is aligned with the NR legacy, for sufficiently high receive SNR, the main parameter that limits the maximum permittable sensed bistatic range is the length the CP. This because the difference of time-of-flights (ToFs) for the propagation between the longest and shortest bistatic path needs to be less than the duration of the CP. In this contribution, for increasing the maximum permittable sensed bistatic range, we redesign the structure of the sensing pulse to increase the maximum permittable sensed bistatic range, without violating the NR nominal structure. In addition, a semi-analytical framework is used for the assessment of the maximum permittable sensed Rx-target distance of the considered nominal structure and its redesigns.

Results: For being aligned with the nominal legacy, the sensing pulse needs to be designed in a way that it can be fitted in one or multiple OFDM symbol durations of a NR or NR variant slot. In addition, the non-sensing OFDM symbols needs to be able to follow the predetermined communication structure where a (small) portions of its samples are allocated for the CP and the rest of the sample are used for the transferred payload. Figure 8-4(a) presents three sensing signalling designs: i) nominal NR OFDN structure; ii) nominal NR OFDM symbol structure with extended CP; and iii) double OFDM symbol transmission with nominal NR structure. The last two designs aim to increase the maximum permittable sensed bistatic range distance. The first modification of the nominal NR structure assumes that the sensing pulse is an OFDM pulse with CP. The OFDM symbol duration is the same as the nominal case. However, the CP duration is extended by taking time from the payload transfer duration (non-CP part). The second modification assumes that the sensing pulses has the duration of two nominal OFDM symbols. In this case, the CP duration is one nominal OFDM symbol duration (including CP) plus one nominal CP duration, while the actually used samples for sensing have the duration of one OFDM symbol (without CP). Note that the last design can be implemented using the same size of discrete Fourier transform (DFT) as the nominal case.

The evaluation of the maximum permittable sensed Rx-target distance is given in Figure 8-4(b)-(d). The evaluation is undertaken for the case when: i) the nominal CP duration is the one adopted by NR for a normal CP duration for the numerology with μ={0} (defined in [38.211]) and ii) the positions of the receiving and transmitting node in the local coordinate system (LCS) of the Rx is at $[100, 0, 0]^T$ and $[0, 0, 0]^T$ (in m). Here, θ and ϕ represents the zenith and azimuth angle of the receiver in its LCS, respectively. From the observation of Figure 8-4(b)-(d), it is concluded that, in OFDM-based radar sensing, the smart pulse design (combination of OFDM symbols and their corresponding CPs) overcomes the hard limitations, with respect to the maximum permittable sensed range, set by the length of the CP.

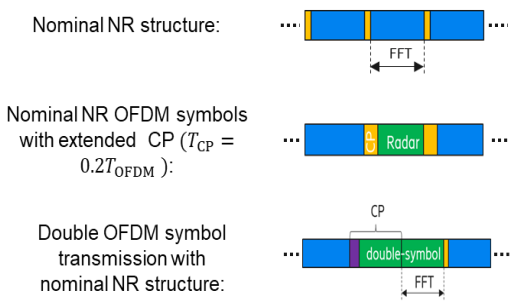

(a) Sensing transmission using the: i) nominal NR OFDN structure; ii) nominal NR OFDM symbols with extended CP; and iii) Double OFDM symbol transmission with nominal NR structure

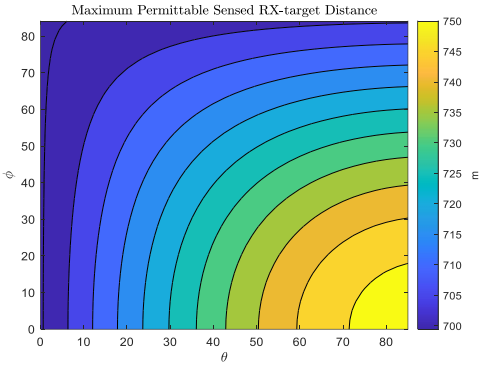

(b) Nominal NR OFDM symbols design

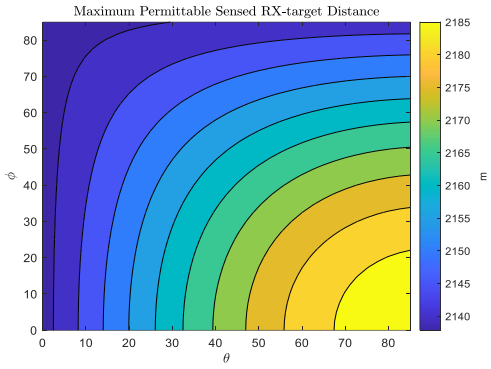

(c) Nominal NR OFDM symbols with extended CP ($T_{CP} = 0.2T_{OFDM}$), where T_{CP} and T_{OFDM} is the duration of the CP and the whole OFDM symbol, respectively.

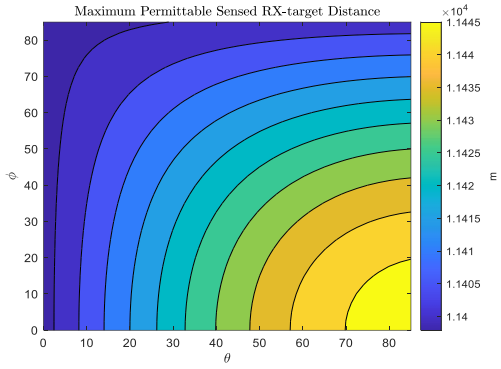

(d) Double OFDM symbol transmission with nominal NR structure

Figure 8-4: Evaluated maximum permittable sensed Rx-target distance for the nominal and the proposed modifications of sensing transmission.

8.2.2 Resource allocation and protocols for inter-UE sensing

Problem statement: This contribution focuses on a bi-static device-to-device ISAC scenario, where two devices collaborate to detect and locate an object or device-less person. Both devices might be without network coverage and in a Global Navigation Satellite System (GNSS)-denied environment.

Methodology: Individual steps from scratch are considered, starting from a discovery process up to the actual sensing process, and security and privacy aspects of the procedure and protocol are discussed.

Results: Discovery facilitates direct communication between nearby devices without relying on cellular networks. The process involves two phases: the initiator (device A in Figure 8-5) listens for discovery signals while devices seeking discovery transmit signals periodically. Discovery can use 3GPP or non-3GPP technologies but assumes out-of-network coverage, making assistance information unavailable. The process concludes when device A identifies device B through its signal, extracting its identifier and quality metrics such as SNR. Discovery operates without encryption.

To secure communication between devices, encryption is implemented post-discovery. Recommended protocols include transport layer security (TLS) 1.3 or QUIC plus TLS for establishing encrypted connections. These protocols utilize efficient, single round-trip-time handshakes comprising "Client Hello," "Server Hello," certificate validation, and key generation steps. Robust cryptography and authentication prevent impersonation attacks. Once encrypted, all data exchanges between the Coordinator (initiator) and Cooperator remain secure.

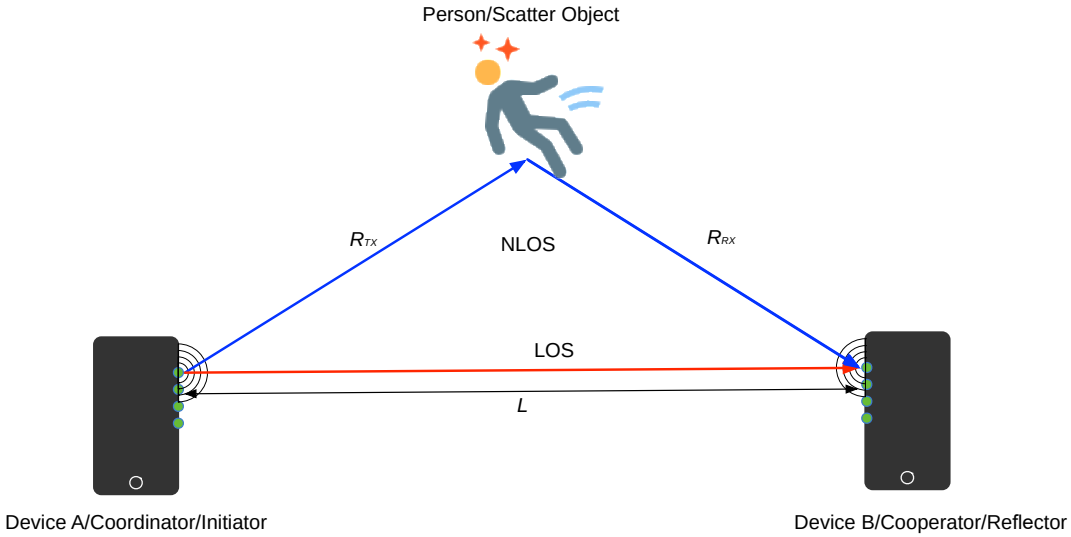

Figure 8-5: Bi-static sensing.

Following encryption, the initiator compiles a list of potential cooperators and assesses their synchronization and sensing capabilities to choose the most suitable partner for the specific application. The initiator may request a general list of capabilities or specify parameters of interest. Responding devices can disclose all capabilities or limit information to requested features, preserving privacy. The geometric configuration, ensuring objects are within the bi-static sensing region, also plays a role in selecting collaborators. Once chosen, the cooperator agrees on a compatible configuration, enabling the establishment of the sensing link.

This step involves phase-based ranging (PBR) using a minimum of two frequencies and a single antenna, with scalability to multiple antennas and frequencies. Frequency offset is first measured and corrected, followed by two-way exchanges of frequencies to synchronize and perform ranging. Several mechanisms are implemented to mitigate ranging security risks.

After synchronization and ranging, bi-static sensing begins. Device A transmits sensing waveforms, and device B processes and analyses received signals for range, AoA, and Doppler frequency. This process relies on earlier configuration agreements, incorporating factors like antenna setups, waveforms, and bandwidth.

From a security perspective, bi-static setups offer unique advantages. Attackers targeting device A may fail to locate device B, reducing jamming effectiveness. However, unintended reflections from other objects or individuals may be captured during the sensing operation. Secure encryption ensures data confidentiality, restricting information exchange to devices A and B, both of which have consented to the operation. Techniques like waveform randomization, frequency hopping, and secure configuration negotiation further protect against spoofing and unauthorized interference. More details about the methodology can be found in Section A.4.

8.3 Summary

In this chapter, JCAS for 6G were explored, focusing on deployment scenarios and resource optimisation. Initially, NTN and RIS-aided localization were analysed, and a multi-stage estimator was proposed for localizing a static UE in urban environments. It was highlighted that BF configurations significantly enhance estimation accuracy compared to random configurations, particularly in estimating RIS-path delay and AoD. Subsequently, multistatic sensing for UAV detection using urban cellular infrastructure was examined. It was demonstrated that 3D positioning accuracy is heavily influenced by coverage, with the predicted RMSE ranging from a few centimetres to just over 4 meters in low-coverage areas. After that, a study on the sensing efficacy of three of 6G's frequency bands in indoor bistatic scenarios was presented. It was shown that indoor scenarios require higher bandwidth and count of antennas to be able to resolve closely packed multipath signals and achieve adequate sensing accuracy. However, achieving high sensing accuracy comes at the expense of utilizing high transmission power and resources, which might not be available in reality. In the resource optimisation analysis, OFDM-based bistatic sensing was studied, and modifications to the CP design were

proposed to extend the maximum permissible bistatic range. These adjustments, such as extending the CP or utilizing double OFDM symbol transmission, were shown to effectively overcome traditional CP limitations. The chapter concluded with a study on inter-UE sensing protocols for bi-static ISAC, where key stages like discovery were emphasized, and challenges related to security and privacy were addressed, providing a foundation for practical implementations in GNSS-denied environments.

9 Flexible spectrum access solutions

Spectrum is valuable and scarce resource. The success of 6G will rely on the ability to leverage existing frequency ranges and the availability of new suitable spectrum enabling macro-cellular deployments to satisfy the requirements of new use cases.

Coexistence between TNs and NTNs will be a key aspect both from spectrum and global coverage point of view. When it comes to potential new 6G spectrum, the possibilities for successful spectrum sharing with fixed satellite services (FSS) UL within the 7-15 GHz range are of great interest. Furthermore, the integration of TN and the NTN is foreseen as an important component to achieve global coverage. Due to the ever-rising demand for spectrum, 6G TN and NTN might need to coexist in the same band, e.g., within the S-band. Even though the NTN would be serving users outside the TN coverage area, the NTN transmissions could still be interfering TN UE.

The mobile industry is starting to focus on how 6G, as a single global standard, can build upon the 5G wireless system foundation to enable further economic growth in a sustainable way. As in 5G rollouts, spectrum availability is a crucial element for future 6G networks. However, 5G deployments already occupy a large portion of the licensed spectrum with the most favourable coverage and capacity properties, also known as FR1 in 3GPP parlance. In practice, this means that flexible and unencumbered solutions allowing the deployment of 5G and 6G RATs in overlapping FDD and TDD spectrum is crucial to ensure broad network rollouts that deliver consistent wireless connectivity from Day-1.

6G is expected to provide low latency access in various deployment scenarios. Since sub-THz APs are expected to be deployed in locations where legacy omni-directional RAT in lower frequency spectrum are available, such co-location can be leveraged and coordinated to speed up spectrum access. Finally, the ability for 6G to reliably predict and proactively react on various types of interference scenarios can be highly beneficial, to guarantee stringent reliability and latency requirements of ultra-reliable low-latency communication (URLLC) services.

Previously finalized studies within this flexible spectrum access area are summarized below:

- TN-NTN Spectrum Sharing in S-Band using stochastic geometry [HEX224-D43, Sec 8.1.2.2]: investigated the impact to DL coverage probability and average data rate of a TN that shared the spectrum with a LEO NTN in S-band. Two co-channel coexistence scenarios from [38.863] were considered. Both scenarios assume FDD bands, but the NTN generated interference affecting the TN DL arises from the satellite-to-earth links (e.g. NTN n256 DL 2170-2200 MHz) in one case and from the earth-to-satellite (e.g. NTN n256 UL 1980-2010 MHz) in the other case (direct and reverse pairing scenarios). Stochastic geometry tools led to exact expressions and results that provided direct insights on several parameters associated with the integrated network such as the satellite altitude, the location of TN users, transmission power of BSs and satellites, traffic load, and ISD, paving the way for appropriate dynamic pairing mechanisms that could be further developed and standardized for 6G.
- Interference prediction-based proactive resource management [HEX224-D43, Sec 8.4]: This work considered proactive management of inter-cell interference with the goal of support URLLC. The proposed approach included decomposing the interference signal into multiple component signals and then applying a transformer model to predict them individually. The resulting outage performance presented in [GSM+23] is found to outperform conventional resource allocation approaches presented in existing literature.

9.1 Spectrum sharing and coexistence

Historically it has been good enough using relatively simple methods for determining conditions for sharing spectrum. As the demands for access to spectrum resources increase it becomes more important to accurately know the boundaries for sharing to avoid overprotecting services and thus wasting spectrum resources. Going forward we will see more and increasingly complex studies.

9.1.1 Assumptions and models to determine sharing possibilities with fixed-satellite service earth stations

Problem statement, scope: For upcoming 6G deployments in the upper mid-bands, i.e., in 3.8-4.2 GHz, there are already fixed satellite services (space-to-Earth) links deployed. Understanding the possibilities for successful coexistence is key for utilizing these bands. The existing models for evaluating coexistence are based on a) conservative, e.g. envelope antenna patterns and b) static interference models that does not tack into account the variable (bursty) traffic patterns of 6G systems. This leads to unnecessarily large separation distances. If we could more accurately evaluate the interference it will be possible to calculate more accurate separation distances and consequently spectrum could be more efficiently used.

Methodology and assumptions: We compare the separation distance in a baseline scenario with two cases with successively more refined models.

In the baseline scenario (Figure **9-1**(a)) we study the impact of a single 6G base station on an FSS (satellite receiver) if they both use the same channel. To be specific we determine the required separation distance around the FSS receiver to achieve an I/N < -10.5 dB less than 20% of the time and an I/N of less than -1.3 dB 0.005% of the time. The FSS antenna used is the 32 m antenna in Fuchstadt (Germany). It is pointing at the geostationary orbit, relatively low over the horizon (8.4 degrees) and has a peak gain of 61 dBi. In the baseline the antenna is modelled using ITU-R S.465.

The 6G base station is pointing directly at the FSS receiver. The BS has an 8x8 antenna array with a peak EIRP of 51 dBm. The BS is serving UEs in a hexagonal cell with a cell range of 400 m. The equivalent cell activity factor is 37.5%.

For the first step of model refinement (Figure **9-1**(b)), the ITU-R S.465 model is replaced by a parabolic reflector radiation pattern [Orf16, Ch. 18.9 Circular apertures]. In this case Bessel functions provide a mathematical description of the electromagnetic fields within parabolic reflectors as used by FSS earth stations.

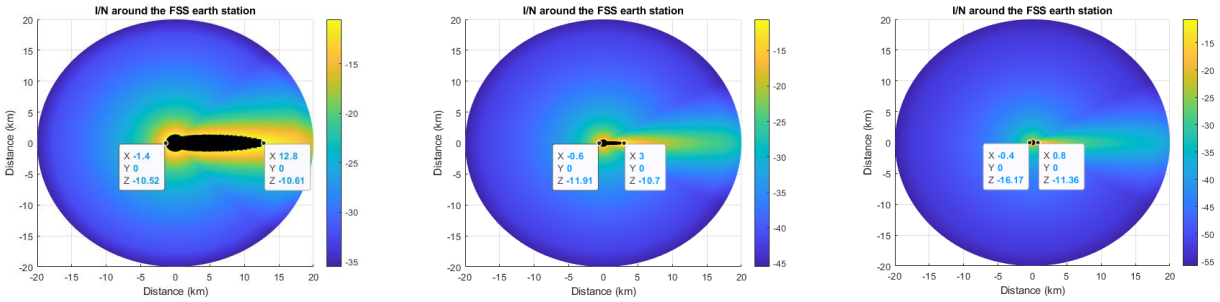

(a) **(b)** **(c)**

Figure 9-1: The darkened area indicates locations where the FSS ES long-term protection criterion is exceeded (I/N = -10.5dB). (a) Using conservative parameters for studies (b) Using more accurate FSS ES radiation patterns. (c) Using more accurate FSS ES radiation patterns and UE deployment for certain scenarios.

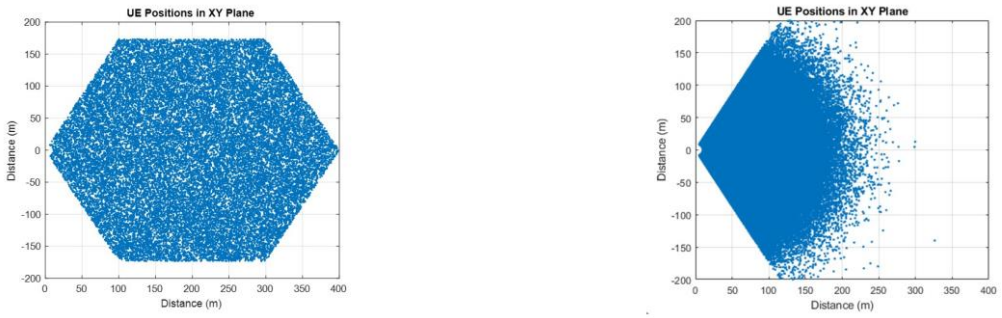

(a) **(b)**

Figure 9-2: UE deployment: (a) uniform distribution and (b) Rayleigh distribution.

In the second step of the model refinement the uniform UE distribution is replaced by a Rayleigh distribution as shown in Figure 9-2. This distribution represents the UE locations in a hotspot more closely. The results are shown in Figure **9-1**(c)).

Results: The resulting exclusion zones are shown in Figure **9-1**. We see that the necessary maximum separation distance is reduced from tens of kilometres to just below one kilometre. Although not shown here the trend is similar for other FSS antennas and 6G BS parameters.

The evaluations highlight the importance of more detailed models when evaluating sharing scenarios between FSS and 6G. If too conservative models are used and applied when deploying 6G networks the available spectrum will be inefficiently used.

9.1.2 Spectrum sharing between 6G and FSS UL in the centimetric range

Problem statement, scope: Additional spectrum from the centimetric range (7-15 GHz) is identified as essential for realizing the high demanding use cases envisioned in future 6G networks [STK+23]. However, since this frequency range is already used for FSS and fixed services (FS), the future 6G networks should be able to share the spectrum with them. This study will focus on investigating the spectrum sharing possibilities between 6G and FSS UL. More specifically, the study will evaluate the level of the interference received at LEO satellites (receiving in UL), caused by the 6G base stations (transmitting in downlink) located within the spot beam of the satellite, see Figure 9-3.

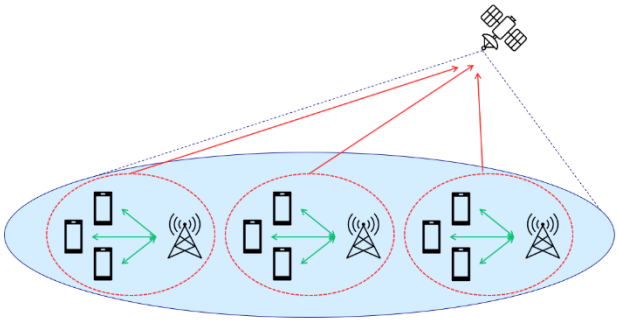

Figure 9-3: Schematic overview of the coexistence scenario, where the victim is the satellite. Several International Mobile Telecommunications (IMT) BSs serve UEs in the footprint of the satellite (in blue). The green lines represent the communication between the BS and UE, and the red solid line.

Methodology, deployment considerations: To study the impact of a mobile system on the FSS UL in the centimetric range, the following frequency ranges are considered: 12.75-13.25 GHz (UL for SpaceX Starlink Gen 2 and OneWeb Phase 1) and 14-14.5 GHz (UL for SpaceX Starlink and OneWeb Phases 1 and 2). After the outcome of WRC23, these frequency bands are not of immediate interest for 6G, compared to for example 6.425-7.125 GHz and 7.125-8.4 GHz, but the conclusions remain valid, and they will be useful for an eventual further future IMT identification.

This study utilizes numerical evaluations to estimate the level of the average cumulative interference towards the victim satellite, caused by a large number of 6G BSs simultaneously serving users within their respective service areas. The numerical evaluations have been performed for two different deployment alternatives. In the first one, the shared frequencies are used within urban macro cells (high-power macro-BSs deployed above the rooftops), while in the second one the shared frequencies are used within urban hotspot cells (medium-power micro-BSs, deployed below the rooftops). In both scenarios, the victim satellites are assumed to be located at an altitude of 550 km. A more detailed description of the overall evaluation methodology, and the assumed models and parameter values can be found in [HEX224-D43].

Results: Figure **9-4** shows the main results. As can be noticed, the received interference, expressed here as the I/N ratio, would typically be reducing together with an increasing elevation angle. This is mainly due to the reduced emission levels from the BS antennas and to a smaller extent the reduced number of interfering 6G BSs because of the reduced size of the satellite footprint. The impact of the latter is reduced considerably because, as the elevation angle is increased, the slant distances and hence the corresponding path losses between the victim satellite and the interfering BSs are reduced. It is also important to note that elevation

angles below 20-25 degrees are not interesting for the assumed co-existence scenario because they are typically not used by systems with large satellite constellations. The situation would be different for satellites with geostationary orbits (GEO), since they would need adequate protection also for the lower elevation angles.

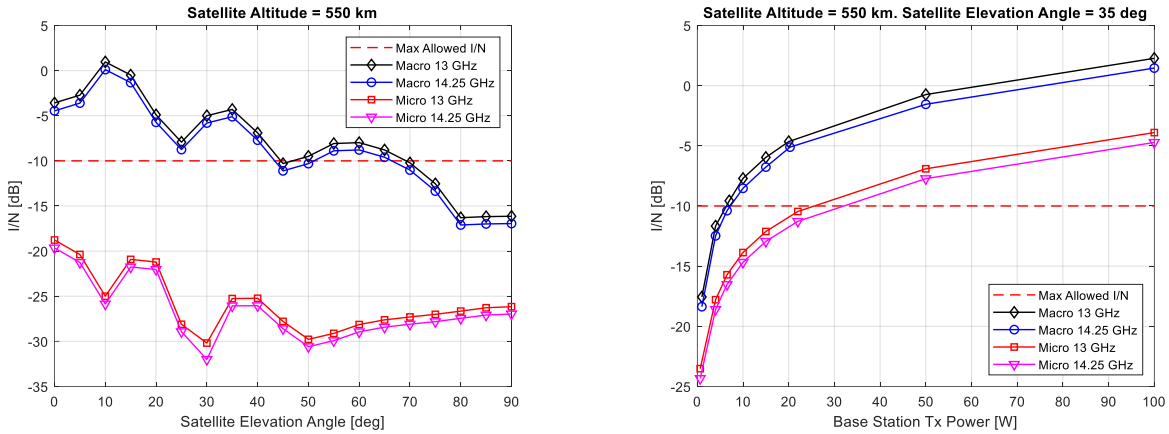

Figure 9-4: Left: Received I/N for the different deployment alternatives. Right: Received I/N for different BS transmission powers when the elevation angle is assumed to be equal to 35 degrees.

The results in Figure **9-4** indicate that co-channel spectrum sharing is not feasible for the macro-BS deployment, unless the BS power spectral density is reduced below 6 W/200 MHz. However, a low output power would make it very challenging to deliver a service capable of satisfying the requirements of the future 6G network. At the same time, the results demonstrate that co-channel spectrum sharing would be feasible for the micro-BS deployment. This is due to the lower BS output power and the additional shielding ("clutter loss") offered by the surrounding buildings when the BSs are deployed at a lower height.

As a summary, if the shared frequencies are to be used in a typical urban macro deployment, the sharing solutions need to address the high interference levels caused by the antenna sidelobes. Different approaches can be explored: use of databases, advanced beamforming methods (e.g., creating a "null" towards the victim), improvement of the 6G BS antenna to reduce emissions above the horizon, adaptive downlink power control to reduce the transmission power for the most harmful beams, spectrum splitting and increase of the victim resilience making sure that satellite antennas can be made to tolerate more interference.

9.2 Multi-RAT Spectrum Sharing

Problem Statement, scope: Optimal spectrum for macro-cellular environments, i.e. offering desirable capacity and coverage properties, is valuable and scarce. Capacity augmentation through network densification is not always an economically viable or sustainable solution either. Reusing the existing network site infrastructure with new spectrum is vital for network planning and cost efficiency. In [HEX224-D43, Sec 8.1.3], we provide a more comprehensive list of requirements and justification for recommending MRSS as an integral part of the Day-1 6G radio design.

Methodology: The evaluation was carried out via advanced system-level simulations allowing a thorough investigation of MRSS DL performance for FDD and TDD bands (Figure 9-5). Full-buffer and best-effort broadband traffic have been considered. The configurable number of NR and 6G UEs per cell controls the load offered to the system. To focus solely on the MRSS performance, carrier aggregation (CA) is not considered in the simulations. For the sake of conciseness, the system model details presented in [HEX224-D43, Sec 8.1.3] are not repeated here. The interested reader can find detailed simulation parameters in Section A.5.

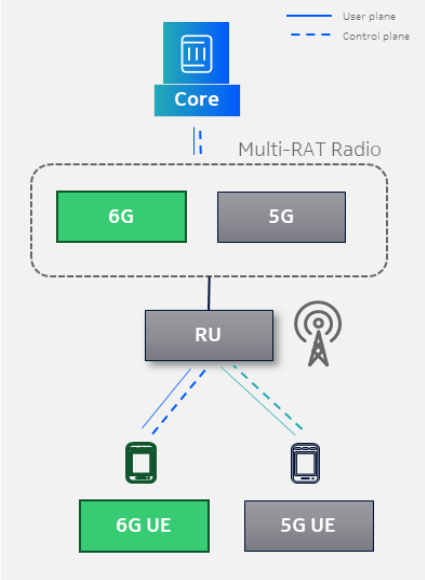

(a) Dynamic baseband capacity allocation between 5G and 6G.

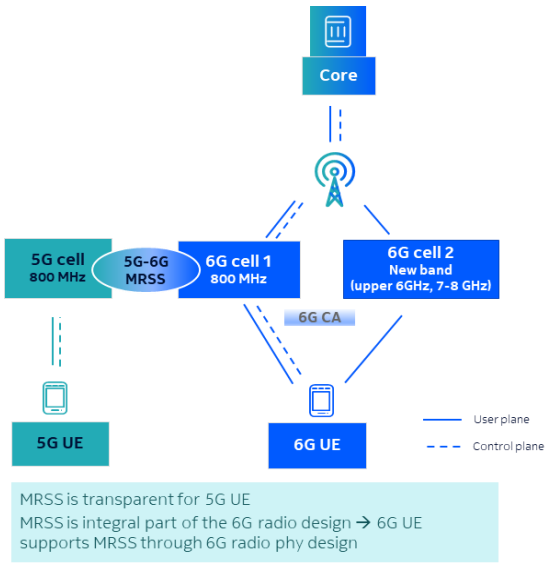

(b) 5G-6G MRSS is easily deployable on any of the existing FR1 FDD and TDD carriers

Figure 9-5: Migration with Standalone 6G System and MRSS.

Results: Figure 9-6 shows a comparison of normalized mean DL cell for a full buffer scenario when 70% of the UEs are legacy NR devices and the remaining 30% are 6G devices. In all cases, aggregate carrier capacity, i.e. NR plus 6G throughputs, is considered. The 4 main cases are:

i. **5G NR only:** baseline
ii. **Joint scheduler (JS) and NR-only control overhead:** the scenario assumes full reuse of the NR control signalling by 6G (lower bound for additional 6G control overhead).
iii. **JS and NR+6G control overhead:** the scenario assumes doubling the NR control signalling (upper bound for additional 6G control overhead).
iv. **Static spectrum refarming:** Carrier bandwidth is split equally (50%-50%) between NR and 6G.

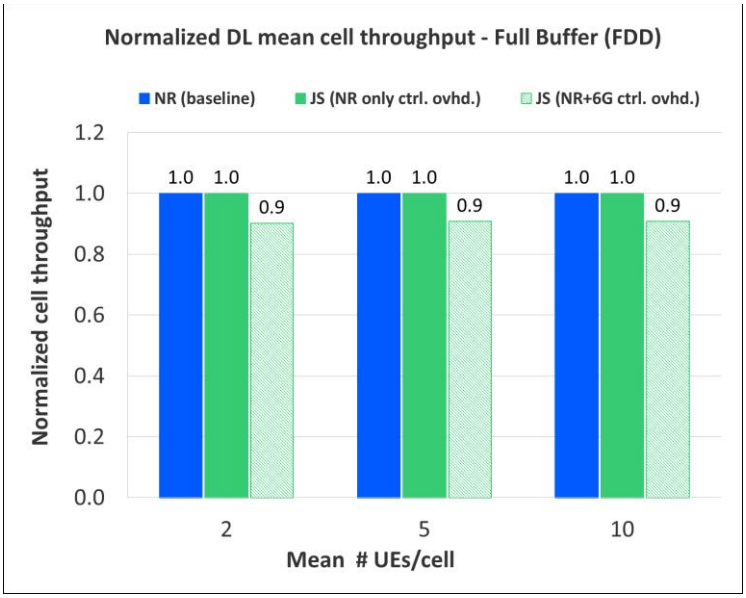

Figure 9-6: Normalized mean DL cell throughput at 800 MHz FDD.

The system simulations results show that MRSS outperforms static refarming. The benefits of MRSS vs. static refarming are especially visible when loads in 5G and 6G are unbalanced. Impact to cell throughput is small, up to 10%, under the worst-case assumption that 6G control overhead is equal to NR control overhead.

Figure 9-7 considers bursty traffic instead of full buffer. The well-known FTP3 traffic model (defined by packet size and mean inter-arrival time parameters) is employed. In Figure 9-7(a) FDD is considered, while Figure 9-7(b) depicts TDD performance. The x-axis shows the mean cell throughput while the y-axis represents the mean UE throughput. It can be noticed that MRSS is highly efficient for FDD and TDD bands. It clearly outperforms static refarming (grey line) across the entire range of offered traffic loads. The small gap between the solid and the dashed green lines is due to the different overhead assumption (ii-iii) previously described. It can be noticed that the maximum cell throughput degradation is further reduced to 3.7%. for bursty broadband traffic.

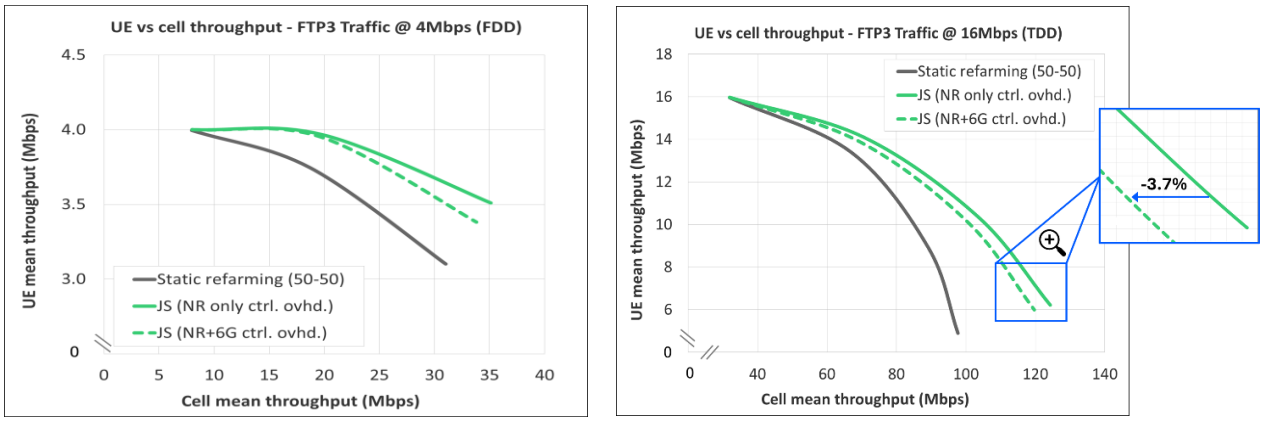

(a) Regular FTP3 Traffic Model (FDD). **(b) Data-intensive FTP3 Traffic (TDD).**

Figure 9-7: Evolution of DL mean cell and DL mean UE throughputs for FTP3 traffic model.

Conclusions: The 5G-6G Multi-RAT Spectrum Sharing (MRSS) mechanism allows dynamic sharing of FDD and TDD carriers between 5G and 6G RATs. Even in the worst case, cell throughput impacts are small and limited to 10%. However, deploying 6G with enhanced radio performance on the same carrier as 5G through MRSS will lead to further SE and throughput gains. The benefits are expected to be further amplified as 6G traffic starts to dominate.

9.3 Low-latency spectrum access

Many services require low-latency spectrum access. Sub-THz characteristics as well as localised services require rethinking of spectrum access. Non-coordinated or coordinated access methods can be applied in sub-THz spectrum. Both have up and downsides. While non-coordinated access has low overhead and can accommodate low amounts of burst traffic efficiently, it suffers from collisions with high amount of traffic and does not provide sufficient QoS. On the other hand, coordinated access typically has inflexible frame structure, high overhead for maintaining the connection, and high delays for initial access. This section presents potential low-latency access solutions aiming to solve both coordinated and non-coordinated access technics.

For coordinated access, a Booster RAT approach is presented, where the downsides of coordinated access are addressed by utilizing an omni-directional RAT for initial access, including transmission and QoS requests and transmission schedule.

For non-coordinated access, risk-informed random access is investigated as a new spectrum access paradigm. Non-coordinated risk-informed random access to localized communication can augment scheduled access, if the risk for interference is expected to be low. Interference assessment is central as it helps in understanding potential risks and their occurrences during sharing.

9.3.1 Sub-THz booster RAT: on-demand access scheme configuration

Problem statement. Coordinated spectrum access has several downsides. First, the resources for initial access should be reserved in a frame separately from the resources for data transmissions. The optimal dimensioning of the frame becomes thus a complex problem of anticipating the demands of new connections and the demands of data transmission of existing users and weighting the trade-off. In practical systems, it often results in under-dimensioning initial access and associated high latencies. Additionally, coordinated access carries high

overhead for bursty traffic with low inactivity periods, where maintaining the connection and maintaining the beams consume considerable amount of power and system resources.

Proposed solution. It is proposed to address these downsides by making use of an omni-directional RAT in addition to a directional higher frequency range RAT. Omni-directional RAT is used for initial access as well as to collect initial transmission requirements. These requirements, along with the knowledge of currently active and already connected devices, are used to configure an optimal access scheme on-demand.

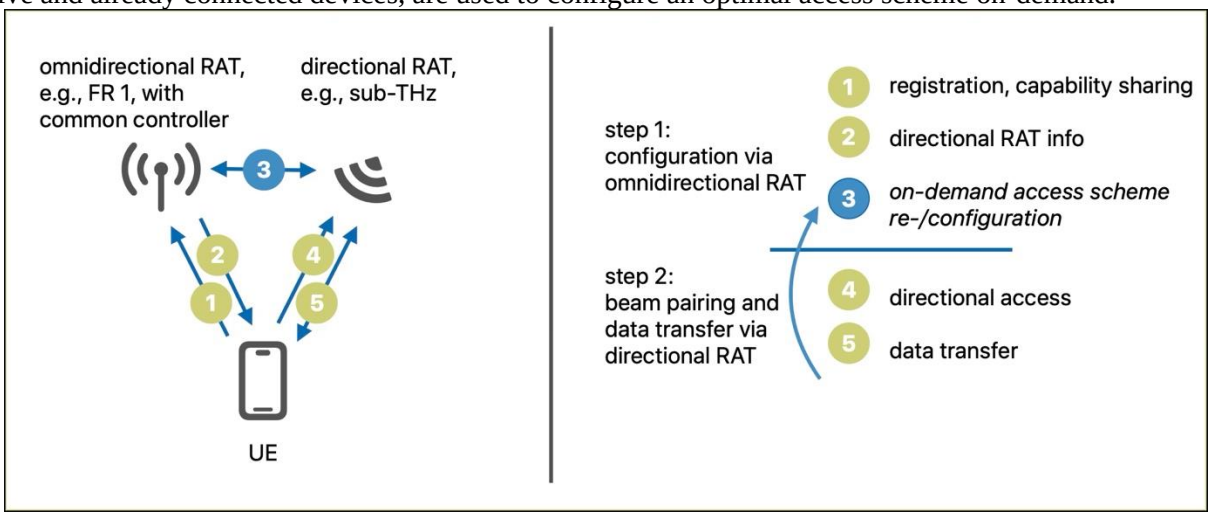

Figure 9-8 Booster RAT Operation with dynamic (re-)configuration of the access scheme.

A Booster RAT operates in two main steps, as illustrated in Figure 9-8. In step 1, access control and configuration via omni-directional RAT is performed. First, UE registers and shares its capabilities and initial transmission demands (if any), e.g., as a buffer status report. If the demand on data volume is low to medium, data-traffic is transmitted directly via the omni-directional RAT. If UE has high amounts of traffic, the controller may decide that a new UE is allowed to access the directional RAT and proceeds to provide the associated information to the UE as well as to inform the directional RAT AP about UE's request. Based on the provided UE information and knowledge about the utilization of the directional RAT, the common controller can optimally configure the directional AP and tailor the current access scheme (e.g., number of access slots, data slots, beam alignment slots) as required to satisfy UEs' latency and data rate requirements. The access scheme can be further tailored and reconfigured during the operation, either based on changing demands of already connecting UEs or based on the information about newly connecting UEs.

Results. Pre-configuration of the directed access avoids conflicts between multiple registered UE and allows a tailoring of the sub-THz access point parameters to the targeted access latency. For a bandwidth of 10 GHz and a set of optimized parameters a data latency in the range of 100–150 µs can be achieved. While the latency within the data period could be further reduced, the limiting factor for the worst-case latency is the repetition and duration of the detection and response period. A frequency-domain decoupling of beam search and refinement from the data period can further reduce latencies.

The two-step approach allows a complete tailoring of the access scheme and AP parameters. For instance, the registration of new UEs to the sub-THz high speed service can be used to exactly match the number of access slots to the number of users. Furthermore, also the data period can be tailored in parallel to guarantee the required data-rate and latency for each UE and dataflow. A change of the initially requested data rate or latency can also be handled via the omni-directional RAT and then lead to an optimum adaption of the access point and scheme parameters.

9.3.2 Risk-informed random access

Problem statement, scope: Spectrum sharing policies usually consider several worst-case assumptions and ignore sites specific contextual which could significantly improve the spectrum usage on use scenario basis. Risk aware interference assessment helps in determining likelihood and consequence of each hazard which can be used to select protocols and fine tune used configurations.

Methodology: The efficiency of spectrum sharing policies and mechanisms is emphasized in high density deployments where two or more radio technologies share, co-operate or compete over same spectrum. IEEE standard 1900.5.2 [SB15, IEEE21] for spectrum consumption models (SCMs) provides a generalized method for modelling spectrum consumption of any type of use of radio spectrum. SCMs are meant to describe boundaries of spectrum usage of a radio vice to facilitate dynamic selection of spectrum resources across a large number of devices. SCMs are used for determining the compatibility of spectrum use between devices (transmitters and receivers) or systems such that interference boundaries of the shared spectrum users are not violated. SCMs are described in machine readable (XML based) language to facilitate automatic compatibility assessment. The compatibility assessment of SCMs considers locations of the devices being assessed, as well as any overlaps in time and frequency of the use and in case of interfering transmitters the analysis follows a typical link budget computation.

The risk aware spectrum access [Dev15] continues from where SCMs typically stop. Namely, it builds on assessing the impact of a risk of violating interference protection criteria and the amount of tolerable risk in a given situation. The impact of a risk is assessed against the expected loss of services performance in a particular context. In other words, risk assessment method complements SCM method to find out how serious a violation of interference protection criteria would be based on the consequence of the outcome of a violating event in each setting. It improves flexible spectrum use and utilization. It helps to select location and context aware MAC and PHY configuration parameters.

Risk aware interference assessment has the following four steps [VSD+17]:

1. Creation an inventory of significant harmful interference hazard modes;
2. Definition of consequence metric for severity of hazards;
3. Assessment of the likelihood and consequence of each hazard;
4. Aggregation of the results to inform decision making;

All impacting variable parameters should be used to represent “parameter space” as probability density functions or as cumulative distribution functions. These are used to quantify the contribution of each parameter to the overall risk. An extensive list of physical and logical domain parameters to be considered is provided in IEEE 1900.2.

Risk aware spectrum access analysis for technology co-existence in the same spectrum requires as inputs a pathloss or a channel model including the frequency, power, direction of signal propagation, geolocation, protocol, modulation schemes that would be used for identifying significant hazards (step 1). In step 2, metrics for consequences of the hazards, such as loss of profit, service outage, throughput degradation and throughput fairness are to be defined. Risk of harmful interference should be defined as a likelihood of a certain risk level to be exceeded, conditioned with information how often the event is expected to occur. In step 3, rough estimates of severity with likelihoods of consequences of interference are estimated that are then combined in step 4 to yield probability distribution for the metrics.

Since spectrum access in cellular networks is based on specific assignments of frequency bands to operators, intra-technology and intra-operator spectrum coordination and (dynamic) spectrum sharing can be built on considerably accurate SCMs and implemented in a coordinated manner by signalling access grants between the relevant network entities (e.g., PCell and SCell) over common control plane. However, inter-technology coordination, e.g., NR unlicensed (NR-U) - Wi-Fi, or NR-U – satellite, involve more heterogenous devices and loose coordination with unlicensed spectrum favouring distributed spectrum sharing mechanisms. Moreover, the inter-technology co-ordination of different incumbents calls for measures that are often location (e.g., needed protection zones), time, power and context depended. These types of settings benefit the most from risk aware spectrum analysis that can capture the spatial, time and frequency level dynamicity. The method has been applied to Wi-Fi - long term evolution (LTE) coexistence in [VSD+17] and to protect meteorological satellite earth stations from interference by cellular mobile transmitters in [DLT+17]. Considering sub-THz communication where the signal propagation will be limited by building structures and materials, the interference and sub-THz channel model of [HEX23-D23] is expected to be very dependent on the location, usage patterns, beam formations and beam directionality. The most prominent inter-technology coexistence cases are indoor and indoor to outdoor scenarios. Conservative statistical interference and path loss models will certainly be too restrictive, but the interference analysis should be based on measured and simulation-driven channel models to assess the risk of interference in a given use scenario.

Results: A critical factor to consider especially in inter-technology (e.g., sub-THz and Wi-Fi) spectrum sharing is the used listen-before-talk (LBT) mechanism as it impacts to transmission attempts, retransmissions and to the traffic load on the selected channel which then impacts to the expected interference. To assess the impact of LBT a simulation environment was created to evaluate ALOHA and carrier-sense multiple access with collision avoidance (CSMA/CA) based device-to-device communication in a shared frequency band, see details and results in [HEX224-D43]. The analysis shows that for ALOHA, interference and throughput are independent of each other, whereas for CSMA/CA, there is an exponential rise in interference with respect to throughput.

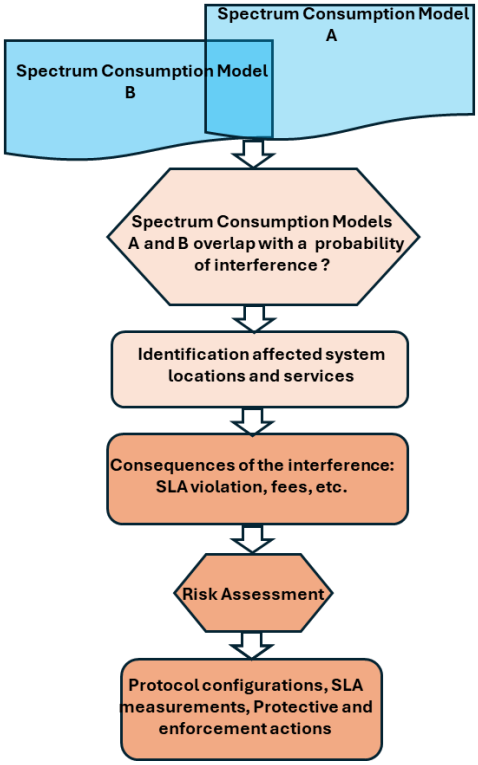

Figure 9-9: Risk aware spectrum access methodology.

9.4 Inclusive radio interface via TN/NTN enhancements

The seamless integration of NTN (including communication through satellites, high-altitude platforms, etc.) and TN will connect the entire environment of human activity. Within WP4 of the project, we have studied enhancements on specific key areas for inclusive TN/NTN radio interface (see Figure 9-10). A critical aspect for TN and NTN integration is the handover (HO) of users between cells. In satellite non-geostationary orbit (NGSO) scenarios, frequent HO (as perceived in legacy TN) of multiple, even stationary, UEs together will be unavoidable. This leads to significant signalling overhead, service interruption and energy consumption at the end device. Another key topic regards the interference between TN and NTN. The current spectrum allocations indicate high probability of TN and NTN radios operating in adjacent bands that could lead to mutual interference and consequent desensitization of TN and/or NTN receiver in a heterogeneous wireless node. Finally, HAPS offer flexible deployment options to cover specific areas, such as the Internet of Things (IoT) in remote regions or during emergencies and can be considered as a complimentary solution to satellite based NTN integration.

In the following, we present the proposed TN/NTN enhancements, and the conclusion of respective study items targeted to address the aforementioned key topics.

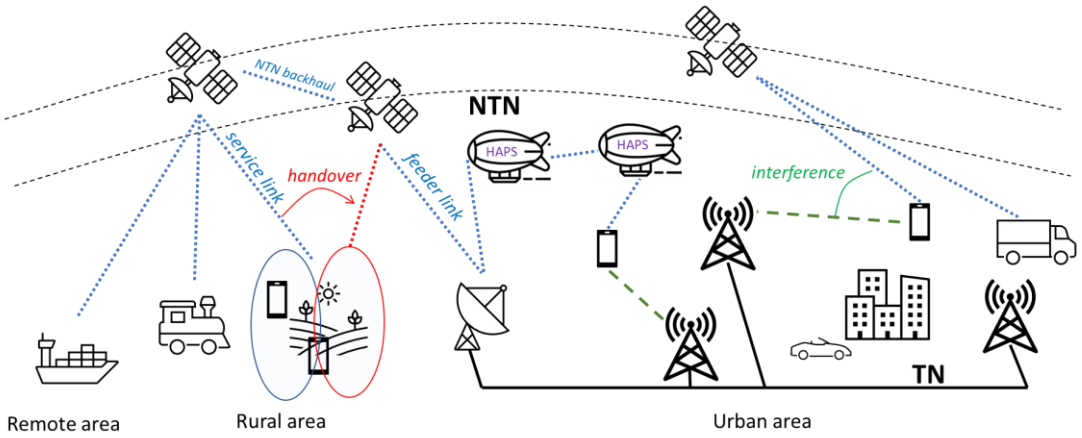

Figure 9-10: Hexa-X-II areas of TN/NTN enhancements for inclusive radio interface.

9.4.1 NTN handover methods

NTN-NTN HO can be predicted to some extent and new designs are considered compared to legacy NT networks, e.g., 3GPP R17/R18 specifies group-based HO or broadcasting of required neighbour cell specific information instead dedicated signalling. In this work, we investigated efficient designs for HO procedures that can also provide efficient directions for TN/NTN handover in 6G integrated architecture. The devised solutions include:

- **QoS-aware signalling of common information**. The key concept proposed is to omit HO common information in HO message when data is only sporadic or delay tolerant. It is also possible to omit common information, if parameters can be obtained from source cell during overlap time with target. This will reduce overall network signalling during HO preparation.
- **Random time-based conditional HO (CHO)**. The proposal here is to perform time-based CHO at a random time during the overlapping time period broadcasted by network. The solution addresses the problem of dense signalling when many devices concurrently need to perform random access for HO execution.
- **Satellite switching with "Physical cell ID (PCI) change only"**. The proposed approach avoids HO procedure altogether, addresses shortcomings of "PCI unchanged" solution specified in Rel.18 NTN, and is also suitable for low-complexity devices that cannot support dual-active protocol stack (DAPS).

The proposed enhancements, including their advantages and drawbacks, have been presented in detail in [HEX224-D43, Sec. 8.3].

An additional solution has been devised (and proposed to 3GPP for NTN Rel.18), regarding an issue we have identified in current specification of the soft switch case, where source and target satellites serve the same area simultaneously for a period during handover. It is reminded that, to ensure seamless communication, synchronisation signal block (SSB) transmissions provide timing information for devices. Hence, in the case of soft switch, a device has to receive SSB from both satellites in different timing to avoid interferences during the overlap time. The challenge arises due to the dynamic adjustment of SSB-timeOffset, either through shifting cell timing or altering SSB location, following the currently specified “PCI unchanged” approach. This impacts satellite measurement timing configurations (SMTCs) in both connected and idle/inactive modes (SMTC, when configured, defines when UEs shall measure the SSB of serving cell). In inbound mobility case (i.e., soft switch handover to a “PCI unchanged” cell), neighbour cells, broadcasting SMTCs for handover to the target cell, must update their timing after every satellite switch, which could occur as frequently as every 2 minutes. This frequent reconfiguration increases signalling overhead and may disrupt seamless transitions. Furthermore, in outbound mobility case, the serving cell's SMTC becomes erroneous when neighbouring cells do not align their timing. This impacts UEs moving out of the coverage area of the "unchanged PCI" cell. The frequent need for updating SMTCs in neighbouring and serving cells complicates synchronization and degrades performance, highlighting a significant limitation of the current soft switch approach.

The proposed solution of "**Temporary SSB timing shifting**" suggests refining the soft switch mechanism by applying the SSB-timeOffset only during the overlap period between source and target satellites (i.e., between t-serviceStart and t-service) as shown in Figure 9-11. This adjustment ensures no permanent changes to SSB timing, thereby, a) reduces signalling overhead by minimizing the frequency of SMTC updates, b) maintains synchronization with less interruption for UEs during handovers, and c) allows an easier transition from hard switch (where SSB location within cell timing does not change) to soft switch deployments.

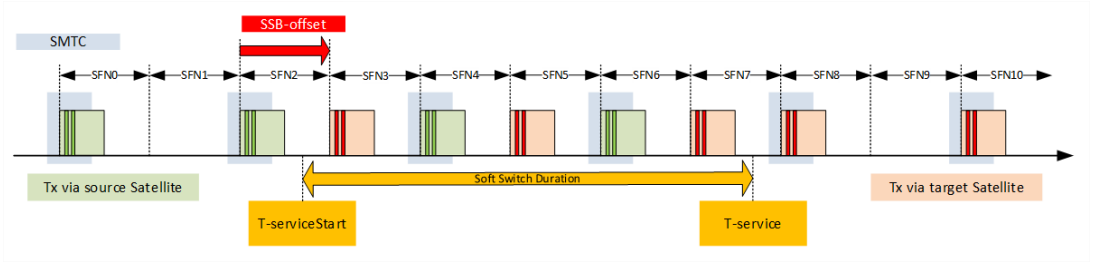

Figure 9-11: Temporary SSB timing shifting for soft switch without SSB timing change.

More detail on the identified issue of soft switch impact on SMTCs and the proposed solution can be found in [R2-2405680].

9.4.2 TN/NTN radio interference mitigation

Frequency spectrum allocated for 5G and 6G TN and NTN overlap in several bands and can lead to mutual jamming at a heterogeneous wireless node receiver. For example, Ku-Band NTN links could interfere with terrestrial bands in Frequency Range 3 (FR3), i.e., between 13 GHz and 15 GHz. Ka-Band (26.5 GHz to 40 GHz), Q-Band (36 GHz to 46 GHz) and V Band (40 GHz to 75 GHz) NTN links could interfere with terrestrial bands in FR2 (24.25 GHz to 29.5 GHz, 37 GHz to 43.5 GHz, 47.2 GHz to 48.2 GHz and 50 GHz to 71 GHz). In addition, new spectrum bands planned for 6G deployments, for example the frequency range between 7.125 – 8.4 GHz, are already used by other systems, e.g., by satellites (FSS) and fixed links (FS). Thus, it will be essential that 6G is able to share the spectrum with the incumbent users in the best possible way.

Mitigation of TN and NTN mutual interference through high-selectivity microwave filters alone cannot provide a solution, since the *Q* factors needed for resonators to build such filters would be unpractical to realize, and such filters would exhibit highly non-linear group delay characteristics which would affect the integrity of modulated signals. It is hence essential to evolve additional schemes. Depending on which frequency range is shared, the victim nodes and the most appropriate spectrum sharing mechanisms will differ (two different spectrum sharing scenarios are discussed in detail in Section A.6). External interference depends upon the locations and strengths of radio emitters in proximity to the wireless node of interest. Internal interference is typically caused by active circuits such as clock sources, LOs, RF amplifiers which can couple through several shared interfaces such as power supply planes and feed networks, clock distribution networks, chassis, etc. The primary receiver desensitization mechanisms include non-linear transfer functions of RF gain blocks, reciprocal mixing caused by phase noise of LOs, cross-modulation and harmonic mixing at the down-conversion stages. The proposed multi-pronged approach consists of a harmonious combination of antenna pattern management, circuit level management, handshaking, and signal processing techniques, depending on the type of interference being encountered (see Figure 9-12). In the following, we present the key aspects and interference scenario applicability for each approach, while more detail can be found in Section A.6.

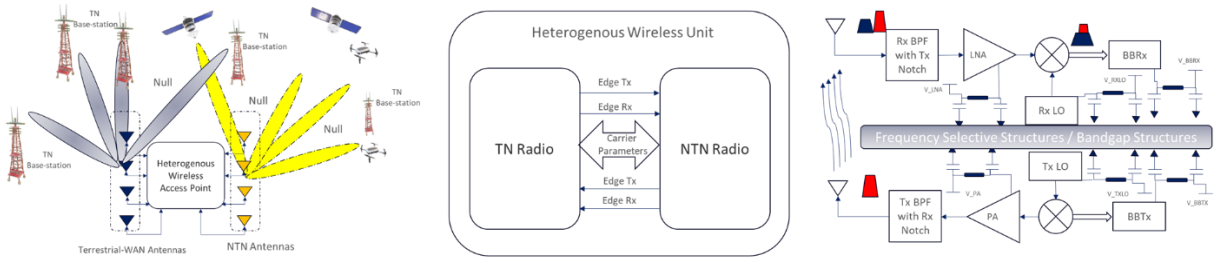

Figure 9-12: Multi-pronged approach to mitigate TN and NTN mutual interference. Antenna pattern management (left), Handshaking (middle), Isolation circuits, Signal processing (right).

Antenna Pattern Management: One way to mitigate interference from radiated signals desensitization (e.g., from TN base stations against weaker satellite signals, or from strong drone or LEO emitters towards TN receiver in fading) is to optimize the radiation pattern of the receivers for beam maxima in the direction of signal of interest and for a beam null in the direction of external interferers. In the simulated example of Figure 9-13, beam maxima are directed at elevation angles denoted by markers m1, m3, m4 and m5, while radiation nulls are directed at elevation angles denoted by markers m6, m7 and m8. These can be steered adaptively depending on operational requirements.

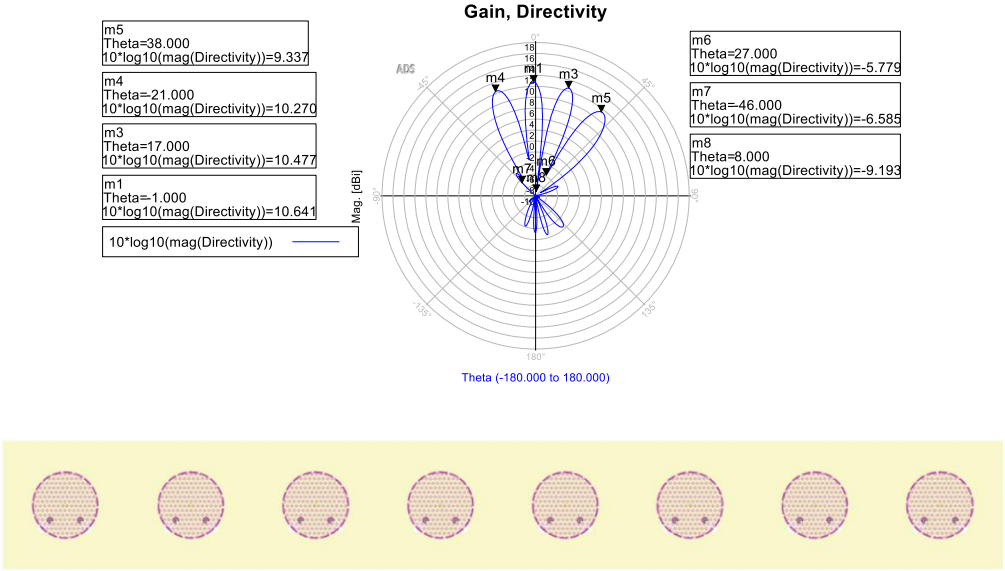

Figure 9-13: Antenna beam maxima and null in simulation example with an 8-element antenna array.

Modern adaptive tuning techniques, such as ANNs, could be applied to the beamforming algorithm to optimize the antenna array's excitation weights for two parameters, i.e., maxima and null.

Handshaking: TN and NTN radios could inform and update each other about their current or scheduled transmission/reception to enable smooth flow of traffic without outages. This is particularly applicable when the TN/NTN radios operate in adjacent bands, for a smooth co-existence of the two radios within the same entity. The information exchanged between TN and NTN radios could consist of current active receive frequencies, bandwidths, and modulation schemes, and could be done using shared registers.

Isolation Circuits: Significant media of mutual coupling between radios in a heterogenous wireless node include shared hardware modules such as power supply planes, clock distribution lines and ground planes. RF signals in the mm-wave spectrum can have several modes of propagation between conducting planes. One way to minimize coupling is by introducing electromagnetic band gap structures on shared circuits. A simulated example of a band gap structure that can be etched on power planes to minimize coupling in Ka-Band is shown in Figure 9-14.

Signal Processing: The impact of non-linear transfer functions (reciprocal mixing, mutual coupling through shared circuits and interfaces, coupling through antennas) can be reduced applying the techniques above, but cannot be eliminated. The extent of suppression of interference can be improved further by applying some signal processing. Adaptive filtering algorithms such as least mean squares filter, and AI/ML schemes can be applied to refine the interference cancellation schemes adaptively.

An intelligent combination of the above techniques depending on the interference scenario and field conditions is expected to be beneficial and can be investigated in future work. We finally note that it is essential to have the co-existence planned when the network infrastructure is designed. Handshaking between network nodes at time slots with high probabilities of mutual interference such as adjacent channel operation would aid smooth co-existence.

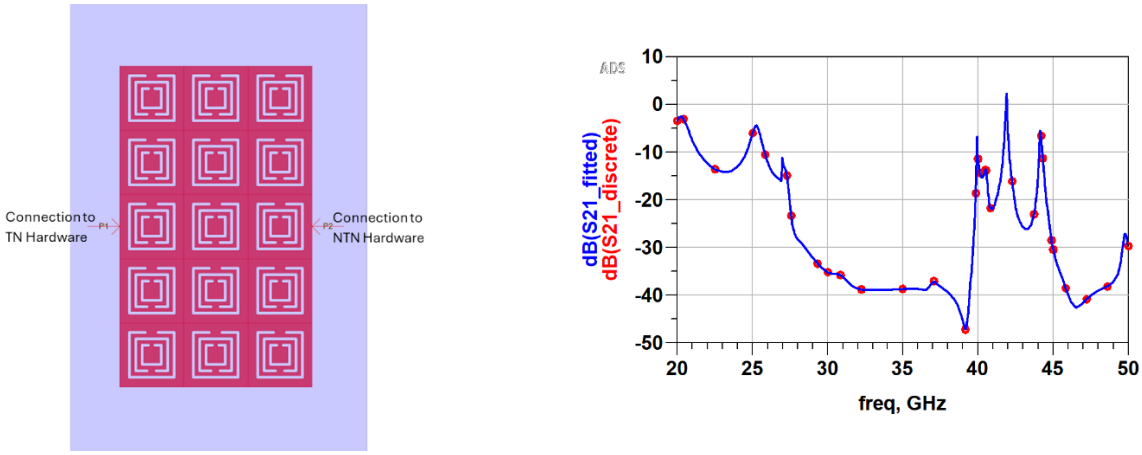

Figure 9-14: Isolation in Ka-Band through electromagnetic band gap (EBG) structure. Shared Power Plane with bandgap structures (left). Simulated isolation in Ka-Band (right).

9.4.3 Inclusive radio interface via high altitude platforms

Motivation: Despite the potential of TN/NTN integration through satellites, some limitations can come with the use of LEO satellites for IoT. For example, due to its non-stationary property, it is hard to guarantee the coverage of a specific area at a given time [BDO+21]. HAPS has been proposed as a complimentary solution that can address these challenges [KKA+21]. It provides better communication links with the lower path loss due to lower heights (from 8 to 50 km) and higher LoS than LEO satellites, which can be crucial for devices with limited power budget. On the other hand, its altitude still enables it to cover large areas with good LOS opportunities. Finally, HAPS can be maneuvered in a way to provide coverage to specific regions, for example, in case of hazards and emergencies.

Problem statement: In this work, we analyse and compare the feasibility and performance of the two low-power, wide-area networks (LPWAN) UL physical layer techniques, LoRa and long-range frequency hopping spread spectrum (LR-FHSS), on a HAPS IoT scenario. We split the analysis in two. First, we check the performance as a function of the distance between the IoT devices and the HAPS for different elevation angles. Second, we investigate the performance under collision for a different number of devices. For both cases, we consider different HAPS heights and its impact. We consider a shadowing plus fading model [CV94] that considers the elevation angle.

Results: Figure 9-15(a) compares the outage probability of a HAPS-mounted (solid line) and a satellite-mounted (dashed line) LoRa link for different spreading factors (SF). Increasing the SF enhances noise resistance, thereby extending the communication range, at the cost of lower data rates and longer transmission times. There is a significant performance gain with the HAPS-mounted link, especially for SF10 and SF8. This indicates that HAPS can provide more favourable link budgets, even when the elevation angle is higher. The maximum distance is set such that it represents the minimum elevation angle. Note that SF8 and SF10 cannot guarantee a reliability above 0.9 for most of the region for satellite-based connectivity. It should however be noted that this considers an idealized path loss model, indicating the theoretical performance upper bound. Nonetheless, such results help us to obtain insights into the relative performance trends and comparison between the two NTN solutions.

Figure 9-15(b) shows the performance of LoRa and LR-FHSS against collision as a function of the number of devices. The C_2probability indicates the probability that there are no collisions. However, the definition of collision changes from LoRa to LR-FHSS. For LoRa, we consider a collision anytime two transmissions overlap in time, i.e., occur simultaneously. Since LR-FHSS presents diversity mechanisms, we consider a loss due to collision anytime all headers are lost, or if more than a pre-specified number of fragments out of the total payload are lost. For the LoRa case, this probability can be evaluated with the ALOHA collision probability, which follows

$$C_{2(LoRa)} = \exp(-2N\lambda\rho), \quad \textbf{(9-1)}$$

where N is the number of devices, λ is the SF and ρ^{-1} is the mean arrival rate. For the LR-FHSS, one could use from combinatorial like in [UMA22] to derive it. However, the approximations might fail due to the increased amount of correlation between the subsequent replication of headers and payload fragments. Thus, we use of a discrete-event simulator to deal with C2LR-FHSS for the LR-FHSS case.

LR-FHSS presents a much higher collision immunity than LoRa [Sem22]. Although the different SF present a semi-orthogonal behaviour, meaning that there could be multiple devices with different SF, it is evident that its summed performance would not match the LR-FHSS.

In conclusion, we have shown through this initial (and somewhat idealistic) studies that there are potential benefits in terms of reliability and collision avoidance when considering a HAPS mounted IoT network. LR-FHSS is found to be a more robust access technology compared to LoRa. The findings are detailed in [SM25].

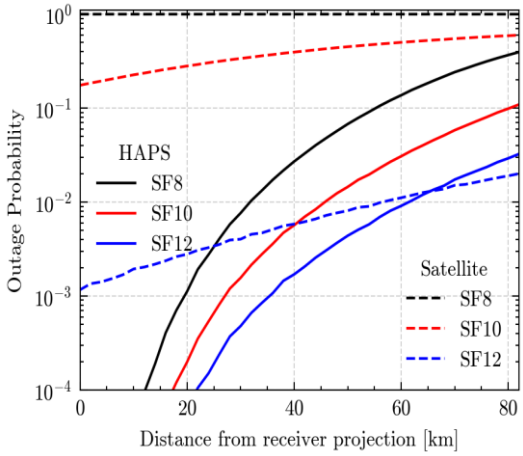

(a) HAPS vs Satellite: outage probability as a function of the distance from the cell centre for different spreading factors with LoRa

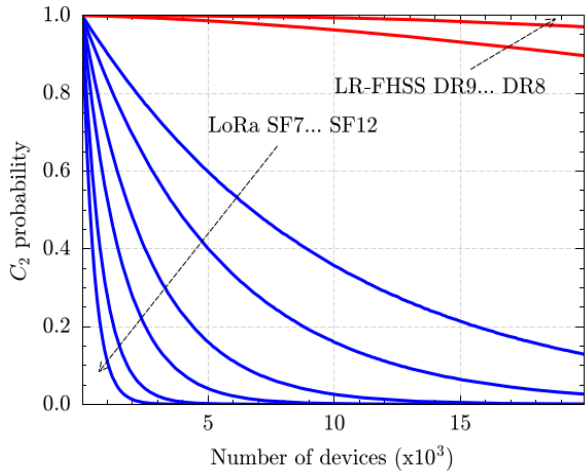

(b) LoRa vs. LR-FHSS: non-collision probability as a function of the number of devices

Figure 9-15: Performance analysis of a HAPS mounted IoT network.

9.5 Summary

In this chapter, enablers for efficient spectrum sharing, coexistence, and low latency spectrum access were studied. First, coexistence enhancements for satellite services were studied. For FSS ES (3–4 GHz, C band), it was shown that by taking more realistic assumptions into account, the required coordination distances between FSS ES and IMT BS can be reduced from tens to just few kilometres. For FSS UL (13–14 GHz, Ku band), it was demonstrated that additional sharing enablers are required, if a high BS Tx power is desired (macro deployments). Examples of potential enablers are null steering, spectrum splitting, scheduling restrictions, or power control. It was further shown that NTN coexistence can be supported by modem-internal measures like antenna techniques, circuit techniques, signal processing, common control of both radios.

The chapter also addressed potential enhancements of NTN efficiency. QoS-aware signalling of common information, random time-based conditional HO, satellite switching with "PCI change only" can improve efficiency of NTN HO procedures. The performance of HAPS in comparison to satellites was analysed and shown that HAPS can offer improved coverage and performance.

The chapter further considered spectrum sharing between new 6G deployments and current generation 5G deployments via MRSS. Initial simulation results suggest a worst-case control overhead (capacity loss) below 10 % compared to non-shared 5G NR.

To enable low-latency spectrum access, a coordinated access scheme for a high-band RAT utilizing a low-band omni-directional RAT was shown to potentially enable access latencies in the order of 100 µs. A risk-aware access can improve the reliability of local spectrum access in uncoordinated scenarios.

10 Trustworthiness

Trustworthiness is one the three core values targeted by Hexa-X-II. Trustworthiness is an inclusive concept encompassing different aspects, including security, privacy and safety. Trust establishment is based not only on mutual identification, but also on the security and privacy preservation capabilities established in the network. A trusted 6G network need to proactively identify risks and threats and take corresponding remedial actions to mitigate them. Hence, trustworthiness can be achieved through a trustworthy architecture design, covering security, privacy, and resilience. As opposed to 5G, 6G networks will be more distributed and diverse in terms of usage scenarios and offered services. These inadvertently leads to an expanded threat landscape as well, thereby requiring new approaches towards ensuring security, privacy, and resilience. A more inclusive trustworthy design that covers the entire lifecycle of communications networks is therefore required.

Different aspects of a trustworthy 6G radio design are explored in this chapter. The first section discusses the important and emerging concept of resiliency in future 6G and beyond 6G wireless networks and proposes a novel four stage resilient-by-design framework. The following two sections discuss specific examples of the implementation of this framework. Section 10.2 analyses the impact of jamming on the system trustworthiness and explores different techniques to counter jamming attacks, particularly through jammer localization. Subsequently, the security and privacy aspects of a general cellular JCAS system deployed for crossroad monitoring are investigated are in Section 10.3.

Previously finalized studies on trustworthiness are summarized below. The interested reader is referred to the respective section in [HEX224-D43] for further details.

- **Secret key generation for D2D communication** [HEX224-D43, Sec. 9.1]: This work investigated key generation in the presence of passive eavesdropping attack for D2D communication systems in use cases requiring low computation power, memory consumption. The key idea was to utilize the received in-phase and quadrature samples at the transmitter and the receiver to distil secret keys. Preliminary test bed results have shown that the proposed scheme can deliver satisfactory key rate (measured in kbps) at relatively low coding rates.
- **UE-related security aspects of JCAS** [HEX224-D43, Sec. 9.5]: While the threats to conventional communication systems are generally well-understood, introducing sensing capabilities as in JCAS adds a whole new attack surface that needs to be studied thoroughly to avoid potential risks, to establish trust and to prevent privacy incidents. The value related requirements for trustworthiness, security, and privacy are especially important for sensing in the vicinity of users that utilize their mobile devices to perform sensing since the sensing results contain sensitive data of the user that may straightforwardly be linked to specific devices and individuals, if no precautions are taken. Potential threats to such UE-centric sensing were explored in this contribution by evaluating and adopting attack schemes from ranging and sensing.

The solutions addressed in this chapter contribute to the project's overall Objective 3 (Enhanced connectivity for 6G services), and Objective 4 (Network sensing, compute, and AI for novel digital services), and *WP4 objective (WPO) 4.1: Develop an inclusive, trustworthy, and flexible radio design tailored to meet given 6G KPIs and KVI requirements through analysis and integration of HW architectures, transmission schemes and security solutions*.

10.1 Resilient-by-design framework for 6G

Problem statement: Recently, it has been agreed that 6G and beyond 6G wireless communication systems will be designed to be **secure**, **open** and **resilient by design**. This contribution focuses on *resiliency*, which enables a network to provide and maintain an acceptable level of service in the face of unexpected disruptions. A significant portion of the unplanned failures are induced by internal and/or external factors such as network glitches, disasters and cyber-security attacks. Such disruptions may incur a hefty cost in terms of network downtime, lost revenues and privacy & security breach, especially since they are often broader in scope and more dynamic in nature than random failures.

Methodology: The network's ability to avoid or cope with failures have traditionally been measured through reliability, availability and survivability. Resilience includes two aspects: maintaining the QoS in the face of

disruptions, and the quality of remediation or recovery from a failure [RH20]. Resilience will be especially important in future 6G and beyond 6G wireless networks given that many services will increasingly be offered by mission-critical applications that will need guaranteed performance with respect to various QoS and quality of security (QoSec) metrics. This contribution provides a comprehensive vision for resiliency in future 6G and beyond 6G networks by presenting a holistic framework for making 6G and beyond 6G networks **resilient-by-design** [MSP+24].

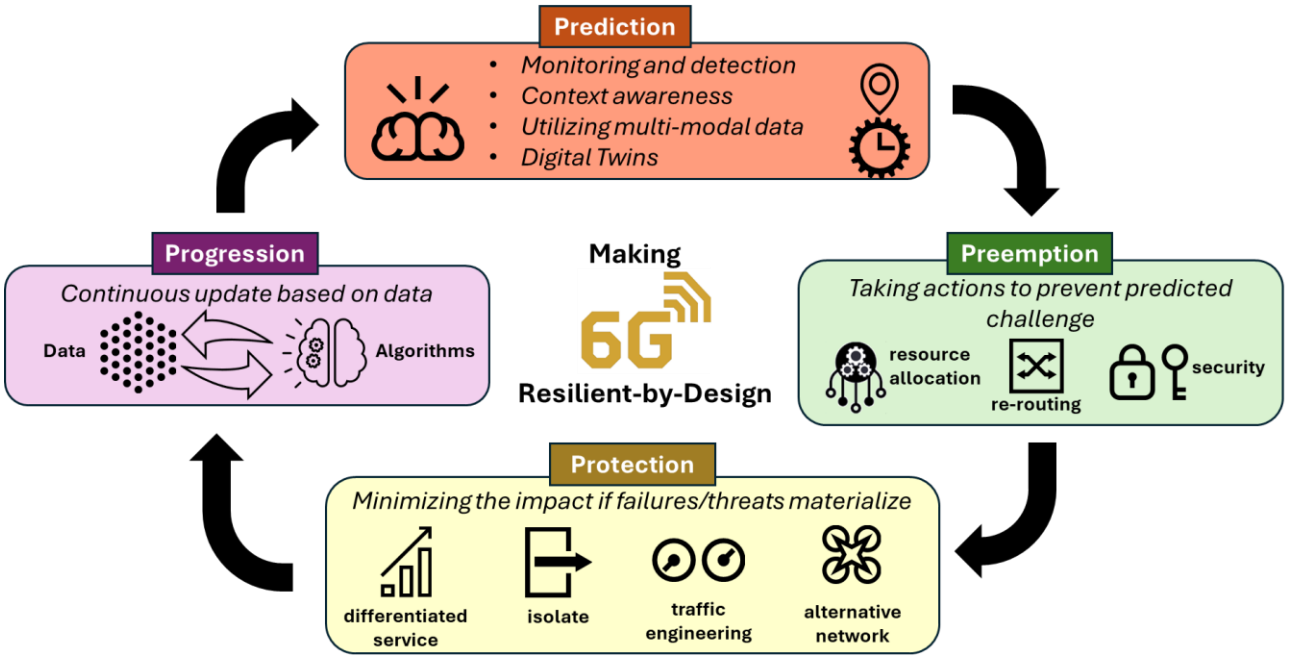

Figure 10-1: Illustration of the proposed resilient-by-design concept for 6G networks [MSP+24].

Result: We envision four different steps in making future 6G networks resilient-by-design, as illustrated in Figure 10-1 and further elaborated below.

A. *Predicting failures and threats*: Ensuring resiliency requires being able to continuously monitor, detect and predict failures, external disruptions and security threats. AI/ML tools can be applied for such prediction, albeit with some challenges in terms of scalability, generalizability and computational complexity. Fortunately, technological advances have made it feasible to accurately model the wireless environment, e.g., using a digital twin. Moreover, RIS has opened the paradigm of engineering the propagation environment, thereby transforming the random wireless environment into a controllable channel that makes it easier to monitor and detect failures.

B. *Preemption*: Once a risk is predicted, preemptive actions are required to address it. Examples of such preemptive actions include proactive resource allocation, centralized or distributed coordination schemes and redundancy measures. Different traffic flows with different service level agreements (SLA) can also be intelligently multiplexed to further enhance the efficiency and maintain an acceptable QoS despite future failure. Predicted node failures on a larger scale can be addressed by proactive rerouting of the traffic. In this case, the correlation / dependency structure between the different possible routes, and causal relation with contextual information needs to be considered to minimize the probability of the predicted failure impacting the rerouted path(s).

C. *Protection*: In the undesirable case that a failure or disruption or security breach occurs, immediate actions must be taken to address this disruption and minimize its impact on the network. These can include (i) isolation – the overall network architecture must be agile enough to isolate and remove subnetworks where a breach or failure occurred while distributing critical network functionalities to ensure that removing the sub-network does not impede operation of the remaining network; (ii) staggered service states – define different system states with different SLAs to ensure service continuity even if it is at a different (often lower) service level; (iii) traffic engineering – to proactively divert or block traffic from the affected parts of the network to protect from traffic surge; and (iv) novel network topologies – such a space, air and ground integrated networks which integrates

satellites, high altitude platform stations and unmanned aerial vehicles with the terrestrial network to provide continuity in service or minimize the disruption in case of failures [HEX25-D35, Ch. 4].

D. *Progression*: The final step's goal is to continuously upgrade and update the resilience mechanisms and the other three steps. This involves updating the underlying model parameters or even adopting new models or tools based on new training data to increase the prediction accuracy. Additionally, continuous monitoring of KPIs of interest can help in evaluating the effectiveness of the adopted preemptive strategies.

10.2 Jamming analysis

Most wireless networks are vulnerable to jamming attacks due to the openness nature of wireless channels. Jamming attacks are also easy to launch, making it urgent to secure wireless networks against intentional and unintentional jamming threats. Second, jamming threats can only be thwarted at the PHY layer but not at the MAC or network layer. When a wireless network suffers from jamming attacks, its legitimate wireless signals are typically overwhelmed by irregular or sophisticated radio jamming signals, making it hard for legitimate wireless devices to decode data packets. This section specifically delves into two aspects of jamming. Firstly, the impact of jamming attacks on network resilience in a coded system is analysed through experimental studies. Different jamming techniques are considered to allow a comparative analysis. The second work investigates blind techniques to localize indoor jammers. This work addresses whether an unknown malicious jammer can be accurately identified and located by only the received signal strength and waveform analysis.

10.2.1 Impact of jamming as a foundation towards resilience

Problem statement: With the increasing threat of jamming attacks on critical services, communication systems must maintain service quality in the presence of such interference. This study investigates the impact of various jamming types on a SISO OFDM system, specifically analysing the role of LDPC channel coding in enhancing resilience.

Methodology: Five types of jamming signals were tested on a SISO-OFDM system over an AWGN channel using BER simulations. The SNR was fixed, and the jamming-to-signal ratio (JSR) was varied to observe performance under different jamming strengths.

Results: The results are shown in Figure 10-2: BER simulation of a jammed OFDM system. Figure 10-2, which include both uncoded and coded simulations. The results provide insight into the performance of the communication system under various interference conditions:

A. *Baseline (no jamming)*: In the absence of jamming, LDPC coding is very effective in ensuring reliable data transmission over the high noise AWGN channel, demonstrating the benefits of channel coding in securing data transmission.

B. *Impact of jamming*: As jamming power increases (JSR increases), BER performance of both coded and uncoded systems degrades, as expected. While LDPC coding generally enhances the resilience of the system against jamming, certain types of jamming can pose significant challenges. For example, pulse noise (a type of noise-based jamming) is particularly effective in disrupting system performance. Even at relatively low jamming power, pulse noise reduces the effectiveness of LDPC coding, with minimal improvement in BER compared to the uncoded case. This result indicates: while channel coding improves resilience under certain jamming conditions, it cannot completely counteract the effects of all jamming types. It is also worth noting the relatively low code rates in this investigation. The limited performance improvement against jamming suggests that a jammer could intentionally force a lower code rate in the system to slow down data transmission. This highlights the need for strategies other than channel coding to mitigate the effects of jamming.

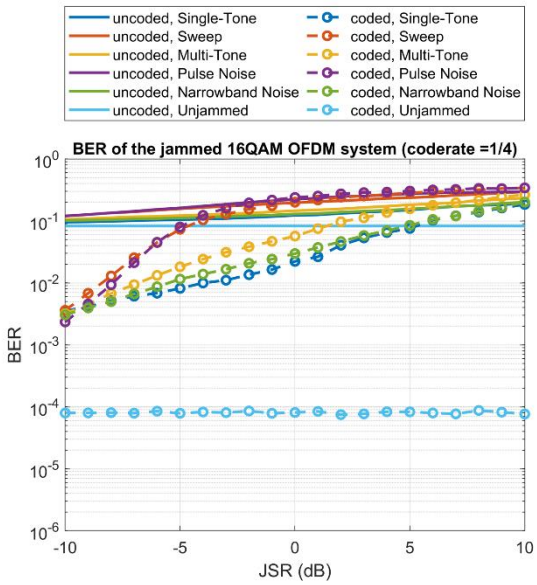

Figure 10-2: BER simulation of a jammed OFDM system.

The investigation demonstrates that while LDPC channel coding provides some degree of resilience, it is not sufficient to counteract all forms of jamming. Further strategies should be developed to secure the resilience of the communications system against jamming.

10.2.2 Indoor jammer localisation

Problem statement: The presence of jammers is a significant concern in both civilian and military contexts, as it can lead to loss of communication, reduced reliability of systems, and potential safety hazards. Therefore, the jammer identification and localization can be useful and essential for maintaining communication integrity, enhancing network security, optimizing resource allocation, ensuring regulatory compliance, supporting spectrum management, and monitoring unauthorized interference [HEX224-D43]. In our study, we have considered a jammer in an indoor space environment using four receivers. The jammer will transmit waveforms, not aimed at compliance but aimed at disrupting communication. The question is whether the jammer can be accurately identified and located by only the received signal strength.

Methodology: In order to identify and locate the jammer, we have considered two approaches: 1. we have continued the work reported in [HEX224-D43] where the received power is measured in a band of interest (sub-6GHz) at the four receivers assuming the presence of a jammer, 2. we have extended our work on radio frequency fingerprint identification (RFFI), also known as radio fingerprinting, as a security measure to identify unique individual devices. While the first study methodology is presented in [HEX224-D43] and [HEX224-D44], below we have presented the methodology followed by the second part of our work, followed by results. The second approach is based on the fact that during the fabrication process, each device experiences slight variations in hardware components, known as hardware imperfections [YH10]. These imperfections impact different parts of radio signals, causing amplitude distortion, phase shifts, and other unique characteristics embedded in the radio signal of each device [US07, BBG+08]. While we can identify and record the imperfections of known and useful transmitters, in case another device (a jammer) is found in the vicinity, our proposed works can identify it. Therefore, we want to use the identified imperfections as an authentication mechanism at the physical layer. In order to perform device classification based on the imperfections we use a deep learning AI based approach [LBH15]. We focus on the length variation of the radio signal overcoming some problems in existing approaches that are caused by focusing on fixed length signals and are impractical for real-world radio communication. Our objective is to improve the classification performance of radio fingerprinting in the context of varying signal lengths. The approach is called FlexiPrint and involves training the model once with a specific signal length, enabling it to classify signals of any length. Our novel method uses multiple inferences to classify devices regardless of signal length by considering 4 different signal lengths for the testing: 256, 512, 1024, and the whole signal length of 2080.

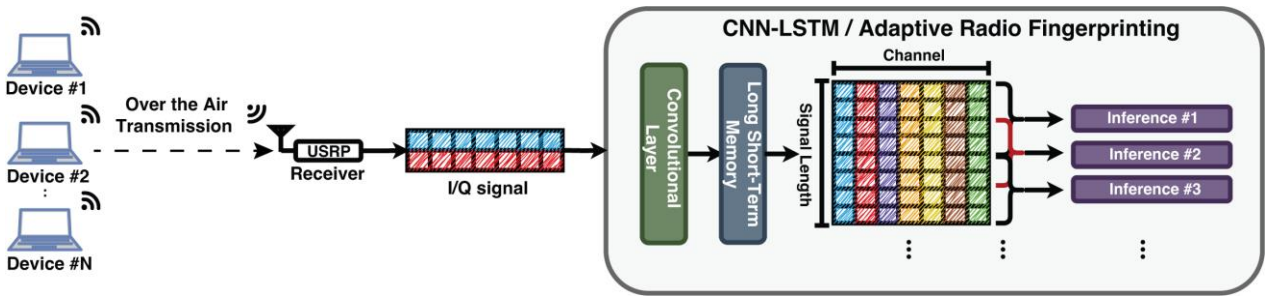

Figure 10-3: Overview of RFFI framework with proposed model CNN-LSTM with multi-inference.

Within the FlexiPrint framework, we investigate two different approaches: incremental multi-inference (IMI) and shifting multi-inference (SMI). Both approaches leverage the radio signal length to perform multiple inferences by analysing different parts of the signal. IMI progressively increases the signal length (k) for classification, while SMI uses a fixed-length window (k) that shifts through the signal. The overall framework of our methods is illustrated in Figure 10-3, where we present an overview of the RFFI framework. The model streams in-phase/quadrature (I/Q) samples through the convolutional neural network (CNN) layer and passes the output to the long short-term memory (LSTM) layer, then a linear classifier is used in different parts of the signal, making multiple inferences [NWP+25].

Results:

Jammer Localization: As presented in [HEX224-D44] the system model included four sensing units (SUs) and one transmitter (Tx1) with known positions in a 22 m² area. We assumed the presence of a jammer (Tx2) with an unknown location. We received signals from both Tx1 and Tx2, and using device identification, we could confirm the presence of two transmitters in the area. We used least-squares estimator [ACN+21] to localize Tx2 using received power in dBm. Results show an average estimation error of 1.5m with a standard deviation of 1.1m.

Jammer Identification: Error! Reference source not found. in Section A.7 shows that a model trained on a certain signal length completely fails when tested on different signal lengths whereas in our approaches, in **Error! Reference source not found.** and **Error! Reference source not found.** our model maintains cl assification performance at 90% accuracy. It is also interesting to note that our model fails when the signal length is at 256 I/Q samples. This can be explained by the special sequences of preamble symbols of IEEE 802.11 packets, which may not be present in such small window sizes. It should be noted that in the baseline, the model still performs well when trained and tested at specific signal lengths and last time steps, meaning fingerprint features are presented, but a unified feature is not learned, requiring further investigation.

10.3 Security and privacy analysis of a general cellular JCAS system deployed for crossroad monitoring

Problem statement: The integration of the anticipated sensing functionality in the forthcoming 6G standard imposes new challenges in terms of privacy and security. Firstly, this is because of the nature of the extracted data, which can belong to the private domain of entities, and secondly because of the way these data can influence the involved cyber-physical systems. Therefore, it is imperative to characterize and treat the new security and privacy issues introduced by JCAS. The objective of this study is to identify the security and privacy risks related to the physical layer elements of a JCAS system tasked to monitor a crossroad.

Methodology: In this study, the security and privacy risks of the physical layer elements of the JCAS system of interest are mapped to the spoofing, tampering, repudiation, information disclosure (breach or leak), denial of service, and elevation of privilege (STRIDE) and linking, identifying, non-repudiation, detecting, data disclosure, unawareness, and non-compliance (LINDDUN) frameworks of thread analysis. This is done in two steps.

- Initially the entities, both virtual and physical, and the way that they interact with each other, are identified via the derived dataflow diagram (DfD).

- Finally, through an exhaustive search, the security and privacy threads of the physical layer elements of the DfD along with the entity that creates this thread, are mapped to the STRIDE and LINDDUN frameworks.

Note that, for the threat analysis, it is assumed that the JCAS system is within one trust domain (all the components (assets) within JCAS are trusted and share same security requirements). The only external entities are the application and the physical environment.

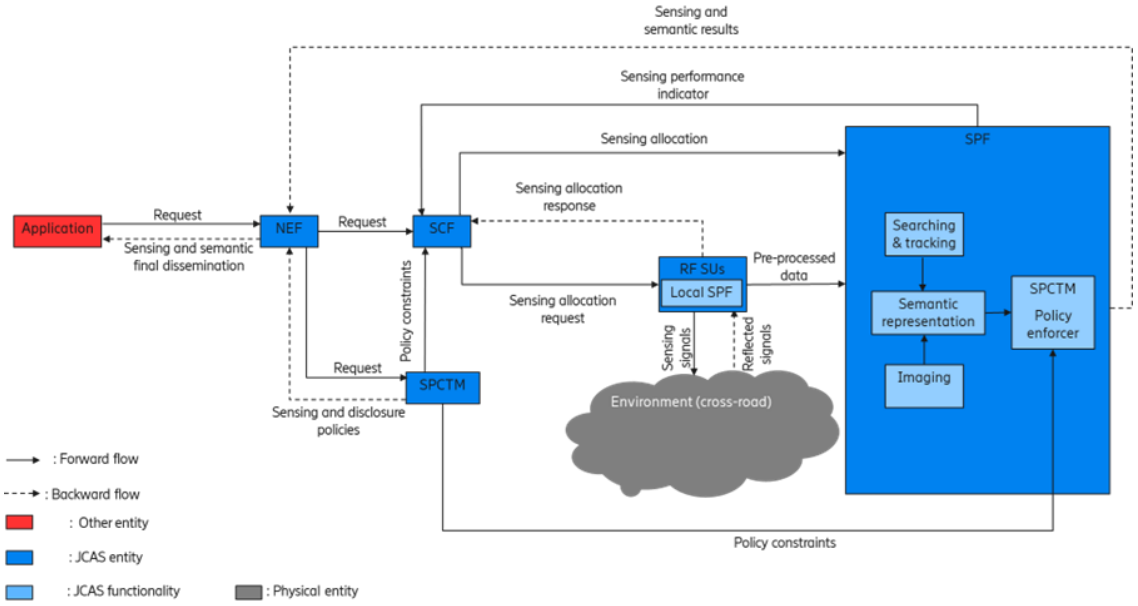

Figure 10-4: DfD of the considered 6G JCAS cross-monitoring system.

Results: In order to identify the security and privacy risks of the physical layer elements of a 6G JCAS cross-road monitoring system, its DfD is derived systematically. The illustration of the DfD of the previous JCAS system is given in Figure 10-4. As it can be seen, it includes the following entities: 1) Network Exposure Function (NEF), 2) Sensing Control Function (SCF), 3) Sensing Policy, Consent, and Transparency Management (SPCTM), 4) RF Sensing Units (RF-SU), and 6) Sensing Processing Function (SPF). The objective of the NEF is to provide an interface with the external world and the 6G sensing functionality. The SCF is responsible for coordinating a sensing procedure from its initiation until the dissemination of the produced sensing results. The SPCT is responsible for creating and passing the security and privacy policy to the SCF and SPF. The SPF is the entity tasked with the processing of the raw sensing data and the enforcement of the produced policies from the SPCT. Based on the DfD of Figure 10-4, the threat and privacy analysis of the physical layer elements of the JCAS cross-road monitoring system of interest is derived exhaustively and presented in Table 10-1.

Table 10-1: Threat and privacy analysis of the physical layer of the JCAS cross-road monitoring system

Asset	Threat Source	Threat	L	I	N	D	D	U	N	-	S	T	R	I	D	E
Inter-element interfaces	Malicious communication and traffic sniffer	Passive over-hearing	X	X		X	X	X	X					X		X
	Malicious transmitter	Coordination and sensing data transfer jamming		X					X			X			X	
		Coordination and sensing data transfer alteration			X				X		X	X	X		X	X
RF SUs		Jamming							X			X			X	
		Target alteration							X			X			X	

	External malicious transmitter	Fake target creation			X				X			X	X		X	
		Target ghosting			X				X			X	X		X	
	External malicious sensing sniffer	Passive over-hearing/sensing	X	X		X	X	X	X				X	X		X

10.4 Summary

This chapter studies enablers for trustworthy holistic 6G radio design.

First, the important and emerging concept of resiliency in 6G networks is discussed. Future networks must be made resilient-by-design to provide and maintain an acceptable level of service in the face of disruptions and challenges to normal operation. A novel four stage resilient-by-design framework in presented to support this goal.

Thereafter, jamming – which is one of the most common forms of attacks against trustworthiness – is analysed from two different perspectives. Firstly, the impact of jamming attacks on network resilience in a coded system is analysed through experimental studies. It was shown that the impact of different forms of jamming attacks have varying degrees of impact on the performance of different coded transmissions. Nonetheless, coding alone is not sufficient to mitigate jamming and protect critical services and hence further safeguarding strategies are needed. Passive localization of potential jammers (i.e., without any role of the jammer) was presented as an example of such a strategy. An ML approach based on LSTM was proposed towards this end and was shown to achieve significant localization accuracy with sufficiently long radio signal length.

The integration of the sensing functionality of cellular JCAS systems in 6G will impose new challenges in terms of privacy and security. The final contribution in this chapter identified the security and privacy risks related to the physical layer elements of a JCAS system tasked to monitor a crossroad and proposed to address the privacy and security challenges of the considered JCAS application scenario by a thorough security and privacy threat mapping of the physical layer elements to identify potential threats.

11 Proof-of-concepts and simulators

In the POC chapter as its name suggests, we give proof for the emerging concepts in 6G. It includes the link modelling for 6G to evaluate the performance of 6G PHY, a flexible transceiver system to adapt to different requirements dynamically without changing the default static system configuration, AI-native air interface to address the emergence of AI in 6G, bi-static joint communication and sensing as a dual use of telecom infrastructure promised for 6G, power consumption analysis for sustainability and energy management mayhems, EMF assessments of D-MIMO deployments in an industrial indoor environment, and channel modelling as an inevitable part for 6G standardization. In the following a concrete subsection is allocated for each of these topics, with reflections on the results, and challenges as an inevitable part of test beds and Demo setups.

11.1 Link modelling of 6G physical layer

Introduction: A link-level simulation tool of the downlink 6G PHY has been developed, including models of multi-cluster propagation channels in the sub-THz bands. The simulator provides performance evaluation of enhanced physical-layer schemes, e.g., D-MIMO and beamforming. The aim is to understand the impact of enhanced physical-layer schemes, to improve the system performance and to optimize the parameters, especially in mmWave (FR2 frequency bands) and sub-THz context.

Methodology: The simulation tool was built using Python and the Sionna open-source libraries to provide flexibility and ease of modification. It evaluates the performance of advanced PHY schemes like D-MIMO and beamforming, following the 3GPP specifications (TR 38.901 [38.901]).

Results and Conclusions: The simulation tool was applied to study D-MIMO performance in scenarios with channel blockages, shedding light on the effects of these blockages on network reliability and performance at high frequencies (see Section 4.1.1). Results, provided in Section 4.1.1, indicate that channel blockages significantly reduce link reliability, underscoring the importance of flexible D-MIMO configurations to mitigate these challenges effectively.

The tool's open-source framework, developed using Python and Sionna libraries, offers flexibility in testing various scenarios and adapting to different 6G network configurations. In the most recent scenario, the tool was used to compare two precoding techniques: the MRT algorithm and beamsteering directed at the most powerful channel cluster. Findings reveal that, under certain conditions, both techniques achieve comparable performance, suggesting that less computationally intensive methods like beamsteering may be effective alternatives to MRT in specific channel environments. More details about performance can be found in Section 4.1.1.

These insights highlight the tool's value in evaluating complex PHY layer strategies and in guiding the development of robust, high-frequency 6G networks that can maintain reliable connections despite challenging propagation conditions.

Figure 11-1 illustrates the main common components defining the PHY layer of digital radio communication chain. These components are developed in Python and shared in the Sionna open-source libraries. They can be used for developing 5G/6G PHY layer radio transmission chains and very generic to be parameterized to define several types of scenarios.

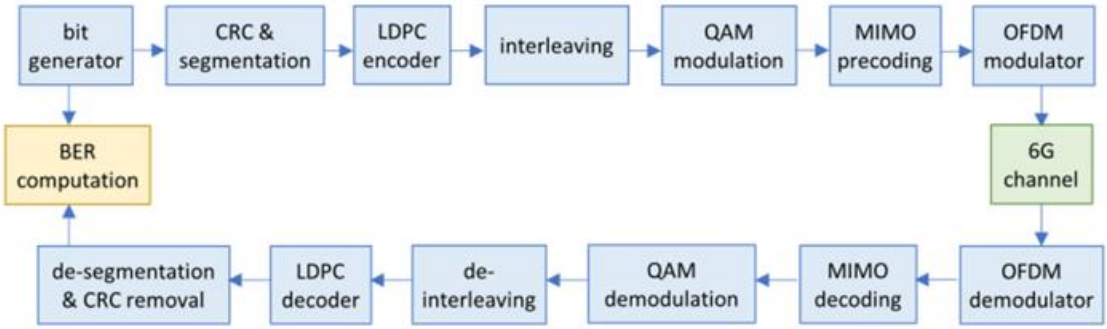

Figure 11-1: Diagram of 6G PHY layer simulation.

11.2 Flexible modulation and transceiver design

Problem Statement: The goal of this PoC is to develop a flexible transceiver system, as outlined in [BCN+24]. Flexibility in this case refers to the ability of the system to adapt to different requirements dynamically without changing the default static system configuration. In a flexible system the choice of parameters is decided at run-time and remains adjustable in real time. This system combines software-define radios (SDRs), field programmable gate arrays (FPGAs), and central processing units (CPUs) as signal processing units, supporting a diverse range of radio configurations. The modem provides multiple options of different waveforms, modulation and coding schemes, and signal processing algorithms at the receiver site. The systems flexibility is demonstrated through its capability for dynamic reconfiguration depending on the mobile communication scenario and its specific requirements.

Methodology: The flexible transceiver system is assembled of SDR devices connected to a central controller (NI PXIe 8133/8880) and corresponding RF frontends. The control software/controller for Tx/Rx is written in NI LabVIEW. Radio transmission parameters are dynamically adjusted during runtime by the controller. Users of the flexible transceiver system interact with it via a Python application programming interface (API) operating on a host machine which sends remote procedure calls (RPC) to the controller. These RPC follow a custom message format, tailored specifically to control signals relating to RF transmission parameters such as signal bandwidth or carrier frequency. I/Q data is streamed over user datagram protocol (UDP) between host and controller via corresponding API calls. This adaptability allows for great diversity in experimental scenarios that can be investigated with this system. Synchronization of system components is achieved by a common 10 MHz reference and a pulse-per-second (PPS signal).

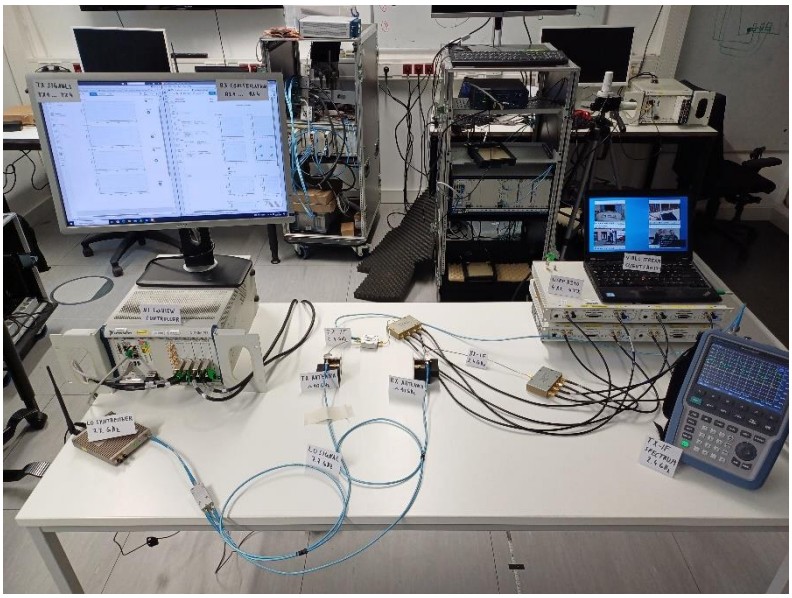

Figure 11-2: Experimentation in lab with flexible transceiver system used for analogue multicarrier with 10 GHz patch antenna frontend.

Results and Conclusions: A working prototype of the flexible transceiver system has been successfully implemented. Its core functionality allows for use of the system in demonstrators. The range of scenarios for which this system can be applied is outlined in [BCN+24] and a Video demo at EUCNC 2024 further corroborates its capabilities. Figure 11-2 shows the flexible transceiver system used for experimentation with a 26 GHz RF frontend [WLP+19]. The phase synchronization capability of the system has been highlighted in the demonstrator "Angle-of-Departure Estimation in True-Time-Delay Antenna Arrays" at 6G Summit Dresden 2024 (corresponding works [CMN+24]).

The flexible transceiver system shows strong potential for experimental verification of mobile communication use cases, especially for dynamic scenarios that require flexibility beyond static configurations. Its SDR-based design allows researchers to explore different applications with minimal overhead in system management and setup, providing both flexibility and ease of use. Overall, the flexible transceiver system provides a

foundational tool for prototyping, testing and validation of mobile communications systems, applications and concepts. This makes it a valuable tool for advancing experimental research in mobile communication.

11.3 AI-native air interface

11.3.1 ML-based channel state feedback compression in a multi-vendor scenario

Problem statement: This PoC aims to demonstrate the feasibility of multi-vendor cooperation, between UE-side ML Model (also referred to as Encoder) and NW-side ML Model (also referred to as Decoder), to enable joint AI solutions for enhanced channel state feedback compression. In Section 7.3.1, OTA evaluations are presented that demonstrate two findings:

- Sequential training enables inter-operability between different gNB vendors and UE vendors.
- ML-based CSF provides a significant gain in terms of DL throughout compared to the baseline Type I CSF.

This indicates that the sequential-based training is a promising solution for ML-based CSF. Please, refer to Section 7.3.1 for the detailed results obtained.

This Section details the OTA testbed for this PoC, i.e., the data collection process and characteristics of the dataset used for training the ML models for evaluation and testing purposes. It details also the ML model training process and the lab and OTA testbed. The block diagram of the OTA ML-based CSF testbed is depicted on Figure 11-3.

Data collection process and characteristics: The OTA data collection was conducted in an outdoor test area, e.g., a parking lot, with the gNB installed at an elevation of approximately 20 meters to cover the area. OTA channel state information reference signal (CSI-RS) channels were collected during both mobility and stationary tests. The mobility routes had reasonable coverage in the test area, while the stationary locations will be chosen to sample different UE-gNB distances (up to 200 meters) as well as different angles. The mobility data will be used for model training, and stationary locations are used for offline and live OTA inference test.

System settings:

- 90MHz system bandwidth
- 80MHz CSI-RS with 220 resource blocks
- 80MHz PDSCH
- Carrier frequency: 3.45GHz
- Qualcomm UE with 4 Antennas
- Nokia gNB with 8 antennas ports with single polarization

Approximately, 520 thousand collected samples were used for training, one sample is an CSI-RS 20MHz channel, 1 layer. The SNR range of the collected data varies between 2 to 22 dB.

ML model training and testing: The ML models were trained with relative high SNR samples, (e.g., higher than 5~10 dB); each model was trained using around 520k samples. For inference test, the SNR can be lower as long as the call was maintained. The data collected was used to train the UE encoder models. Two different UE encoder models were trained to replicate a multi-vendor scenario. The corresponding data sets were shared with the network to train a common decoder model for both encoders. The trained UE encoder and gNB decoder models are then used to run inference tests applied to the OTA stationary data and to channel emulated data.

Inference test stage for CSI accuracy: Different UE encoder and network decoder models were deployed at the UE and gNB sides. The gNB decoder output is used to calculate the DL precoder for the PDSCH. The SGCS is evaluated. The SGCS is calculated based on the UE logging of encoder input (ground truth CSI) and the corresponding gNB logging of decoder output (reconstructed CSI).

Inference test stages for DL throughput: similarly to the previous test, different UE encoder and network decoder models were deployed at the UE and gNB sides. The gNB used a common decoder model for different

UE encoder models at stationary locations, and the PDSCH beamforming coefficients will be derived based on gNB decoder output and applied to PDCSH.

For lab test, a gNB and a UE device were connected through an 8x4 channel emulator. The ML models were trained with lab collected samples. To evaluate performance at varying Doppler frequencies a channel emulator was used with a specified fading tapped delay line type A channel (TDL-A). The downlink throughput was measured with a full buffer data traffic, making the effective DL throughput dependent on the quality of the beamforming.

For OTA test, the ML models are trained with OTA samples. The downlink throughput was measured with a full buffer data traffic.

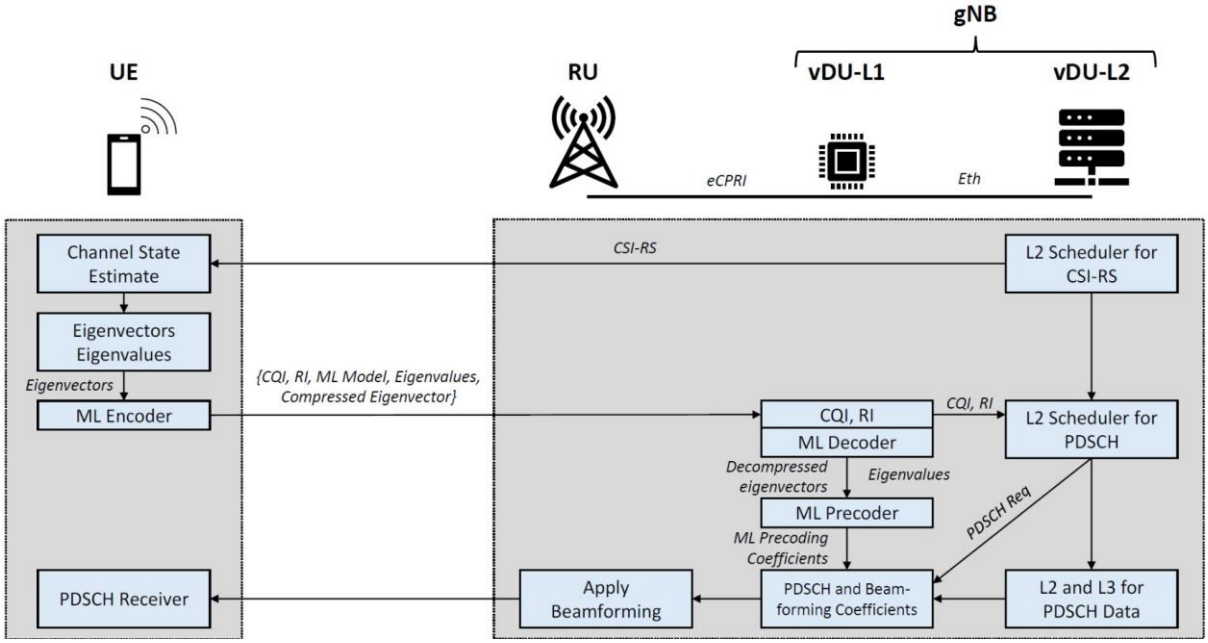

Figure 11-3: Block diagram of the implement OTA ML-based CSF testbed.

11.3.2 Pilotless operation with a partially learned air interface

Problem statement: In this PoC, the target is to demonstrate the practical feasibility and performance gain of and end-to-end learned transmission link. The setup was described in detail in [HEX224-D43], and essentially it consists of an OFDM-transmitter utilizing a machine learned constellation, which is transmitting data to an ML-based receiver (DeepRx). The constellation and DeepRx are learned jointly with simulated data to communicate without any DMRS pilots, which results in increased SE. The target of the PoC is to validate that this results in higher throughput also with real equipment and with real channels.

Methodology: As described in [HEX224-D43], the PoC has been implemented with graphics processing units (GPUs) such that the Tx and Rx algorithms are executed on the GPU and the resulting digital baseband signal is fed to an SDR. The SDR acts as the transmitter and receiver, using either physical antennas for the OTA measurements, or a channel emulator for the emulated lab experiments. The hardware setup is described in Figure 11-4.

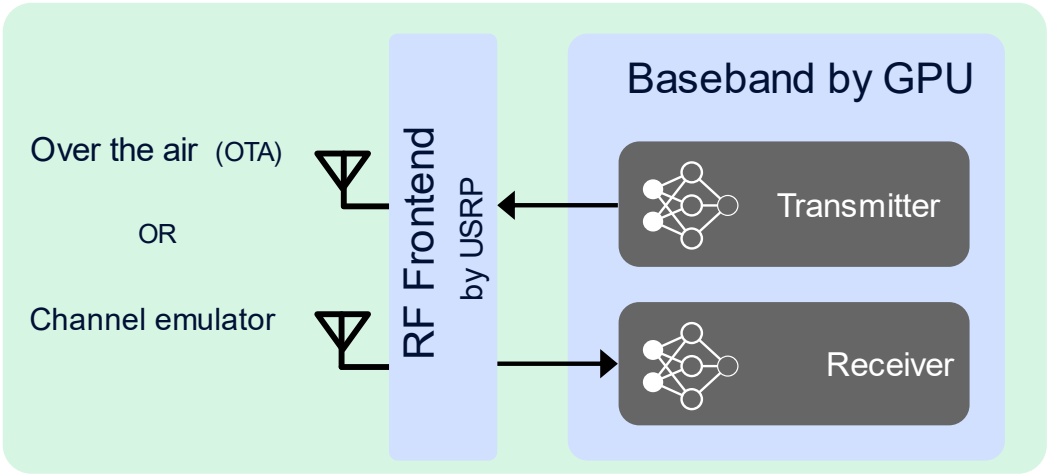

Figure 11-4: Hardware setup for the PoC.

Final results and conclusions: The PoC was tested in two different setups: through a channel emulator, and OTA inside the laboratory. The channel emulator experiments were repeated with three different mobility levels, corresponding to pedestrian, car, and train scenarios. Moreover, each measurement was also repeated with non-ML algorithms, which correspond to a 5G air interface. The resulting throughput gains are depicted in Figure 11-5, where the highest throughput gain of 30% is achieved with the highest velocity scenario (train). With lower velocities, the throughput gain is in the order of 15-20%. The gain is mostly caused by the reduced overhead of the AI-based approach, as it has been trained to communicate without DMRS pilots. Since the proposed approach achieves similar bit error rate performance without the DMRS overhead as the conventional approach achieves with DMRS, a higher SE is achieved.

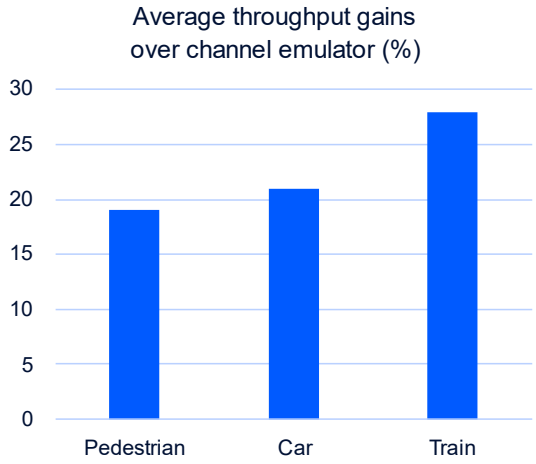

Figure 11-5: Throughput gains measured over channel emulator.

In the OTA measurements, a throughput gain of 19.2% was achieved, which is similar to the low-velocity pedestrian scenario in the channel emulator experiments. This also demonstrates that the proposed approach performs with true physical radio channels.

11.4 Bistatic joint communication and sensing

The main advantage of joint communication and sensing is that the same hardware can be used for several purposes, i.e. communication, sensing and positioning. It is not only the hardware that is used more efficiently, though, but also the frequency spectrum as the same waveforms is used. As always when trying to combine functionalities, additional challenges arise. In the case of bi-static JCAS, one of the main challenges has turned out to be the time synchronisation between the transmitter and receiver. In a communication system a minor time offset in the order of some ns can be handled with the CP and pilot symbols. For a sensing system a time offset of just a single ns would introduce a systematic error of 30 cm. Thus, to obtain a position accuracy of 10 cm, a time synchronisation well below ns level is needed.

System model: The JCAS PoC which has been described earlier in [HEX224-D43, Sec. 10.4] uses two RF evaluation kits from Sivers Semiconductors in the 60 GHz band together with a Xilinx board for data processing. The bi-static sensing system is setup inside an office building in a rich-scattering environment. The waveforms used are modified 5G NR signals for communication where the subcarrier spacing has been increased to 960 kHz. The communication is done in a line-of-sight link. The sensing utilises the beam steering capability of the radios and sweeps the beams at both the transmitter and receiver in a coordinated pattern. The signals are recorded and used to generate a beam power map. After background subtraction targets are identified and the time of arrival is calculated for each target. With this data there is information both on the direction and distance of the target which is used to project the position of the target on a 2D map.

Time synchronisation: In the measurements performed, the time synchronisation has been done using the LoS channel in combination with the known static positions of the transmitter and receiver. This is a simplified case, though, as the relative positions between the two in normal cases is unknown. However, even in this simplified case it can be challenging to obtain the needed sub-ns synchronisation. One limiting factor is the clock jitter in the system. Even though the same clock is used and distributed to both the transmitter and receiver, there is an uncertainty in the time synchronisation. In Figure 11-6, the time synchronisation distribution is showed when a synchronisation signal was sent 10 000 times. The Gaussian fit shows a standard deviation of 0.09 samples. The sampling speed in the setup is 983 MSps which would mean that the standard deviation in space would be around 2.7 cm.

Gesture recognition using communication signals: In addition to radar-like sensing, tests have also been performed with the setup for gesture recognition. The same setup with two radios in 60 GHz were used as transmitter and receiver with one meter separation according to Figure 11-7. An adjusted 5G NR waveform, similar to what was explained in [HEX224-D43, Sec. 10.4.1], was used for the measurements. Ten different people maintained 8 different gestures and the data for each person and each gesture was recorded. Then the data was fed to a convolutional neural network for training. As is depicted in Figure 11-7, an accuracy of 92-96% for all 8 different gestures could be obtained.

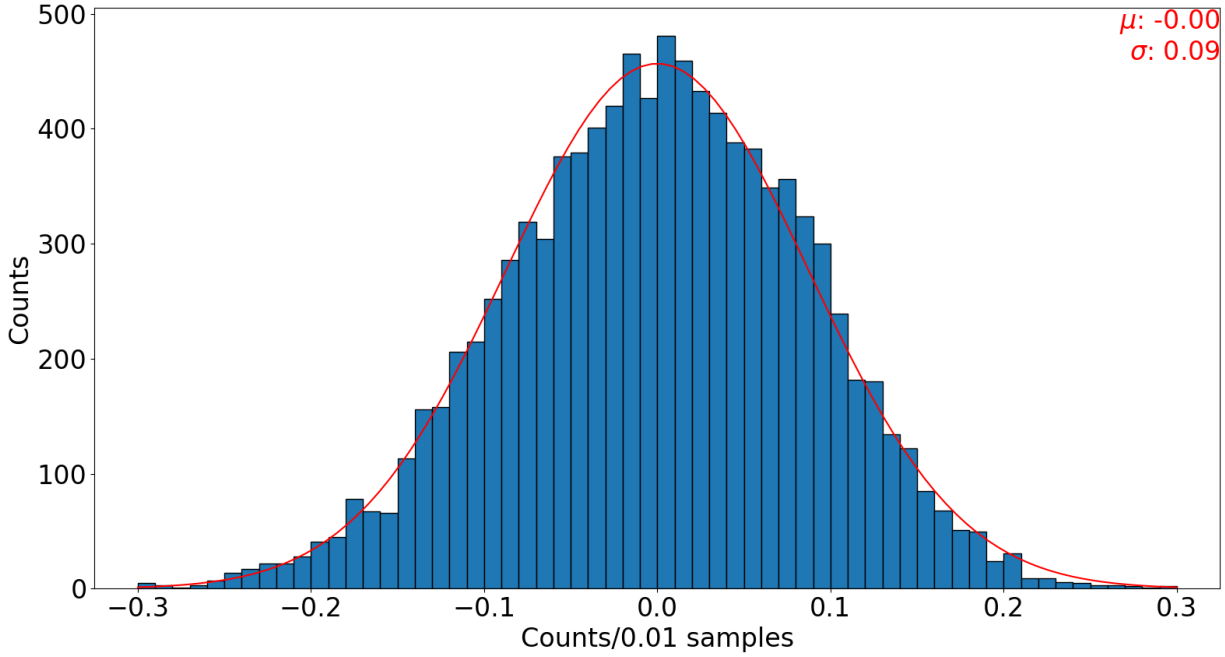

Figure 11-6: The distribution of 10 000 consecutive time synchronisations. The red line shows a Gaussian fit to the data together with the parameter values in the upper right corner.

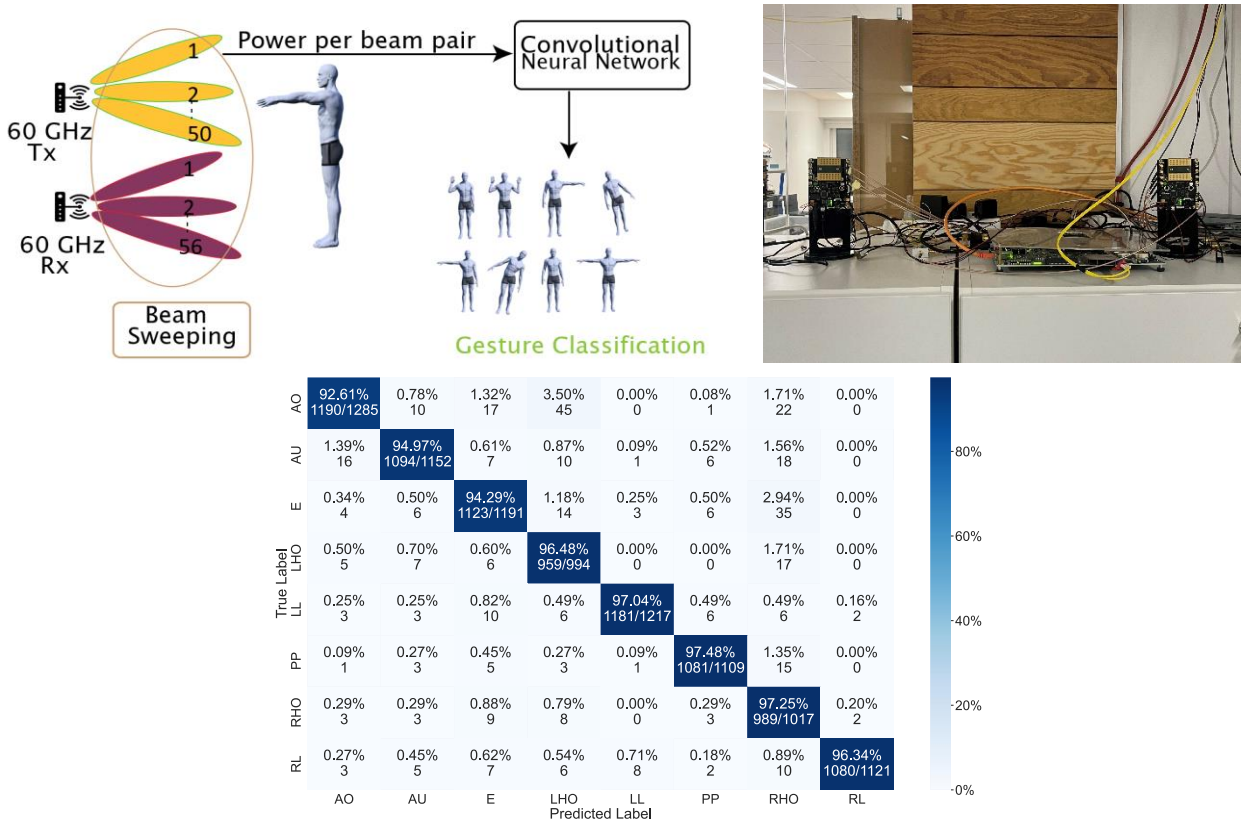

Figure 11-7: top right: Qamcom RF setup, top left: 8 different gestures used for CNN training, down: performance results.

11.5 Power consumption of JCAS

Problem statement: JCAS aims to enable numerous high accuracies sensing applications, improving SE, sensing performance, and reducing hardware costs. However, JCAS demands more bandwidth, higher carrier frequencies (resulting in higher losses), MIMO systems, etc., as it is expected to have more end devices, network users, and applications. These factors can lead to increased power consumption, affecting power efficiency. Thus, we want to use consumption factor (CF) to have power related analysis.

Methodology: We have simulated a communication system intended for use in sensing applications. For analysis, as performance metrics "A" as defined in previous deliverables versus power consumption, we have analysed the minimum variance on the time and angle parameters. The system features a transmitter and receiver operating at mmWave 28 GHz with a bandwidth of 400 MHz, which is equal to the maximum bandwidth for FR2 in the 3GPP standard. To analyse transceiver power consumption, we assume analogue beamforming at both the BS and UE.

Results: As illustrated in Figure 11-8, as the SNR increases, the CF also increases, meaning better Fisher Information or better range and angle accuracy, however higher SNR requires higher power consumption. First figure shows the trend values of power consumption when increasing SNR. In two other figures we present the Fisher information for time of arrival (I_{TOA}) and angle of arrival (I_{AOA}). We can see that beyond 50 dB SNR, the growth slows down, showing diminishing returns. If SNR keeps increasing as power consumption

grows, the accuracy improvements become marginal. This outcome and solution can be used for finding a balance between power consumption and sensing performance as essential for energy-efficient JCNS.

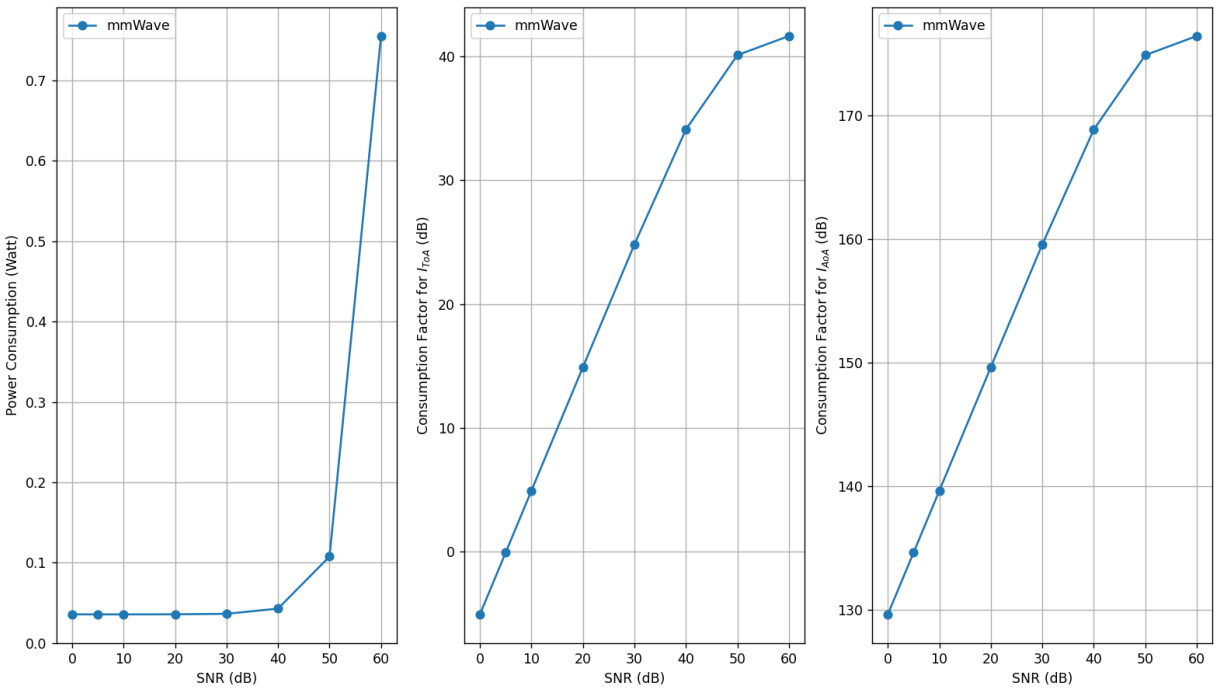

Figure 11-8: Power consumption.

11.6 EMF assessment for D-MIMO

Problem statement: For each new generation of mobile communication technologies, proper methods are needed to assess EMF exposure levels. For 2G-5G, it has been shown that the typical environmental EMF exposure levels are far below the limits prescribed in the international EMF exposure guidelines [ICNIRP20]. The existing simulation approaches to assess EMF exposure levels are mostly fit to co-located BS deployment. New simulation approaches are needed to assess the EMF exposure levels from 6G D-MIMO deployments.

Methodology: A hybrid simulation scheme to perform EMF studies for 6G D-MIMO deployments is developed. The hybrid simulation scheme is the combination of asymptotic solver and the time-domain solver in CST Studio Suite. The workflow is fully controlled by MATLAB scripts. The DL EMF exposure levels for 6G D-MIMO technology in an industrial indoor scenario at 3.5 GHz are assessed and compared with the EMF exposure levels for the 5G mMIMO technology, as shown in Figure 11-9. The equal gain transmission (EGT) precoding and the centralized zero forcing (CZF) precoding methods are used to compute the DL precoding weights from different antenna elements.

Results: As can be seen in Figure 11-10, CZF (see Figure 11-10(b)) leads to statistically lower power density (S_{inc}) than EGT (see Figure 11-10(a)) because of the lower radiated power resulting from the power tapering for both D-MIMO and mMIMO deployment scenarios. The EMF levels at the 95th and 99th percentiles for D-MIMO are lower than the corresponding levels for mMIMO deployment. For the median value, there is no such difference that can be observed. For both D-MIMO and mMIMO deployment scenarios, the EMF exposure levels are below 0.1% of the ICNIRP limit values for a total configured power of 1 W. Similar observations are made for a total radiated power of 1 W and 1 μW fixed power received by UE.

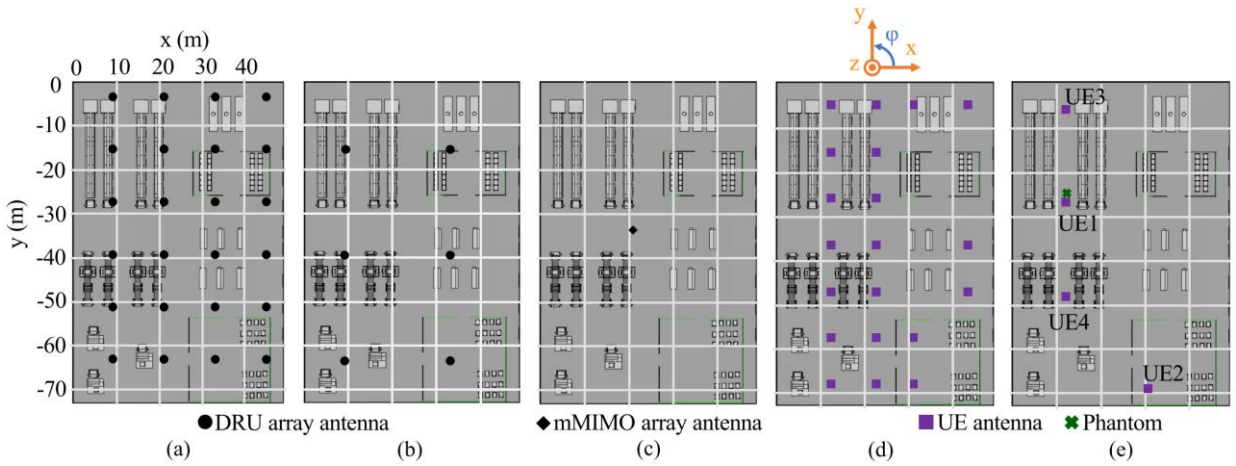

Figure 11-9: Deployment scenarios. Top view of the battery factory model (the ceiling is hidden) with visual representation of (a) D-MIMO deployment scenario with 24 distributed radio unit (DRU) array antennas, (b) D-MIMO deployment scenario with 6 DRU array antennas, (c) mMIMO deployment scenario with one array antenna, (d) all 20 UE locations used in the study, and (e) UEs and phantom positions for 1 out of 20 studied cases, for CZF precoding with a combination of 4 UEs. (© IEEE 2025)

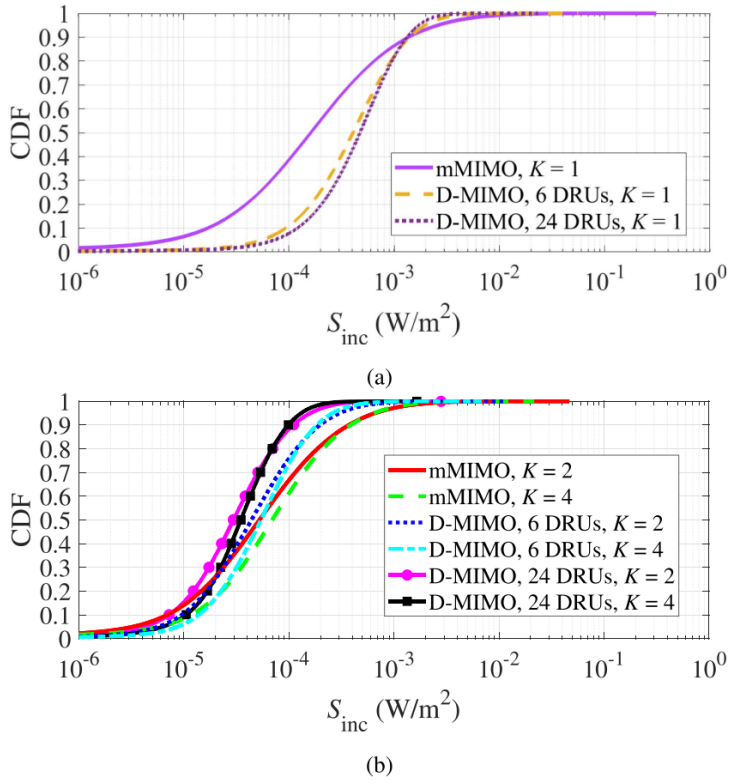

Figure 11-10: CDFs of power density (S_{inc}) from 20 study cases for mMIMO, D-MIMO (6 DRUs), and D-MIMO (24 DRUs) deployments and for total configured power of 1 W from all DRUs (a) EGT precoding (b) CZF precoding. K is the number of active UEs. (© IEEE 2025)

11.7 Channel measurement data and model

Problem statement: Channel measurements are essential for channel modelling, including stored, deterministic, and stochastic approaches, which all rely on multipath data from measurements. Stored models replay measured channel impulse responses directly, providing realistic outputs limited to available measurements. Deterministic models calculate channel responses by simulating ray propagation and interactions based on each object's electromagnetic properties based on existing standards or by calibrating the

ray-tracer tool using measured multipath data. Stochastic models use multipath data to set channel parameters, generating extensive data with probability distributions matching measured channels.

Methodology: The measurement campaigns are summarized in Table 11-1. The multipath data collected from the 142 GHz measurement campaigns are reported in [DHK23]. A 3GPP-like channel model based on 142 entrance hall and residential measurement data is described in [HEX224-D43, Sec. 3.1].

Table 11-1: Simulation settings and parameters for the channel measurement campaign at various frequencies.

Frequency	Environment	Measurement Description
142 GHz [DHK23]	Entrance hall, suburban, residential, and city centre	VNA, single-directional, discrete Tx/Rx locations
234 and 318 GHz	Factory hall and warehouse	VNA, bi-directional, discrete Tx/Rx locations
15 GHz [ATK+25]	Residential, campus, and parking lot	USRP-based, linear route measurements

Results: Initial results from 234 and 15 GHz measurements are shown in Figure 11-11 and Figure 11-12. The measurement setup and analysis of the measured channels are detailed in Sections 3.3 of this Deliverable for the sub-THz dual-band indoor campaign and in Section 3.7 for the 15 GHz outdoor campaign.

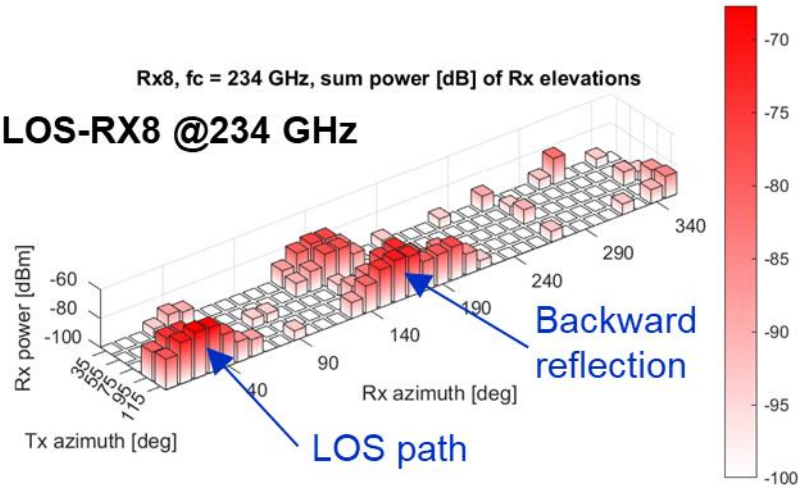

Figure 11-11: Bi-directional power angular spectrum of Tx-Rx8 link at 234 GHz in factory hall.

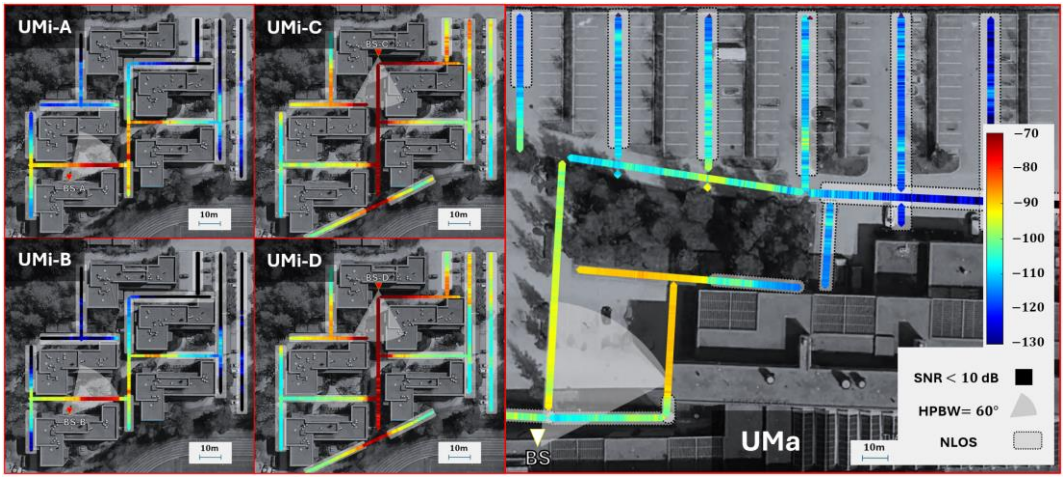

Figure 11-12: Coverage map showing path gain (dB) along the measurement routes in a UMi (left) scenario (residential area) and a UMa (right) scenario (university campus/ parking lot) at 15 GHz.

11.8 Phase noise modelling

Problem Statement: Accurate modelling of phase noise is of high importance for upcoming 6G technologies. Phase noise adversely affects system performance by causing intercarrier interference (ICI) in JCAS systems, reducing data transmission efficiency, and degrading spatial multiplexing gains in MIMO systems due to disrupted coherent signal combination. Existing phase noise models either lack empirical validation, fail to connect theoretical models with practical measurements, or inadequately represent phase-locked loop (PLL) dynamics. This highlights a critical need for a reliable, empirically validated phase noise model that accurately represents both time-domain dynamics and spectral characteristics to enhance system performance in communication systems.

Methodology: To address these limitations, a simplified parametric phase noise model is developed, derived from time-domain modelling of the phase noise process and PLL dynamics. The approach begins with modelling a free-running voltage-controlled oscillator (VCO) in the time domain and deriving its corresponding phase noise spectrum. This model is then expanded to include PLL circuit dynamics by formulating stochastic differential equations that capture both the intrinsic noise sources and the feedback control actions of the PLL, subsequently deriving the associated phase noise spectrum. Empirical validation is performed by measuring the phase noise spectrum of common SDR devices, specifically analysing the impact of different USRP daughterboard models and operating frequencies. Estimators are provided for extracting the model parameters from the empirical data, effectively linking the theoretical model with practical observations. Results illustrate the accuracy of the stochastic differential equation-based modelling of phase noise.

Results: Figure 11-13 illustrates the characteristics of PLL spectrum, which is comprised of a section dominated by the influence of the reference signal with phase noise bandwidth f_{REF} up until the transition frequency f_{TR}, where the spectrum remains flat until the PLL bandwidth f_{PLL}. Thereafter, the PLL characteristics follows the behaviour of VCO.

$$S(f) = 10\log_{10}\left(\frac{1}{\pi f_{REF}} \cdot \frac{1+\left(\frac{f}{f_{TR}}\right)^2}{1+\left(\frac{f}{f_{REF}}\right)^2} \cdot \frac{1}{1+\left(\frac{f}{f_{PLL}}\right)^2}\right). \quad \textbf{(11-1)}$$

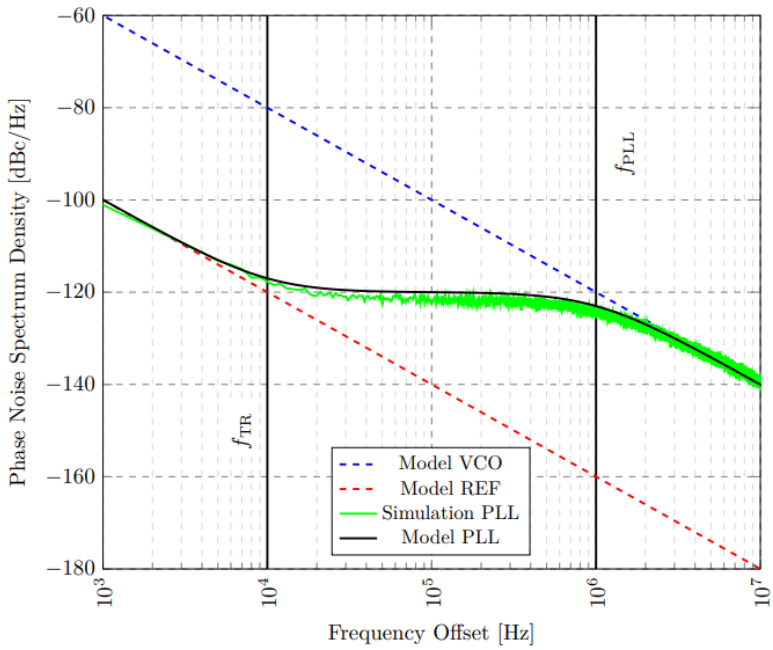

Figure 11-13: Comparison between simulation and analytical model of phase noise for PLL frequency of 1 MHz, sampling frequency of 100 MHz and 100K samples

11.9 Summary

This chapter outlines the progress and implementation of proof-of-concepts and simulation setups for 6G technologies, focusing on innovations in radio transceiver systems, AI-native interfaces, JCAS, and EMF assessments. It includes developments in flexible transceiver designs, enabling dynamic configuration adaptability for diverse communication scenarios, as well as advancements in AI-based channel feedback compression for multi-vendor compatibility and pilotless operations for increased SE. JCAS implementations address hardware reusability for communication and sensing, with attention to synchronization challenges. Power consumption and EMF exposure of 6G configurations are assessed for efficiency and compliance with the ICNIRP limits. Channel measurement campaigns are conducted for modelling purposes, while phase noise modelling aims to enhance MIMO performance by addressing intercarrier interference issues. Each section presents detailed methodologies, experimental setups, and results that collectively support the future 6G framework.

12 Conclusions and Key Take-Aways

This deliverable describes the necessary components towards an **inclusive, trustworthy, and flexible radio design** for future 6G networks. Further on, the deliverable adopts a holistic radio design framework that considers the entire radio system, and the interdependencies between different elements. The proposed framework focuses on four different aspects of holistic radio design, namely radio link modelling, architecture, deployment and optimization algorithms for JCAS, signal processing and algorithms, and flexible spectrum access solutions.

This deliverable presents the final results of the work done in WP4 of HEXA-X-II project, aiming at fulfilling the five objectives outlined for WP4 at the onset of the project. The first objective aims to *develop an inclusive, trustworthy, and flexible radio design tailored to meet given 6G KPIs and KVI requirements through analysis and integration of HW architectures, transmission schemes and security solutions*. This is done by defining a **holistic radio design framework**, radio scenarios and related KPIs/KVIs, integrating radio architectures and transmission schemes from WP4 tasks, investigating enablers on PHY security, resilience schemes, and E2E radio optimization framework, and working on the PoC: Flexible transceiver design.

A holistic approach ensures future-proof 6G networks that combine performance, scalability, efficiency, sustainability, and trustworthiness. Holistic radio design integrates technical and societal values, emphasizing environmental, social, and economic sustainability in 6G development. The design process adopting a holistic approach must be dynamic, evolving with each technological generation to meet diverse use case requirements. Finally, the system design must consider propagation environments, hardware constraints, and deployment strategies for optimal performance.

Flexible topologies support adaptable TN-NTN integration, D2D communication, and varying deployment environments. Flexible RAN architectures (centralized/distributed MAC/PHY) balance deployment flexibility, fronthaul capacity, and processing demands. Such flexible architecture is an example of use case-driven radio design guide that addresses extreme coverage, data rate, connection density, and low latency/high reliability. Sustainability is achieved through energy-efficient hardware, resource allocation, and deployment, alongside novel materials for reduced environmental impact and recyclability.

Some of the inclusive, trustworthy, and flexible radio enablers proposed in WP4 have been validated through simulations, modelling, and proof of concept. Examples of such validated key enabling technologies include new spectrum utilization & sharing techniques for sub-THz (above 100 GHz), cm-Wave (7-15 GHz), NTN-TN integration, and multi-RAT (5G-6G) spectrum sharing, advanced MIMO for improved spectral/energy efficiency and coverage, AI-driven signal processing, resource allocation, and hardware impairment compensation, JCAS for optimized network infrastructure usage, and RIS for mitigating blockages and enhancing coverage via adaptive radio environments.

The second WP objective is aimed at *providing a suitable channel model and developing novel broadband air-interface techniques to enable energy-efficient operations in the (sub-)THz bands, including new energy-efficient waveforms/modulations and advanced massive MIMO techniques*. To enable this, the research done in this task investigated identification and evaluation of enablers for sub-THz, such as beamforming architectures (hybrid and fully digital with one-bit quantization) and HW-aware waveforms and modulation (ZXM, polar constellation). Further contributions include link-level simulation carried out to evaluate the proposed modulation and coding schemes with legacy solutions, and work on channel measurement and modelling.

The findings of these studies reveal that while the FR3 band has recently attracted increased attention for the initial implementation of 6G, the sub-THz spectrum remains crucial for the long-term development of 6G and future generations. This should serve as a strong motivation to continue the research in this area. Moreover, while channel modelling, RF transceiver design, and physical-layer enablers for sub-THz communications have been studied extensively in an individual manner, the interplay between these factors is still an open question.

WP4's third objective was to *provide solutions that enable flexible, cross-functional joint communication and sensing over a unified radio infrastructure, including new architectures, signals, methods, and protocols*. This was done by identifying and evaluating JCAS enablers, including different JCAS architectures (monostatic, bistatic, and multistatic, with support from RIS and NTN), as well as the corresponding waveforms and resource allocation (in time, frequency, and space).

It was found that 6G LEO-based NTN can provide localization services by utilizing a single LEO satellite with the aid of RIS, where meter-level accuracy can be achieved at higher SNR. The main bottleneck towards achieving better accuracy lies in having a better channel parameter estimation of the RIS path. Leveraging existing network infrastructure and UEs for radar sensing increases the probability of LoS and enhances diversity, thereby improving positioning accuracy in urban environments. This highlights the potential of JCAS deployments for accurate UAV positioning in urban settings, utilizing existing cellular infrastructure and advanced waveform configurations.

Bistatic sensing, which involves separate units for transmitting and receiving signals, is particularly useful for tracking moving objects and mapping terrains due to the differing locations of the transmitter and receiver. Bistatic sensing in indoor scenarios was found to require high resource allocation in terms of power and bandwidth, making it a particularly amenable for deployment at higher frequency bands. However, the trade-off here is that higher bands have more pronounced hardware impairments, this affecting the sensing accuracy. On the other hand, combining OFDM waveforms with an appropriate CP demonstrated the potential for enhancing sensing performance. Lastly, two devices can collaboratively detect and locate objects or individuals in GNSS-denied and network-less environments in a bistatic device-to-device ISAC scenarios. This approach demonstrates secure, decentralized sensing and communication in challenging environments.

The next objective was to *design intelligent radio air interface to improve one or a combination of KPIs including spectral efficiency, energy efficiency, coverage, or lower cost at FR1 and FR2 spectrum*. The key enabler of the intelligent radio interface design includes solutions for transmitter and receiver enhancement such as AI-based schemes to reduce CSI overhead, optimization of modulation and coding, optimization of resource allocation for efficient utilization, enhancement of MU-MIMO, architectures and transmission schemes for D-MIMO, and RIS. The research done investigating this WP objective also contributed to the PoC: AI based air interface design. The key findings of the project on AI/ML for physical layer are as follows:

AI-Driven Waveform and Coding offers substantial improvements in SE and reduces transmission overhead. *AI-Based CSI compression* can significantly enhance network SE while minimizing the feedback overhead. These solutions are especially advantageous in dynamic network scenarios, and it has been shown that it is possible to design solutions that can operate also in multi-vendor scenario. *AI-Based MIMO Transmission* including power control, user pairing, and antenna management unlocks potential for more efficient communication schemes, including pilot-free transmissions, and introduce flexible strategies for maximizing throughput and user QoS; and finally *AI solutions for hardware impairment compensation* provides innovative approach to manage power amplifier non-linearities and other hardware impairments, ensuring stable performance in the presence of distortion or non-ideal components. These AI-based compensations allow for higher efficiency, and robustness in practical system implementations. The integration of these solutions within 6G networks requires a framework for AI/ML life cycle management and specific changes in the standard that are discussed and outlined in this deliverable.

The key findings of the project related to the MIMO technology is as follows: for D-MIMO transmissions *coherent beamforming* is feasible with analogue fronthaul signalling and the proposed *non-coherent beamforming* in the absence of CSI can ensure robust system performance. In terms of D-MIMO deployments, the use of rotary and movable antennas has opened new opportunities and presented major performance improvements in both MIMO and D-MIMO systems. Additionally, the optimization of JCAS beamforming within D-MIMO systems has been identified as a promising area for future research. For massive MIMO, energy-efficient hybrid beamforming architectures and deployment strategies have been proposed to minimize power consumption while maintaining high performance, supported by the development of a link-level signal model to optimize hybrid beamforming. In the context of MU-MIMO, low-complexity, data-driven channel estimation techniques have been introduced to handle scenarios where pilot-based CSI is unavailable, or channels vary rapidly. Lastly, for low-complexity MIMO, techniques to enhance the performance of 1-bit ADCs have been proposed for both single-cell and multi-cell scenarios, addressing quantization challenges,

and the performance of 1-bit ADCs and DACs has been analysed and compared to full-resolution counterparts, showcasing their potential for energy-efficient massive MIMO implementations.

The key findings related to RIS technology is as follows: RIS has shown potential for coverage enhancement only when the direct propagation path is strongly attenuated or fully blocked; however, RIS control is a complex challenge that needs further investigations towards possible standardization. In addition, there are several challenges to be addressed, e.g. Aggregated channel state information between transmitter, RIS, and receiver is difficult to acquire in dynamic environments; Uncontrolled interference, especially between operators, is a challenge due to broadband nature of RIS, requiring complex interference management techniques; Dynamically configuring the RIS in real time based on CSI and user needs might require complex algorithms that are challenging to implement with low cost and high energy efficiency; Multi-RIS deployment requires efficient algorithms and network protocols; RIS might need to be regulated, depending on deployment and adaptive control mechanisms. The existing technologies, e.g. network control repeater (NCR) can be considered as an alternative to RIS and the associated signalling and procedures for NCR can be investigated for possible integration of RIS in future network.

Finally, the last WP objective was aimed at *developing spectrum sharing and medium access mechanisms for enabling an efficient transition to 6G (coexistence) and low-latency service access*. The work items towards achieving this objective included research and evaluation of techniques for spectrum sharing with 5G, improved coexistence with other services in the same spectrum, specifically with satellite services, low-latency sub-THz spectrum access, and risk-informed random-access.

A key observation arising from these research activities is that the transition to 6G requires advanced spectrum management technologies to address spectrum scarcity, coexistence with incumbents, and low-latency spectrum access. Along this direction, spectrum sharing technologies including MRSS for 5G-6G spectrum sharing were investigated. It was shown that MRSS can mitigate inefficiencies associated with legacy spectrum-sharing techniques. It is further shown that separation distances to FSS-ES (3-4 GHz) can be reduced by applying more realistic system assumptions. In case of NTN integration, frequent NTN handovers are expected. Enablers like QoS-aware signalling of common information or time-based conditional handovers can improve efficiency of NTN HO procedures. Also, HAPS can offer improved coverage and performance compared to satellites. Lastly, to reduce spectrum access latency, techniques like a two-step booster-RAT methodology and a risk-informed random access were introduced, where it was shown that a low-band omni-RAT can enable ultra-low latency below 100 µs in the high-band RAT.

The deliverable also includes a description of the PoCs developed by WP4 in Chapter 11, detailing the implementation of PoCs and simulation setups for 6G technologies, focusing on innovations in radio transceiver systems, AI-native interfaces, JCAS, and EMF assessments.

References

[1999/519/EC] European Union, "Council Recommendation of 12 July 1999 on the limitation of exposure of the general public to electromagnetic fields (0 Hz to 300 GHz)," July 1999.

[2013/35/EU] European Union, "Directive of the European Parliament and of the Council of 26 June 2013 on the minimum health and safety requirements regarding the exposure of workers to the risks arising from physical agents (electromagnetic fields) (20th individual Directive within the meaning of Article 1 6(1) of Directive 89/391/EEC) and repealing Directive 2004/40/EC," June 2013.

[38.211] 3GPP TS 38.211 "Physical channels and modulation," v18.0.0, Technical Specification, 3rd Generation Partnership Project, 2023.

[38.214] 3GPP TS 38.214 "Physical layer procedures for data (Release 18)," v18.1.0, Technical Specification, 3rd Generation Partnership Project, 2023.

[38.843] 3GPP TR 38.843, "Study on artificial intelligence (AI)/machine learning (ML) for NR air interface," v18.0.0, Technical Report, 3rd Generation Partnership Project, 2024.

[38.863] 3GPP TR38.863, "Solutions for NR to support non-terrestrial networks (NTN)," Technical Report, 3rd Generation Partnership Project, Sep. 2022.

[38.901] 3GPP TR 38.901, "Study on channel model for frequencies from 0.5 to 100 GHz," v18.0.0, Technical Report, Mar. 2024.

[3GPP22] 3GPP, "Evaluation on AIML for CSI feedback enhancement," 3GPP TSG RAN WG1 #109-e, e-Meeting, May 9th – 20th, 2022.

[ACN+21] I. B. F. de Almeida, M. Chafii, A. Nimr, G. and Fettweis, "Blind Transmitter Localization in Wireless Sensor Networks: A Deep Learning Approach," IEEE 32nd Annual International Symposium on Personal, Indoor and Mobile Radio Communications (PIMRC), 2021

[AGT21] I. Atzeni, B. Gouda and A. Tölli, "Distributed precoding design via over-the-air signaling for cell-free massive MIMO," in IEEE Transactions on Wireless Communications, vol. 20, no. 2, pp. 1201-1216, Feb. 2021.

[APK+23] G. C. Alexandropoulos, D.-T. Phan-Huy, K.D. Katsanos et al., "RIS-enabled smart wireless environments: Deployment scenarios, network architecture, bandwidth and area of influence," EURASIP J. Wireless Comm. Network., vol. 2023, no. 1, p. 103, 2023.

[AT22] I. Atzeni and A. Tölli, "Channel estimation and data detection analysis of massive MIMO with 1-bit ADCs," IEEE Transactions on Wireless Communications, vol. 21, no. 6, pp. 3850–3867, 2022.

[ATD21] I. Atzeni, A. Tölli, and G. Durisi, "Low-resolution massive MIMO under hardware power consumption constraints," in Proc. Asilomar Conf. Signals, Syst., and Comput. (ASILOMAR), 2021.

[ATK+25] A. Kourani, J. Tuomela, V. Kurvi, L. Vähä-Savo, and K. Haneda, "Dynamic wideband channel sounding in an urban macrocellular scenario at 15 GHz," submitted at EuCAP 2025.

[ATM19] R. Ahmed, F. Tosato and M. Maso, "Overhead reduction of NR type II CSI for NR Release 16," WSA 2019; 23rd International ITG Workshop on Smart Antennas, Vienna, Austria, 2019, pp. 1-5.

[ATN+23] I. Atzeni, A. Tölli, D. H. N. Nguyen, and A. L. Swindlehurst, "Doubly 1-bit quantized massive MIMO," in Proc. Asilomar Conf. Signals, Syst., and Comput. (ASILOMAR), 2023.

[BBG+08] V. Brik, S. Banerjee, M. Gruteser, and S. Oh, “Wireless device identification with radiometric signatures,” pp. 116–127, Association for Computing Machinery, 2008.

[BC66] A. Ben-Israel and D. Cohen, “On iterative computation of generalized inverses and associated projections,” SIAM J. Numer. Anal. 3(1966), 410-419.

[BCN+24] B. Banerjee, C. Collmann, A. Nimr and G. Fettweis, “Flexible transceiver platform for holistic radio design analysis,” in Proceedings of 2024 3rd International Conference on 6G Networking (6GNet 2024), Paris, France, (p. 5), Oct 2024.

[BDO+21] A. Baltaci, E. Dinc, M. Ozger, A. Alabbasi, C. Cavdar, and D. Schupke, “A survey of wireless networks for future aerial communications (FA-COM),” IEEE Communications Surveys & Tutorials, vol. 23, no. 4, pp. 2833–2884, 2021.

[BHK+14] E. Björnson, J. Hoydis, M. Kountouris, and M. Debbah, “Massive MIMO systems with non-ideal hardware: Energy efficiency, estimation, and capacity limits,” IEEE Transactions on Information Theory, vol. 60, no. 11, pp. 7112-7139, Nov. 2014.

[CAC+24] J.-M. Conrat, M. Aliouane, J.-C. Cousin, and X. Begaud, “Material permittivity and conductivity estimation from 2 to 260 GHz and extension of the ITU-R P.2040 model at frequency above 100 GHz,” Personal, Indoor, Mobile Conference (PIMRC) 2024, Valencia, Spain, Sept. 2024.

[CAC+24a] J.-M. Conrat, M. Aliouane, J.-C. Cousin, and X. Begaud, “Building material permittivity and conductivity estimation from 2 to 260 GHz,” European Microwave Conference (EuMC) 2024, Paris, France Sept. 2024.

[CCB25] J.-M. Conrat, J.-C. Cousin, and X. Begaud, “Impact of rough building material surfaces on reflection coefficients from 5 GHz to 260 GHz,” submitted at EuCAP 2025.

[CMN+24] C. Collmann, A.B. Martínez, A. Nimr and G. Fettweis, “Angle-of-departure estimation algorithms for true-time-delay antenna arrays with software-defined radio,” in Proceedings of 4th IEEE International Symposium on Joint Communications & Sensing (JC&S 2024), Leuven, Belgium, Mar 2024.

[Con24] J.-M. Conrat, “Impact of rough and coated building material surfaces on reflection coefficients from 5 GHz to 260 GHz,” TD vol. 24, pp. 09023, COST Action CA20120, Linz, Austria, Sept. 2024.

[CV94] G. Corazza and F. Vatalaro, “A statistical model for land mobile satellite channels and its application to nongeostationary orbit systems,” IEEE Transactions on Vehicular Technology, vol. 43, no. 3, pp. 738–742, 1994.

[DD16] C. Desset and B. Debaillie, “Massive MIMO for energy-efficient communications,” in EuMC, London, UK, Oct. 2016.

[Dev15] J. P. De Vries, “Risk-informed interference assessment: A quantitative basis for spectrum allocation decisions,” Proc. TPRC, 2015, [online] Available: http://ssrn.com/abstract=2574459.

[DH23] M. F. De Guzman, and K. Haneda, “Analysis of wave-interacting objects in indoor and outdoor environments at 142 GHz,” IEEE Transactions on Antennas and Propagation, 2023.

[DH25] M. F. de Guzman and K. Haneda, “3GPP-like channel model at sub-Terahertz: Improved cluster generation and experimental verification,” IEEE Trans. Ant. Prop., to appear.

[DH25a] M. F. de Guzman and K. Haneda, “Calibration of ray-launcher based on indoor and outdoor sub-THz channel measurements,” IEEE Trans. Ant. Prop., under review.

[DHK23] M. F. de Guzman, K. Haneda, and P. Kyösti, “Measurement-based MIMO channel model at 140 GHz,” https://doi.org/10.5281/zenodo.7640353.

[DLT+17] J. P. De Vries, U. Livnat, and S. Tonkin, “A risk-informed interference assessment of MetSat/LTE coexistence,” in *IEEE Access*, vol. 5, pp. 6290-6313, 2017, doi: 10.1109/ACCESS.2017.2685592.

[DWZ+20] C. Desset, P. Wambacq, Y. Zhang, M. Ingels, and A. Bourdoux, “A flexible power model for mm-wave and THz high-throughput communication systems,” In PIMRC Workshop on Enabling Technologies for Terahertz Communications (ETTCOM), London, UK, August 2020.

[DZK25] S. Das, P. Zhang, P. Kyösti, “Wideband near-field extension for the 3GPP geometry based stochastic channel model,” https://doi.org/10.5281/zenodo.14843297.

[EHH+20] M. Elkhouly M. J. Holyoak, D. Hendry et al., “D-band phased-array TX and RX front ends utilizing radio-on-glass technology,” 2020 IEEE Radio Frequency Integrated Circuits Symposium (RFIC), Los Angeles, CA, USA, 2020.

[Ell21] S.W. Ellingson, “Path loss in reconfigurable intelligent surface-enabled channels,’’ IEEE 32nd Annual International Symposium on Personal, Indoor and Mobile Radio Communications (PIMRC), Sept. 2021.

[EN50385] CENELEC, “Product standard to demonstrate the compliance of base station equipment with radiofrequency electromagnetic field exposure limits (110 MHz - 100 GHz), when placed on the market,” EN50385, Oct. 2017.

[ETSI24] ETSI, “Reconfigurable intelligent surfaces,” https://www.etsi.org/technologies/reconfigurable-intelligent-surfaces, accessed Nov. 28, 2024.

[ETSI25] ETSI, “ETSI releases first use cases for reconfigurable intelligent surface,” https://www.etsi.org/newsroom/press-releases/2236-etsi-releases-first-use-cases-for-reconfigurable-intelligent-surface, accessed Feb. 13, 2025.

[FDB+19] G. Fettweis, M. Dörpinghaus, S. Bender, L. Landau, P. Neuhaus, and M. Schlüter, “Zero crossing modulation for communication with temporally oversampled 1-bit quantization,” in Proc. 53rd Asilomar Conf. Signals, Syst. Comput., Pacific Grove, CA, USA, Nov. 2019, pp. 207–214

[GAT24] B. Gouda, I. Atzeni and A. Tölli, “Pilot-aided distributed multi-group multicast precoding design for cell-free massive MIMO,” in IEEE Transactions on Wireless Communications, vol. 23, no. 8, pp. 9282-9298, Aug. 2024.

[GRD+25] F. Gast, F. Roth, M. Dörpinghaus, P. Sen, S. Zeitz, G. Fettweis “The role of oscillator phase noise in maximizing transceiver energy efficiency,” submitted for review to WCNC 25

[GRH+22] I.E. Gordon, L.S. Rothman, R.J. Hargreaves et al., “The HITRAN2020 molecular spectroscopic database,” J. Quant. Spectrosc. Radiat. Transfer, vol. 277, pp. 1–82, Jan. 2022.

[GSM+23] S. Gunarathne, T. Sivalingam, N. H. Mahmood, N. Rajatheva, and M. Latva-aho, “Decomposition based interference management framework for local 6G networks,” in Globecom Workshops, 2023, KL, Malaysia.

[GWJ+22] J. Guo, C. -K. Wen, S. Jin and G. Y. Li, “Overview of deep learning-based CSI feedback in massive MIMO systems,” in IEEE Transactions on Communications, vol. 70, no. 12, pp. 8017-8045, Dec. 2022. {arXiv:2206.14383v1}

[HEX223-D22] Hexa-X-II, “Deliverable D2.2: Foundation of overall 6G system design and preliminary evaluation results,” Dec. 2023.

[HEX223-D42] Hexa-X-II, “Deliverable D4.2: Radio design and spectrum access requirements and key enablers for 6G evolution,” Oct. 2023.

[HEX224-D43] Hexa-X-II, “Deliverable D4.3: Early results of 6G radio key enablers,” April 2024.

[HEX224-D44] Hexa-x-II, “Deliverable D4.4: Final design of 6G radio solutions and promising radio innovations (preview),” Dec. 2024.

[HEX224-D53] Hexa-X-II “Deliverable D5.3: Initial design and validation of technologies and architecture of 6G devices and infrastructure,” Feb. 2024.

[HEX23-D23] Hexa-X, “Deliverable D2.3: Radio models and enabling techniques towards ultra-high data rate links and capacity in 6G,” Mar. 2023.

[HW21] H. Halbauer, T. Wild, “Towards power efficient 6G Sub-THz transmission,” Joint EuCNC & 6G Summit, June 8-11, 2021, Porto, Portugal

[HWW+18] H. Halbauer, A. Weber, D. Wiegner, and T. Wild, “Energy efficient massive MIMO array configurations,” 2018 IEEE Globecom Workshops (GC Wkshps), Abu Dhabi, UAE, Dec. 2018.

[ICNIRP20] ICNIRP, “Guidelines for limiting exposure to electromagnetic fields (100 kHz to 300 GHz)”, Health Physics, vol. 118, no. 5, pp. 483-524, May 2020.

[ICNIRP98] ICNIRP, “Guidelines for limiting exposure to time-varying electric, magnetic, and electromagnetic fields (up to 300 GHz),” Health physics, vol. 74, no. 4, pp. 494-522, April 1998.

[IEC62232] International Electrotechnical Commission, “Determination of RF field strength, power density and SAR in the vicinity of radiocommunication base stations for the purpose of evaluating human exposure,” IEC 62232:2022, Oct. 2022.

[IEEE21] IEEE, “IEEE Draft Standard Method for Modeling Spectrum Consumption,” in IEEE P1900.5.2/D1.0, Nov. 2021, vol., no., pp.1-270, 14 Dec. 2021.

[KHR23] F. E. Kadan, O. Haliloglu, and A. Reial, “Alamouti-like transmission schemes in distributed MIMO networks,” arXiv preprint arXiv:2302.03969, 2023.

[KKA+21] G. Karabulut Kurt, M. G. Khoshkholgh, S. Alfattani, A. Ibrahim, T. S. J. Darwish, M. S. Alam, H. Yanikomeroglu, and A. Yongacoglu, “A vision and framework for the high-altitude platform station (HAPS) networks of the future,” IEEE Communications Surveys & Tutorials, vol. 23, no. 2, pp. 729–779, 2021.

[KKP+14] M. R. Khanzadi, D. Kuylenstierna, A. Panahi, T. Eriksson, and H. Zirath, “Calculation of the performance of communication systems from measured oscillator phase noise,” IEEE Trans. Circuits and Syst. I: Regul. Pap., vol. 61, no. 5, 2014.

[KRR+24] P. Karunasena, N. Rajatheva, N. Rajapaksha, D. Dampahalage, D. Marasinghe and M. Latva-Aho, “Jointly-mapped reflection modulation with reconfigurable intelligent surfaces,” ICC 2024 - IEEE International Conference on Communications, Denver, CO, USA, 2024, pp. 581-586, doi: 10.1109/ICC51166.2024.10622855.

[LAL23] M. Letafati, S. Ali, and M. Latva-aho, “Diffusion models for wireless communications,” arXiv preprint arXiv:2310.07312, Dec. 2023.

[LAL24] M. Letafati, S. Ali, M. Latva-aho, “Denoising diffusion probabilistic models for hardware-impaired communications,” 2024 IEEE Wireless Communications and Networking Conference (WCNC), Dubai, United Arab Emirates, 2024, pp. 1-6.

[LAL24a] M. Letafati, S. Ali, and M. Latva-Aho, “Diffusion model-aided data reconstruction in cell-free massive MIMO downlink: A computation-aware approach,” IEEE Wireless Communications Letters, Sep. 2024, doi: 10.1109/LWC.2024.3457008.

[LBH15] Y. LeCun, Y. Bengio, and G. E. Hinton, “Deep learning,” Nature, vol. 521, pp. 436–444, 2015.

[LCW+22] S. Lin, F. Chen, M. Wen, Y. Feng, and M. Di Renzo, "Reconfigurable intelligent surface-aided quadrature reflection modulation for simultaneous passive beamforming and information transfer," IEEE Transactions on Wireless Communications, vol. 21, no. 3, pp. 1469–1481, 2022.

[LDL+21] G. Larue, L.-A. Dufrene, Q. Lampin, P. Chollet, H. Ghauch, and G. Rekaya, "Blind neural belief propagation decoder for linear block codes," EnCNC 2021, Jun 2021, Porto, Portugal. ffhal-03275838.

[LMS+21] A. Li, C. Masouros, A. L. Swindlehurst, and W. Yu, "1-bit massive MIMO transmission: Embracing interference with symbol-level precoding," IEEE Commun. Mag., vol. 59, no. 5, pp. 121–127, 2021.

[LZA+21] S. Lin, B. Zheng, G. C. Alexandropoulos, M. Wen, M. D. Renzo, and F. Chen, "Reconfigurable intelligent surfaces with reflection pattern modulation: Beamforming design and performance analysis," IEEE Transactions on Wireless Communications, vol. 20, no. 2, pp. 741–754, 2021.

[MNM+24a] D. Marasinghe, L.H. Nguyen, J. Mohammadi, Y. Chen, T. Wild and N. Rajatheva, "Constellation shaping under phase noise impairment for Sub-THz Communications," in ICC 2024 - IEEE International Conference on Communications, 2024, pp. 3833–3838.

[MNM+24b] D. Marasinghe, L.H. Nguyen, J. Mohammadi, Y. Chen, T. Wild and N. Rajatheva, "Waveform learning under phase noise impairment for sub-THz communications," IEEE Transactions on Communications, pp. 1–1, 2024, doi: 10.1109/TCOMM.2024.3430982.

[MSP+24] N. H. Mahmood, S. Samarakoon, P. Porambage, M. Bennis and M. Latva-aho, "Resilient-by-design: A resiliency framework for future wireless networks," arXiv, Oct. 2024. https://arxiv.org/pdf/2410.23203

[Mur97] B. Murmann, "ADC performance survey 1997-2024," [Online]. Available: https://github.com/bmurmann/ADC-survey.

[NHM+24] L. H. Nguyen, H. Heimpel, D. Marasinghe, H. Halbauer and T. Wild, "Sub-THz waveform evaluation in the D-band: A proof of concept study," in 2024 Joint European Conference on Networks and Communications & 6G Summit (EuCNC/6G Summit), 2024, pp. 1027–1032

[NSN21] L. V. Nguyen, A. L. Swindlehurst, and D. H. N. Nguyen, "Linear and deep neural network-based receivers for massive MIMO systems with one-bit ADCs," IEEE. Transactions on Wireless Communications, vol. 20, no. 11, pp. 7333–7345, 2021.

[NWP+25] T. Nhem, M. Weyn, M. Peeters, and R. Berkvens, "FlexiPrint: Adaptive radio fingerprinting for length variability," submitted to IEEE JCNS symposium 2025.

[ORAN23] O-RAN, "O-RAN use cases detailed specification," v12.0, Oct. 2023.

[Orf16] S. J. Orfanidis, "Electromagnetic waves and antennas," Rutgers University, 2016. Available: https://eceweb1.rutgers.edu/~orfanidi/ewa/

[Par24] A. V. Parambath, "Integration of reconfigurable intelligent surfaces (RISs) in D-MIMO networks for 6G," M.S. Thesis, Sch. of Electr., Chalmers Univ., Göteborg, 2024.

[Online]. Available: http://hdl.handle.net/20.500.12380/307987.

[PFM+24] A. V. Parambath, J. Flordelis, C. Madapatha, F. Rusek, E. L. Bengtsson, T. Svensson, "Integrating reconfigurable intelligent surfaces (RISs) into indoor D-MIMO networks for 6G," in Proc. IEEE Veh. Technol. Conf., VTC2024-Fall, Washington, D.C., 2024.

[RAT24] A. Radbord, I. Atzeni, and A. Tölli, "Enhanced uplink data detection for massive MIMO with 1-bit ADCs: Analysis and joint detection," IEEE Trans. Signal Process. (submitted), 2024.

[Raz21] B. Razavi, “Jitter-power trade-offs in PLLs,” IEEE Trans. Circuits Syst.I: Regul. Pap., vol. 68, no. 4, 2021.

[RFZ+24] F. Rusek, J. Flordelis, K, Zhao, E. Bengtsson, O. Zander, “Spatially selective reconfigurable intelligent surfaces through element permutation,” in IEEE Inter. Conf. Comm., ICC 2024, Denver, CO, USA, 2024.

[RH20] J. Rak and D. Hutchison (ed.), “Guide to disaster-resilient communication networks,” Springer, 2020, Zurich, Switzerland.

[RKL+20] K. Rikkinen, P. Kyosti, M. E. Leinonen, M. Berg, and A. Parssinen, “THz radio communication: Link budget analysis toward 6G,” IEEE Communications Magazine, vol. 58, no.11, pp.22-27, 2020.

[RMW+24] N. Rajapaksha, J. Mohammadi, S. Wesemann, T. Wild and N. Rajatheva, “Minimizing energy consumption in MU-MIMO via antenna muting by neural networks with asymmetric loss,” in IEEE Transactions on Vehicular Technology, vol. 73, no. 5, pp. 6600-6613, May 2024, doi: 10.1109/TVT.2023.3339340.

[RRL+24] N. Rajapaksha, N. Rajatheva and M. Latva-Aho, “Deep learning-based joint pilot and data power control in cell-free massive MIMO networks,” 2024 IEEE 100th Vehicular Technology Conference (VTC2024-Fall), Washington, DC, USA, 2024, pp. 1-6, doi: 10.1109/VTC2024-Fall63153.2024.10757576.

[RXM+17] T. S. Rappaport, Y. Xing, G. R. MacCartney, A. F. Molisch, E. Mellios and J. Zhang, “Overview of millimeter wave communications for fifth-generation (5G) wireless networks - with a focus on propagation models,” in IEEE Transactions on Antennas and Propagation, vol. 65, no. 12, pp. 6213-6230, Dec. 2017, doi: 10.1109/TAP.2017.2734243.

[SB15] J. A. Stine and C. E. Caicedo Bastidas, “Enabling spectrum sharing via spectrum consumption models,” in IEEE Journal on Selected Areas in Communications, vol. 33, no. 4, pp. 725-735, April 2015, doi: 10.1109/JSAC.2015.2393451

[Sem22] Semtech Corp., “AN1200.64: LR-FHSS system performance,” Oct. 2022, rev. 1.3. [Online]. Available: semtech.com/products/wireless-rf/lora-edge/lr1110#documentation.

[SM25] J. Sant'Ana and N. H. Mahmood, “Performance Analysis of LoRa and LR-FHSS in HAPS Systems for Remote Area IoT Coverage”, submitted to EuCNC & 6G Summit 2025.

[SSH+20] A. Singh, M. Sayginer, M. J. Holyoak et al., “A D-band radio-on-glass module for spectrally-efficient and low-cost wireless backhaul,” 2020 IEEE Radio Frequency Integrated Circuits Symposium (RFIC), Los Angeles, CA, USA, 2020.

[STK+23] E. Semaan, E. Tejedor, R. Kumar Kochhar, S. Magnusson, S. Parkwall,” 6G spectrum - enabling the future mobile life beyond 2030”, GFTL-23:000243 Uen, Ericsson White Paper, March 2023

[STM+22] R. A. Salem, F. Tosato, M. Maso, W. Hillery, “US11424807 patent: Enhanced frequency compression for overhead reduction for CSI reporting and usage,” Publication date: 2022-Aug-23.

[Tau88] O. Taussky, “How I became a torchbearer for matrix theory,” The American Mathematical Monthly, Vol. 95, No. 9, Nov. 1988, pp. 801-812.

[Tel99] I. E. Telatar, “Capacity of multi-antenna Gaussian channels,” European Transactions on Telecommunications, vol. 10, no. 6, pp. 585-595, Nov. 1999.

[TLP+20] O. Tervo, T. Levanen, K. Pajukoski, J. Hulkkonen, P. Wainio and M. Valkama, “5G New Radio evolution towards Sub-THz communications,” 2020 2nd 6G Wireless

Summit (6G SUMMIT), Levi, Finland, 020, pp. 1-6, doi: 10.1109/6GSUMMIT49458.2020.9083807.

[TLS+24] E. N. Tominaga, O. L. A. López, T. Svensson, R. D. Souza and H. Alves, "Distributed MIMO networks with rotary ULAs for indoor scenarios under rician fading," in IEEE Open Journal of the Communications Society, vol. 5, pp. 6367-6380, 2024, doi: 10.1109/OJCOMS.2024.3474170.

[UMA22] M. A. Ullah, K. Mikhaylov, and H. Alves, "Analysis and simulation of LoRaWAN LR-FHSS for direct-to-satellite scenario," IEEE Wireless Communications Letters, vol. 11, no. 3, pp. 548–552, 2022.

[US07] O. Ureten and N. Serinken, "Wireless security through rf fingerprinting," Canadian Journal of Electrical and Computer Engineering, vol. 32, no. 1, pp. 27–33, 2007.

[Var04] R. S.Varga, "Gersgorinand and his circles," Springer, 2004.

[VSD+17] A. M. Voicu, L. Simić, J. P. de Vries, M. Petrova, and P. Mähönen, "Risk-informed interference assessment for shared spectrum bands: A Wi-Fi/LTE coexistence case study," in IEEE Transactions on Cognitive Communications and Networking, vol. 3, no. 3, pp. 505-519, Sept. 2017, doi: 10.1109/TCCN.2017.2746567.

[WDV23] S. Wesemann, J. Du, and H. Viswanathan, "Energy efficient extreme MIMO: Design goals and directions," IEEE Communications Magazine, Oct. 2023.

[WLP+19] X. Wang, M. Laabs, D. Plettemeier, K. Kosaka and Y. Matsunaga, "28 GHz multi-beam antenna array based on wideband high-dimension 16x16 butler matrix," 2019 13th European Conference on Antennas and Propagation (EuCAP), Krakow, Poland, 2019, pp. 1-4.

[WTL+22] J. Wang, W. Tang, J. C. Liang, L. Zhang, J. Y. Dai, X. Li, S. Jin, Q. Cheng, and T. J. Cui, "Reconfigurable intelligent surface: Power consumption modeling and practical measurement validation," 10.48550/arXiv.2211.00323, 2022.

[XAC+22] B. Xu, D. AnguianoSanjurjo, D. Colombi, and C. Törnevik, "A Monte Carlo analysis of actual maximum exposure from a 5G millimeter-wave base station antenna for EMF compliance assessments," Frontiers in Public Health 9, Jan. 2022.

[XCJ+22] B. Xu, D. Colombi, P. Joshi, F. Ghasemifard, D. Anguiano Sanjurojo, C. Di Paola, and C. Törnevik, "A summary of actual maximum approach studies on EMF compliance of 5G radio base stations," 2022 16th European Conference on Antennas and Propagation (EuCAP), Madrid, Spain, Mar. 2022, pp. 1-5.

[XWL+22] H. Xiao, Z. Wang, D. Li, et al, "AI enlightens wireless communication: A transformer backbone for CSI feedback," {arXiv:2206.07949}, Jun. 2022.

[YH10] H. Yuan and A. Hu, "Preamble-based detection of Wi-Fi transmitter RF fingerprints," Electronics Letters, vol. 46, pp. 1165–1167, 2010.

[ZMZ24] L. Zhu, W. Ma, and R. Zhang, "Movable antennas for wireless communication: Opportunities and challenges," in IEEE Communications Magazine, vol. 62, no. 6, pp. 114-120, June 2024, doi: 10.1109/MCOM.001.2300212.

A Appendix

A.1 MU-MIMO optimisation in diverse device scenarios

When the UE Tx/Rx EA sets are constrained to be the same it allows to apply the powerful concepts of "learning channel from the decoded data" (see [HEX224-D43, Sec. A.2.2). This addresses the channel ageing problem in TDD systems where BS:

- decodes the UL transmissions (with forward error correction) from the UE Tx EAs.
- uses Rx signals and the abundant symbols (decoded) and from pilots (if present) to decode the channel matrices by using frequency/time averaging and *pinv* (or its regularisations and generalizations with forgetting weights and post-processing).
- then, using this most recent estimated channel (deduced from the UL decoded transmissions), constructs the MU-MIMO DL precoder.

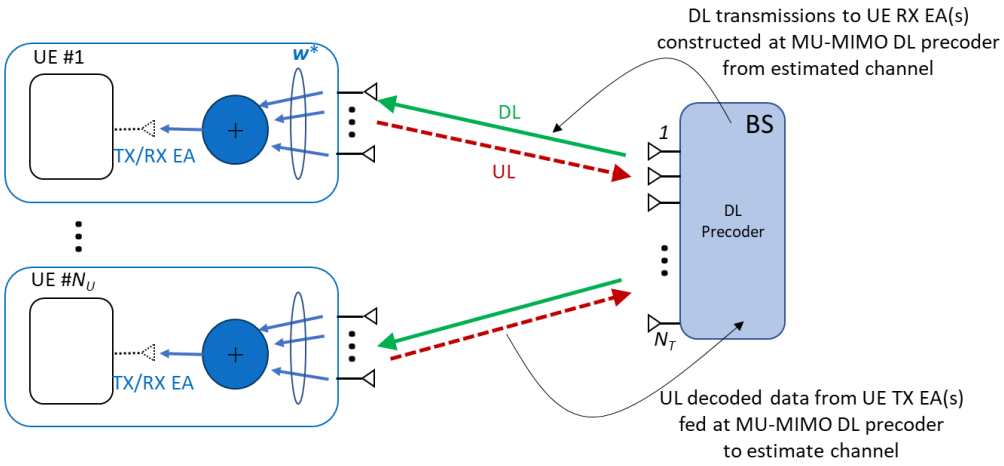

Figure A-1: Optimized dimensionality approach including UL decoding usage (from all UEs) to construct the BS DL precoder and perform DL transmission. Example for single Tx/Rx EA UEs.

As we presented above, the challenge for channel decoding from data is not only in the large dimensions of the matrices MU-MIMO matrices but especially in the low-moderate SNR of the UL signals from which (together with the decoded data) the large MU-MIMO matrix individual components have to be estimated. It is important to stress that the actual engineeringly interesting working point is in this SNR range for large arrays, since the following MIMO decoding algorithms are capable to rise the SNR up to estimate the unknown symbols but not for estimation of the channel matrix components, which are essentially lager than the total number of the information layers of all users.

For example, with 4 EAs for 4 users (having each 1 EA) and the BS having array of 32 antennas, the MU-MIMO matrix size per every RE is 4x32, while the total number of information layers in this example is 4. The signal processing uses array gain (e.g. but not necessarily via QR maximum-likelihood detection approach) to decode 4 layers with 32 antennas. Due to this gain, the constellation size can be large e.g. 64QAM. 32 antennas, ideally bring gain of 10*log10(32) = 15 dB (in MIMO processing the actual gain is smaller), thus the SNR=10 dB on the BS antennas can be enough to decode the 64QAM constellation (6 bits demands 6*3=18 dB SNR for the Shannon capacity, and we have 10+15 minus some MIMO reduction of the gain. Thus 10 dB SNR after array processing is expected to leave enough gap for the decoding). However, the question arises if we can rise up the channel reconstruction accuracy from 10 dB to 25 dB.
The channel reconstruction equations follow [HEX224-D43, Eq. (A.2.19-23)]. One may heuristically expect that the channel matrix reconstruction noise power (despite this is not a scalar but matrix estimation) is inverse to the size N_E of "support" RE set namely of the REs over which the pinv operation is applied. For example, with averaging over 45 REs we might approximately have the factor 10*log10(45) = 16.5 dB. This averaging

thus may (which we observe in the simulation, see Figure 4-16) work close to the ideal array gain of 32 antennas (corresponding to 15 dB).
The limit on the ability to average is placed by channel frequency selectivity/behaviour. For channel with high selectivity, we may apply 2D frequency-time averaging to limit the support size in the frequency domain and redistribute the averaging over frequency-time domain preserving the total number of REs used in the pinv.

Since the pinv in [HEX224-D43, Eq. (A2.22)] contains inverse of the correlation matrix, we also performed analytical investigation of the classical Ben-Israel and Cohen iterative matrix inversion method stability with non-classical initial seed to partially reduce complexity. Namely for correlation matrix $\boldsymbol{C}$ its inverse $\boldsymbol{M} = \boldsymbol{C}^{-1}$ can be calculated following the classical Ben-Israel and Cohen iterative matrix inversion method [BC66] as

$$\boldsymbol{M}_{k+1} = 2\boldsymbol{M}_k - \boldsymbol{M}_k\boldsymbol{C}\boldsymbol{M}_k \tag{A-1}$$

where the first step can be simplified, as we propose, by using

$$\boldsymbol{M}_0 = \alpha_* \mathbf{1} \tag{A-2}$$

which is different and simpler from the Classical [BC66] $\boldsymbol{M}_0 = \alpha_* \boldsymbol{C}\boldsymbol{C}^H$. One may show that the iterative process always converges for (or smaller value, but we use the maximal one for faster convergence)

$$\alpha_* = \frac{1}{\max\limits_i\left(\sum_{k=1}^{N_U}|C_{ik}|\right)} \tag{A-3}$$

The convergence, with some elaboration, follows from the Gershgorin's circles result (see similar [BC66] and for general information on Gershgorin circles: [Var04] and [Tau88]). To accelerate the convergence, one may apply (in the heuristic manner) initially larger gain which decrease as:

$$\begin{gathered}\boldsymbol{M}_{k+1} = (1+\gamma_k)\boldsymbol{M}_k - \gamma_k\boldsymbol{M}_k\boldsymbol{C}\boldsymbol{M}_k \\ \gamma_k = 1 + 1/k\end{gathered} \tag{A-4}$$

We observe practical (and slightly faster than with $\gamma_k = 1$) convergence here.

A.2 D-MIMO assisted with RIS

Here, we collect some figures referred to in Section 5.2 but not included due to a lack of space. Figure A-2 shows the evolution of the service coverage probability for various cluster sizes as a function of the number of RIS elements, and it complements the plots in Figure 5-2 for the UE SINR and the system's energy efficiency.

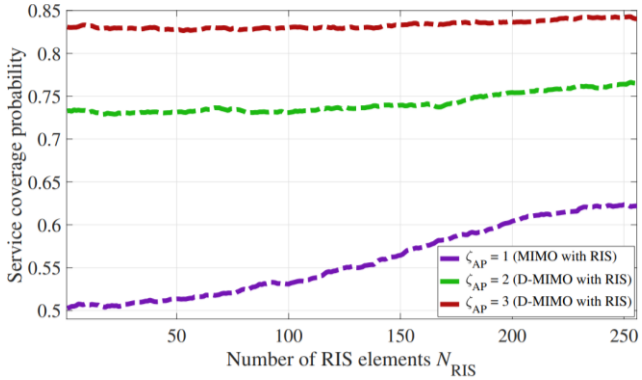

Figure A-2: Service coverage probability of D-MIMO assisted with RIS when varying the number of RIS elements N_{RIS} from 1 to 256 (f_c = 4 GHz, B = 100 MHz, P_T = 25 dBm).

In computing the plots of Figure A-2: Service coverage probability of D-MIMO assisted with RIS when varying the number of RIS elements N_{RIS} from 1 to 256 (f_c = 4 GHz, B = 100 MHz, P_T = 25 dBm).

, the service coverage probability has been defined as [PFM+24]:

$$\text{Service Coverage}_{\text{prob}} = \Pr(R_{\text{UE}} \geq R_{\text{th}}), \quad \textbf{(A-5)}$$

where R_{UE} is the instantaneous UE data rate and R_{th} is a predefined threshold. For the results presented in this work, we have used $R_{\text{th}} = 100$ Mbps. Figure A-3(a) suggests that multi-RIS assistance (i.e., a single UE assisted by more than one RIS) and higher RIS deployment densities can yield significant advantages in terms of UE SINR. Active RISs that amplify and redirect incident signals can also be used to enhance the system performance, as shown in Figure A-3(b). To obtain the latter plots, the noise introduced by active RISs needs to be considered. For that, we have used the noise model presented in Section 5.1.

RISs with low power consumption, should the overall system's energy efficiency not deteriorate.

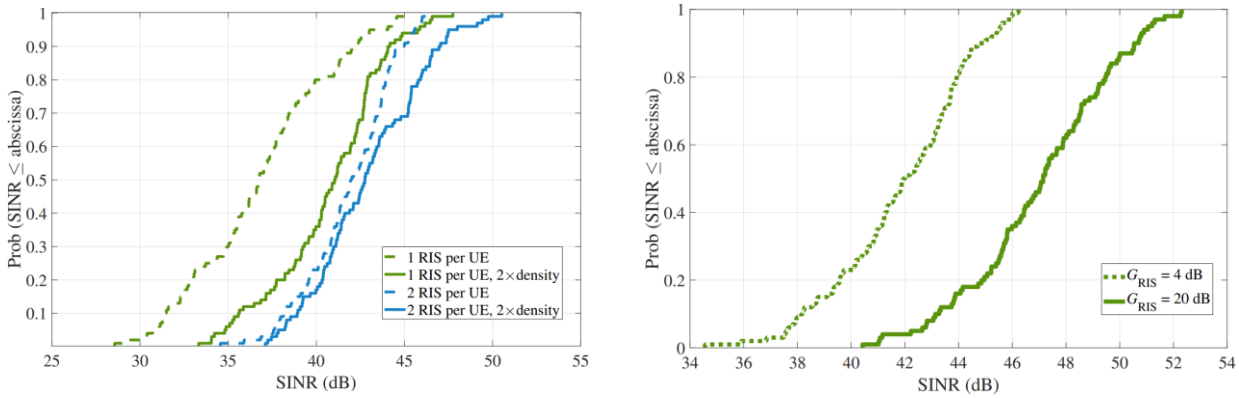

(a) Multi-RIS assistance. **(b) Active RIS.**

Figure A-3: Evaluation of (a) multi-RIS assistance and (b) active RIS ($f_c = 4$ GHz, $B = 100$ MHz, P_T = 25 dBm, and N_{RIS} = 256, in both cases).

A.3 Intelligent CSI compression

We propose to pre-process these inputs via linear transforms (Figure A-4) to make the new modified inputs be more similar and for better compression

$$\boldsymbol{x}_n^{(\text{modified})} = \boldsymbol{x}_n \boldsymbol{M}_n \text{ for } n = 1{:}\, N_{SB} \quad \textbf{(A-6)}$$

Here, $\boldsymbol{x}_n$ is a precoder matrix for UE per SB with v columns (representing e.g. v best channel matrix eigenvectors). Dimension of $\boldsymbol{M}_n$ is $\dim \boldsymbol{M}_n = v \times v$. Here v is the number of information layers for UE.

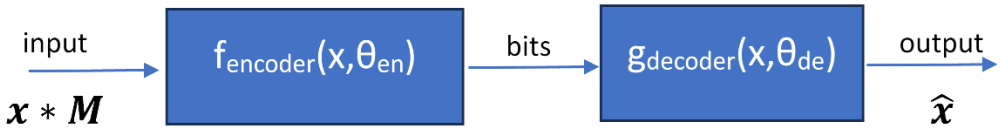

Figure A-4: Pre-processing of the input via M (which is an optimized Unitary Matrix), per every SB.

Optimization (maximization or minimization) can now use not only $\{\boldsymbol{\theta}_{\text{en}}, \boldsymbol{\theta}_{\text{de}}\}$ parameters, but also $\{\boldsymbol{M}_n\}$. The compression-decompression is for a given number of bits (notations of [3GPP22] are used here):

$$\hat{\boldsymbol{x}} = \hat{\boldsymbol{x}}(\boldsymbol{x}, \{\boldsymbol{M}_n\}, \boldsymbol{\theta}_{\text{en}}, \boldsymbol{\theta}_{\text{de}}) = g_{\text{decoder}}(f_{encoder}\,(\boldsymbol{x} * \boldsymbol{M}, \boldsymbol{\theta}_{\text{encoder}}), \boldsymbol{\theta}_{\text{decoder}}) \quad \textbf{(A-7)}$$

For given $\boldsymbol{x}$, optimizations can be e.g. for the following criteria:

1. Reconstruction error minimization: $E^{(\text{modified})} = \left\|\hat{\boldsymbol{x}} - \boldsymbol{x}^{(\text{modified})}\right\|^2 = \frac{1}{N_S}\sum_{n=1}^{N_S}\|\hat{\boldsymbol{x}}_n - \boldsymbol{x}_n * \boldsymbol{M}_n\|^2$ vs. previous $E^{(\text{direct})} = \|\hat{\boldsymbol{x}} - \boldsymbol{x}\|^2$
2. Capacity maximization of precoder based on $\hat{\boldsymbol{x}}$ (and assuming UE knows H)

3. Average CS (cosine similarity) maximization between $\hat{\boldsymbol{x}}$ and $\boldsymbol{x}^{(\text{modified})}$.

The transform matrices are hidden CSI compression degrees of freedom preserving the communication properties e.g. capacity (or the total power over UE array antennas). Unitary matrices $\mathbb{U}_n$ can be such transforms optimized per SB: $\boldsymbol{M}_n = \mathbb{U}_n$.

$$\dim \mathbb{U}_n = \upsilon \times \upsilon \tag{A-8}$$

$\mathbb{U}_n$ may be the general unitary transform. A special case of diagonal unitary matrices is:

$\mathbb{U}_n = \text{diag}\left(e^{j\boldsymbol{\phi}_n}\right)$, $\dim \boldsymbol{\phi}_n = \upsilon \times 1$, $n = 1{:}\,N_S$. For example, for a number of columns is three, a diagonal unitary transform may be written:

$$\mathbb{U}_n = \begin{pmatrix} e^{j\phi_{(1)n}} & 0 & 0 \\ 0 & e^{j\phi_{(2)n}} & 0 \\ 0 & 0 & e^{j\phi_{(3)n}} \end{pmatrix}, \text{ for every } n = 1{:}\,N_S \tag{A-9}$$

If the SB input matrix per n comprises three columns $\boldsymbol{x}_n = \left[\boldsymbol{c}_{(1)n}, \boldsymbol{c}_{(2)n}, \boldsymbol{c}_{(3)n}\right]$, then they are modified (at SB n) as:

$$\boldsymbol{x}_n^{(\text{modified})} = \left[e^{j\phi_{(1)n}} * \boldsymbol{c}_{(1)n}, e^{j\phi_{(2)n}} * \boldsymbol{c}_{(2)n}, e^{j\phi_{(3)n}} * \boldsymbol{c}_{(3)n}\right] \tag{A-10}$$

The direct optimization can use the Barrier Function approach adding to minimization criterion (e.g. to an error) a penalty (or alternatively, subtracting it from the maximization criterion such as capacity or CS):

$$BarrierTerm(\boldsymbol{M}) = \sum_{n=1}^{N_S} Barrier(\|\boldsymbol{M}_n\boldsymbol{M}_n^H - \mathbf{1}_{\upsilon\times\upsilon}\| + \|\boldsymbol{M}_n^H\boldsymbol{M}_n - \mathbf{1}_{\upsilon\times\upsilon}\|) \tag{A-11}$$

Such direct optimization conveniently represents the addition of a single NN layer with (i.) linear activation function (no nonlinearity), (ii.) zero bias (in NN coefficient sense), and (iii.) with weights $\boldsymbol{M}$ which are (via Barrier functions) constrained to be unitary.

Alternative, we propose for diagonal unitary matrices a more intuitive method. Let us modify N_S columns $\boldsymbol{x}_{(\ell)n}$ of the inputs $\boldsymbol{x}_{(n)}$ per layer ℓ (e.g. they can be N_S columns of the eigenvectors for layer ℓ):

$$\boldsymbol{x}_{(\ell)n}^{(\text{modified})} = \boldsymbol{x}_{(\ell)n} * \frac{\boldsymbol{x}_{(\ell)n}^H \boldsymbol{a}_{(\ell)}}{\left|\boldsymbol{x}_{(\ell)n}^H \boldsymbol{a}_{(\ell)}\right|} \tag{A-12}$$

with vector $\boldsymbol{a}_{(\ell)}$ which is **independent** of n. This vector is named "auxiliary" vector (per layer) and the approach is the ASV approach. Direct substitution shows that the modified input columns scalar products with the auxiliary vector have identical phase (hence the "synchronization" name):

$$\text{angle}\left(\boldsymbol{x}_{(\ell)n=1}^{(\text{modified})H}\boldsymbol{a}_{(\ell)}\right) = \cdots = \text{angle}\left(\boldsymbol{x}_{(\ell)n=N_S}^{(\text{modified})H}\boldsymbol{a}_{(\ell)}\right) \text{ for } \ell = 1{:}\,\upsilon \tag{A-13}$$

This vector may be optimized as (i.) continual optimization via $\boldsymbol{a}_{(\ell)}$ (ii.) heuristic constructions named "strategies" bringing the advantage of physical meaning of the synchronization.

A heuristic (and as we observe from simulations better performing) approach may be to synchronize multiple columns of the SB precoders with the single (per layer) column of the **wideband** precoder.

E.g. they can be constructed form the (best) eigenvectors of the averaged correlated matrix (per layer). Namely $\boldsymbol{a}_{(\ell)} = \boldsymbol{e}_{(\ell)}$, where $\langle \boldsymbol{C} \rangle \boldsymbol{e}_{(\ell)} = \lambda_{(\ell)} \boldsymbol{e}_{(\ell)}$ and $\langle \dots \rangle$ denotes averaging, $\boldsymbol{C} = \boldsymbol{H}^H \boldsymbol{H}$ or $\boldsymbol{C} = \boldsymbol{H}_A^H \boldsymbol{H}_A$ and for factorized precoder $\boldsymbol{H}_{(A)}^{(e)} = \boldsymbol{H}^{(e)} \boldsymbol{W}_{(A)n}$ (see details for $\boldsymbol{W}_{(A)n}$ in the Note #1). This may be referred to as "strategy" 0.

Note that the strategy "0" goes beyond the input, using the original "raw" channel matrix. We then alternatively for every (fixed) layer ℓ, may perform the SVD of the 2D slice: $[\boldsymbol{x}_{(\ell)1}, \dots, \boldsymbol{x}_{(\ell)N_S}] = \sum_k \sigma_{(\ell)k} \, \boldsymbol{u}_{(\ell)k} \boldsymbol{v}_{(\ell)k}^H$. Then we choose $\boldsymbol{a}_{(\ell)} = \boldsymbol{u}_{(\ell)1}$, where the eigenvector's "1" corresponds to the largest sigma.

It is also may be proposed to synchronize all columns toward a selected column (in general there may be N_S such selections per layer). This may be referred to as "strategies" 1: N_S. For limited number of strategies, a column in the center of the bandwidth (e.g., with index $\lceil N_S/2 \rceil$) may be used as $\boldsymbol{a}_{(\ell)}$.

The ASV approach is also computationally efficient for column length be smaller than the number of SB N_S.

The prior art ([ATM19], [STM+22]) assumes that $\boldsymbol{x}_{(\ell)n}$ are in the 5G beam coordinate basis and then it proposes the phase modification of columns (eigenvectors), $\boldsymbol{x}_{(\ell)n}$ for $n = 1$ to N_S and a fixed ℓ (ranging from ℓ =1 to υ), based on dephasing the element of the most significant beam row containing the maximal amplitude of the matrix element per layer. The amplitudes of that row are then further artificially warped and set all be equal 1 (after scaling) to force a further compression of that row. This scheme already performs better than a no-pre-processing approach. However, in many wireless environments multiple beams can be needed and the strongest beam loses its dominance. Historically, the Prior Art approach may resemble the Type1 precoder (which uses a single beam). In the ASV approach terminology, it corresponds to the simplistic case of $\boldsymbol{a}_{(\ell)}$ be a δ vector with all coefficients be zero and a single component be 1. For example, for $L = 4$ beams, the input columns have size of 8 (due to two polarizations the size is $2L$). If the 3rd row (as an example) contains the largest coefficient per some layer ℓ, then the ASV for the Prior Art is given by the following simple expression: $\boldsymbol{a}_{(\ell)} = [0,0,1,0,0,0,0,0]^T$. Our simulation shows that better optimizations for the ASV bring about average 1[dB] gain for 3 and 4 layers cases, while the maximal gain can be larger, e.g. about 2 dB.

For AI/ML approaches the Prior Art pre-processing for the AI engine has been the scaling of the data of the amplitude interval (see [GWJ+22]) or artificially randomized during the training for robustness or non-overfitting (see [XWL+22]), which are different from the proposed approach.

Further, unitary matrices interestingly allow iterative improvements, adjustments, and optimizations: "train" of subsequent optimizations can be used. This is since multiplication of unitary matrices is a unitary matrix.

$$\mathbb{U}_n^{(1)} * \mathbb{U}_n^{(2)} * \dots * \mathbb{U}_n^{(\text{Noptimizations})} \in Unitary \text{ if } \mathbb{U}_n^{(k)} \in Unitary. \quad \textbf{(A-14)}$$

Importantly, the initial set of parameters of the AI/ML engines may benefit form be learned based on the pre-processing approach, since the input modification during the learning phase makes different environments hopefully be more similar, thus facilitating faster learning and re-learnings.

An observation related to the construction of precoders. The interference is unknown at the base station but known at the UE.

The precoder acts on channel as (below "e" denotes the index of an RE element): $\boldsymbol{r}^{(e)} = \boldsymbol{H}^{(e)} \boldsymbol{W}^{(e)} \boldsymbol{s}^{(e)} + \boldsymbol{n}^{(e)}$. However, the noise term $\boldsymbol{n}^{(e)}$ may contain not only the ambient white noise but also the interference. To cancel or reduce the interference the received signal $\boldsymbol{r}^{(e)}$ at UE array is further pre-processed a linear transformation $\boldsymbol{T}^{(e)}$ as:

$$\boldsymbol{r}^{(e)(\text{with interf. treatment})} = \boldsymbol{T}^{(e)} \boldsymbol{r}^{(e)} = \boldsymbol{T}^{(e)} \boldsymbol{H}^{(e)} \boldsymbol{W}^{(e)} \boldsymbol{s}^{(e)} + \boldsymbol{T}^{(e)} \boldsymbol{n}^{(e)} \quad \textbf{(A-15)}$$

For example, for a single strong interferer channel $\boldsymbol{\hbar}^{(e)}$ the canceller eliminates its direction as: $\boldsymbol{T}^{(e)(\text{canceller})} \equiv \boldsymbol{1} - \frac{\boldsymbol{\hbar}^{(e)} \boldsymbol{\hbar}^{(e)H}}{\|\boldsymbol{\hbar}^{(e)}\|^2}$. The transform $\boldsymbol{T}^{(e)}$ can also act as noise whitener. It can be e.g. constructed as from any factorization of the interference plus ambient noise correlation matrix $\boldsymbol{C}_{\text{noise}}$ as: $\boldsymbol{T}^{(e)(\text{whitening})} = \left(\boldsymbol{F}^{(e)}\right)^{-1}$, where $\alpha_{\text{scaling}} * \boldsymbol{C}_{\text{noise}} = \boldsymbol{F}^{(e)} \boldsymbol{F}^{(e)H}$ with an optional scaling.

The classical Telatar's 1999 eigen-vector solution [Tel99] for precoder construction based on the SVD of the physical channel matrix represents precoder optimization under the white noise.

Hence, it may be used but after the whitener (or heuristically also after the canceller as if it takes out the interference and approximately remains with the ambient noise) i.e., it be applied to the $\boldsymbol{T}^{(e)}\boldsymbol{H}^{(e)}$ channel. Therefore, the precoder which incorporates the interference treatment, is to be constructed based on the modified channel:

$$\boldsymbol{H}^{(e)(\text{with interf. treatment})} = \boldsymbol{T}^{(e)}\boldsymbol{H}^{(e)} \quad \textbf{(A-16)}$$

e.g. from the eigenvectors of the modified channel to and *not* from the eigenvectors of physical channel matrix $\boldsymbol{H}^{(e)}$. In general, any CSI compression method can be used but it is applied now to $\boldsymbol{H}^{(e)(\text{with interf. treatment})}$. This approach effectively merges the interference treatment into the CSI report delivering "surficial information" only. It thus represents an additional compression.

No other information related to the interference, e.g. no total noise correlation matrices need to be conveyed from UE to the BS.

Note #1: on effective Tx number of antennas $\bar{N}_T$: Input to CSI-compression for incorporating precoder matrix factorization.

The input to the CSI-Compression engine can incorporate precoder matrix factorization:

$$\begin{gathered}\boldsymbol{W}_n = \boldsymbol{W}_{(A)n}\boldsymbol{W}_{(B)n}, \text{ e.g. dimensions: } (32 \times 8)^*(8 \times 3) \\ \dim \boldsymbol{W}_n = N_T \times \upsilon, \\ \dim \boldsymbol{W}_{(A)n} = N_T \times \bar{N}_T, \dim \boldsymbol{W}_{(B)n} = \bar{N}_T \times \upsilon\end{gathered} \quad \textbf{(A-17)}$$

The $\boldsymbol{W}_{(A)n}$ is assumed to be known or optimized separately (e.g. based on historical data patterns or e.g. as fixed basis reduction of wideband precoder), and it is $\boldsymbol{W}_{(B)n}$ which is to be compressed. The input to compression can thus be based on the new channel matrix $\boldsymbol{H}_{(A)}^{(e)}$ (e is an index of RE):

$$\boldsymbol{H}_{(A)}^{(e)} = \boldsymbol{H}^{(e)}\boldsymbol{W}_{(A)n} \quad \textbf{(A-18)}$$

E.g., in the 5G prior art, the basis is of the Fourier Transform, as it is done in 5G. Every of the two BS array polarizations (transmitted from different antenna array elements) are treated identically and these columns are named "beams":

$$\begin{gathered}\boldsymbol{W}_{(A)n} = \begin{bmatrix}\boldsymbol{B} & \boldsymbol{0} \\ \boldsymbol{0} & \boldsymbol{B}\end{bmatrix}, \boldsymbol{B} = [\boldsymbol{b}_1, \dots, \boldsymbol{b}_L], \\ \dim \boldsymbol{W}_{(A)n} = N_T \times 2L \text{ , } \dim \boldsymbol{B} = \frac{N_T}{2} \times L \text{ , } \dim \boldsymbol{0} = \frac{N_T}{2} \times L \text{ (zero components), } \dim \boldsymbol{b}_i = \frac{N_T}{2} \times 1\end{gathered} \quad \textbf{(A-19)}$$

Here number of beams, $\boldsymbol{b}_i$, is L. As mentioned, the same beams are used in 5G are simultaneously used for two polarizations.

Note #2: Proof of Capacity conservation. The original SBs precoder acts per RE e as $\boldsymbol{r}^{(e)} = \boldsymbol{H}^{(e)}\boldsymbol{W}\boldsymbol{s}^{(e)} + \boldsymbol{n}^{(e)}$ and its modification (for a given precoder $\boldsymbol{W}$) $\boldsymbol{r}^{(e)} = \boldsymbol{H}^{(e)}\boldsymbol{W}\mathbb{U}\boldsymbol{s}^{(e)} + \boldsymbol{n}^{(e)}$

The capacity of the effective channels is:

$$C_{(e)} = \log_2 \det\left(\boldsymbol{1}_{\upsilon\times\upsilon} + snr * \boldsymbol{H}_{\text{eff}}^{(e)H}\boldsymbol{H}_{\text{eff}}^{(e)}\right) \quad \textbf{(A-20)}$$

One thus needs to proof that capacity is preserved for:

$$\boldsymbol{H}_{\text{eff}}^{(e)} = \boldsymbol{H}^{(e)}\boldsymbol{W} \text{ and } \boldsymbol{H}_{\text{eff}}^{(\text{modified})(e)} = \boldsymbol{H}^{(e)}\boldsymbol{W}\mathbb{U} \quad \textbf{(A-21)}$$

where $\mathbb{U}$ is the unitary transform matrix. (We assume matrices $\boldsymbol{W}$ and $\mathbb{U}$ be constant per every SB and thus do not mark them with the element indices. We may mark it as $\mathbb{U}_n$). The capacity conservation can be seen immediately by factoring the relation below (using $\mathbf{1}_{\upsilon\times\upsilon} = \mathbb{U}^H\mathbb{U}$) as:

$$\begin{aligned}\mathbf{1}_{\upsilon\times\upsilon} + \alpha\boldsymbol{H}_{\text{eff}}^{(\text{modified})(e)H}\boldsymbol{H}_{\text{eff}}^{(\text{modified})(e)} &= \mathbb{U}^H\mathbb{U} + \alpha\mathbb{U}^H\boldsymbol{H}_{\text{eff}}^{(e)H}\boldsymbol{H}_{\text{eff}}^{(e)}\mathbb{U} \\ &= \mathbb{U}^H\left(\mathbf{1}_{\upsilon\times\upsilon} + \alpha\boldsymbol{H}_{\text{eff}}^{(e)H}\boldsymbol{H}_{\text{eff}}^{(e)}\right)\mathbb{U},\ \alpha \equiv snr\end{aligned} \quad \textbf{(A-22)}$$

$$\mathbf{1}_{\upsilon\times\upsilon} + \alpha\boldsymbol{H}_{\text{eff}}^{(\text{modified})(e)H}\boldsymbol{H}_{\text{eff}}^{(\text{modified})(e)} = \mathbb{U}^H\mathbb{U} + \alpha\mathbb{U}^H\boldsymbol{H}_{\text{eff}}^{(e)H}\boldsymbol{H}_{\text{eff}}^{(e)}\mathbb{U} = \mathbb{U}^H\left(\mathbf{1}_{\upsilon\times\upsilon} + \alpha\boldsymbol{H}_{\text{eff}}^{(e)H}\boldsymbol{H}_{\text{eff}}^{(e)}\right)\mathbb{U},\ \alpha \equiv snr$$

Since for any matrices $\boldsymbol{A}$, $\boldsymbol{B}$ and $\boldsymbol{C}$: $\det(\boldsymbol{ABC}) = \det(\boldsymbol{A}) * \det(\boldsymbol{B}) * \det(\boldsymbol{C})$ and since

$1 = \det(\mathbf{1}_{\upsilon\times\upsilon}) = \det(\mathbb{U}\mathbb{U}^H) = \det(\mathbb{U}) * \det(\mathbb{U}^H)$, the determinant is the same value with the original and for the modified precoders. Then its $\log_2 \det(...)$ is identical and thus the capacity preserves. QED.

Note #3: Total power (over all Rx antennas) conservation proof for unitary transform. The sum of the information signal powers on all UE antennas is $P_e = \left\|\left(\boldsymbol{H}^{(e)}\boldsymbol{W}\right)_{\text{at RE with index } e}\right\|_2^2$ which follows from the RX equation for UE RX antenna array $\boldsymbol{r}^{(e)} = \boldsymbol{H}^{(e)}\boldsymbol{W}\boldsymbol{s}^{(e)} + \boldsymbol{n}^{(e)}$, ($\dim \boldsymbol{r} = N_R \times 1$) . We may rewrite the power equation as:

$$P_e = \text{Trace}\left(\boldsymbol{W}^H\boldsymbol{H}^{(e)H}\boldsymbol{H}^{(e)}\boldsymbol{W}\right)_{\text{at RE with index } e} \quad \textbf{(A-23)}$$

One thus needs to show that the unitary transform of precoder, $\boldsymbol{W} \to \boldsymbol{W}\mathbb{U}$, preserves the total power:

$$\text{Trace}(\boldsymbol{W}^H\boldsymbol{C}_{\text{eff}}\boldsymbol{W}) = \text{Trace}(\mathbb{U}^H\boldsymbol{C}_{\text{eff}}\mathbb{U}) \text{ , where } \boldsymbol{C}_{\text{eff}} \equiv \boldsymbol{W}^H\boldsymbol{H}^{(e)H}\boldsymbol{H}^{(e)}\boldsymbol{W} \quad \textbf{(A-24)}$$

The trace conservation (and thus the total power conservation) is a direct result of capacity conservation, which can be seen from the Taylor expansion of the determinant in the capacity expression:

$$D(\boldsymbol{C}_{\text{eff}}) = \det(\mathbf{1}_{\upsilon\times\upsilon} + snr * \boldsymbol{C}_{\text{eff}}) = snr * \text{Trace}(\boldsymbol{C}_{\text{eff}}) + O(snr^2) \quad \textbf{(A-25)}$$

Since $D(\boldsymbol{C}_{\text{eff}}) = D(\mathbb{U}^H\boldsymbol{C}_{\text{eff}}\mathbb{U})$, then all expansion coefficients about SNR parameter are identical including the linear term represented by the trace, which thus is preserved.

A.4 Resource allocation and protocols for inter-UE sensing

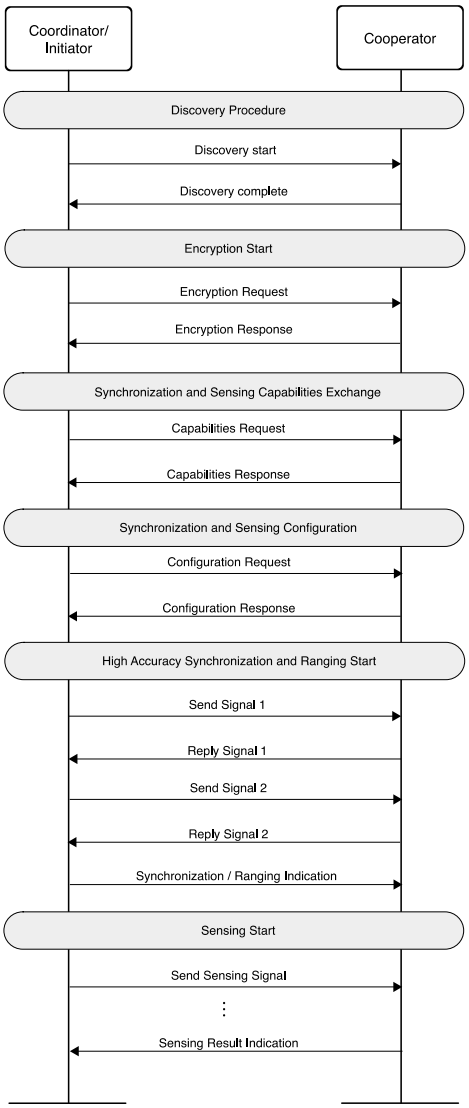

Figure A-5: Message sequence chart for the resource allocation protocols for inter-UE sensing.

Discovery: The primary purpose of discovery is to find and communicate with a nearby device without relying on a cellular base station. As shown in Figure A-5 the discovery process basically consists of two steps: Discovery Start and Discovery Complete. In Discovery Start device A/initiator listens for discovery signals. Devices that want to be discovered activate the discovery process by sending discovery signals at regular intervals. This discovery process could be based on 3GPP or non-3GPP technology depending detailed requirements. But as this use case assumes to out-of-network coverage, discovery cannot rely on assistance information. The discovery is deemed complete whenever device A/initiator is able to receive and decode signals from device B and extracts the necessary information, such as device B identifier along with some quality measures like e.g. SNR. The discovery process is not encrypted.

Encryption: The encryption procedure shall ensure that information exchanged between the Coordinator/Initiator and the Cooperator is transmitted encrypted, thereby safeguarding security and privacy. It is recommended to utilize an existing security protocol. Specifically, TLS 1.3 (or QUIC as the general protocol for communication between Coordinator/Initiator and the Cooperator) is suggested. For the security handshake, both TLS 1.3 and QUIC can employ a single round-trip-time handshake:

1. Initiator “Client Hello” (key agreement protocol, cipher suite, key share),
2. Cooperator “Server Hello” (key agreement protocol, certificate, key share) + Server Finished,
3. Initiator Check Certificate, Generate Keys, Client Finished and

4. Secured Communication.

An impersonation attack, where an attacker attempts to break the authentication by impersonating the legitimate transceivers is thus prevented using good cryptography and a state-of-the-art authentication/signature protocol. Data exchange between Coordinator and Cooperator devices occurs on an encrypted connection.

Synchronization and Sensing Capability Exchange and Configuration: After Discovery and Encryption, the initiator has a list of potential cooperators. To identify a suitable sensing partner, it is necessary that the initiator knows about the capabilities of potential collaborators such that he may select the most suitable one for the targeted use case. Capabilities include both, synchronization and sensing capabilities, that need to complement the respective other capability. First, the initiator requests the capabilities from potential cooperators. The request may be generic such that the responder provides all options and parameters it is capable of, or it may include a list of parameters/ features the initiator is interested in. The potential cooperator may respond with a general list of capabilities or limit the list to the specific capabilities it has been asked for. If a specific configuration was requested, it may simply accept or decline the request. This method is beneficial in terms of privacy since the potential collaborator does not have to reveal its full capabilities to allow the coordinator to judge the collaborators further properties. In addition, the geometric constellation should be considered such that the object finds itself in the bi-static region (Figure A-6). This could be achieved, e.g. by application support on the coordinator device. The coordinator may select the most suitable collaborator device and request a specific configuration that is common to both devices. If the potential cooperator accepts the request, the sensing link is established.

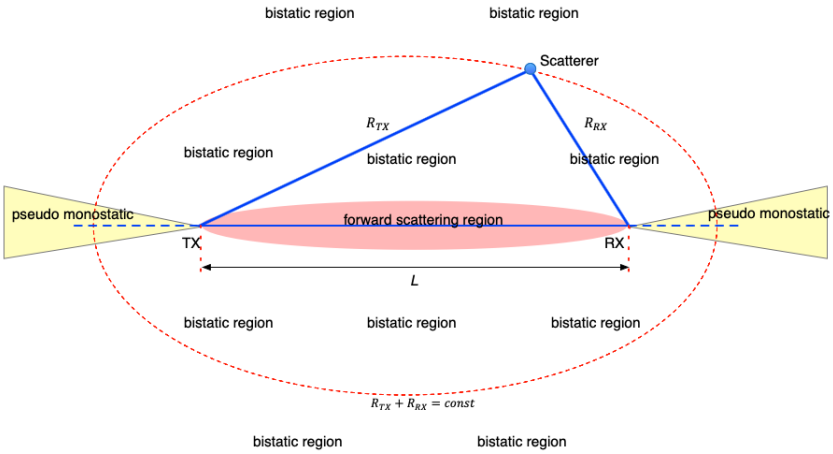

Figure A-6: Figure illustrating the bi-static sensing region for a Tx-Rx pain in the presence of a scatterer.

High Accuracy Synchronization and Ranging: Exemplary this procedure is described on PBR with single antenna element and a minimum of two frequencies. It can logically be extended to a higher number of antenna elements and more frequencies, depending on the previous steps of capability exchange and synchronization. First a measurement of frequency offset between the coordinator and cooperator is performed. The compensation of the fractional frequency offset could be compensated on either side. After aligning the frequency offset, the proposed PBR can start with a two-way exchange of two frequencies and corresponding synchronization/ranging indication.

From a privacy and security aspect, there are various security features to detect and reduce the probability of distance spoofing. Range extender attacks where an attacker amplifies the signal without altering the phase or frequency, making the devices appear closer to each other than they actually are. PBR based measurement cannot prevent this kind of attack since an attacker can amplify or relay the signal beyond the ambiguity range. However, additional ToF measurement, i.e. round-trip time (RTT) approach, can prevent such attacks since time does not roll over. The discrepancy between RTT and PBR measurement results can be used to detect such attempt. Phase manipulation attack where an adversary manipulates the phase of the constant tone signal to reduce the estimated distance. This kind of attack only affects phase and not the time. Thus, RTT can be used with PBR to provide additional security layer to detect this kind of attacks. Early detect late commit (EDLC) where an attacker aims at decreasing the ToF, for instance, by detecting a bit in a symbol and

predicting the symbol even before receiving it completely. This kind of attack affects modulated time sequences. However, PBR can offer some protection against such attacks within the ambiguity range. Another way to detect an attack could be via mono-static sensing by the coordinator device which is executed in a later step.

Bi-Static Sensing: After establishing synchronization and ranging indication complete, the actual sensing procedure can start. The *coordinator device A* transmits sensing waveforms, which are captured and processed by the *cooperator device B*. Processing by *device B* may involve range $R_{TX} + R_{RX}$, AoA and Doppler frequency estimation. The details of signal waveform or signal processing were defined by the sensing configuration step above and depend heavily on the negotiated sensing capabilities, e.g antenna configurations, waveforms, bandwidth, just to name a few. Eventually *device B* will communicate back estimation results to *device A*.

From a security and privacy point of view more aspects are different to monostatic sensing. If e.g. an attacker is jamming, he will be targeting the coordinator but isn't aware of the cooperator's position. With that jamming becomes less effective. Although a single person is targeted other persons and objects not targeted intentionally might be reflecting back signals and thus will be captured in the signal response. Depending on whether they carry a device a broadcast of the ongoing sensing operation will reach them. With strong encryption and the bi-static device setup, no information/results are forwarded to another entity outside of *device A* and *B*. Also keeping in mind that *device A* and *B* have given consent and established encrypted communication. This results in highly trusted communication but also ranging results. The sensing procedure is also negotiated and configured in a secure way. Spoofing of NLoS *person* echo by an attacker will be difficult assuming waveform randomization plus time and frequency hopping. The attacker has an additional challenge as it doesn't know the LoS and dominant NLoS seen by *device B*.

A.5 Multi-RAT Spectrum Sharing

Table A-1: Simulations parameters for the simulation setup evaluating multi-RAT spectrum sharing.

	Attribute	Value or assumption
PHY	Carrier frequency	800 MHz
	System bandwidth	FDD: 20 MHz (106 RBs) TDD: 100 MHz (276 RBs)
	Subcarrier spacing	FDD: 15 kHz TDD: 30 kHz
	Symbols per subframe	14
	MIMO	4x4 (Rank = 2)
	Physical Layer	6G PHY ≡ NR PHY
MAC	Scheduling policy	Proportional Fairness (TD) Round Robin (FD)
	HARQ	Asynchronous with CC (Max. 4RTx)

NW deployment	Model	3GPP NR UMa
	# Macro cells	21
	ISD	500 m
	Duplexing mode	FDD TDD (Frame structure: DDDSUDDDSU)
	Subcarrier Spacing SCS, FDD	15 KHz
	Subcarrier Spacing SCS, TDD	30KHz
	Number of UEs in the cell	2-30 UEs/Cell FDD 2-60 UEs/Cell TDD
	Splitting Ratio	RAT1: RAT2 = {100:0, 80:20, 70:30, 50:50}

A.6 TN/NTN radio interference mitigation

The current spectrum allocations indicate high probability of TN and NTN radios operating in adjacent bands that could lead to mutual interference and consequent desensitization of TN and/or NTN receiver in a heterogeneous wireless node. It is essential that 6G will be able to share the spectrum with the incumbent users in the best possible way. Depending on frequency range shared, the victim nodes and the most appropriate spectrum sharing mechanisms will differ. Two different spectrum sharing scenarios between 6G TN and NTN are discussed below in more detail.

1) TN is sharing the spectrum with satellite earth stations and the implemented spectrum sharing mechanisms are **protecting the downlink (FSS DL) of the earth station** from any harmful interference, which would typically be caused by the nearby TN BS transmissions. This kind of spectrum sharing scenario can be enabled by defining a minimum required separation distance (coordination area) around the victim satellite earth station, where the deployment of BSs will not be allowed. Since the earth station antennas are highly directional, the required separation distance could vary from tens of kilometres to less than a kilometre, depending on whether the interfering BS is located in front of the earth station antenna, on the side, or behind it. The size of the coordination area will also depend for example on the type of environment between the nodes, transmit power of the interfering BSs, the type and orientation of the BS antennas, and the number of simultaneously interfering BSs. Another challenge related to spectrum sharing with NGSO satellite systems is that the earth station antenna beam directions would be dynamically changing, which would have a corresponding impact on the size of the coordination area. The spectrum sharing mechanisms applicable for this scenario could be based on the use of databases to reduce the complexity and to make the spectrum sharing more efficient. Furthermore, the use of more realistic set of models and assumptions for both the victim and interfering nodes would lead to a more accurate estimate of the interference between the nodes and further, to a more efficient spectrum sharing scheme compared to a “worst case” interference analysis. Examples of the more realistic models include the use of an earth station antenna pattern based on Bessel functions, more realistic distribution of the BS beam directions and a more realistic assumption of the average BS resource utilization.

2) TN is sharing the spectrum with satellites, and the spectrum sharing mechanisms are **protecting the UL (FSS UL) of the satellite** from any harmful interference caused by the transmissions from the BSs located within the satellite spot beam. The main challenges for this spectrum sharing scenario are: a) the total interference is cumulated from a potentially large number of BSs, b) the victim satellites are located above the horizon reducing the path losses between the nodes, c) the victim satellites may be moving (NGSO satellites). Hence, the interference cannot be avoided by limiting the emissions from a selected group of BSs, but a more global solution is required instead. During the WRC-23 a new concept called the expected EIRP requirement was introduced to protect the FSS UL within the upper-6 GHz band (6425 – 7125 MHz) while allowing as much freedom as possible for the actual design of the BS or how the BSs are deployed. The expected EIRP requirement defines the maximum allowed average EIRP emission limit for the BS as a function of the elevation angle (vertical angle above the horizon), averaged over the different beamforming directions and the azimuth (i.e., horizontal) angles. The benefits of the expected EIRP requirement are that it is a simple, static and global requirement, does not require any knowledge of the location of the victim node and does not specify any specific type of implementation for the BS antenna. The downside is that the emission limit may be too restrictive for scenarios (geographical locations or time instants) without any victim nodes. To fix that, more dynamical but also more complex solutions would be required instead. The dynamic spectrum sharing solutions would typically rely on having at least information about the existence and/or location of the victim nodes and would aim at reducing the BS emissions towards the victim nodes, when needed. Furthermore, they could include for example the use of databases, advanced beamforming methods (e.g., null steering), and advanced radio resource management methods (e.g., scheduling restrictions, adaptive downlink power control, spectrum splitting).

It becomes thus more evident that a multi-pronged approach consisting of a harmonious combination of various techniques will be needed. In the following, we provide additional insights and conclusions on the key techniques presented in Sec. 9.4.2.

Antenna Pattern Management: Presence of TN base stations that operate in a spectral band at close proximity or harmonically related to the spectrum of the (typically weaker) NTN signal of interest could lead to desensitization of the NTN receiver. Similarly, a strong NTN emitter such as a drone or a LEO satellite could desensitize a TN receiver attempting to operate in a typical urban environment with deep in-band fading. The proposed scheme to mitigate such interference with optimization of the radiation pattern of the receivers for beam maxima and null (with, e.g., ANN-based adaptive tuning) is depicted in Figure A-7.

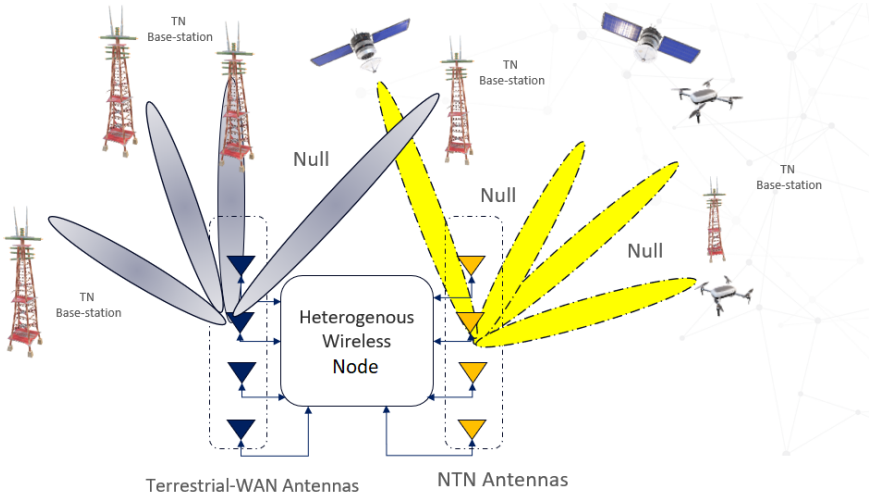

Figure A-7: Interference mitigation via antenna beam maxima and null.

Handshaking: TN and NTN radios Tx and Rx information handshake is important, especially when radios operate in adjacent bands. Nonlinear transfer functions are inherent characteristics of most key RF circuits such as RF amplifiers and mixers. The typical relation between the output signal y and input signal x in a non-linear RF circuit may be expressed in the form of a power series as:

$$y = ax + bx^2 + cx^3 + dx^4 + ex^5 \quad \textbf{(A-26)}$$

Envelope masking by square law component in the transfer function is an adverse impact on a wireless receiver which could happen when a strong jamming signal enters the receive chain along with the signal of interest. This can be analysed by considering a multi-tone input:

$$x = A1 * \cos \omega_1 t + B1 * \cos \omega_2 t \quad \textbf{(A-27)}$$

subject to the non-linear transfer function described by (A-26). In (A-27), $A1$ and $B1$ are modulated envelopes of two carriers at frequencies ω_1 and ω_2 respectively.

Typical wireless receivers involve coherent demodulation where the LO is tuned to the carrier frequency of interest. Consider for example, it is intended to receive the carrier at frequency ω_1, which involves mixing the input signal with the LO signal $\cos \omega_1 t$. When multiplied with the input signal of (A-26), the first term yields $A1 * \cos \omega_1 t = A1/2 * [1 + (\cos(2\omega_1 t)]$, consisting of the intended baseband envelope $A1/2$ and the double frequency component at $\omega_1/2$, which can be filtered out using a low pass filter. Now, if the signal described in (A-27) is subject to the nonlinear transfer function described by (A-26), the envelope $A1$ that is demodulated by the receiver can be masked by the parasitic component $B1^2$. This may be verified with ease by taking the square of the input signal x: $x^2 = \frac{A1^2}{2} + \cos \omega_1 t + \frac{B1^2}{2} + \cos \omega_2 t + \frac{A1B1}{2} \cos(\omega_1 - \omega_2 t) + \cos(\omega_1 + \omega_2 t)$. The envelope components $A1^2$ and $B1^2$ will occupy the same spectrum as $A1$ when demodulated. If the first part of signal x denoted by $A1 * \cos \omega_1 t$ is the intended carrier to be received, say by the NTN receiver, and if the second $B1 * \cos \omega_2 t$ is the carrier being transmitted by the TN transmitter at power much higher than the received signal strength in the same physical entity and coupled into the NTN receiver's path, the envelope $B1^2$ can completely mask the demodulated NTN carrier's envelope $A1$ thereby desensitizing it.

An example handshaking arrangement between TN and NTN radios in a heterogenous wireless node could be realised as below:

- TN/NTN information exchange
  - Inform each other when transmitting or receiving at band edges: Carrier frequency, bandwidth, power
  - Terrestrial wireless area network (WAN) informs NTN its transmission time slots and vice versa.
  - NTN time aligns transmission slots with terrestrial WAN where possible and vice versa.
- Terrestrial Tx ready to transmit when NTN is receiving at band edge
  - Backoff Tx power at the terrestrial Tx.
  - Report poor CQI at edge affected resource blocks/spectrum points before commencing transmission and update link budget.
  - Consequently, expect lower MCS or partial resource block allocation for transmission.
- NTN Tx ready to transmit when TN Rx is receiving
  - Backoff Tx power at NTN.
  - Consequently, expect lower MCS for link budget
  - Reduce Tx bandwidth for a slot if possible else shift carrier frequency if possible.

Signal Processing: Suppression of interference can be further improved via signal processing. The square law non-linearity described above is just one of the mechanisms that can desensitize receivers. Odd harmonic mixing, third order non-linearity, reciprocal mixing are equally significant desensitization mechanisms along with parasitic circuit and antenna coupling. In general, the input signal matrix to a receiver's demodulator may be expressed as a weighted sum of several inputs, where the intended input is one of them and the others are parasitically coupled inputs. The demodulator's output may therefore be expressed as the outcome of a MIMO process where the coupling paths form the MIMO elements. This can be mathematically denoted as:

$$\begin{bmatrix} y_1 \\ \vdots \\ y_N \end{bmatrix} = \begin{bmatrix} a_1 1 & \cdots & a_1 N \\ \vdots & \ddots & \vdots \\ a_N 1 & \cdots & a_N N \end{bmatrix} \begin{bmatrix} x_1 \\ \vdots \\ y_N \end{bmatrix} \Rightarrow [Y] = [A][X] \quad \textbf{(A-28)}$$

Digitally assisted calibration process could be executed at start-up or periodically based on preset criteria to estimate the coupling matrix A in (A-27), multiply the demodulated output Y by the inverse of matrix A for interference cancellation to yield a signal similar to the intended signal X as shown below:

$$[A]^{-1}[Y] = [A]^{-1}[A][X] = [X] \quad \textbf{(A-29)}$$

The worst cases of mutual interference can be expected when one of the entities transmits while the other one receives at a frequency band that is in proximity or harmonically related. The transmitter's signal being inherently high in power would cross modulate the envelope of the received signal if the latter is weak, around 40 dB lower in power. This is depicted in Figure A-8. If X_1 is the intended signal at the receiving antenna, X_2 is the transmitter's output signal that couples into the receiving antenna, and Y_1 is the demodulated baseband at the receiver, Y_1 could be represented as a weighted sum of inputs X_1 and X_2 in the form of $Y_1 = H_{11}X_1 + H_{21}X_2$, where H_{11} is the gain of the received signal in the receiver's RF chain in the receiver's band, H_{21} is the gain of the coupled transmitted signal in the receiver's RF chain in the receiver's band. Both H_{21} and H_{11} are vectors with magnitudes and phases. Now, X_2 is known since the same hardware generated it, H_{21} can be determined through factory calibration. Therefore, $H_{21}X_2$ can be cancelled adaptively from the demodulated baseband in the DSP to recover the intended receiver signal. This is one of the cases covered under the scope of equation (A-28) and (A-29). In practice, the values of H_{21} and H_{11} are functions of input signal power and the factory calibration would need to be done across a range of powers covering the entire dynamic range of the receiver. The values of H_{21} and H_{11} can vary with temperature and would need to be monitored and calibrated adaptively in the field.

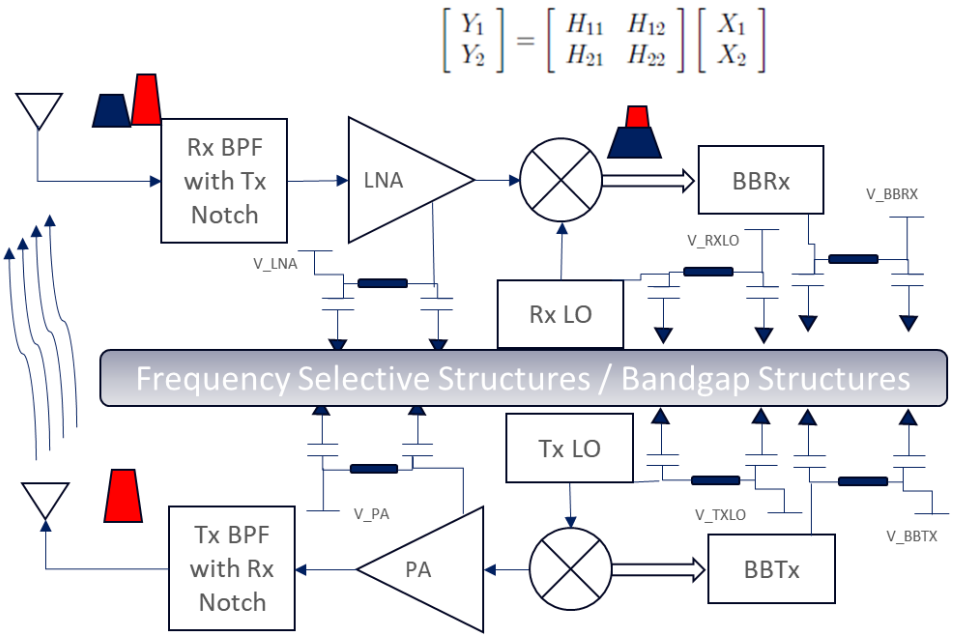

Figure A-8: Typical interference scenario between TN transmitter and NTN receiver and vice versa.

A.7 Indoor jammer localisation

Table A-2: Baseline-last: Model performance when individually trained using the 4 different signal lengths and evaluated across all signal lengths.

Last Time Steps	Test Signal Length

	256	512	1024	2080
k = 64	**99.94%**	**8.45%**	**5.01%**	**4.82%**
k = 128	**36.15%**	**99.93%**	**5.31%**	**5.80%**
k = 256	**15.63%**	**27.87%**	**99.23%**	**5.00%**
k = 512	**7.05%**	**7.05%**	**5.61%**	**98.67%**

Table A-3: Model performance with IMI approach at different k values.

Incremental Multi-Interference length	**Test Signal Length**			
	256	**512**	**1024**	**2080**
k = 64	**47.91%**	**70.39%**	**75.97%**	**99.96%**
k = 128	**50.67%**	**96.50%**	**99.90%**	**99.97%**
k = 256	**30.13%**	**90.05%**	**99.36%**	**99.87%**
k = 512	**30.37%**	**96.07%**	**99.88%**	**99.97%**

Table A-4: Model performance with SMI approach at different k values.

Shifting Multi-Interference window	**Test Signal Length**			
	256	**512**	**1024**	**2080**
k = 64	**48.28%**	**96.99%**	**99.43%**	**99.92%**
k = 128	**43.32%**	**90.75%**	**99.90%**	**99.97%**
k = 256	**66.73%**	**98.15%**	**99.95%**	**99.97%**
k = 512	**42.44%**	**84.92%**	**99.31%**	**99.85%**